January 2009

Oxy-Coal Combustion: Submicrometer Particle Formation, Mercury Speciation, And Their Capture

Achariya Suriyawong
Washington University in St. Louis

WASHINGTON UNIVERSITY

School of Engineering and Applied Science

Department of Energy, Environmental and Chemical Engineering

Dissertation Examination Committee:
Pratim Biswas, Chair
Da-ren Chen
Richard L. Axelbaum
Daniel E. Giammar
Himadri Pakrasi
Ye Zhuang
Christopher J. Hagedorn

OXY-COAL COMBUSTION: SUBMICROMETER PARTICLE FORMATION, MERCURY SPECIATION, AND THEIR CAPTURE

by

Achariya Suriyawong

A dissertation presented to the
Graduate School of Arts and Sciences
of Washington University in
partial fulfillment of the
requirements for the degree
of Doctor of Philosophy

August 2009

Saint Louis, MO

Acknowledgments

Since I was very young, I had dreamed of becoming a scientist and getting a Ph.D. Through God's grace and the people He put in my life, my dream has become a reality. I thank God for His kindness and blessing, and for everything He has provided me. I am also grateful for the remarkable experience toward earning this degree — it had stretched me and helped me grow both professionally and personally. There are so many people who helped me and to whom I owe my appreciation and gratitude.

My deepest and most sincere gratitude goes to Prof. Pratim Biswas for fostering my intellectual knowledge, supporting and always believing in me. I am, indeed, thankful for the time I had spent working closely with and learning from him. His efforts in mentoring me will significantly influence my future.

I thank Drs. Richard L. Axelbaum, Da-ren Chen, Dan E. Giammar, Himadri Pakrasi, Ye Zhuang, and Christopher J. Hagedorn for serving on my committee. Their valuable comments and suggestions have made this dissertation completed.

Many thanks also go to Mr. Jim Ballard, and Ms. Sandra Matteucci, the Engineering Technical Writing Center, for their diligently work through my manuscripts and improve their language. The help from Mary Clemens, Engineering Student Coordinator, Graduate School of Arts &Sciences, and the staff of the EECE department of Washington University – Kim Coleman, Rose Baxter, Beth Mehringer, Angela Weatherspoon, and others, is appreciated as well.

I wish to extend my warmest thanks to the members of the Aerosol & Air Quality Research Laboratory and EECE-friends for their countless discussions and assistance throughout these years in Saint Louis.

I want to thank the Dept. of Environmental Engineering, the Environmental Research Institute, and the National Center of Excellence for Environmental and Hazardous Waste Management, Chulalongkorn University, for supporting and allowing me to pursue my Ph.D. In particular, I want to offer my sincere thanks to Assoc. Prof. Suree Khaodhiar, Assoc. Prof. Dr. Orathai Chavalparit and Ms. Wannee Puttitavorn for the long-distance assistances and supports.

I am immensely grateful to Mr. Alan P. Giang (Rock), who believes in and is always proud of me. I would not make it here today without your supports and encouragements.

I wish to offer my heartfelt thanks to Dr. Subramanya V. Nayak for his continuous love, support and caring. Thank you for constantly encouraging, and being patient with me. You always challenge me to come up higher and to see the best in every situation.

As I look back, I am so thankful to all my teachers for providing me the strong foundations, which now allow me to achieve my dreams. I wish to express my sincere thank-you to all of them.

I owe everything I have accomplished to my family:

- My Father, Pa, thank you for the adventurous heart, strength, and "never give up" attitude that you have passed on to me and to all four of us. These are the key elements for everything I have and will achieve in my life.
- My Mother, Ma, "a big smile, be kind, and try to compromised" approach you taught me, has made many things in my life go smoothly. Your laps are the softest- and safest-place, where I always want to rest upon; your hug and your smile are the continual blessing to me.

- My dear sister, J, your open mind-set, your tirelessly caring, constant support and understanding have given me confidence to follow my dream and to always do the best that I possibly can. You are an incredible, unbelievable and the best-sister in the world.
- Marisa and Vitaya, thank you for constantly inspiring and showing me that you can be whatever you dream about. You are the ones whom I always look up to, and the accomplishments you have made are the foot-steps I will follow.

I am so grateful to be born and raised by this loving and supportive family. Just only the "unconditional love" that all of you have given me initiates and prospers everything in my life……and it is much more than I could ever ask for …

As my dream of earning Ph.D has become a reality, I also wish to thank, from the bottom of my heart, to all those who directly and indirectly sharpened me and helped making this dream come true.

…Thank you

Achariya Suriyawong
Washington University in Saint Louis

Dedicated to:

My Parents (Pa & Ma)
My Sisters (Siriphan and Marisa)
and My Brother (Vitaya)

Table of Contents

List of Tables

Chapter 2

Chapter 3

Chapter 4

Chapter 5

Chapter 6

List of Figures

Chapter 1

Chapter 2

Chapter 3

Chapter 4

Chapter 5

Chapter 6

ABSTRACT OF THE DISSERTATION

Oxy-coal Combustion: Submicrometer Particle Formation, Mercury Speciation, and Their Capture

by

Achariya Suriyawong

Doctor of Philosophy in Energy, Environmental and Chemical Engineering

Washington University in Saint Louis, 2009

Professor Pratim Biswas, Advisor

Energy is the issue of great importance at the present. Coal, the cheapest and the most abundant reserve fossil fuel, is currently one of the most widely used energy source globally and will continue to be in the foreseeable future. The use of coal has also posed many world-wide environmental challenges, including the control of particulate matter, mercury, and trace metals, and carbon oxide (CO_2) emissions. The rising of CO_2 level in the atmosphere due to burning of fossil fuels is one of the major factors contributing to the global climate change. Capturing CO_2 from coal combustion exhaust has been receiving significant attention; however, the volume fraction of CO_2 in conventional coal combustion system (with air) ranges only 13%-15%, making it difficult to cost-effectively design the systems. Oxy-coal combustion or O_2/CO_2 recycled coal combustion is one of the promising techniques to overcome the limitation of low CO_2 concentration in the exhaust. Before this technology can be employed, the effects of oxy-

coal combustion on the pollutants associated with coal combustion, including fine particle, gaseous mercury and heavy metal emissions, need to be established. In addition, the influences of oxy-coal combustion on the performance of the current pollution control technologies, such as an electrostatic precipitator (ESP), need to be addressed.

This dissertation investigated two aspects of coal combustion process: (1) pollutant formation, specifically submicrometer particles and mercury, and (2) pollutant control. The first part of dissertation addresses the impact of oxy-coal combustion on the formation submicrometer particles and the speciation of gaseous mercury. The second part focuses on the performance of two pollutant control technologies, including an ESP for capturing submicrometer particles and nano-structured TiO_2 with UV irradiation for mercury capture. The findings presented here can be broadly divided into three parts. The first part reports the influence of oxy-coal combustion on submicrometer particle formation and capture using an ESP. The second part addresses the impacts of oxy-coal combustion on mercury speciation. The third part investigates the performance of nano-structured sorbent for capturing mercury and controlling heavy metal emissions from combustion process. The findings presented here can be used as a guideline for proper operation and control of pollutants generated from both oxy-coal and conventional combustion systems.

Chapter 1

Introduction

1.1 BACHGROUND AND MOTIVATION

Energy is an issue of great importance in current times. Fossil fuels, including coal, oil, and natural gas, are currently the world's most important energy sources, and will continue to be dominant for many decades. Fossil fuels provide approximately 86% of global energy supplies, and the remainder is supplied by nuclear power and renewable sources, including solar, wind and geothermal power. At the present, the world primary energy consumption is approximately 230 million barrels per day of oil equivalent (MBDOE), and it is expected to reach 325 MBDOE, or approximately 40 percent more in 2030 [1]. Fossil fuels are also projected to supply approximately 80% of the global energy consumption in 2030 [1]. Currently, there is no other cost-effective alternative energy source to overcome the demand for fossil fuels. While extensive research and development in renewable energy is in progress, fossil fuels will continue to be the dominant energy source in the foreseeable future.

Coal plays a significant role in meeting our energy needs. It is the most abundant fossil reserve: 70% of the world's known fossil reserves, and 94% of the US reserves. According to the U.S. Energy Information Administration and the International Energy Agency [1], coal reserves are projected to provide about 200 years of energy, while natural gas will provide it of 120 years, and oil for 60 years with at current usage rate. A projection reported at the World Energy Conference

shows that the use of coal will continue to increase throughout this century, becoming the world's most important fossil fuel. At the present, majority of coal demand is for electricity generation, accounting for approximately 74%. This demand is projected to dramatically increase and will be accounting for nearly 90% of the increase in the energy demand between 2000 and 2030 [1].

Increasing use of coal has also posed many challenges, including control of particulate matter, mercury, trace metals, and carbon dioxide (CO_2) emissions. Global climate change is of great concern at the present. The rising of CO_2 levels in the atmosphere due to human activities, such as burning of fossil fuels and deforestation, is one of the major factors contributing to the climate change. Capturing CO_2 from coal combustion exhaust has been receiving significant attention; however, the volume fraction of CO_2 in a conventional coal combustion system (with air) ranges only 13% - 15%, making it difficult to do so in a cost-effectively manner. One approach to overcome the limitation of low CO_2 concentration in the exhaust is oxy-coal combustion, or O_2/CO_2 recycled coal combustion. Coal is combusted in an oxygen-enriched stream (by removing nitrogen) with recycled exhaust gas to serve the role of the diluent. An oxy-coal combustion system is shown in Figure 1.1. At steady state operation, such a configuration would result in CO_2 concentration of 98% in the exhaust, making it more feasible to capture [2-5]. There have been several studies on the design and evaluation of coal combustion efficiency in oxy-coal

combustion [3, 6-9]. While advantages with respect to the potential for CO_2 capture, reduction of NO_X emissions, and improvement in combustion efficiency have been demonstrated; the effects of oxy-coal combustion on the other pollutants associated with coal combustion, such as fine particles, mercury and heavy metal emissions, have not yet been established. In addition, the influence of oxy-coal combustion on the performance of current pollution control technologies, such as electrostatic precipitators (ESPs) and mercury control technologies need to be evaluated.

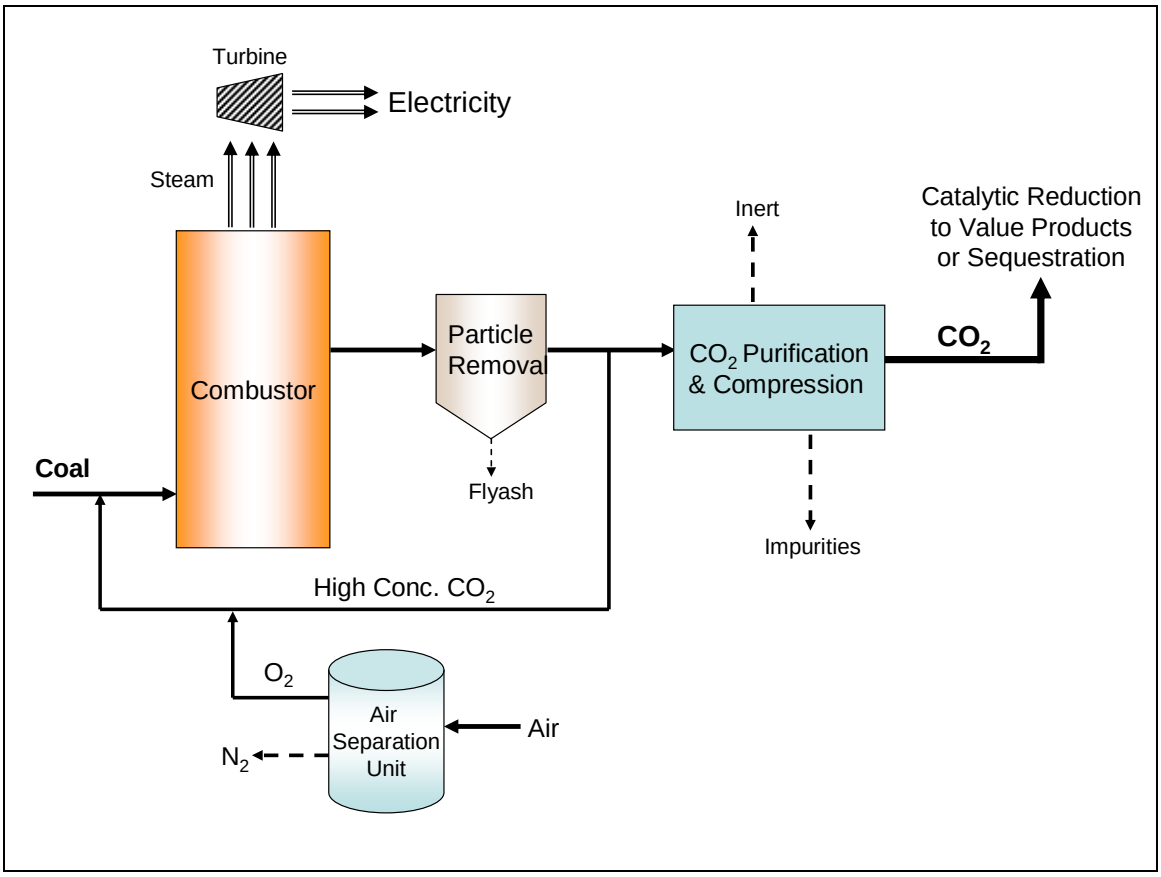

Figure 1.1. A schematic diagram of oxy-coal combustion.

This dissertation investigated two aspects of coal combustion process: (1) pollutant formation, specifically submicrometer particles and mercury, and (2) pollutant control. The first part of dissertation addresses the impact of oxy-coal combustion on the formation submicrometer particles and the speciation of mercury. The second part focuses on the performance of two pollutant control technologies, including an ESP and nano-structured TiO_2 with UV irradiation for mercury capture. The findings presented here can be broadly divided into three parts. The first part reports the influence of oxy-coal combustion on submicrometer particle formation and capture using an ESP. The second part addresses the impacts of oxy-coal combustion on mercury speciation. The third part investigates the performance of nano-structured sorbent for capturing mercury and controlling heavy metal emissions from combustion process.

1.1.1 Submicrometer particle formation and their capture in an electrostatic precipitator

Coal combustion is one of the largest anthropogenic sources for particulate matter emission. Coal combustion accounted for 570 ktons/yr of $PM_{2.5}$ in the United States in 2001 [10]. Submicrometer size particles (100 nm < diameter < 1μm) and ultrafine particles (diameter < 100nm) generated from coal combustion have been

reported to pose harmful health effects to human due to their high surface area, enrichment with toxic heavy metals, long residence times in the atmosphere, and ability to penetrate deep in alveolar regions of the lungs [11]. Many studies have contributed to understanding the formation of these particles as well as the fate of metallic species during coal combustion [11-14]. There are two pathways for the formation of the submicrometer mode of ash in coal-air combustion: vaporization and chemical transformation via reduction and oxidation reactions. Heavy metals and organically associated cations, such as Na, Pb, Cd, and Hg, are directly vaporized from the burning coal particle. These volatile species may undergo gas phase chemical reactions and subsequently nucleate to form new particles or condense on the surface of existing particles. Another mineral transformation pathway for non-volatile species, such as silica, during coal combustion was proposed by Quann et al. [13]. These species with a high melting temperature are released from the burning char particle in the form of sub-oxides via a reduction reaction at the inclusion surface of the particle. These metal or mineral sub-oxides which are more volatile than the corresponding refractory oxides, diffuse away from the parent coal particle, re-oxidize, become supersaturated, and form particles by nucleation, followed by growth by condensation and collision mechanisms. A number of studies reported that the parameters, including coal type, combustion temperature, fuel-air ratio, and residence time, play an important role on the final particle size distribution [12-16]. Improving a fundamental understanding the formation pathways as well as the characteristics of

the submicrometer particles will allow the appropriate operation of particle control devices, and subsequently help minimize their emission.

In United States, the majority of coal-fired power plants utilize electrostatic precipitators (ESPs) to collect particles generated from coal combustion processes. The mass-based collection efficiencies of ESPs are typically over 99% [12]. ESP operation can be classified as a two-steps process: (1) particle charging, and (2) collection of the charged-particles. In the first step, ESPs utilize ions generated by a corona discharge to charge particles. In positive coronas, the dominant ion production mechanism is ionization by electron impact. Free electrons in the gas acquire energy from an applied electric field and collide violently with gas molecules, which in turn, remove electrons from the gas molecules. The net result is the creation of additional free electrons and positively charged gas ions [17]. In negative coronas, free electrons are directed out of the plasma region by strong electrical fields, and attach to neutral gas molecules, creating negative gas ions. In this first step, type of carrier gas is critical for the ion production.

In the second step, in the presence of an electric field the charged particles migrate and are collected on the opposite charged electrode. Extensive research has been conducted and reported that there is a “penetration window” in the submicrometer size ranges, where the collection efficiency is as low as 70-80% [11,

12]. For ultrafine particles, the collection efficiency decreases with decreasing particle size due to inefficient diffusion charging mechanism. For submicrometer particles, the collection efficiency decreases with increasing size due to the increase in drag force with increase in particle size. This results in an "inverse U-shaped" particle collection efficiency curve in the ultrafine and submicrometer particle size ranges. Conversely, coarse particles are charged efficiently by field charging mechanism, resulting in high particle collection efficiency with increasing particle size, and subsequently, giving rise to the high mass-based collection efficiencies of ESPs. While effects of particle size on the collection efficiency of ESPs have been studied, little research has been done on the impact of using different gas mixtures, primarily composed of CO_2 and O_2 on the performance of ESPs. Before oxy-coal combustion systems can be employed, the change in ESP performance due to the change in composition of combustion flue gas needs to be assessed.

1.1.2 Mercury speciation and current control technologies

Mercury is one of the pollutants that persist in the environment and bio-accumulate in the food chain. U.S. EPA estimates that 87% of the man-made emissions of mercury come from point sources of combustion. Despite being a trace element in coal with relatively low contents varying with coal rank (0.01-3.3 ppm_w),

mercury emission from coal combustion is significant due to large quantity of coal burned. In United States, coal-fired power plants contribute about 40 percent of the total emitted mercury into the atmosphere [17]. Mercury is released from the coal matrix to the gas phase via a direct vaporization process. At temperatures greater than 1200°C, mercury exists primarily in the elemental form ($Hg^0_{(g)}$)[18, 19]. As the flue gas subsequently cools, the gaseous elemental mercury interacts with other combustion by-products, such as hydrochloric acid (HCl), carbon monoxide (CO), nitrogen oxides (NO_X) and fly ash, resulting in a portion of $Hg^0_{(g)}$ being converted to other mercuric compounds, such as mercury (II) chloride ($HgCl_2$) and mercury (II) oxide (HgO) [20]. The oxidized forms of mercury ($Hg^{2+}X_{(g)}$) are always preferred over the elemental form of mercury because of their distinct properties. $HgCl_2$ is water-soluble; hence it can be removed in a wet scrubber. HgO, on the other hand, is less volatile, and may form particles by nucleation process or condense onto fly ash and be capture in particulate control devices. The fraction of each species of mercury in the flue gas varies depending on coal and flue gas composition, combustion conditions, and the time-temperature profile in the system. Hence, to effectively prevent mercury emissions it is important to understand the transformation of mercury in the system.

The sorbent injecting technique is the simplest and the most mature approach to control mercury. The gas phase mercury in flue gas contacts the sorbent and

attaches to its surface; and the sorbent with mercury attached is then collected by existing particle control devices. The most common used sorbent for mercury control is activated carbon and other inorganic sorbents, such as titanium-, calcium- and iron-based oxides [21, 22]. Activated carbon (AC) and activated carbon impregnated with sulfur, chlorine, or iodine, are one of the most effective sorbents for mercury capture, especially in the system where its concentration is high (i.e. Municipal Waste Incinerators) because they provide high surface area, approximately 300 m^2/gr, for mercury oxidation and adsorption. However, their use for mercury capture in coal-fired power plants is limited because of their low capacity at elevated temperatures. In addition, there are serious fly-ash disposal problems.

A number of researchers are proposing the use of inorganic sorbents, such as titanium-, calcium- and iron-based sorbent, for mercury capture [21, 22]. Titanium dioxide (TiO_2) with ultraviolet (UV) irradiated is one of the promising technologies for mercury capture [23-25]. Wu et al (1998) had demonstrated that mercury capture efficiency of in-situ generated TiO_2 with UV light was greater than 98 percent in their lab-scale studies [23]. Mercury capture using TiO_2 with UV irradiation occurs in a two step processes: photocatalytic activation of TiO_2 particle, and mercury oxidation and adsorption. The photocatalytic activation occurs when TiO_2 particles are exposed to UV radiation, resulting in the formation of highly reactive hydroxyl radicals ($OH^{\cdot}$) on the surface of the particles. Gaseous mercury molecules ($Hg^0_{(g)}$) adsorbed on the

surface are oxidized to form a $HgO\text{-}TiO_{2(complex)}$. The $HgO\text{-}TiO_{2(complex)}$ is retained on the particle surface; therefore, it can be removed from the gas stream by any particulate control device. Lee et al. (2004) reported a linear dependence of Hg oxidation on the surface area for a differential bed reactor and an aerosol flow reactor. Lee et al. (2006) evaluated the effect of light source on mercury removal efficiency by TiO_2- the efficiency was highest at 365 nm wavelength. Rodríguez et al. (2004) and Li and Wu (2006) revealed that Hg^0 oxidation was promoted by low water vapor concentrations (700-1800 ppm_v); however, the competitive adsorption of Hg^0 mercury and water vapor occurs at high moisture condition (greater than 2,000 ppm_v). In addition to the gas phase mechanistic and kinetic studies, sequential leaching from TiO_2 after mercury capture was also evaluated. Mercury was found to be bound very strongly to the sorbent as a stable sorbent-mercury complex. Thus, the sorbent-fly ash mix could be readily disposed or re-used [26]. Coal combustion systems pose several challenges to the performance of sorbents, such as the interference of fly ash and other flue gas constituents, and short residence time of flue gas in the system. While nano-structured TiO_2 with UV irradiation has been successfully demonstrated in many laboratory-scale experiments using simulated flue gas, before this sorbent can be selected for full-scale application, its effectiveness in coal combustion systems needs to be evaluated. As cost is important, minimizing mass loading while achieving desirable capture efficiencies is always preferred. Sorbent injection needs to be designed such that the sorbent is effectively and efficiently utilized.

1.2 DISSERTATION OUTLINE

The dissertation has been organized where each chapter is self-contained with an introduction and conclusions. Chapter 1 (this chapter) provides an introduction to this dissertation and reviews some of the important literature pertaining to the main focus of this dissertation. Chapter 2 presents the results on the submicrometer particle formation during oxy-coal combustion. Chapter 3 reports the effects of oxy-coal combustion on charged fraction and electrostatic collection of submicrometer and ultrafine particles by an ESP. Chapter 4 presents the influence of oxy-coal combustion on homogeneous mercury oxidation. Chapter 5 reports the results on mercury capture by nano-structured TiO_2 during coal combustion--tests at different scales. Chapter 6 discusses sorbent injection strategies that would result in optimal heavy metal capture. A theoretical model for describing the evolution of the aerosol size distribution and the formation of heavy metal species in high temperature environment is also discussed in this Chapter. Finally, major conclusions and significant contributions of this study are summarized in Chapter 7.

1.3 REFERRENCES:

1. U.S. Energy Information Administration and the International Energy Agency, Department of Energy (2008). "Global Energy Reserves." Retrieved August 8, 2008< http://www.eia.doe.gov>

2. Desideri, U. and A. Paolucci (1999). "Performance modeling of a carbon dioxide removal system for power plants" *Energ Conversion and Manage.* **40**: 1899-1915.

3. Doctor, R.D., J.C. Molburg, and P.R. Thimmapuram, *Oxygen Blown Gasification Combined Cycle: Carbon dioxide recovery, transport and disposal.* Energy Conversion Management, 1997. **38**: p. 575-580.

4. Hektor, B., *Cost effectiveness of measures for the reduction of net accumulation of carbon dioxide in the atmosphere.* Biomass and Bioenergy, 1998. **15**: p. 229-309.

5. White, C.M., et al., *Separation and Capture of CO2 from Large Stationary Sources and Sequestration in Geological Formations -- Coalbeds and Deep Saline Aquifers.* Journal of the Air and Waste Management Association, 2003. **53**: p. 645-715.

6. Kiga, T., *O2/RFG Combustion-Applied Pulverized Coal Fired Power Plant for CO2 Recovery,* in *Advanced Coal Combustion,* M. Takatoshi, Editor. 2001, Nova Science Publisher: Huntington, N.Y. p. 185-241.

7. Krishnamoorthy, G. and J.M. Veranth, *Computational Modeling of CO/CO2 Ratio Inside Single Char Particle during Pulverized Coal Combustion.* Energy & Fuels, 2003. **17**: p. 1367-1371.

8. Okazaki, K. and T. Ando, *NOx Reduction Mechanism in Coal Combustion with Recycled CO2.* Energy, 1997. **22**: p. 207-215.

9. Payne, R., et al., *CO2 Recovery via Coal Combustion in Mixtures of Oxygen and Recycled Flue Gas.* Combustion Science and Technology, 1989. **67**: p. 1-16.

10. Davidson, C.I., R.F. Phalen, and P.A. Solomon, *Airborne particulate matter and human health: A review.* Aerosol Science And Technology, 2005. **39**(8): p. 737-749.

11. Zhuang, Y. and P. Biswas, *Submicrometer particle formation and control in a bench-scale pulverized coal combustor.* Energy & Fuels, 2001. **15**(3): p. 510-516.

12. Linak, W.P. and J.O.L. Wendt, *Trace-metal transformation mechanisms during coal combustion.* Fuel Processing Technology, 1994. **39**: p. 173-198.

13. Quann, R.J., et al., *Mineral Matter and Trace-Element Vaposization in a Laboratory-Pulverized Coal Combustion System.* Environmental Science and Technology, 1982. **16**: p. 776-781.

14. Senior, C.L., et al. *Formation of ultrafine particulate matter from pulverized coal combustion.* in *219th American Chemical Society National Conference*. 2000. San Francisco, CA, USA.

15. Helble, J.J. and A.F. Sarofim, *Factors Determining the Primary Particle-Size of Flame-Generated Inorganic Aerosols.* Journal of Colloid and Interface Science, 1989. **128**(2): p. 348-362.

16. Kauppinen, E.I. and T.A. Pakkanen, *Coal Combustion Aerosols - a Field-Study.* Environmental Science & Technology, 1990. **24**(12): p. 1811-1818.

17. EPA, *1999 National Emission Inventory for Hazadous air pollutants*. 1999, Office of Air Quality Planning and Standards and Office of Research and Development, U.S. Environmental Protection Agency.

18. Wu, C.Y. and P. Biswas, *An Equilibrium-Analysis to Determine the Speciation of Metals in an Incinerator.* Combustion and Flame, 1993. **93**(1-2): p. 31-40.

19. Senior, C.L., et al., *Gas-phase transformations of mercury in coal-fired power plants.* Fuel Processing Technology, 2000. **63**(2-3): p. 197-213.

20. Niksa, S., et al., *A mechanism for mercury oxidation in coal-derived exhausts.* Journal of the Air & Waste Management Association, 2002. **52**(8): p. 894-901.

21. Zhuang, Y., et al., *Impact of calcium chloride addition on mercury transformations and control in coal flue gas.* Fuel, 2007. **86**(15): p. 2351-2359.

22. Pavlish, J.H., et al., *Status review of mercury control options for coal-fired power plants.* Fuel Processing Technology, 2003. **82**: p. 89-165.

23. Wu, C.Y., et al., *Capture of mercury in combustion systems by in situ-generated titania particles with UV irradiation.* Environmental Engineering Science, 1998. **15**(2): p. 137-148.

24. Wu, B.C., et al., *Interactions between vapor-phase mercury compounds and coal char in synthetic flue gas.* Fuel Processing Technology, 2000. **63**(2-3): p. 93-107.

25. Lee, T.G., P. Biswas, and E. Hedrick, *Overall kinetics of heterogeneous elemental mercury reactions on TiO2 sorbent particles with UV irradiation.* Industrial & Engineering Chemistry Research, 2004. **43**(6): p. 1411-1417.

26. Noel, J. D., Biswas, P., Giammar, D.E, *Evaluation of a sequential extraction process used for determining mercury binding mechanisms to coal combustion byproducts*, Journal of Air & Waste Management Association, 2007. **57**(7), p. 856-867.

Chapter 2

Submicrometer Particle Formation and Mercury Emission during O_2-CO_2 Coal Combustion*

* This work was published *Energy & Fuels,* 20, 2357-2363, 2006.

ABSTRACT

The characteristics of the submicrometer mode of ash and mercury speciation on combustion of coal in oxygen-carbon dioxide and air (conventional) systems were compared. The experiments were conducted at different mixing ratios of O_2/CO_2 and $O_2/N_2/CO_2$. When nitrogen in air was replaced with carbon dioxide, the total mass of the particles in the submicrometer mode (particle diameter smaller than 0.5 μm) of ash was smaller. Correspondingly, the geometric mean size (d_{pg}) of the submicrometer aerosol was smaller by approximately 28%. When the O_2/CO_2 ratio was increased from 1:4 to 4:4, the geometric mean size of the submicrometer mode increased from 29 to 54 nm due to faster vaporization as a result of higher coal particle temperature during combustion. For the same reasons, an increase in the geometric mean size was observed on increasing the N_2/CO_2 ratio at a fixed O_2 concentration. The shape of the primary particles was spherical in all the tests, indicating that a vapor to particle transformation pathway was prevalent. The ratios of elemental to oxidized mercury (approximately 4:1) were similar for O_2/CO_2 and air combustion.

2.1 INTRODUCTION

Coal is one of the cheapest and most abundant reserve source of energy. Approximately 60% of the total electricity in the United States is generated by coal combustion [1]. Due to the large amount of coal burned, emissions from coal combustion are significant and of potential environmental concern. The major environmental issues associated with coal combustion are potential climate change due to emissions of carbon dioxide (CO_2), oxides of nitrogen (NO_X), fine particles (particle diameter smaller than 1 μm), and mercury to the atmosphere. Due to the potential impacts of global warming, capture of CO_2 from coal combustion exhausts is receiving attention. However, the volume fraction of CO_2 in a conventional coal combustion system (with air) ranges from only 13% to 15%, making it very difficult to design cost-effective capture systems. One approach to overcome the limitation of low CO_2 concentration in the exhaust gas is to combust the coal in oxygen-enriched environment (by removing nitrogen), and recycle the exhaust gas to serve the role of the diluent. Such a configuration would result in CO_2 concentration of 95% [2-5], making it more feasible to capture CO_2. Other advantages of this combustion configuration have also been reported, including reduced volume of flue gas to exhaust, potential for increasing boiler thermal efficiency, elimination of thermal NO_X (due to removal of nitrogen from the air stream), decreasing the conversion ratio of fuel-N to exhaust NO, and increasing the reduction of NO to N_2 [6, 7].

While there are clear advantages to combustion in an O_2-CO_2 environment, the impact on other pollutants, such as fine particle and mercury emissions, have not yet been established. The formation of fine particles, specifically in submicrometer size range, of ash in coal-air combustion systems has been studied extensively [8-11]. There are two pathways for the formation of the submicrometer mode of ash in coal-air combustion: vaporization and chemical transformation via reduction and oxidation reactions. Heavy metals and organically associated cations, such as Na, Pb, Cd, and Hg, are directly vaporized from the burning coal particle. These volatile species may undergo gas phase chemical reactions and subsequently nucleate to form new particles or condense on the surface of existing particles. Submicrometer-sized particles with a mode around 0.1 μm are formed via this pathway [8-11]. The other mineral transformation pathway for non-volatile species, such as silica, during coal combustion was proposed by Quann et al. [10]. These species with a high melting temperature are released from the burning char particle in the form of sub-oxides via a reduction reaction at the inclusion surface of the particle. These metal or mineral sub-oxides, which are more volatile than the corresponding refractory oxides, diffuse away from the parent coal particle, re-oxidize, become supersaturated, and form particles by nucleation, followed by growth by condensation and collision mechanisms.

Linak and Peterson [12] studied the effect of coal type and residence time on particle size distributions and concluded that the accumulation of particles in the submicrometer size range results from vaporization, nucleation, condensation, and coagulation. Zhuang and Biswas [8] reported that the submicrometer size particles are initially formed by nucleation due to chemical transformation, followed by growth by condensation. Most studies have reported that the submicrometer particle formation mechanisms in coal combustion are very complex and depend on a number of factors, such as coal type, combustion temperature, fuel-air ratio, and residence time. These factors also play an important role on the final particle size distribution [9-11, 13, 14].

Mercury emission from coal combustion has also been an issue of great concern because of its high toxicity, difficulty to control, and tendency to bio-accumulate in the environment. Despite a low concentration (1 to 30 $\mu g/m^3$) of mercury in the flue gas, coal combustors contributing about 40 percent of the total emitted to the atmosphere in the United States [15] are the largest anthropogenic source of mercury emission. The chemical forms of emitted mercury can be classified as elemental mercury ($Hg^0_{(g)}$), various oxidized mercury compounds ($Hg^{2+}X_{(g)}$), and mercury in association with particulate matter ($Hg_{(p)}$). Mercury is released from the coal matrix to the gas phase via a direct vaporization process. At temperatures greater than 1200°C, mercury exists primarily in the elemental form

($Hg^0_{(g)}$) [16, 17]. As the flue gas subsequently cools, the gaseous elemental mercury interacts with other combustion by-products, such as HCl, CO, NO_X and fly ash. This results in a portion of the elemental mercury being converted into other mercuric compounds, such as $HgCl_2$ and HgO [18]. The fraction of each species of mercury in the flue gas varies depending on coal and flue gas composition, combustion conditions, and the time-temperature profile in the combustion system. The speciation of mercury is an important aspect for appropriate choice of mercury control methodology [19].

There have been several studies on the design and evaluation of coal combustion efficiency in O_2-CO_2 systems [3, 20-23]. While advantages with respect to the potential for CO_2 capture, reduction of NO_X emissions, and improvement in combustion efficiency have been demonstrated; the impacts on fine particle formation and speciation of mercury have not been studied. In this paper, a mechanistic understanding of submicrometer particle formation and mercury speciation in O_2-CO_2 combustion is established. Comparisons with combustion in air are reported and differences are highlighted.

2.2 METHODOLOGY

2.2.1 Experiments.

The experimental setup is shown in Figure 2.1 and consists of a coal feeding system, a tubular furnace (Lindberg/Blue M, Model HTF55342C, T_{max}=1200ºC, Thermoelectron Corporation, USA) with an alumina reactor tube (5.72 cm inside diameter and 121.92 cm long), a cascade impactor and measuring systems. Pulverized Powder River Basin (PRB) sub-bituminous coal with a mean particle size of 50 μm is introduced into the electrically heated alumina tubular reactor by a fluidized bed coal feeder. The oxidant is introduced into the combustor at a total flow rate of 1.75 lpm, either as air (conventional) or a mixture of O_2, CO_2 and N_2 (varying ratios). At the exit of the combustor, particle-free air, at a flow rate of 12.25 lpm, is added to quench the aerosol dynamics and chemical reactions. All measurements are made at the conditions at the exit of the combustor. A six-stage cascade impactor (Mark III, Pollution Control System Corp., Seattle, WA) with a final stage 50% cut-off particle size of 0.5 μm, is used to remove the large (coarse) ash particles. A slip stream (0.3 lpm) downstream of the impactor is then introduced into a real time Scanning Mobility Particle Sizer (SMPS, TSI Inc., Shoreview, MN, USA) to determine the particle size distribution ranging from 12 to 500 nm. The submicrometer particles are also collected on Teflon filters for elemental analysis. X-

Ray fluorescence spectroscopy (XRF) is used to obtain the elemental concentration of 72 species. In addition, the morphology of the submicrometer particles is examined by a scanning electron microscopy (SEM, Hitachi S-4500).

A 1.0 lpm flow downstream of the impactor is passed through a mercury sampling train to determine oxidized and elemental mercury concentrations. A total of 90 liters of gas is sampled over a 90 minute duration. The sampling train and technique used for gaseous mercury measurement is based on the method developed by Hedrick et al. [24]. The sampling train consists of the following five impinger solutions: two impingers of 1.0 M tris-buffer and EDTA for capture of oxidized mercury, one impinger of 10% hydrogen peroxide and 2% nitric acid for oxidizing and capture elemental mercury, and two impingers of 0.05 M potassium iodide and 2% hydrochloric acid for capture of elemental mercury. The impinger solutions are analyzed by inductively coupled plasma mass spectrometry (ICP-MS) to determine the elemental and oxidized fractions of mercury in the exhaust gas.

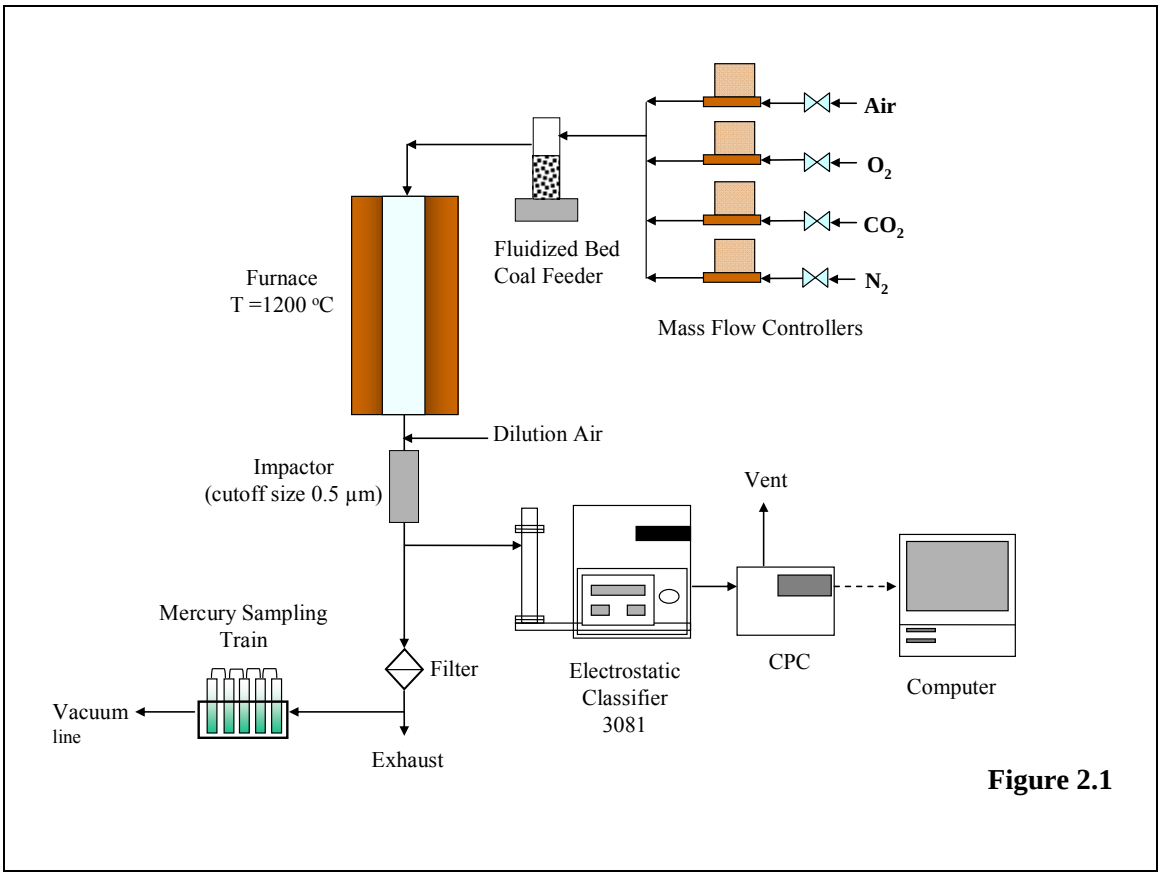

Figure 2.1: Schematic diagram of experimental setup.

2.2.2 Flame Temperature Calculation.

A computer code for chemical equilibrium, STANJAN [25], is used to calculate the equilibrium compositions and the adiabatic flame temperature. The temperature in the vicinity of the burning coal particle is assumed to be the adiabatic flame temperature. The database of thermodynamic information for various species was obtained from Wu and Biswas [16].

2.2.3 Test Plan.

The overall objective is to understand the effects of O_2-CO_2 coal combustion on submicrometer particle formation and mercury speciation. The experimental plan is outlined in Table 2.1. The objective of the first set of experiments (Set I) is to compare characteristics of the submicrometer particles when N_2 from air is completely replaced by CO_2. Set II experiments are designed to study the effects of varying N_2 and CO_2 on the particle size distribution. The experiments are conducted at a fixed concentration of O_2 (20% by volume) and varying ratios of N_2/CO_2. Set III experiments are carried out to study the influence of the O_2-CO_2 ratio. Set IV experiments are designed to determine the effect of O_2-CO_2 combustion on mercury speciation. Experiments are conducted for coal combustion in air, 20%O_2-80%CO_2, and 25%O_2-75%CO_2.

Table 2.1: Summary of the experiments performed.

Set	Analysis	Test	Coal Combustion Condition		Objective
			Mixing Ratio (by volume)	Gas Compositions	
I	SMPS, SEM, XRF, Coarse and Fine Mass	1	1:3.76	Air (O_2/N_2)	Comparing characteristics of submicrometer particles formed under conventional (air) and O_2-CO_2 combustions at the same amount of O_2
		2	1:4	O_2/CO_2	
II	SMPS	1	1.25:1:4	$O_2/N_2/CO_2$	Determining the influence of N_2 on aerosol characteristics
		2	1.25:2:3	$O_2/N_2/CO_2$	
		3	1.25:2.5:2.5	$O_2/N_2/CO_2$	
		4	1.25:3:2	$O_2/N_2/CO_2$	
		5	1.25:4:1	$O_2/N_2/CO_2$	
III	SMPS	1	1:4	O_2/CO_2	Determining effects of the mixing ratio of O_2-CO_2 on aerosol characteristics
		2	1:3	O_2/CO_2	
		3	2:3	O_2/CO_2	
		4	3:3	O_2/CO_2	
IV	Mercury Measurement	1	1:3.76	Air (O_2/N_2)	Determining effects of the O_2-CO_2 system on mercury speciation and comparing to conventional combustion (air).
		2	1:4	O_2/CO_2	
		3	1:3	O_2/CO_2	

SMPS: Scanning Mobility Particle Sizer

2.3 RESULTS AND DISCUSSION

2.3.1 Characteristics of Submicrometer-sized Particles

Set I. Air versus 20%O_2-80%CO_2. The resultant ash is classified into two fractions: a coarse mode (dp > 0.5 μm) and a submicrometer mode (dp < 0.5 μm). The total mass of ash formed (7 mg/g of coal) is approximately the same in both combustion in air and in 20%O_2-80%CO_2, confirming that the carbonaceous species is completely oxidized. The fine/coarse ash mass fraction in air combustion is 2.5 times higher than that in the O_2-CO_2 system (Table 2.2(A)). As described in the Introduction, there are two pathways (direct vaporization of volatile metals and vaporization by chemical transformation) for the formation of fine particle (Figure 2.2). Both pathways are a strong function of temperature. The temperature in the vicinity of the burning coal particle is higher for combustion in air than in the O_2-CO_2 system. One reason is that specific heat capacity (C_P) of N_2 is lower than that of CO_2, especially at elevated temperatures (C_P at 1200 ºC: N_2 = 20.78 kJ/kmol-ºC, and CO_2 = 58.84 kJ/kmol-ºC). The higher specific heat capacity of CO_2 leads to lowering the surface temperature of the burning coal particles by approximately 400-500 ºC [20] and increasing the ignition time of coal and char particles [26]. The mass diffusivity of O_2 in CO_2 is lower than that of O_2 in N_2 ($D_{O2/CO2}$ = 1.3 x 10^{-4} m^2/s and $D_{O2/N2}$ = 1.7 x 10^{-4} m^2/s). The coal burning process is a diffusion limited reaction; oxygen diffuses

from the bulk gas to the surface of the burning particles. A lower diffusivity of O_2 in CO_2 (compared to O_2 in N_2) slows down the particle burning and heat generation rates. As diffusivity is a strong function of temperature, a lower temperature in the vicinity of the burning coal particles in the O_2-CO_2 system results in a slower diffusion rate of oxygen to the surface of the burning coal particle compared to that in air (O_2-N_2). This leads to lower vaporization and particle formation rates when combustion occurs in an O_2-CO_2 mix compared to air. The excess carbon dioxide in the vicinity of the coal particle is also expected to alter the reaction equilibrium, and slow down the burning rate. While the adiabatic temperature represents only an ideal case, it was calculated using the equilibrium code. The estimated temperature in the vicinity of the burning coal particle (determined by STANJAN) in air is 2311K, compared to 1772K in the O_2-CO_2 system.

Table 2.2(A). Summary of size distribution statistics for experiment Set I (air versus 20%O_2-80%CO_2).

Test	Gas Composition	Adiabatic Flame Temp (K)	Mass Fraction (fine/coarse)	Geometric Mean Size (nm)	Total Number Conc. (# cm^{-3})	Total Volume Conc. (nm^3 cm^{-3})	Geometric Standard Deviation
1	Air	2311.1	0.971	40.3 ± 0.49	6.39×10^4	1.2×10^{10}	1.53
2	20%O_2-80%CO_2	1771.9	0.396	29.1 ± 0.39	3.85×10^4	8.17×10^9	1.44

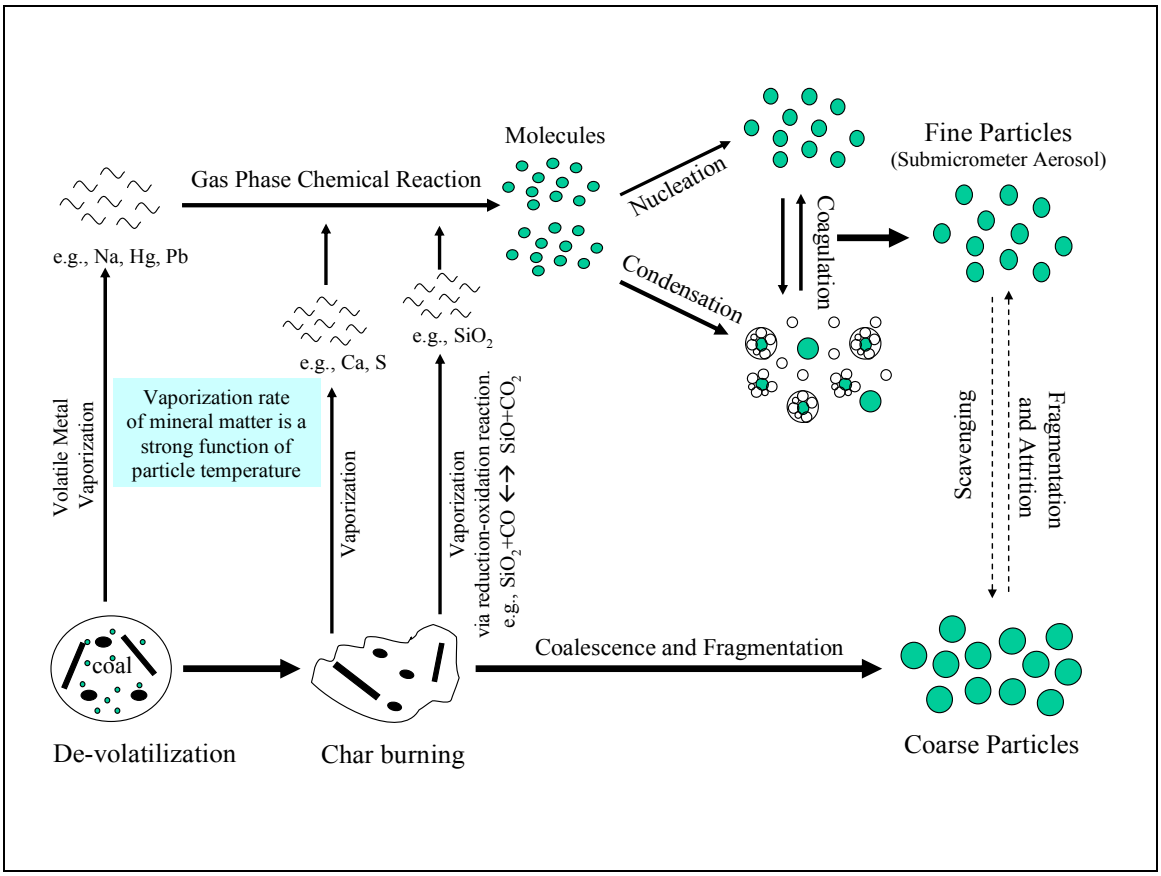

Figure 2.2 Mineral transformation and particle formation pathways during coal combustion. Based on Linak and Wendt [9].

The major elemental compositions (by mass) in PRB coal are silicon (32%), calcium (20%), aluminum (17%), and iron (8%). The major elements are found in the fine particles for both 20%O_2-80%CO_2 and air combustion, as shown in Figure 2.3. The mass of each elemental species found in the submicrometer ash reflects the amount of the species vaporized during the combustion of coal. Even though silicon is in higher concentrations than calcium and iron in PRB coal, it is found in a lower mass fraction in fine ash particles. Silicon that is present as mineral inclusions

coalesces and forms a glassy-type complex during combustion. This prevents further vaporization of silicon, thus retaining in the coarse ash particles [27]. The heavy metal species, such as nickel and lead, are also found in the submicrometer mode, confirming that vaporization and nucleation steps are their formation pathway. However, their mass (~1 μg/g coal) in the submicrometer mode is small compared to the elements illustrated in Figure 2.3, and hence they do not contribute to the size distribution characteristics of ash discussed later.

The normalized masses of the vaporized elements are lower for the 20%O_2-80%CO_2 combustion compared with that of air for most of the major elements, particularly calcium, iron, and silicon. In the chemical transformation pathway via reduction-oxidation reactions, proposed by Quann et al. [10]. A high concentration of CO_2 in the bulk gas deters chemical transformation rate of mineral oxides to mineral sub-oxides because CO_2 is one of the products of the reduction reaction of mineral oxide. For example, an equilibrium vapor pressure of silicon suboxide (SiO) at the surface of coal particle was 1.77×10^{-2} atm when coal was combusted in air, and it was 1.46×10^{-7} atm when coal was combusted in 20%O_2-80%CO_2 (See Appendix A for sample calculations). For most mineral oxides, the chemical nucleation step is very fast due to very rapid reaction of the sub-oxides with oxygen. However, the transformation rate of mineral oxides to sub-oxides is slow in a 20%O_2-80%CO_2 system, resulting in slower particle formation rate. The measured elemental

compositions in submicrometer particles indicates that the change of combustion system from air to 20%O_2-80%CO_2 does not alter the fraction of the major species in submicrometer particles. It affects only their amount in the submicrometer ash.

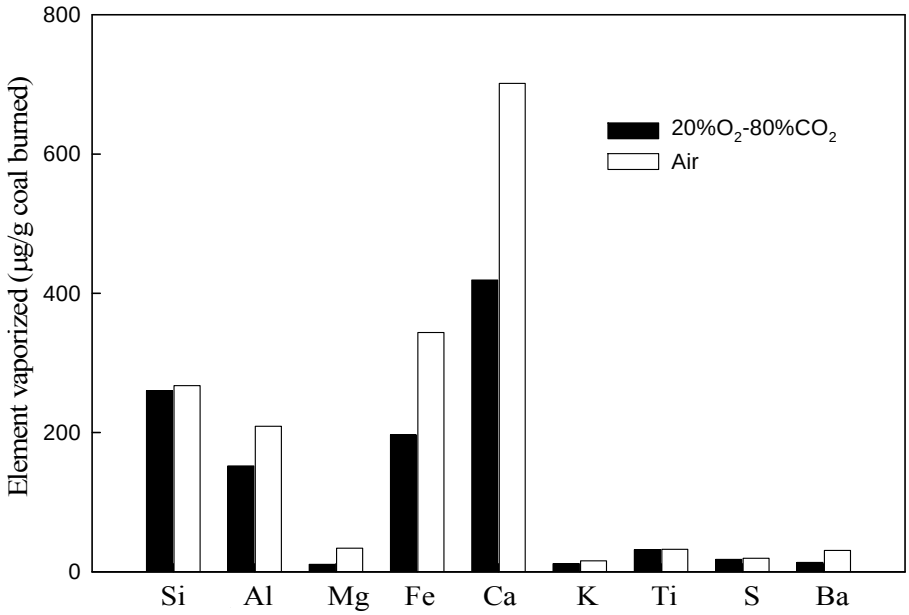

Figure 2.3 Measured elemental compositions in submicrometer-sized ash at air and 20%O_2-80%CO_2 combustions.

The submicrometer particle size distributions formed under 20%O_2-80%CO_2 and air combustion and are shown in Figure 2.4. The size distribution statistics are summarized in Table 2.2(A). When N_2 is replaced by CO_2, the geometric mean particle size reduces from 40.3 nm to 29.0 nm. The total number concentration in the diluted exhaust decreases by 40% from an average of 6.39×10^4 #/cm^3 to 3.85×10^4 #/cm^3. The total particle volume decreases by 38% from an average of 1.12×10^{10} nm^3/cm^3 to 8.17×10^9 nm^3/cm^3. The geometric standard deviation decreases from 1.53 to 1.44.

Figure 2.4

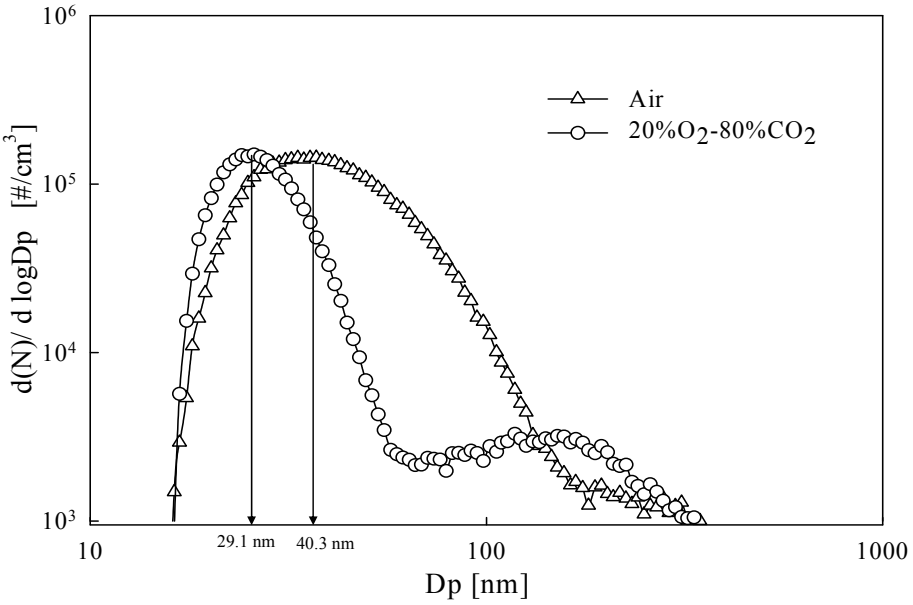

Figure 2.4 Submicrometer particle size distributions of air and 20%O_2-80%CO_2 coal combustions.

Since the total residence time in all tests is the same, the retardation of particle formation from both vaporization and chemical transformation pathways (shown in Figure 2.2) results in less time available for the growth processes, such as condensation and coagulation, for combustion of coal in an O_2-CO_2 mix; thus, the particles formed are not only smaller in number, but also smaller in size as observed experimentally.

The SEM pictures in Figure 2.5 show that the primary particles formed under both combustion conditions are spherical, which implies that nucleation and condensation mechanisms are the primary cause of formation and growth of submicrometer particles. This indicates that the change in combustion condition (i.e replacing N_2 with CO_2) does not alter particle formation mechanisms, but rather the rates at which they take place. Agglomerates consisting of spherical and irregular shape particles are also found for both combustion conditions.

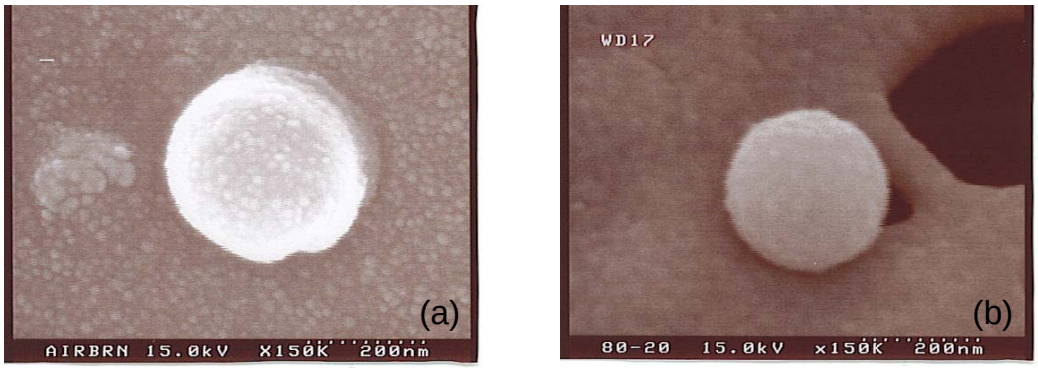

Figure 2.5: SEM pictures of submicrometer particles formed during combustion of coal with (a) air and (b) 20%O_2-80%CO_2.

Set II. O_2-N_2-CO_2 System. This is representation of a system where nitrogen is partially replaced with carbon dioxide. Additional tests are performed at a fixed concentration of O_2 but varying the mixing ratio of N_2 to CO_2. The particle size distributions are shown in Figure 2.6 and the data are summarized in Table 2.2(B). As the N_2/CO_2 ratio increases from 1:4 to 4:1, the geometric mean particle size increases from 31.2 nm to 40.5 nm, the total particle volume increases from 1.55 $x10^{10}$ nm^3/cm^3 to 4.40 $x10^{10}$ nm^3/cm^3, and the geometric standard deviation increases from 1.46 to 1.60. The total number concentrations are relatively constant for all mixing ratios (ranging between 9.22 $x10^4$ to 1.37 $x10^5$ # cm^{-3}). The geometric mean particle sizes and the adiabatic flame temperatures for all mixing ratios in this set of experiments are between that of air and 20%O_2-80%CO_2. The results of this set of experiments are consistent with the explanation in the previous section. The coal particle surface temperature increases as the ratio of N_2/CO_2 increases, resulting in faster vaporization rates followed by faster particle formation and growth mechanisms.

Figure 2.6

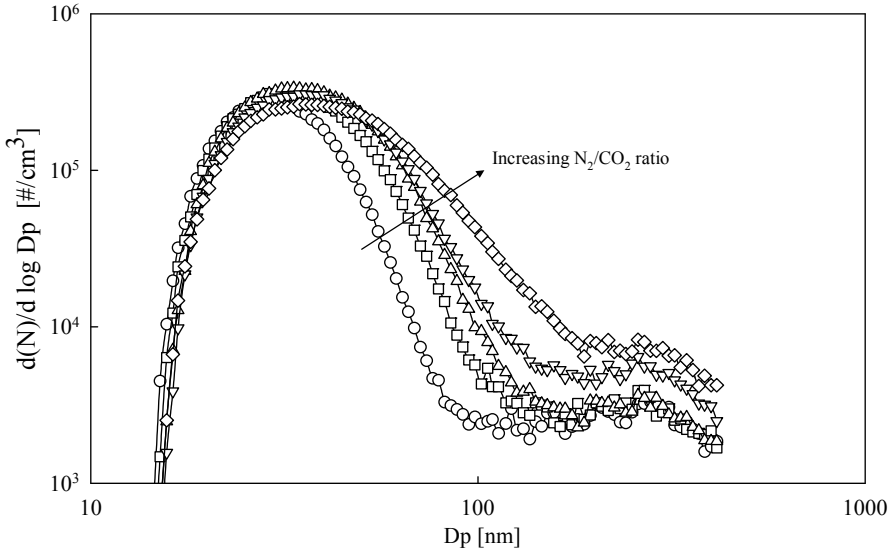

Figure 2.6: Submicrometer particle size distributions at fixed concentration of O_2 (20% by volume) and different mixing ratios of N_2/CO_2. Legend O_2:N_2:CO_2 mixing ratio: —○— 1.25:1:4, —□— 1.25:2:3, —△— 1.25:2.5:2.5, —▽— 1.25:3:2, —◇— 1.25:4:1.

Table 2.2(B). Summary of size distribution statistics for experiment Set II (O_2:N_2:CO_2)

Test	Mixing Ratio of O_2:N_2:CO_2	Adiabatic Flame Temperature (K)	Geometric Mean Size (nm)	Total Number Concentration (# cm^{-3})	Total Volume Concentration (nm^3 cm^{-3})	Geometric Standard Deviation
1	1.25:1:4	1848.7	31.2 ± 1.2	1.13 x 10^5	1.55 x 10^{10}	1.46
2	1.25:2:3	1932.2	34.6 ± 1.0	1.23 x 10^5	1.84 x 10^{10}	1.47
3	1.25:2.5:2.5	1977.3	36.4 ± 1.2	1.37 x 10^5	2.06 x 10^{10}	1.48
4	1.25:3:2	2024.6	37.8 ± 1.1	1.14 x 10^5	3.02 x 10^{10}	1.54
5	1.25:4:1	2129.3	40.5 ± 1.6	9.22 x 10^4	4.40 x 10^{10}	1.60

Set III. O_2-CO_2 System. The submicrometer particle size distributions formed at different ratios of O_2/CO_2 are shown in Figure 2.7. The geometric mean particle size ranges from 29.1 nm to 54.3 nm as the O_2/CO_2 mixing ratio varies from 1:4 to 4:4. The geometric mean particle size and geometric standard deviation (σ_g) of particle size distributions increase with oxygen concentration in the system (d_{pg} increases from 29 nm to 54 nm and σ_g increases from 1.53 to 1.74). This is attributed to the increase in oxygen volume fraction from 20% to 50%, which increases the particle surface temperature from 1772 K to 2679 K. Although the particle size distribution of submicrometer particles is shifted to larger sizes as the concentration of oxygen increases, the particle number concentration in the smaller sizes (sizes smaller than 50 nm) are similar for all combustion conditions studied. This is the result of two competing mechanisms: nucleation and condensation. The vaporized species tend to nucleate when the concentration of the small particles is below a critical concentration. When the number concentration of the smaller particles is higher than the critical number concentration, condensation dominates over nucleation [28].

Figure 2.7

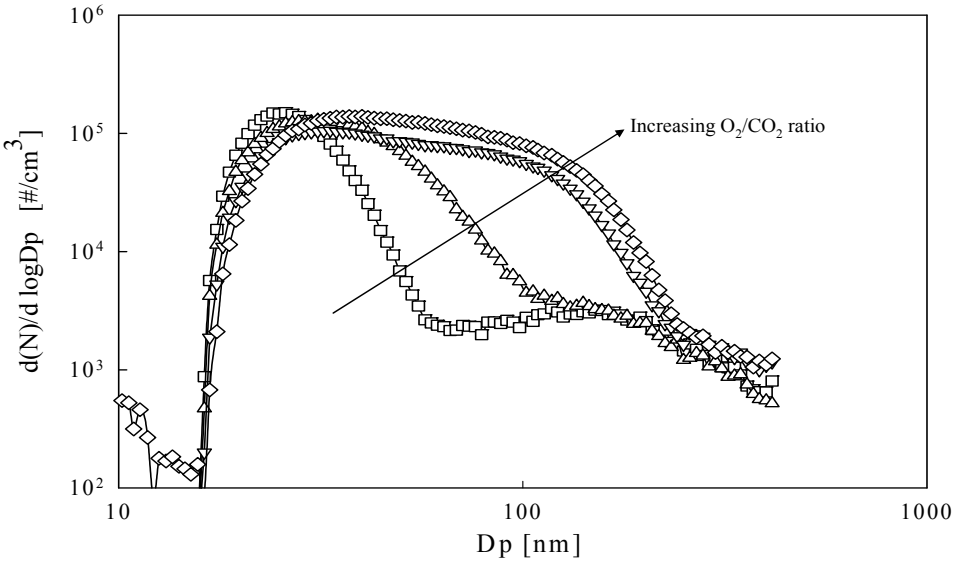

Figure 2.7: Submicrometer particle size distributions at different O_2-CO_2 mixing ratios. Legend O_2:CO_2 mixing ratio: —□— 1:4, —△— 1:3, —▽— 2:3, —◇— 4:4

Table 2.2(C). Summary of size distribution statistics for experiment Set III (O_2:CO_2)

Test	Mixing Ratio of O_2:CO_2	Adiabatic Flame Temperature (K)	Geometric Mean Size (nm)	Total Number Concentration (# cm^{-3})	Total Volume Concentration (nm^3 cm^{-3})	Geometric Standard Deviation
1	1:4	1771.9	29.1 ± 0.39	3.7 x 10^4	8.17 x 10^9	1.53
2	1:3	2033.0	36.1 ± 0.77	5.2 x 10^4	9.12 x 10^9	1.55
3	2:3	2493.6	50.7 ± 2.06	6.7 x 10^4	2.46 x 10^{10}	1.76
4	3:3	2678.8	54.3 ± 0.98	8.9 x 10^4	3.50 x 10^{10}	1.73

2.3.2 Mercury Speciation

The measured mercury concentration in the gas phase in the combustion exhaust is plotted in Figure 2.8. For conventional air combustion (Set IV, Test # 1), an average of 0.1 $\mu g/m^3$ is oxidized mercury, and 0.4 $\mu g/m^3$ is elemental mercury. This range of speciation is consistent with values reported in the literature [29-31]. Reynolds [29] reported that approximately 10 to 20 % of the mercury emissions from western sub-bituminous coals are in the oxidized state with the remainder in the elemental state. Lee and Srivastava [30] reported similar speciation results in the gas phase during the combustion of PRB coal. For 25%O_2-75%CO_2 combustion, an average of 0.08 $\mu g/m^3$ is oxidized mercury, and 0.38 $\mu g/m^3$ is elemental mercury. For 20%O_2-80%CO_2 combustion, an average of 0.1 $\mu g/m^3$ is oxidized mercury, and 0.6 $\mu g/m^3$ is elemental mercury. The experimental results are averaged from four repeated tests of the same condition. The total gaseous mercury concentrations of both O_2-CO_2 conditions are relatively the same as that of air, indicating that the O_2-CO_2 system had no effect on vaporization of mercury. Mercury is released via direct vaporization and not by chemical reduction-oxidation (Figure 2.2). The burning temperature at the surface of coal particle is high enough in both the air and O_2-CO_2 systems to vaporize mercury from the coal matrix (boiling point of mercury is only 629 K at 1 atm). The ratio of oxidized mercury to elemental mercury for both O_2-CO_2 combustion conditions is also close to that of air, indicating that the O_2-CO_2

system does not have a significant effect on mercury speciation at the combustor exit. The experimental results here agree well with previous studies which show that mercury is primarily in the elemental form at high temperatures [16].

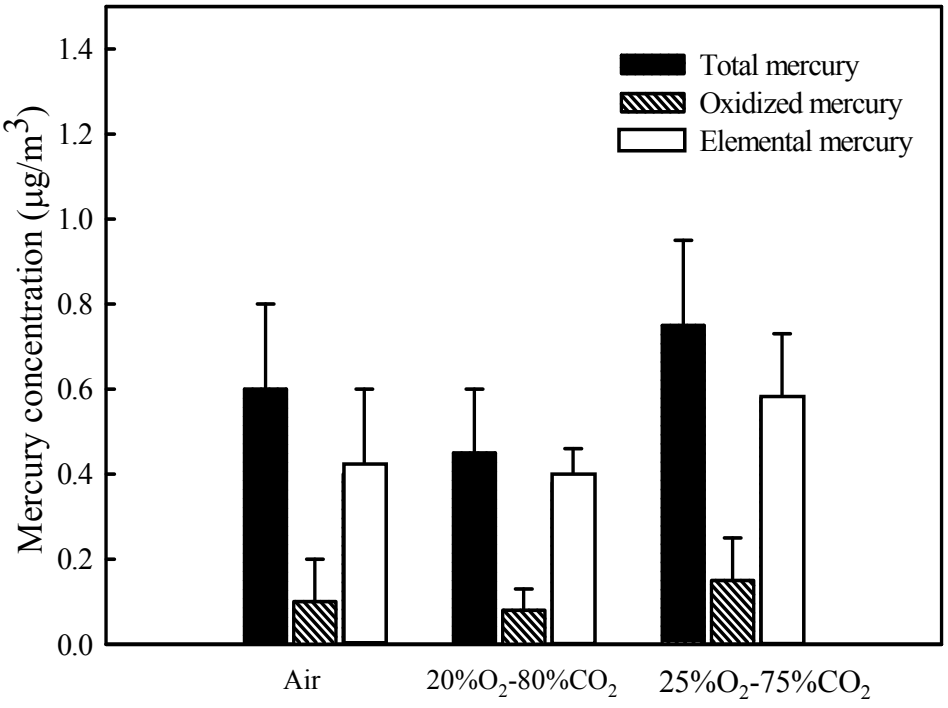

Figure 2.8 Mercury concentration measured at the combustor exit at different combustion conditions.

2.4 CONCLUSIONS

This study investigated the effects of coal combustion in an O_2-CO_2 environment on submicrometer particle formation and mercury speciation. The combustion conditions investigated in this study represented two cases of oxygen-enriched combustion with carbon dioxide recycle: (1) complete separation of O_2 from N_2 in air, and (2) partial separation of O_2 from N_2 in air. When N_2 is replaced with CO_2, the mass, number concentration and mean size of submicrometer particles are smaller. When N_2 is partially removed from the air stream, the mean particle size, mass and number concentration increase with increasing N_2-CO_2 ratio. When coal is combusted at different mixing ratios of O_2-CO_2, mean particle size and total number concentration increase as the mixing ratio of O_2-CO_2 increases. The total particle volume increases drastically when the mixing ratio of O_2-CO_2 is greater than 2:3. The results are attributed to the change in the temperature in the vicinity of the burning particle since the temperature plays an important role in the vaporization process of metals and mineral inherent with coal particle. O_2-CO_2 combustion may only affect vaporization process and not influence other aerosol growth mechanisms. O_2-CO_2 combustion does not have an effect on mercury speciation measured at the exit of the combustor.

APPENDIX A

To determine the effects of O_2-CO_2 on this chemical transformation pathway, the vaporization of selected mineral oxides, such as silica (SiO_2), under air and O_2-CO_2 system are compared using the mechanism proposed by Quann et al. [10]. The vaporized mole fraction of silica is calculated by assuming the mineral oxides undergo reduction reaction during vaporization as follow:

$$SiO_2 + CO \Leftrightarrow SiO + CO_2 \qquad Ke = \frac{P_{SiO} P_{CO_2}}{a_{SiO_2} P_{CO}} \qquad (1),$$

where *Ke* is the equilibrium constant for the mineral oxides of interest, in this case SiO_2, P_{SiO} is an equilibrium vapor pressure of silicon sub-oxide (SiO) at the surface of coal particle, P_{CO} and P_{CO2} are the local partial pressures of *CO* and CO_2, respectively, and a_{SiO2} is the activity of solid metal oxide (which is assumed to be ~1).

From stoichiometry, P_{CO} at the surface of the particle is estimated to be:

$$P_{CO,surface} = \frac{2P_{O_2,bulk}}{1 + P_{O_2,bulk}} \qquad (2),$$

where $P_{O2,\ bulk}$ is the partial pressure of oxygen in the bulk gas. Assuming that the partial pressure of O_2 in both the air and O_2-CO_2 system are equal (0.21 atm), the partial pressure of carbon monoxide at the particle surface, $P_{CO,surface}$, is 0.33 atm for both systems. The equilibrium constant (*Ke*) for vaporization of the selected mineral

oxide is calculated from the equilibrium equation and equilibrium coefficients, obtained from Senior et al. [11] as follow:

$$\ln(Ke) = A + Bx10^4 / T \qquad (3),$$

where A and B are equilibrium coefficients, for silicon A = 18.8256 and B = -5.97, and T is the temperature at the surface of the particle, using the adiabatic flame temperature, for air, T_{ad} = 2311 K, and for 20%O_2-80%CO_2, T_{ad} = 1772 K.

For air combustion, the mineral oxide vaporization reaction is assumed to be the only source of carbon dioxide, P_{CO2}, at the surface of coal particle[10, 11]. Thus, the partial pressure of MO_{n-1} can be calculated

$$P_{SiO} = (a_{SiO} K_e P_{CO})^{1/2} \qquad \text{for air combustion} \qquad (4).$$

For O_2-CO_2, P_{CO2} at the surface of coal particle is estimated to be equal that of bulk gas. The pressure in the combustor is assumed to be 1 atm, therefore 80%CO_2 in the bulk gas results in a partial pressure of CO_2 of 0.8 atm. P_{CO2} from metal oxide vaporization reaction is negligible comparing with P_{CO2} from the bulk gas.

$$P_{SiO} = \left(\frac{a_{SiO} K_e P_{CO}}{P_{CO_2}}\right) \qquad \text{for } O_2\text{-}CO_2 \text{ combustion} \qquad (5).$$

By substituting P_{CO2} *and* $P_{O2,bulk}$ *and* T_{ad} in equation (4) and (5), the partial pressures of *SiO* at the surface of coal particle are estimated to be 1.77 $x10^{-2}$ atm and 1.46 $x10^{-7}$ atm, for air and 20%O_2-80%CO_2, respectively. This calculation shows that vaporization of mineral oxides via reduction-oxidation reactions is suppressed in the O_2-CO_2 system due to the presence of a high CO_2 concentration.

2.5 REFERENCES

1. DOE (2005), "U.S. Coal Supply and Demand 2004 Review". Energy Information Administration, Office of Energy Statistics.

2. Desideri, U. and Paolucci, A. (1999) "Performance modeling of a carbon dioxide removal system for power plants", *Energy Conversion and Management.* **40**, 1899-1915.

3. Doctor, R. D., Molburg, J. C. and Thimmapuram, P. R. (1997) "Oxygen blown gasification combined cycle: carbon dioxide recovery, transport and disposal", *Energy Conversion Management.* **38**, 575-580.

4. Hektor, B. (1998) "Cost effectiveness of measures for the reduction of net accumulation of carbon dioxide in the atmosphere", *Biomass and Bioenergy.* **15**, 229-309.

5. White, C. M., Strazisar, B. R., Granite, E. J., Hoffman, J. S. and Pennline, H. W. (2003) "Separation and capture of CO_2 from large stationary sources and sequestration in geological formations-coal beds and deep saline aquifers", *J. Air Waste Manag. Assoc.* **53**, 645-715.

6. Liu, H., Katagiri, S., Kaneko, U. and Okazaki, K. (2000) "Sulfation behavior of limestone under high CO_2 concentration in O_2/CO_2 coal combustion", *Fuel.* **79**, 945-953.

7. Liu, H. and Okazaki, K. (2003)"Simultaneous easy CO_2 recovery and drastic reduction of SO_X and NO_X in O_2/CO_2 coal combustion with heat recirculation", *Fuel.* **82**, 1427-1436.

8. Zhuang, Y. and Biswas, P. (2001) "Submicrometer particle formation and control in a bench-scale pulverized coal combustor", *Energ Fuel*. **15**(3), 510-516.

9. Linak, W. P. and Wendt, J. O. L. (1994) "Trace-metal transformation mechanisms during coal combustion", *Fuel Process. Technol.* **39**, 173-198.

10. Quann, R. J., Neville, M., Janghorbani, M., Mims, C. A. and Sarofim, A. F. (1982) "Mineral matter and trace-element vaposization in a laboratory-pulverized coal combustion system", *Environ. Sci. Technol.* **16**, 776-781.

11. Senior, C. L., Panagiotou, T., Sarofim, A. F. and Helble, J. J. (2000) "Formation of ultrafine particulate matter from pulverized coal combustion" *219th American Chemical Society National Conference*, San Francisco, CA, USA., pp. U671-U672.

12. Linak, W. P. and Peterson, T. W. (1984) "Effect of coal type and residence time on the submicrometer aerosol distribution from pulverized coal combustion", *Aerosol Sci. Technol.*, *77*-96.

13. Helble, J. J. and Sarofim, A. F. (1989) "Influence of char fragmentation on ash particle-size distributions", *Combust Flame* **76** (2), 183-196.

14. Kauppinen, E. I. and Pakkanen, T. A. (1990) "Coal combustion aerosols - a field-study", *Environ Sci Technol.* **24** (12), 1811-1818.

15. EPA. (1999) "1999 national emission inventory for hazardous air pollutants", Office of Air Quality Planning and Standards and Office of Research and Development, U.S. Environmental Protection Agency.

16. Wu, C. Y. and Biswas, P. (1993) "An equilibrium-analysis to determine the speciation of metals in an incinerator", *Combust Flame* **93**(1-2), 31-40.

17. Senior, C., Sarofim, A. F., Zeng, T., Helble, J. J. and Mamani-Paco, R. (2000) "Gas phase transformations of mercury in coal-fired power plants", *Fuel Process. Technol.* **63** (2-3), 197-213.

18. Niksa, S., Fujiwara, N., Fujita, Y., Tomura, K., Moritomi, H., Tuji, T. and Takasu, S. (2002) "A mechanism for mercury oxidation in coal-derived exhausts", *J. Air Waste Manage. Assoc.* **52**(8), 894-901.

19. Brown, T. D., Smith, D. N., Hargis, R. A. and O'Dowd, W. J. (1999) "Mercury measurement and its control: What we know, have learned, and need to further investigate", *J. Air Waste Manage. Assoc.* **49**(6), 628-640.

20. Kiga, T. (2001) "O2/RFG combustion-applied pulverized coal fired power plant for CO2 recovery", *Advanced coal combustion*, Takatoshi, M., ed., Nova Science Publisher, Huntington, N.Y., 185-241.

21. Krishnamoorthy, G. and Veranth, J. M. (2003) "Computational modeling of CO/CO2 ratio inside single char particle during pulverized coal combustion", *Energ Fuel* **17**, 1367-1371.

22. Okazaki, K. and Ando, T. (1997) "NO_X reduction mechanism in coal combustion with recycled CO2", *Energy*, **22**, 207-215

23. Hedrick, E., Lee,T.G.,Biswas, P. Zhuang, Y. (2001) "The development of iodine based impinger solutions for the efficient capture of Hg^0 using direct injection nebulization-inductively coupled plasma mass spectrometry analysis", *Environ. Sci. Technol.* **35** (18), 3764-3773.

24. Reynolds, W. C. (1990) "STANJAN-interactive computer programs for chemical equilibrium analysis", Department of Mechanical Engineering, Stanford University.

25. Molina, A. and Shaddix, C. R. (2005) "Effect of O2/CO2-firing on coal particle ignition", *22nd Annual International Coal-Energy, Environment and Sustainable Development Conference*, Pittsburgh, PA.

26. Bool III, L. E. and Helble, J. J. (1995) "A laboratory study of the partitioning of trace elements during pulverized-coal combustion", *Energ Fuel.* **9**, 880-887.

27. Biswas, P. and Wu, C. Y. (1998) "Control of toxic metal emissions from combustors using sorbents: A review", *J. Air Waste Manage. Assoc.* **48**(2), 113-127.

28. Reynolds, J. (2004) "Mercury removal via wet ESP", *Platts Power* **148**(8), 54-59.

29. Lee, C. W. and Srivastava, R. K. (2003) "SCR impact on mercury speciation in coal-fired boilers", *2003 DOE-NETL Conference on Selective Catalytic Reduction and Non-catalytic Reduction for NOx Control*, Pittsburgh, PA.

30. Hammel, C. (2004), "Pahlman process shows promise", *Platts Power* **148**(8), 60-63.

Chapter 3

Charged fraction and electrostatic collection of ultrafine and submicrometer particles formed during O_2–CO_2 coal combustion*

* This work was published in *Fuels*, 87(6), 673-682, 2008

ABSTRACT

The charged fraction of submicrometer and ultrafine particles generated during bench-scale coal combustion and the subsequent penetration of particles through a cylindrical-wire electrostatic precipitator (ESP) in O_2–CO_2 and O_2–N_2 environments were investigated. In all of the combustion environments used, natural particle charging within the combustor was not adequate for high efficiency particle collection in the ESP; thus, corona generation was necessary for enhanced particle charging. With a positive applied potential, the corona inception voltage and voltage required to reach a given current level in the ESP in gas mixtures composed of O_2 and CO_2 were higher than those composed of O_2 and N_2, while similar voltages were needed for negative corona generation. In positive coronas, particle penetration through the ESP in O_2–CO_2 environments was 1–2 orders of magnitude higher than in O_2–N_2 environments. Little difference in particle penetration between O_2–N_2 and O_2–CO_2 was seen in negative coronas.

3.1 INTRODUCTION

Coal is widely used as an energy source because of its relative abundance and stable cost [1]. However, environmental issues are associated with coal combustion, namely, the emission of heavy metals [2, 3] and CO_2 to the atmosphere. Because CO_2 is a known greenhouse gas and has potential effects on global warming, the capture of CO_2 from coal combustion exhaust is receiving increased attention [4]. In a typical coal combustion system, the CO_2 volume fraction is only 0.13-0.15, and current CO_2 capture methodologies are not cost effective [5]. A potential method to increase the volume fraction of CO_2 in coal combustor exhaust is to combust coal in an oxygen-enriched environment and then recycle the exhaust gas to serve as the diluent gas. The stable operation of such a system would result in a CO_2 volume fraction of up to 0.95 in exhaust gases [5-11]. Under such CO_2-rich conditions, capture methodologies would be more economically feasible. Changing the composition of the gas mixture that coal is combusted in may have numerous effects on other pollutants associated with coal combustion. Suriyawong et al. [5] found that the size distribution of ultrafine and submicrometer particles was altered when N_2 was replaced by CO_2 in an oxygen-enriched combustion system. In the O_2-CO_2 system, the mean particle size and number concentration of fine particles (particles less than 2.5μm in diameter) decreased, the ratio of coarse (particles larger than 2.5μm) to fine particles increased, and the size distribution shifted toward smaller sizes. The

collection efficiency of particulate control devices is size dependent; thus, the performance of particulate control devices will be altered in O_2-CO_2 combustion.

In the United States, the majority of coal-fired power plants utilize electrostatic precipitators (ESPs), which can have mass-based collection efficiencies of over 99% [12]. ESPs collect fine, submicrometer (less than 1μm and greater than 100nm in diameter) and ultrafine (less than 100nm in diameter) particles. Previous researchers have determined the penetration (1 minus the collection efficiency) of particles through ESPs in conventional gas environments as a function of particle size. Zhuang and Biswas [13] studied the formation of submicrometer and ultrafine particles within a bench scale coal combustor and their penetration in a cylindrical-wire ESP [14]. Huang and Chen [15] measured ultrafine, submicrometer, and supermicrometer particle penetration through single stage and two-stage ESPs, as well as the loading characteristics of wire-plate ESPs [16]. Both sets of studies showed that particle penetration through ESPs is dependent on particle size for all ESP geometries [12]. For ultrafine particles, particle penetration increases with decreasing particle size due to inefficient diffusion charging. For submicrometer particles, penetration increases with increasing size due to the increase in drag force resulting from an increase in particle size. There is, therefore, a window of penetrating particle sizes in the ultrafine and submicrometer size ranges, which is a function of the ESP geometry and is typically in the 10-100nm range [13, 15].

Conversely, larger fine particles are charged efficiently by field charging and have low penetrations, giving rise to the high mass-based collection efficiencies of ESPs. Submicrometer size particles and ultrafine particles generated from coal combustion have been reported to pose harmful health effects to human beings due to their enrichment with toxic metals [2]. Since particles in these size ranges are not effectively captured by ESPs, the emission of these particles into the environment is critical. Thus, this study focused on the effects of O_2-CO_2 combustion on the performance of ESPs in the submicrometer and ultrafine particle sizes.

While the effects of particle size on the collection efficiency of ESPs have been studied, little research has been done on the impact of using different gas mixtures. ESPs utilize the formation of a corona discharge to charge and collect aerosol particles. The dominant ion production mechanism in positive coronas is ionization by electron impact, in which free electrons in the gas acquire energy from an applied electric field and collide violently with gas molecules, which, in turn, removes electrons from the gas molecules. The net result is the creation of additional free electrons and positively charged gas ions [17]. For this process to occur, the free electron-gas molecule collisions must be sufficiently energetic, i.e., the collision energy must be greater than the ionization energy, which is a characteristic of the gas molecule or atom bombarded [18]. In negative coronas, free electrons are directed out of the plasma region by strong electrical fields, and ion production primarily

occurs through photoionization near the discharge electrode. Free electrons readily attach to neutral gas molecules, creating negative gas ions. Presumably, a change in gas composition from conventional air combustion to O_2-CO_2 combustion would affect ion production within the ESP and further affect ESP collection efficiency. Negative corona formation in a O_2-CO_2 environment has been investigated previously [19]. However, the effect of using a gas mixture primarily composed of CO_2 and O_2 on the performance of ESPs has not been addressed with regard to particle collection. Before O_2-CO_2 combustion systems can be employed, the change in ESP performance due to the change in coal combustion exhaust gas composition needs to be assessed. This work investigated the effects of O_2-CO_2 combustion on the performance of ESPs which remove coal combustion aerosol particles. Ultrafine and submicrometer particles generated from coal combustion are typically formed by nucleation and are therefore enriched in toxic metals [2, 3]. The penetration of these particles through ESPs is of particular concern in this study. Since ESP performance is dependent on the charging efficiency of particles, the charged fractions of ultrafine and submicrometer particles in conventional combustion and in O_2-CO_2 combustion was also measured. Particle charging in the combustion process itself would make particle charging in the ESP unnecessary and mitigate the effects of changing gas composition. The penetration of coal combustion-generated particles through a cylindrical-wire ESP with different gas mixtures was determined both experimentally

and numerically, using diffusion charging theory [20]. The data presented here can be used to create guidelines for proper ESP operation in O_2-CO_2 systems.

3.2 EXPERIMENTS AND METHODS

The gas mixtures examined were chosen to mimic gas mixtures that would potentially be used in coal combustors where CO_2 is recycled and used as the diluent gas. The performance of an electrostatic precipitator in O_2-CO_2 gas mixtures was compared to its performance in mixtures of N_2 and O_2. Mixtures of 50%O_2-50%N_2 (by volume) and 50%O_2-50%CO_2 represented oxygen enriched combustion conditions, while air and 20%O_2–80%CO_2 represented more typical oxygen combustion concentrations. Also, 30%O_2–70%CO_2 was studied because the adiabatic flame temperature of combustion for this gas mixture is similar to that of air [5]. In addition, pure CO_2 and pure N_2 were studied for comparison with the O_2-N_2 and O_2-CO_2 gas mixtures.

Four sets of experiments were performed and are described in Table 3.1. A schematic of the experimental systems is shown in Figure 3.1. In set I of the experiments, the fractions of positively and negatively charged particles produced in a coal combustor were measured. A bench scale coal combustor, described previously [5, 13], was used for the combustion of Powder River Basin sub-bituminous coal.

Coal was fed continuously using an impinger as a coal feeder (AGI-4, ACE Glass Inc., Vineland, NJ, USA) into the combustor at a flowrate of 1.75 lpm of the desired gas mixture. The combustor was operated with a wall temperature of 1473K. At the combustor outlet, charged particle fractions were determined by mobility selecting unneutralized particles with a differential mobility analyzer (DMA, model 3071, TSI Inc., Shoreview, MN, USA) and measuring their number concentration with a condensation particle counter (CPC, model 3022a, TSI Inc.). The number concentration of particles penetrating through the DMA after passing through a Po-210 radioactive source was also measured. The radioactive source brought the particles to a known charge distribution [21-23]. The fraction of charged particles at the coal combustor outlet was calculated using the known charge distribution of particles after the radioactive source and the number concentration measurements of particles penetrating through the DMA, with and without prior passage through the radioactive source. This equation is [24]:

$$Cf = \frac{Nc}{Nc_{eq}} Cf_{eq} \quad (1),$$

where Cf is the fraction of charged particles, Nc is the number concentration of charged particles of diameter d_p, Nc_{eq} is the number concentration of charged particles of diameter d_p detected after charge neutralization, and Cf_{eq} is the equilibrium charge fraction for particles of diameter d_p calculated as described by Wiedensohler [22]. For simplicity, only charged particles of +1 or -1 unit charges (1.6×10^{-19}C) were

considered. The DMA was operated using both a negative and positive applied voltage to determine the fraction of particles with +1 and -1 unit charges, respectively.

Table 3.1: Summary of the experiments performed.

Table 3.1

Set	Purpose	Gases Used
I	Measure the fraction of positively and negatively charged particles at the outlet of the coal combustor	Air, 20%O_2-80%CO_2, 50%O_2-50%CO_2
II	Determine voltage-current characteristics of the electrostatic precipitator to determine corona initiation in different gases	100%N_2, 50%O_2-50%N_2, Air, 100%CO_2, 20%O_2-80%CO_2, 30%O_2-70%CO_2, 50%O_2-50% CO_2
III	Measure the penetration of combustion particles through the electrostatic precipitator as a function of applied voltage	50%O_2-50%N_2, Air, 20%O_2 - 80%CO_2, 30%O_2-70%CO_2, 50%O_2-50%CO_2
IV	Measure particle penetration through the electrostatic precipitator as a function of particle diameter	100% N_2, 50%O_2-50%N_2, Air, 100% CO_2, 20%O_2-80%CO_2, 30%O_2-70%CO_2, 50%O_2-50% CO_2

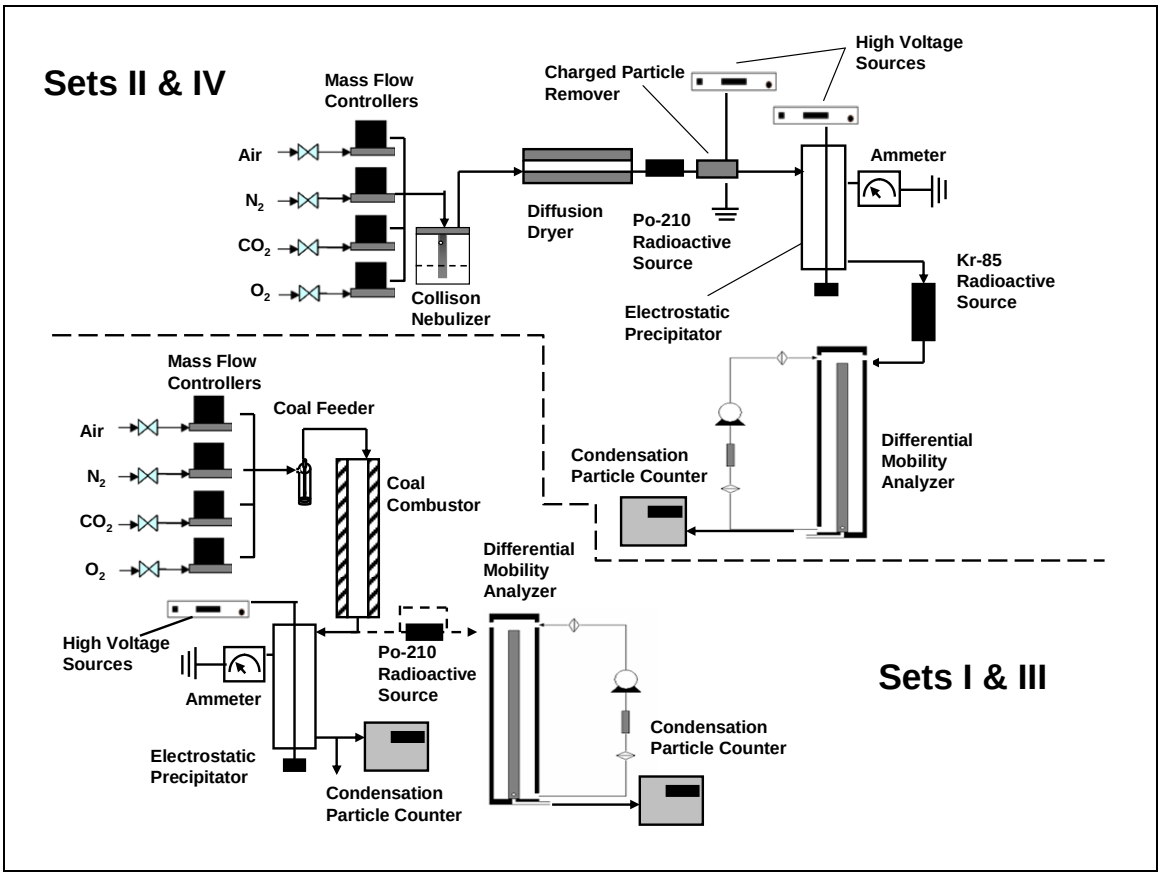

Figure 3.1: Schematic diagram of experimental setup.

For experimental sets II-IV, a cylindrical-wire ESP, described previously [14], was used. In experimental set II, the voltage-current characteristics of the ESP with different gas compositions were determined. Positive and negative voltages were applied to the central wire electrode of the ESP using a Bertan High Voltage power supply (Model 206-20, Spellman, Valhalla, NY, USA). The ionic current generated after corona inception was measured using a microammeter connected to the ESP ground electrode. A total flow rate of 7 lpm was sent through the ESP with the desired volume fractions of dry air, N_2, CO_2, and O_2. The residence time in the ESP was approximately 1 second. Aerosol particles were not produced for these experiments, and the gas filtered stream entering the ESP was particle free.

In set III experiments, the penetration of coal combustion-generated particles through the ESP was determined as a function of the voltage applied to the ESP. To the ESP to calculate penetration values, total particle number concentrations were measured with a CPC, with and without a voltage applied. Particle penetration though the ESP would result from the combined effects of ESP performance and particle charging within the combustor itself at different combustion gases influenced.

To separate the influenced of gas mixtures on particle charging in the combustor from particle charging within the ESP, Set IV experiments were performed using a charged-neutralized Na_2SO_4 aerosol particles. The particles, with a fixed size

distribution in the 6-225nm size-range, were produced by nebulizing a 20mM solution of Na_2SO_4 using a six-jet collision nebulizer (BGI Inc., Waltham, MA, USA) with different gas mixtures at a flow rate of 7.0 lpm. The droplets produced by the nebulizer were subsequently dried in a diffusion dryer (model 3062, TSI Inc., Shoreview, MN, USA), leaving dry, particle-laden gas of the desired composition. Particles were charge-neutralized by exposing them to a Po-210, α-particle source, and any remaining charged-particles were removed electrostatically using a charged-particle removal device (plate condenser). Uncharged particles then entered the ESP, which was operated so that an inner electrode to ground electrode current of 0.5μA was present. Particles exiting the ESP were charge neutralized using a Kr-85 radioactive source and then size classified and counted using the DMA and CPC operated together as a scanning mobility particle size spectrometer [25, 26]. For each measured particle size, penetration was calculated by dividing the particle number concentration with a voltage applied, by the number concentration measured with no applied voltage.

To further study the differences in ESP performance, a numerical simulation of nanoparticle diffusion charging and collection was used. Fuchs limiting-sphere theory [23] was coupled to a transport model to calculate the penetration of particles through the ESP. A detailed description of the model can be found elsewhere [20].

3.3 RESULTS AND DICUSSION

3.3.1 Charged Fraction of Coal Combustion Particles.

Nanoparticle collection in ESPs depends primarily on particle charging efficiency within an ESP and therefore on particle size [20]. Although the charging efficiency of particles within an ESP may change with changes in gas composition, coal combustion particles could still be successfully captured regardless of charging efficiency within the ESP if a large fraction of the particles were charged. That is, if diffusion charging within the ESP was unnecessary for particle collection, then the effects of different gas compositions on particle penetration through ESPs would be minimal. It was, therefore, necessary to determine the fraction of positively and negatively charged particles at the outlet of a combustor where different gas mixtures were used as the diluent gas (Set I). Particle charging in coal combustion systems could occur in the high temperature region near the combusting coal particle, where ion concentrations would be greater. Greater ion concentrations would potentially cause ion-induced nucleation [27] of vapors which evaporate from the coal particle during combustion, as well as increased diffusion charging. Thermal ionization processes could also have been prevalent throughout the combustor. Figure 3.2 shows the fraction of charged particles with +1 and -1 unit charges with respect to total particle number concentration at sizes of 20, 30, 40, 60, 100 and 200nm. Also

shown is the bipolar diffusion charging equilibrium charged fraction for particles with +1 (dashed line) and -1 (solid line) unit charges [22]. Coal combustion particles had non-equilibrium, bipolar charge distribution, with the total charged fraction higher than the equilibrium charged fraction for all measured sizes. For 100nm and 200nm particles, an increased fraction of positively charged particles was measured, indicating that there was an excess of positive ions present in the combustor or that larger coal combustion particles were charged via thermal ionization during the high temperature combustion process. The non-equilibrium nature of the measured coal combustion particles charge fraction agreed well with previous measurements of combustion aerosol particle charge [28, 29], and the fraction of both positively and negatively charged particles increased with particle size. No distinguishable effects of combustion gas mixture on the charged fractions of either +1 or -1 charged particles with changing combustion gas mixture were apparent. Although the total fraction of charged particles was found to be greater than 0.50 for some particle sizes, this fraction was not sufficient for high efficiency particle collection within an ESP, where the total concentration of particles should decrease by several orders of magnitude [12, 30]. Therefore, additional particle charging is necessary within an ESP for particle collection, which is dependent on corona formation and ion production in the exhaust gases from a combustor.

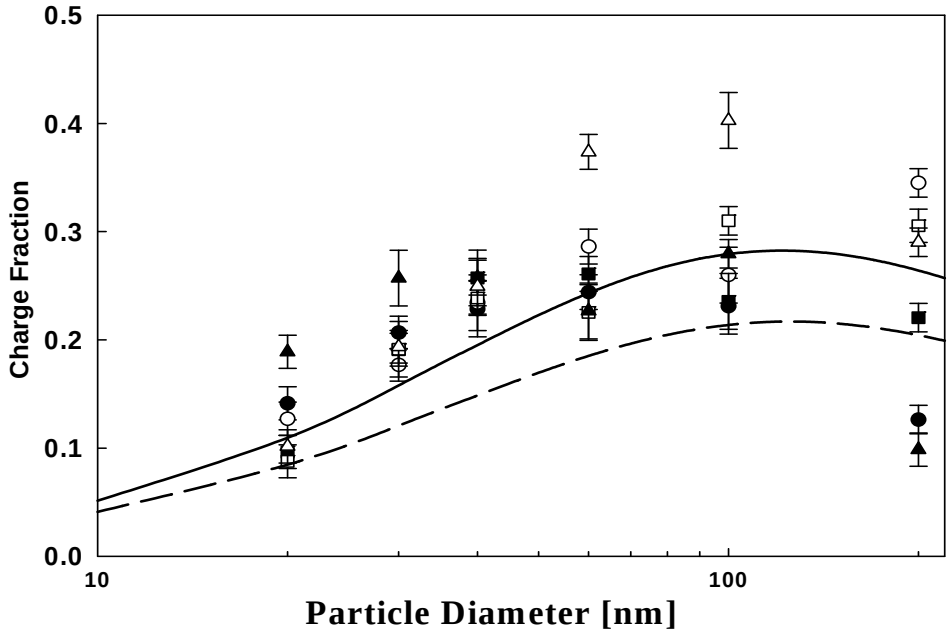

Figure 3.2: Fraction of +1 and -1 charged particles at the outlet of the coal combustor (Set I). Legend: —●— Air (-1), —○— Air (+1),—■— 20%O_2-80%CO_2 (-1), —□— 20%O_2-80%CO_2 (+1), —▲—50%O_2-50%CO_2 (-1), —△—50%O_2-50%CO_2 (+1). Equilibrium lines: Weidensohler, 1988. Solid Line (-1), Dashed Line (+1).

3.3.2 Voltage-Current Characteristics.

Ion production can be quantified by measuring voltage-current characteristics. The voltage-current characteristics of the ESP with positive and negative applied voltages are shown in Figures 3.3a and 3.3b, respectively. Establishment of a stable current with pure N_2 and a negative applied voltage was not possible experimentally. The electrode to electrode current within the ESP increased rapidly once a corona was established. This behavior is characteristic of most corona systems, where the

current is quadratically dependent on the applied voltage [19]. With a positive applied voltage in both O_2-N_2 and O_2-CO_2 mixtures, the voltage required to reach a given current level was lowest for gas mixtures with the highest volume fraction of O_2. Presumably, more ions were generated in the gas mixtures with higher O_2 volume fractions because O_2 has a lower ionization potential than does either N_2 or CO_2 (12.6V for O_2, as compared to 16.3V and 14.3V for N_2 and CO_2, respectively) [31]. This finding is also consistent with the voltage-current characteristic of pure N_2, where a higher positive applied voltage was required to reach the same current level as in O_2-N_2 mixtures. With the same O_2 volume fraction, the O_2– CO_2 gas mixtures required several kilovolts higher positive voltage to reach the same current level as in O_2–N_2 mixtures. CO_2 has a higher dielectric constant than N_2 (1.6 as compared to 1.0 for N_2) [32]; thus, at a given applied voltage the effective electric fields in CO_2 environments were reduced, preventing corona formation. Furthermore, CO_2, which has no electron affinity, commonly dissociates into carbon monoxide (CO) and an oxygen atom (O) when it collides with an electron having energy greater than 5.5 electron volts. Atomic oxygen can act as an electron trap in gases, resulting in reduced electron ionization and suppressing electric discharge in gas [17]. Coronas generated in pure CO_2 had a slightly different behavior than in O_2-CO_2, presumably due to the generation of different ionic species. In pure CO_2, the primary ions are CO_2^+, CO^+, O^+, and C^+, which have corresponding ionization potentials of 14.4, 20.4, 19.6, and 28.3 V, respectively [33]. In pure O_2, the primary ions are O_2^+ and O^+,

occurring at 13.5 and 20.0V, respectively [34]; thus, the primary ions present in O_2-CO_2 gas mixtures are different than those in pure CO_2, resulting in different ion production behavior. With negative applied voltages, however, there was no difference in the voltage-current characteristics of CO_2 and N_2 gas mixtures. This implies that negative corona systems are primarily dependent on direct photoionization of the discharge electrode, which has a lower work function than any gas used in this study, and on the presence of O_2 (an electronegative element), which would presumably lead to the formation of the O_2^- ion [35].

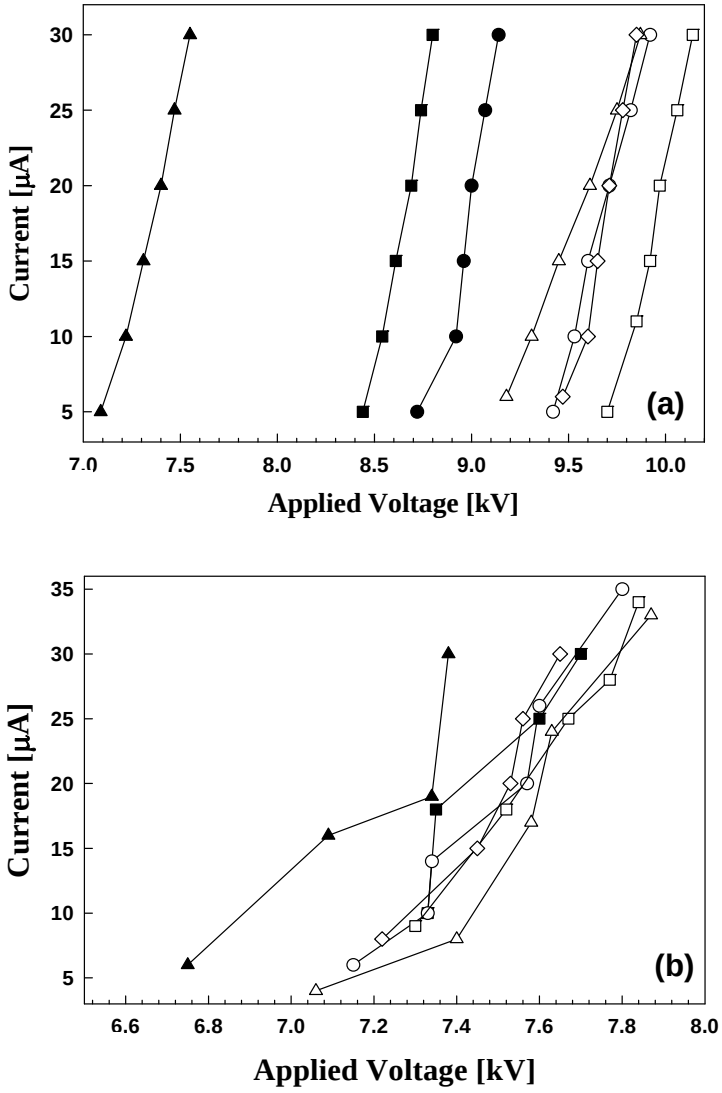

Figure 3.3: The voltage-current characteristics of the ESP with (**a.**) positive applied voltages, and (**b.**) negative applied voltages (Set II).
Legend: 100%N_2, Air, 50%O_2-50%N_2, 100%CO_2, 20%O_2-80%CO_2, 30%O_2-70%CO_2, 50%O_2-50%CO_2

3.3.3 Capture Efficiency of the ESP.

The penetration of coal combustion aerosols through the ESP as a function of applied voltage is shown in Figures 3.4a and 3.4b for positive and negative applied voltages, respectively. The corona inception point can be seen in these figures as the point when particle penetration decreased below unity. As expected, with positive applied voltages, a greater applied voltage was needed to reach corona inception in O_2-CO_2 systems than in O_2-N_2 systems. Furthermore, even after corona inception, the particle penetration was 1-2 orders of magnitude higher in O_2-CO_2 systems. With negative applied voltages, no clear differences were apparent between coal combustion particle penetrations in different gas mixtures. This was also expected based on voltage-current characteristics found in experimental sets II for negative applied voltages, where little difference was observed between different gas mixtures.

The change from an O_2-N_2 gas mixture to O_2-CO_2 also influences the production of ultrafine and submicrometer particles within a coal combustor [5]. Since emission standards are not based on the performance of the particulate removal devices used, but rather on the total mass of particulate material emitted from a power plant, the effects of a change in particle production rate with a change in the combustion gas mixture must be taken into account. This study calculated the ratio of the total number concentration of particles at the ESP outlet with different

combustion conditions to the number concentration at the ESP outlet with air used as the diluent gas. Figures 3.5a and 3.5b show this ratio as a function of applied voltage, with positive and negative applied voltages, respectively. For positive applied voltages, it was necessary to use higher applied voltages for corona generation in O_2-CO_2 gas environments than for air. At a fixed voltage, the number concentration of particles at the ESP outlet was between 10^1 to 10^5 times greater with O_2-CO_2 gas mixtures than with conventional combustion. The difference in number concentration increased with applied voltage below the corona inception voltage in O_2-CO_2 systems because a corona was already present in air at these voltages. Thus, an increase in voltage increased particle collection in air but had no effect in O_2-CO_2. Beyond the O_2-CO_2 corona inception voltage, the difference in number concentration slowly began to decrease with increasing voltage. In other words, particle collection in air changed very little with increasing applied voltage, while particle collection increased with increasing applied voltage in O_2-CO_2. Even at high applied voltages, where a corona was present in both air and in O_2-CO_2 environments, the difference in number concentration was greater than 10^1 for O_2-CO_2 gas mixtures. Conversely, when a negative corona was used a lower number concentration of particles exiting the ESP was observed when the combustor was operated with O_2-CO_2 gas mixtures than with air (Figure 3.5b). For voltages larger than -8kV, the concentration of particles at the ESP outlet in O_2-CO_2 systems was only 10% to 60% of the concentration of particles in conventional combustion systems.

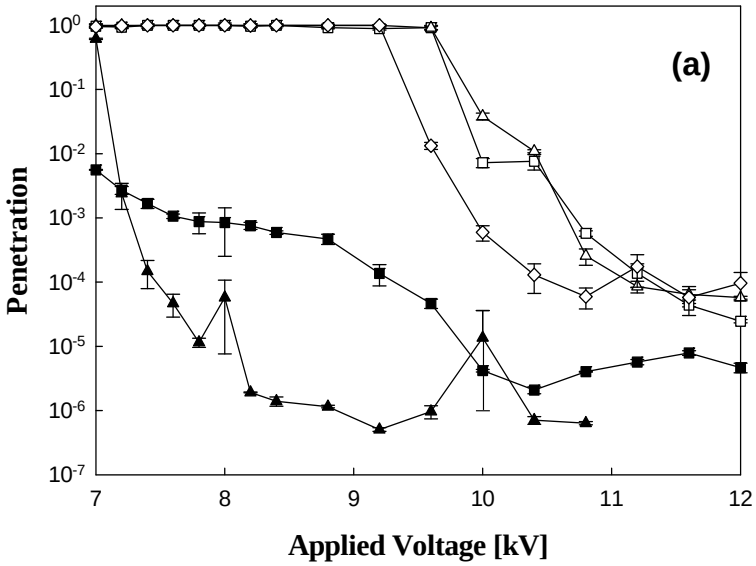

Figure 3.4: Coal combustion generated particle penetration with (**a.**) positive applied voltages and (**b.**) negative applied voltages (Set III). Legend: Air, $50\%O_2$-$50\%N_2$, $20\%O_2$-$80\%CO_2$, $30\%O_2$-$70\%CO_2$, $50\%O_2$-$50\%CO_2$.

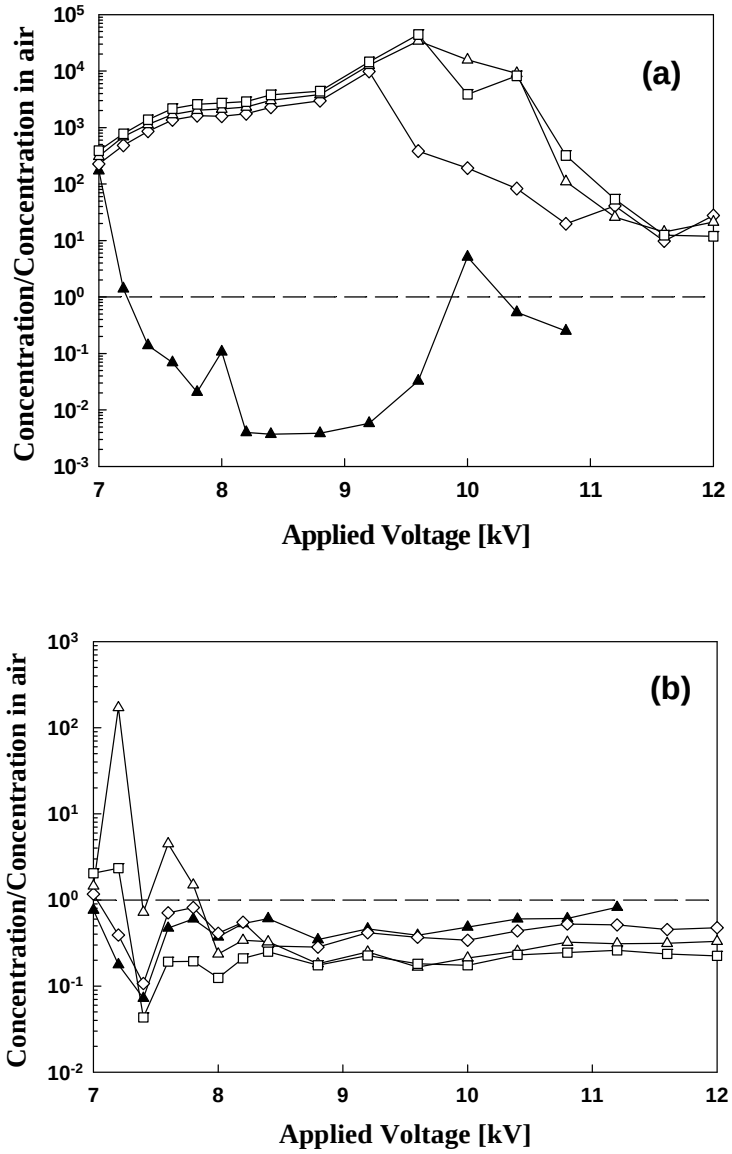

Figure 3.5: Ratio of concentration at ESP outlet when different gases are used to concentration at ESP outlet when air is used in the combustor, for (**a.**) positive applied voltages and (**b.**) negative applied voltages. Legend: —▲— 50%O_2-50%N_2, —□— 20%O_2-80%CO_2, —△— 30%O_2-70%CO_2, —◇— 50%O_2-50%CO_2.

3.3.4 Effects of Carrier Gas on Particle Charging and Capture.

The extreme difference in particle penetration through the ESP with positive coronas between O_2-CO_2 and O_2-N_2 systems implies that there is also a difference in ion structure or ion concentration in these systems. In the particle penetration experiments with Na_2SO_4 test aerosol particles, voltages were applied so that an electrode to electrode current of 0.5μA was present. A current of 0.5μA can be regarded as a relatively "weak" corona current. This current level was intentionally used to maximize particle penetration, which allowed the differences between gas mixtures to be seen, i.e., with high corona currents, particle penetration was too low in all cases to observe differences between gas mixtures. The particle penetration curves for the ESP with pure CO_2 and pure N_2 are shown in Figure 3.6, while the particle penetration curves for O_2-N_2 and O_2-CO_2 gas mixtures are shown in Figures 3.7a (positive voltages) and 3.7b (negative voltages). For the ESP used here, the minimum size of penetrating particles was approximately 50-60nm.

As seen in Figure 3.6, particle penetration for almost all tested particle sizes was lower in pure CO_2 than in pure N_2. However, the particle penetration in O_2-N_2 systems was 1-2 orders of magnitude lower than in O_2-CO_2 systems for positive coronas (Figure 3.7a). These data are not contradictory; interactions between gas

molecules within a gas mixture play an important role in determining ion concentrations and mobility [19, 36] as well as molecular clustering around ions [37]. With negative applied voltages (Figure 3.7b), the particle penetration in O_2-N_2 systems was lower than in O_2-CO_2, although the magnitude of the difference between the two gas mixture types was less than it was for positive applied voltages. This implies the ions in O_2-N_2 and O_2-CO_2 systems formed in negative coronas are more similar in mobility and number concentration than the ions formed in positive coronas. This interpretation is consistent with our previous supposition that ion generation in negative corona systems is dependent primarily on photocharging of the discharge electrode and the presence of O_2, resulting in similar ion concentrations and ion mobility in both O_2-N_2 and O_2-CO_2 systems.

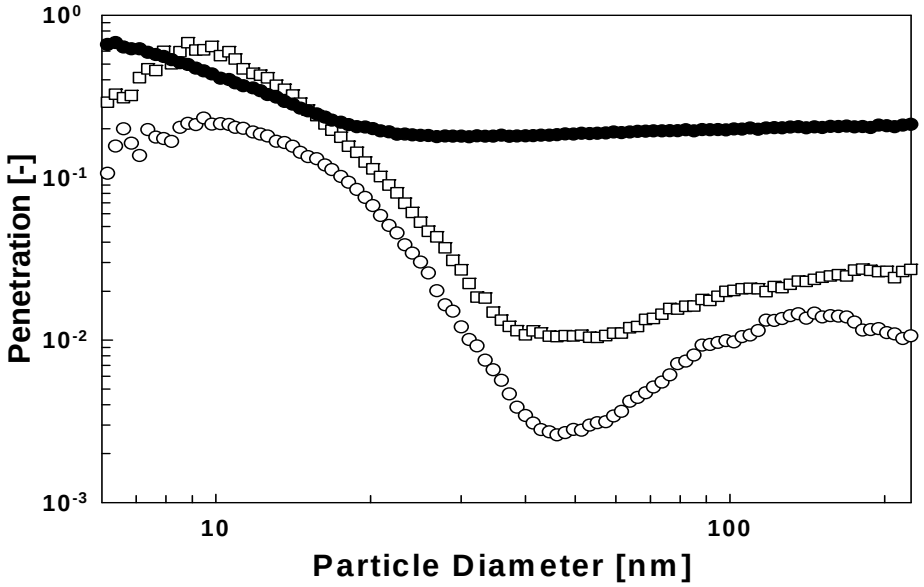

Figure 3.6: Particle penetration through the ESP in pure gas environments (Set IV). Legend: —●— 100%N_2 (positive voltage), —○— 100%CO_2 (positive voltage), —□— 100%CO_2 (negative voltage).

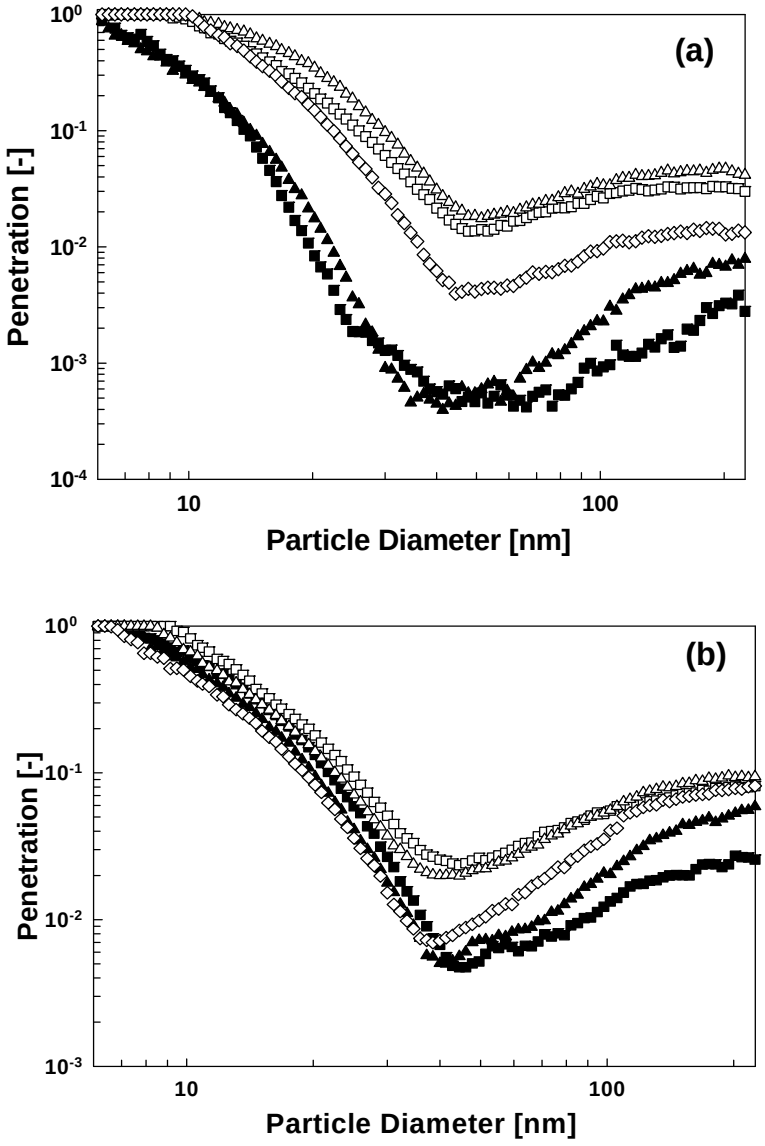

Figure 3.7: Particle penetration through the ESP in mixed gas environments with (**a.**) positive applied voltages and (**b**) negative applied voltages (Set IV). Legend: Air, $50\%O_2$-$50\%N_2$, $20\%O_2$-$80\%CO_2$, $30\%O_2$-$70\%CO_2$, $50\%O_2$-$50\%CO_2$.

To further study the effects that the change from O_2-N_2 to O_2-CO_2 has on ESP performance with a positive applied potential, a nano-particle collection model accounting for diffusion charging [20] was used to calculate particle penetration. Simulated gas environments were developed that were qualitatively similar to those used in the experiments. Particle charging and collection were first modeled in simulated O_2-N_2 gas environment, using known values for the mobility and mass of ions in air [21] with an applied potential of 8kV in an ESP with identical dimensions to the one used in the experiments. Particle charging and collection were then modeled in a simulated O_2-CO_2 gas environment with an applied potential of 10kV, as it had been found in experiments that higher applied positive potentials were necessary to reach a given corona current level in O_2-CO_2 gas mixture. However, the mass and mobility of ions in O_2-CO_2 systems were unknown; thus, simulations were performed using (1) the same mass and mobility for O_2-CO_2 ions as for O_2-N_2 ions, (2) a higher mass and lower mobility for O_2-CO_2 ions as compared to O_2-N_2 ions, and (3) a lower mass and higher mobility for O_2-CO_2 ions as compared to O_2-N_2 ions. The parameters used in the simulation and the simulation conditions are shown in Table 3.2. Using the test ion mobility, fixed corona current, known applied voltage, and fixed ESP geometry, the number concentration of ions in the ESP was determined using the equation:

$$I = n_p * e * Z_p * E_c * (2 * \pi * R * L), \quad (2),$$

where I is the corona current (A), n_p is the ion concentration (ions/m^3), e is the charge on an electron, Z_p is the ion mobility (m^2/V-s), E_c is the electric field at the outer electrode (V/m), R is the radius of collection surface of ESP (m), and L is the length of ESP (m).

Table 3.2: The parameters used in the simulation and the simulation conditions

Table 3.2

Parameters used in simulation				
Pressure	1 atm			
Temperature (T)	298 K			
Elementary charge (e)	1.602×10^{19} C			
Dielectric constant of fly ash	12 for SiO_2			
Length of the ESP	0.15 m			
Radius of collection surface of the ESP	0.025 m			
Radius of corona wire	0.00017 m			
Simulation conditions				
	1.O_2-N_2	**2.O_2-CO_2**	**3.O_2-CO_2**	**4.O_2-CO_2**
Ion mobility (m^2/V-s)	1.5×10^{-4}	1.5×10^{-4}	5.0×10^{-5}	8.0×10^{-4}
Ion mass (amu)	1.5×10^{2}	1.5×10^{2}	6.0×10^{2}	3.20×10^{1}
(1 amu= 1.661×10^{-27} kg)				
Ion concentration (ions/m^3)	1.88×10^{13}	1.50×10^{13}	4.51×10^{13}	2.82×10^{12}
Applied voltage (V)	8,000	10,000	10,000	10,000
Electric field at outer electrode (V/m)	1.568×10^{5}	1.96×10^{5}	1.96×10^{5}	1.96×10^{5}
Corona current (mA)	1.0	1.0	1.0	1.0

Running simulations at fixed applied voltage, where the corona current in O_2-N_2 is significantly greater than the corona current in O_2-CO_2 did not allow for the influences of different ion mass and mobility to be discerned. Hence, as in experiments, simulations with O_2-N_2 and O_2-CO_2 gas mixtures were performed using a fixed corona current. Simulation results are shown in Figure 3.8. For all particle sizes, particle penetration was highest for the highest ion mobility ($8cm^2/V\text{-}s$). The penetration of particles decreased with decreasing ion mobility because lower mobility ions led to higher ion concentrations for a fixed corona current. These simulations imply that the mobility of ions of O_2-CO_2 gas mixtures is higher than the ion mobility of O_2-N_2 mixtures. Presumably, clustering of gas molecules around positive charges is more prevalent in mixtures of N_2 and O_2 as compared to CO_2 and O_2. Furthermore, CO_2 often dissociates into CO and O radicals upon collision with energetic electrons, reducing the mass and increasing the mobility of the species present. Enhanced ion mobility will typically enhance particle charging. At a fixed corona current, however, increases in ion mobility come at the expense of ion concentration, the effects of which on particle charging outweigh those of ion mobility. Therefore, even at equal positive corona currents, more ions are present in O_2-N_2 gas mixtures than in O_2-CO_2 gas mixtures. The combined effects of increased corona inception voltage and lower ion concentrations in positive coronas in O_2-CO_2 severely hinder particle collection in electrostatic precipitators operating under these conditions.

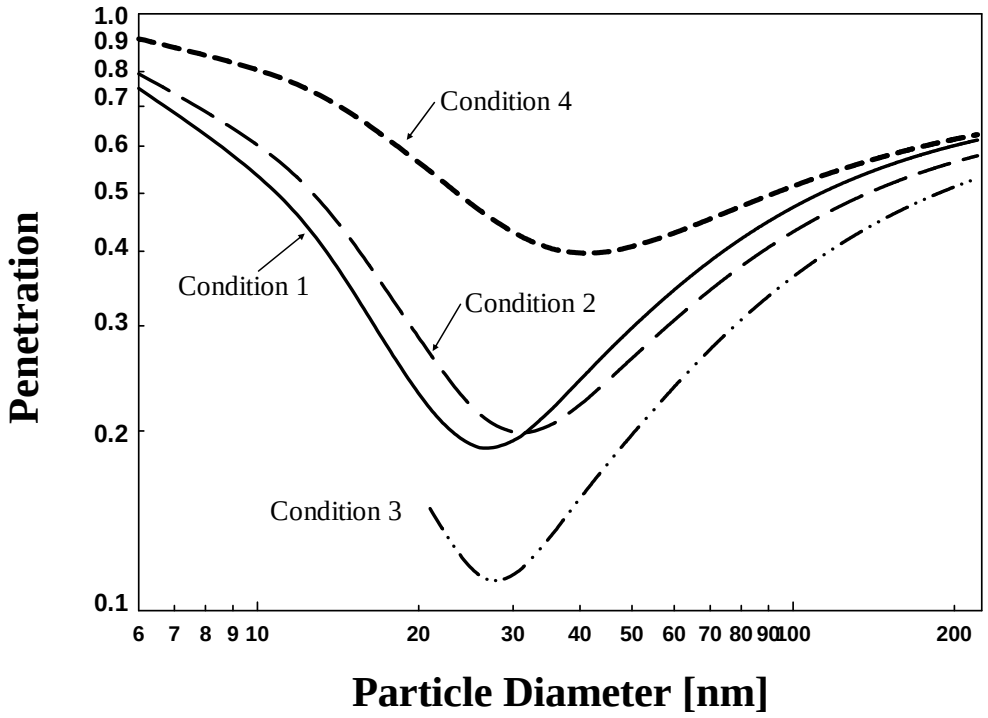

Figure 3.8: Calculated particle penetration though an ESP by numerical simulation. The conditions used are listed in Table 3.2.

3.4 CONCLUSIONS

The results of the four experimental sets shown here have clear implications on the effect that O_2-CO_2 coal combustion will have on particulate emissions from power plants. The sizes of particles examined in this study were in the ultrafine and submicrometer size regimes. Coal combustion generated particles of this size are enriched in toxic heavy metals, and efficient removal of these particles from combustion exhaust flow is extremely important. To minimize ultrafine and submicrometer particle emissions, power plants operating electrostatic precipitators with positive applied voltages, as is common for two stage ESPs [38] will need to increase the applied voltage to the ESP. The necessary increase in power consumption necessary can be estimated from the ratio of the voltage applied in the O_2-CO_2 system to the voltage applied in air that was necessary to obtain a given electrode-to-electrode current in the measurements made here. For example, a 15% increase in power would be needed to operate a positive corona at 10μA in 80% CO_2-20%O_2 as compared to air. Even at the same current level, numerical simulations revealed that the ion concentration of positive ions in O_2-CO_2 systems is lower than in O_2-N_2 systems, thus decreasing the diffusion charging efficiency within ESPs and greatly increasing particle penetration. Particle charging within the combustor itself is so low that diffusion charging within ESPs is essential for low particle penetration, regardless of the combustion gases used. The effects of O_2-CO_2 gas mixtures on ESP

performance will lead to a substantially greater number concentration of particles emitted from power plants using O_2-CO_2 combustion and applying positive voltages to their electrostatic precipitators. If negative applied voltages are used, the effects of using O_2-CO_2 in coal combustion on the performance of electrostatic precipitators are minimized.

3.5 REFERENCES

1. Buhre, B. J. P., Elliott, L. K., Sheng, R. P., Gupta, R. P. and Wall, T. F. (2005) "Oxy-fuel combustion technology for coal-fired power generation", *Prog Energ Combust* **31**, 283-307.

1. Bool III, L. E. and Helble, J. J. (1995) "A laboratory study of the partitioning of trace elements during pulverized-coal combustion", *Energ Fuel.* **9**, 880-887.

2. Biswas, P. and Wu C.Y. (2005) "Critical Review: Nanoparticles and the environment", *J. Air Waste Manag. Assoc.*, **55**(6), 708-746.

3. Hughes, R. W., Lu, D. Y., Anthony, E. J. and Macchi, A. (2005) "Design process simulation and construction of an atmospheric dual fluidized bed combustion system for in situ CO2 capture using high-temperature sorbents", *Fuel Process Technol.* **86**, 1523-1531.

4. Suriyawong, A., Gamble, M., Lee, M.-H., Axelbaum, R. L. and Biswas, P. (2006) "Submicrometer particle formation and mercury speciation under O2-CO2 coal combustion with carbon dioxide recycle", *Energ Fuel.* **20**(6), 2357-2363.

5. Chui, E.H., M.A. Douglas, and Y. Tan (2003) "Modeling of oxy-fuel combustion for a western Canadian sub-bituminous coal" *Fuel* **82**(10), 1201-1210.

6. Andersson, K. and Johnsson F. (2007) "Flame and radiation characteristics of gas-fired O2/CO2 combustion" *Fuel*. **86**(5-6): 656-668.

7. Tan, Y. W., Croiset, E., Douglas, M. A. and Thambimuthu, K. V. (2006) "Combustion characteristics of coal in a mixture of oxygen and recycled flue gas", *Fuel* **85**(4), 507-512.

8. Hektor, B. (1998) "Cost effectiveness of measures for the reduction of net accumulation of carbon dioxide in the atmosphere", *Biomass and Bioenergy*. **15**, 229-309.

9. Doctor, R. D., Molburg, J. C. and Thimmapuram, P. R. (1997) "Oxygen blown gasification combined cycle: carbon dioxide recovery, transport and disposal", *Energy Conversion Management.* **38**, 575-580.

10. Desideri, U. and Paolucci, A. (1999) "Performance modeling of a carbon dioxide removal system for power plants", *Energy Conversion and Management.* **40**, 1899-1915.

11. Kulkarni, P., Namiki, N., Otani, Y. and Biswas, P. (2002) "Charging of particles in unipolar coronas irradiated by in-situ soft x-rays: Enhancement of capture efficiency of ultrafine particles", *J Aerosol Sci.* **33**(9), 1279-1296.

12. Zhuang, Y. and Biswas, P. (2001) "Submicrometer particle formation and control in a bench-scale pulverized coal combustor", *Energ Fuel*. **15**(3), 510-516.

13. Zhuang, Y., Kim, Y. J., Lee, T. G. and Biswas, P. (2000) "Experimental and theoretical studies of ultra-fine particle behavior in electrostatic precipitators", *J Electrostat.* **48**(3-4), 245-260.

14. Huang, S.H. and Chen, C.C. (2002) "Ultrafine aerosol penetration through electrostatic precipitators" *Environ. Sci. Technol.* **36**(21), 4625-4632.

15. Huang, S.H. and Chen C.C. (2003) "Loading characteristics of a miniature wire-plate electrostatic precipitator" *Aerosol Sci. Technol.* **37**(2), 109-121.

16. White, H.J., *Industrial Electrostatic Precipitation*. 1963, Reading: Addison-Wesley Inc.

17. Flagan, R.C. and J.H. Seinfeld, *Fundamentals of Air Pollution Engineering*. 1988: Prentice Hall.

18. Mikoviny, T., Kocan, M., Matejcik, S., Mason, N. J. and Skalny, J. D. (2004) "Experimental study of negative corona discharge in pure carbon dioxide and its mixtures with oxygen", *J Phys D Appl Phys*, **37**(1), 64-73.

19. Jiang, J., Lee, M. H., and Biswas P. (2007) "Model for nanoparticle charging by diffusion, direct photoionization, and thermionization mechanisms" *J Electrostat.* **65**(4), 209-220.

20. Adachi, M., Kousaka, Y., Okuyama K. (1985) "Unipolar and Bipolar Diffusion Charging of Ultrafine Aerosol Particles". *J Aerosol Sci.*, **16**(2), 109-123.

21. Wiedensohler, A. (1988) "An Approximation of the Bipolar Charge-Distribution for Particles in the Sub-Micron Size Range". *J Aerosol Sci.* **19**(3), 387-389.

22. Fuchs, N.A. (1963) "On the Stationary Charge Distribution on Aerosol Particles in a Bipolar Ionic Atmosphere", *Geofis. Pura Appl.* **51,** 185-193.

23. Eisele, F. L., Lovejoy, E. R., Kosciuch, E., Moore, K. F., Mauldin, R. L., Smith, J. N., McMurry, P. H. and Iida, K. (2006) "Negative atmospheric ions and their potential role in ion-induced nucleation", *J Geophys Res-Atmos.* **111**, D04305.

24. Wang, S.C. and Flagan, R.C. (1990) "Scanning Electrical Mobility Spectrometer", *Aerosol Sci. Technol*. **13**(2), 230-240.

25. Hogan, C. J., Kettleson, E. M., Ramaswami, B., Chen, D. R. and Biswas, P. (2006) "Charge reduced electrospray size spectrometry of mega- and gigadalton complexes: Whole viruses and virus fragments", *Anal. Chem.* **78**(3), 844-852.

26. Friedlander, S.K. (2000), *Smoke, Dust, and Haze*. New York: Oxford University Press.

27. Kim, S. H., Woo, K. S., Liu, B. Y. H. and Zachariah, M. R. (2005) "Method of measuring charge distribution of nanosized aerosols", *J Colloid Interf Sci* **282**(1), 46-57.

28. Burtscher, H., Reist A., and Schmidt-Ott A. (1986) "Particle Charge in Combustion Aerosols", *J Aerosol Sci.* **17**(1), 47-51.

29. Hogan, C.J., Lee, M.H., and Biswas P. (2004) "Capture of viral particles in soft X-ray-enhanced corona systems: Charge distribution and transport characteristics" *Aerosol Sci. Technol.* **38**(5), 475-486.

30. Mackay, C.A. (1924) "Ionizing potentials of multi-atomic gases", *Phys. Review*. **24**(4), 319-329.

31. *Handbook of Chemistry and Physics, 80th ed.,* ed. CRS-Press. 1999-2000, Cleveland, OH.

32. Smyth, H.D. and Stueckelberg E.C.G. (1930) "The ionization of carbon dioxide by electron impact" *Phys. Review*. **36**, 472-477.

33. Stueckelberg, E.C.G. (1929) "Simultaneous Ionization and Dissociation of Oxygen and Intensities of the Ultra-violet O2+ Bands" *Phys. Review*. **34**, 65-67.

34. Frey, B. L., Lin, Y., Westphall, M. S. and Smith, L. M. (2005) "Controlling gas-phase reactions for efficient charge reduction electrospray mass spectrometry of intact proteins", *J Am Soc Mass Spectr* . **16**(11), 1876-1887.

35. Skalny, J. D., Matejcik, S., Mikoviny, T., Eden, S. and Mason, N. J. (2004) "Ozone generation in a negative corona discharge fed with N2O and O2", *J Phys D Appl Phys.* **37**(7), 1052-1057.

36. Nikolaev, E., Riter, L. S., Laughlin, B. C., Handberg, E. and Cooks, R. G. (2004) "Trace analysis of organics in air by corona discharge atmospheric pressure ionization using an electrospray ionization interface", *Eur J Mass Spectrom.* **10**(2), 197-204.

37. Crawford, M., *Air Pollution Control Theory*. 1976: McGraw-Hill Education.

Chapter 4

Homogeneous Mercury Oxidation under Simulated Flue Gas of Oxy-coal Combustion *

*The contents in this chapter will be submitted to *Chemosphere* for publication.

ABSTRACT

This study investigated the effects of oxy-coal combustion on Hg-oxidation by HCl using simulated flue gas. Experiments were conducted with different carrier gases that one might find in oxy-coal combustion and conventional coal combustion. The extents of Hg-oxidation in pure CO_2, pure N_2 and air were also studied for comparison. Our experimental results demonstrated that CO_2 weakly assisted Hg-oxidation by HCl; however, its significance was outweighed by the presence of O_2. For all carrier gases, the presence of NO or H_2O inhibited Hg-oxidation. The inhibitory effects strongly depended on concentrations of NO, but not moisture content. The synergistic inhibitory effects were shown when both NO and H_2O were present together. The extents of Hg-oxidation were not significantly different for O_2-N_2, O_2-N_2-CO_2 and O_2-CO_2 gas mixtures for all conditions investigated in this study.

Keywords: coal combustion, mercury emission, oxy-coal combustion, mercury speciation

4.1 INTRODUCTION

Global climate change is an issue of great concern, exacerbated by the rising levels of carbon dioxide (CO_2) in the atmosphere due to human activities, such as burning of fossil fuels and deforestation. Coal, the cheapest and most abundant fossil fuel, is currently one of the most widely used energy sources globally, and it will continue to be dominant for many decades. Capturing CO_2 from coal combustion exhaust has been receiving significant attention; however, the volume fraction of CO_2 in a conventional coal combustion system (with air) ranges between 13% - 15%, making it difficult to cost-effectively design these systems. One approach to overcome the limitation of low CO_2 concentration in the exhaust is oxy-coal combustion. Coal is combusted in an oxygen-enriched stream (with nitrogen removed) with recycled exhaust gas as a diluent. At steady state operation, such a configuration would result in a CO_2 concentration of 95% in the exhaust, making it more feasible to capture [1-4]. Many studies have reported other advantages of this combustion system, including reduction of volume of flue gas, elimination of thermal NO_X, and potential for increasing boiler thermal efficiency [5, 6].

While the benefits of the oxy-coal combustion are clear, changing the composition of the combustion gas mixture may have numerous effects on the pollutants associated with coal combustion, and subsequently the performance of

pollution control devices. In our laboratory, we have previously investigated the effects oxy-coal combustion on the formation of submicrometer-sized particles and their capture by an electrostatic precipitator (ESP) [7, 8]. The submicrometer particle size distribution was shifted toward a smaller size when N_2 in air was replaced by CO_2 [7], and penetration of the particle through an ESP was 1-2 orders of magnitude higher in O_2-CO_2 environments than in O_2-N_2 environments [8]. Croiset and Thambimuthu (2001)[9] and Lui and Okazaki (2003)[6] observed a significant reduction in NO_X emissions from oxy-coal combustion. Croiset and Thambimuthu (2001)[9] also reported a decrease in the conversion of sulfur to sulfur dioxide (SO_2) from 91% to 75% when N_2 was replaced by CO_2, and to 64% when CO_2 came from the recycled flue gas.

Mercury is one of the most toxic environmental pollutants and highly bio-concentrated metals in the human food chain. Coal-fired utility plants are the largest anthropogenic source in the United States [10]. On March 15, 2005, the United States Environmental Protection Agency (US EPA) issued the Clean Air Mercury Rule (CAMR) to regulate Hg emissions from coal-fired power plants using a cap-and-trade approach. Mercury emission from coal-fired power plants would be reduced from 48 tons per year to 15 tons per year, a reduction of nearly 70% (US EPA, 2005). However, many states and organizations challenged the CAMR. On February 8, 2008, the U.S. Court of Appeals for the District of Columbia Circuit vacated the CAMR,

and required the US EPA to reconsider the Mercury Rule (Edison Electric Institute, 2008). It is expected that mercury regulation will become more stringent and the power plants will be required to install Hg control devices. As a result, extensive research and development are in progress for control methodologies.

Like other pollutants, mercury capture methodology relies primarily on the knowledge of mercury speciation in flue gas. Mercury exists in three forms in coal-combustion flue gas: elemental mercury (Hg^0), oxidized (Hg^{2+}), and particulate-bound ($Hg_{(p)}$). During combustion, mercury is liberated from coal as Hg^0. As the flue gas cools, some of the Hg^0 is oxidized – presumably to $HgCl_2$ due to the presence of chlorine in coal. While Hg^0 is insoluble in water and difficult to capture, $HgCl_2$ is water-soluble and readily captured in the pollution control devices, such as scrubbers. Several factors play an important role in the fate of mercury emission, including chlorine species, carbon monoxide (CO), moisture (H_2O), sulfur dioxide (SO_2), and nitrous oxide (NO). Chlorine species have been regarded as the key factor affecting mercury oxidation. Many studies indicated a strong correlation between chlorine content in coal and oxidized mercury in flue gas; high chlorine content typically resulted in more oxidized mercury in flue gas [11-14]. Extensive efforts have also been made in unraveling the reaction mechanism for homogeneous mercury oxidation through a sequence of elementary reactions. To date, it has been widely accepted that Hg^0 was first oxidized into the intermediate HgCl, which further reacted with

chlorinating species to form thermodynamically stable $HgCl_2$ [15-17]. The dominant mercury oxidizing species is atomic chlorine (Cl) and to a lesser extent of other chlorinating species, such as molecular chlorine (Cl_2), hypochlorite (HOCl) and hydrogen chloride (HCl) [11, 15, 18, 19]. Other constituents in flue gas and their concentrations also affect mercury oxidation. CO promotes mercury oxidation, while moisture and SO_2 impede the oxidation [19-23]. NO can either inhibit or promote mercury oxidation and $HgCl_2$ formation, depending on its concentration [18, 19].

In oxy-coal combustion, the constituents in flue gas are different than those generated in conventional (coal-air) combustion. In this context, the fate of mercury emission may be significantly affected. This study established the understanding of mercury oxidation under oxy-coal combustion using simulated flue gas. The influences of NO and H_2O on the oxidation are also reported. The results presented here will be beneficial to the current development of mercury control methodology, and will help to facilitate the transition of the technology when it is applied in oxy-coal combustion.

4.2 EXPERIMENTAL ANS METHODS

4.2.1 Test Plan. The experimental plan is outlined in Table 4.1. Set I experiments evaluated the effects of carrier gases on Hg oxidation by HCl.

Experiments were conducted at different temperatures, ranging between 500 to 900^{o}C. The gas mixtures examined were chosen to mimic gas mixtures that one might find in oxy-coal and conventional (coal-air) combustions. Pure CO_2, pure N_2 and air were also studied for comparison. Set II and Set III experiments were designed to independently evaluate the roles of H_2O and NO on the extent of Hg oxidation by HCl in different carrier gas. In these sets of experiments, concentrations of NO and H_2O were chosen based on the values typically reported in coal combustion systems. The concentration of HCl was held constant at 100 ppm_v, while concentrations of NO and H_2O were varied between 40-200 ppm_v and 0-20% by volume, respectively. Set IV experiments were conducted to examine the combined effects of H_2O and NO on Hg oxidation by HCl. In this set of experiments, the concentration of HCl and H_2O were held constant at 100 ppm_v and 7% by volume, respectively, while the selected concentrations of NO were 40 to 100 ppm_v.

Table 4.1: Summary of the experiments performed.

Set	Objective	Gas Composition						
		N_2 (%)	O_2 (%)	CO_2 (%)	H_2O (%)	NO (ppm_v)	Hg ($\mu g/m^3$)	HCl (ppm_v)
1	Investigate the role of carrier gas on Hg-oxidation by HCl	100	-	-	-	-	20	100
		-	-	100	-	-		
		90	10	-	-	-		
		-	10	90	-	-		
		-	10	14	-	-		
		79	21	-	-	-		
2	Evaluate the effects of H_2O on Hg-oxidation by HCl in different carrier gas	balance	-	-	0-20	-	20	100
		-	-	balance		-		
		balance	10	-		-		
		-	10	balance		-		
		balance	10	14		-		
		balance	21	-		-		
3	Evaluate the effects of NO on Hg-oxidation by HCl in different carrier gas	balance	-	-	-	40-400	20	100
		-	-	balance	-			
		balance	10	-	-			
		-	10	balance	-			
		balance	10	14	-			
		balance	21	-	-			
4	Determine the combined effects of NO and H_2O on Hg-oxidation in different carrier gas	balance	-	-	7, 20	40,100	20	100
		-	-	balance				
		balance	10	-				
		-	10	balance				
		balance	10	14				
		balance	21	-				

4.2.2 Experimental Setup.

The experimental setup, shown in Figure 4.1, consisted of inlet manifolds, where Hg, carrier gases and other gases were introduced, a quartz tube reactor (50 cm long with an inner diameter of 2.54 cm), a furnace (1100^{o}C laboratory tube furnace, Lindberg) to simulate a high temperature environment, and a mercury sampling train. Mercury vapor was introduced into the system by passing particle-free CO_2, N_2 or air above liquid mercury contained in a glass bottle at precisely controlled flow rates using a mass flow controller (MKS Mass-Flow Controller, MKS Instruments, Inc.). The bottle resided in a water-filled beaker with the bath temperature held constant at 40ºC. To minimize mercury condensation, the tubing connecting the Hg feed bottle to the entrance of the furnace was wrapped with heating tape (Type 45500, Thermolyne), and set at 80ºC. The carrier gases, either N_2, CO_2, or gas mixtures of O_2, N_2 and CO_2, and other constituents, including H_2O, HCl (2000 ppm-N_2, Wright Bothers) and NO (5000 ppm-N_2, Airgas), were introduced into the reactor via other inlet manifolds using mass flow controllers (MKS Mass-Flow Controller, MKS Instruments, Inc.). Water vapor (H_2O) was introduced into the reactor by bubbling N_2 or CO_2 through milli-Q water. The flow rates of N_2 or CO_2 were calibrated to establish the desired water vapor concentrations at the inlet of the reactor. The total flow rate through the reactor was 2.0 lpm, resulting in the residence time of 2 s inside the reactor at 800 ^{o}C. At the exit of the system, a mercury sampling train was connected downstream of the tubular reactor to determine oxidized and elemental mercury concentrations.

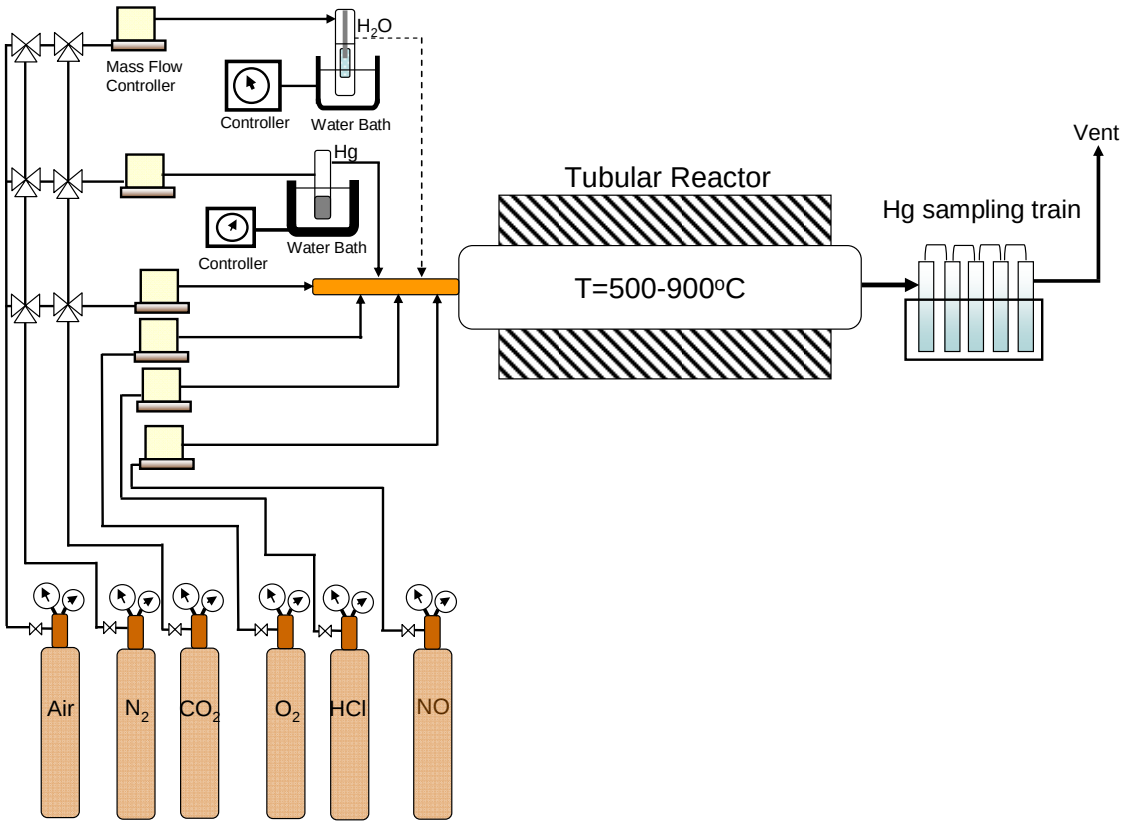

Figure 4.1: Schematics of the experimental setup.

4.2.3 Mercury Measurement. The sampling train and technique used for gaseous mercury measurement was based on the method developed by Hedrick et al. (2001) [24]. The sampling train consisted of the following five impinger solutions: two impingers of 1.0 M tris-buffer and EDTA for capture of oxidized mercury, one impinger of 10% hydrogen peroxide and 2% nitric acid for oxidizing and capture of elemental mercury, and two impingers of 0.05 M potassium iodide and 2% hydrochloric acid for capture of elemental mercury. The impinger solutions were analyzed by inductively coupled plasma mass spectrometry (ICP-MS) to determine the elemental and oxidized fractions of mercury in the exhaust gas. Due to the tendency of mercury to adsorb, extra precaution was exercised. To prevent cross-contamination between experimental runs, the reactor and all impingers were acid cleaned. The reactor was purged with particle-free carrier gases at the furnace temperature of 1100^{o}C for 30 min before every run. The baseline mercury concentration was periodically verified during each set of experiments. At least four measurements were averaged for each run. Since mercury was introduced as Hg^0, the extent of Hg oxidation was calculated as follows:

$$Hg^0 oxidation\ (\%) = \frac{\{[Hg^0]_{w/o\ HCl} - [Hg^0]_{w/HCl}\}}{[Hg^0]_{w/oHCl}} * 100 \qquad (1).$$

4.3 RESULTS AND DICUSSION

The study evaluated the effects of flue gas constituents associated with oxy-coal combustion in post-combustion Hg-oxidation by HCl. The first part of this section discusses the influence of carrier gas on the extent of Hg-oxidation. The second and third parts focus on understanding the roles of moisture and NO on the oxidation. In the last part, the combined effects of carrier gases, moisture and NO on Hg-oxidation are discussed. It should be noted that no Hg-oxidation was observed in the absence of HCl for all conditions investigated in this study, and the measured Hg^0 concentrations for each condition without adding HCl were used as a baseline to determine the extent of Hg-oxidation.

4.3.1 Role of carrier gas in Hg-oxidation. The first set of experiments was conducted to evaluate the effects of carrier gases on Hg-oxidation. The gas mixtures examined in the study, including 10%O_2-90%CO_2, 10%O_2-90%N_2, and 10%O_2-14%CO_2-76%N_2, were chosen to mimic flue gas constituents that would be in oxy-coal and conventional (coal-air) combustion. Pure CO_2, pure N_2 and air were also studied for comparison. The extents of mercury oxidation in different carrier gases at HCl concentration of 100 ppm_v are shown in Figure 4.2. This HCl concentration represented the concentration in a typical combustion of bituminous and sub-bituminous coal with medium chlorine content [25, 26]. Our experimental

results indicated that carrier gases evaluated in this study had significant effects on Hg-oxidation. The extent of Hg-oxidation, when it occurred at flue gas temperature of 800^{o}C, was highest (32%) when air was a carrier gas and lowest (8%) when CO_2 was a carrier gas. No data were shown when N_2 was a carrier gas since no Hg-oxidation was observed for temperature evaluated in this set of experiments. For gas mixtures with the same O_2 concentration, the extent of Hg-oxidation was highest (28%) in a 10%O_2-90%CO_2 gas mixture, followed by a 10%O_2-14%CO_2-76%N_2 gas mixture (26%), and a 10%O_2-90%N_2 mixture (25%). The extent of Hg-oxidation increased with temperature for all carrier gases investigated in this study.

The differences in Hg-oxidation were attributed to the concentrations of the reactive Cl-species generating in air, N_2, CO_2 or gas mixtures. Since HCl has been at the reduced state and it can not directly oxidize Hg^0 [13], Hg-oxidation must occur via the reactive chlorine intermediates derived from HCl. Previous research has established the pathways for Hg^0 oxidation, reaction 1-8 shown in Table 2 [15, 16, 19]. The reaction rate constant, *k*, suggested that only Cl can initiate Hg^0 oxidation at a substantial rate, shown in reaction 1, Table 4.2. Roesler et al. (1995) and Mueller et al. (1998) reported that HCl can dissociate to Cl in the presence of oxygen (O), hydrogen (H) or hydroxyl (OH) radicals, shown in reactions 9, 10 and 11, Table 4.2 [27, 28]. Even though HCl dissociation via attack by OH radicals (reaction 11) would be the primary pathway for releasing Cl atoms into flue gas, for carrier gases

investigated in this study, O radicals are the species initiating HCl dissociation reactions, and they must derive from O_2 or CO_2. The highest Hg-oxidation found in air, which contained the highest volume fraction of O_2 (air, 21%O_2-79%N_2), and the lowest found in pure CO_2, indicated that O_2 was the primary source of O. With the same volume fraction of O_2, slight differences in Hg-oxidation among the gas mixtures further verify that the volume fraction of O_2 controls the pool of Cl that is available to react with Hg^0. These results are in agreement with Agarwal and Stenger (2006). Little effect of CO_2 on Hg-oxidation was observed in simulated flue gas of conventional coal combustion [29]. It should be also noted that N_2 did not assist dissociation of HCl as no Hg-oxidation was observed when N_2 was a carrier gas.

In oxy-coal combustion, concentration of O_2 would be higher than that in conventional coal combustion flue gas to maintain the same boiler temperature or to increase boiler thermal efficiency [7]. Our experimental results suggested that Hg-oxidation would be higher than that found in conventional coal combustion systems.

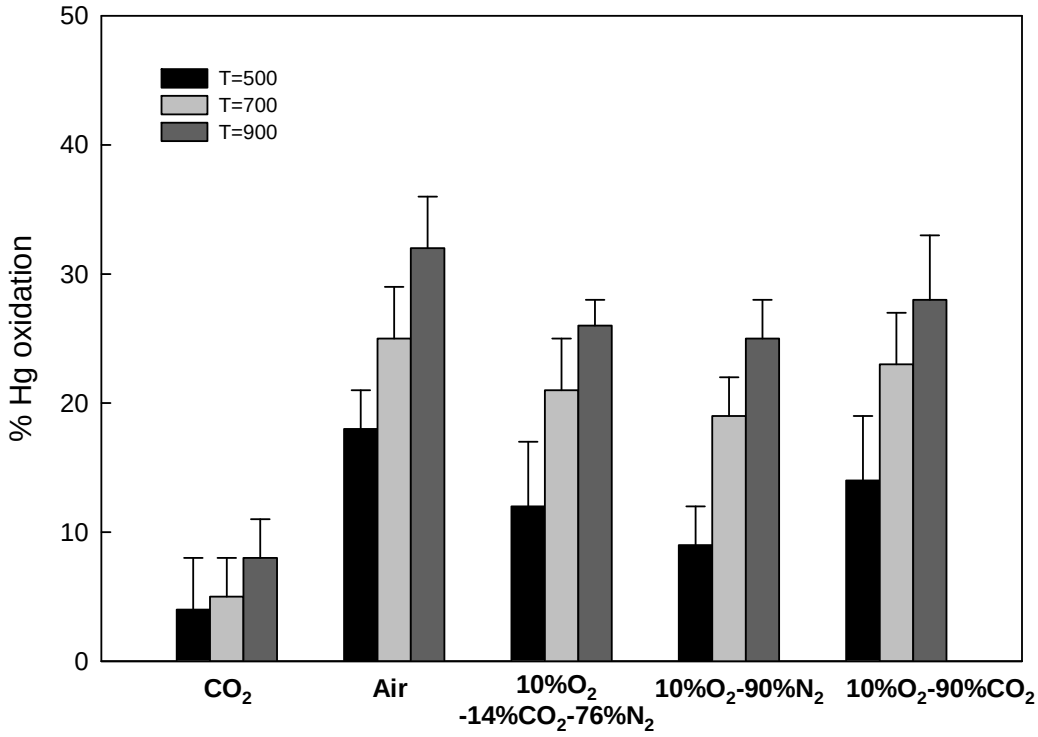

Figure 4.2: Effects of carrier gas on Hg-oxidation by 100 ppm_v HCl.

Table 4.2

Reaction No.	Reactions	A (cm^3/mol-s)	β	E_a kcal/mol	Ref.
1	Hg+Cl+M → HgCl+M	$2.4x10^8$	1.4	-14.4	20
2	Hg+Cl_2 → HgCl+Cl	$1.39x10^{14}$	0.0	34.0	20
3	HgCl+Cl_2 → $HgCl_2$+Cl	$1.39x10^{14}$	0.0	1.0	20
4	HgCl+Cl+M →$HgCl_2$+M	$2.19x10^{18}$	0.0	3.1	20
5	Hg+HOCl → HgCl+OH	$4.27x10^{13}$	0.0	19.0	20
6	Hg+HCl → HgCl+H	$4.94x10^{14}$	0.0	79.3	20
7	HgCl+HCl → $HgCl_2$+H	$4.94x10^{14}$	0.0	21.5	20
8	HgCl+HOCl → $HgCl_2$+OH	$4.27x10^{13}$	0.0	1.0	20
9	HCl+O → OH+Cl	$3.37x10^3$	0.0	3.51	27,28
10	HCl+H → H_2+Cl	$1.69x10^{13}$	1.65	4.14	27,28
11	HCl+OH → H_2O+Cl	$2.71x10^7$	2.87	-0.22	27,28
12	NO+O+M → NO_2+M	$4.72x10^{24}$	-2.87	1.55	28,35
13	NO+H+M → HNO+M	$5.0x10^{19}$	-1.32	0.74	28,35
14	NO+OH+M → HONO+M	$5.08x10^{23}$	-2.51	-0.007	28,35
15	HONO+Cl → HCl+NO_2	$5.00x10^{13}$	0.0	0.0	28,35

Note: $k = AT^{\beta} exp(-E_a/RT)$

4.3.2 Role of moisture in Hg-oxidation.

Several studies reported that H_2O is an important factor influencing the degree of Hg oxidation [19, 30]. In conventional coal combustion flue gas, moisture content ranges between 7 to 15% [25, 31]. Depending on flue gas recycled ratio, moisture content in oxy-coal combustion flue gas would range between that in conventional flue gas and that in the flue gas of coal combustion in pure oxygen (27%) (Sandia National Laboratories, 2009) ([32]. In this set of experiments, the moisture content, ranging from 7% to 20%, was chosen to correspond to that in conventional and oxy-coal combustions. The

effects of moisture on Hg-oxidation by 100 ppm_v HCl in different carrier gases are reported in Figure 4.3. For all gas mixtures and air, the extent of the oxidation drastically decreased in the presence of H_2O; however, the effect of moisture content on the oxidation was not significant. For example, when air was a carrier gas, the extent of Hg-oxidation decreased from 32% without H_2O present to 25% with 7% H_2O added, but it decreased to 18% when moisture content increased from 7% to 20%. The decrease in Hg-oxidation was attributed to the abundant supply of OH radicals that dissociated from H_2O and competed with Hg^0 for Cl radicals to form less reactive chlorinating species, such as HOCl. In addition, high concentration of OH radicals substantially increased reduction rate of HgCl to form Hg^0 and HOCl-thus, lowering Hg-oxidation [19]. In comparing gas mixtures and air, the effects of moisture in Hg-oxidation were not found significantly different. The extents of Hg-oxidation at 20%H_2O were 18% for air, ranging between 15%-16% for gas mixtures. This indicated that the impact of H_2O on Hg-oxidation outweighed that of O_2 concentrations demonstrated in Set I experiments.

When CO_2 and N_2 were carrier gases, in contrast to the gas mixtures, the presence of H_2O promoted Hg-oxidation at low moisture content (7%) and suppressed the oxidation when moisture content increased (15% and 20%). The former result suggested that OH radicals dissociated from H_2O initiated the formation of Cl radicals from HCl (shown in reaction 11, Table 4.2), which subsequently

provided the channel towards Hg-oxidation. At high moisture content, the inhibitory effect on Hg-oxidation indicated that Cl radicals would mostly be consumed by OH radicals to form their respective oxidized products, or the reduction rate HgCl via attack by OH radicals substantially increased and it became a significant competing mechanism on Hg-oxidation. The results from this set of experiments clearly indicated the importance of flue gas constituents and their concentrations on Hg-oxidation.

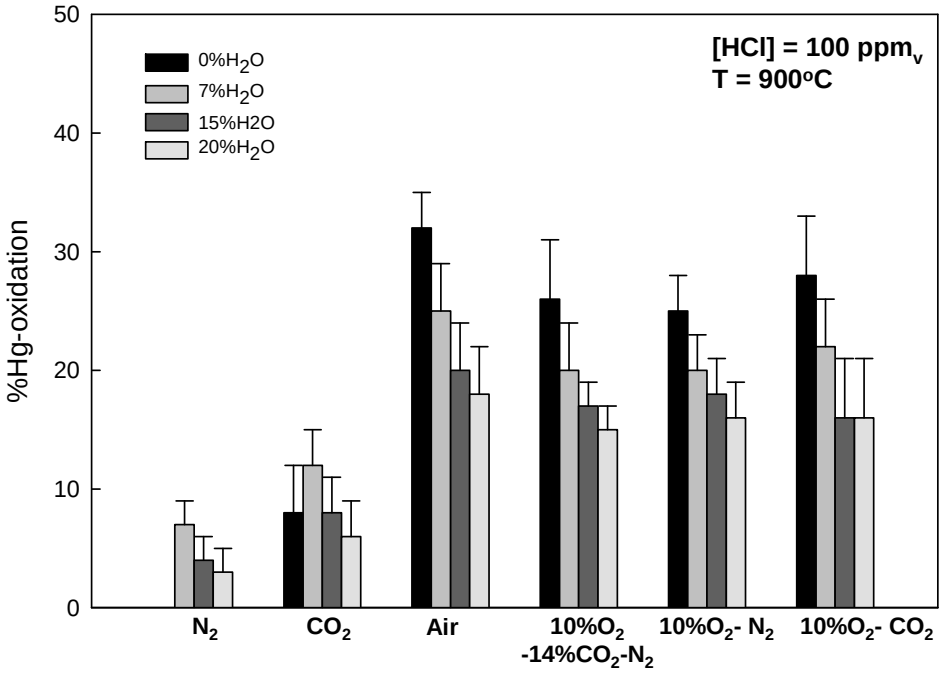

Figure 4.3: Effects of H_2O on Hg-oxidation by 100 ppm_v HCl in different carrier gas.

4.3.3 Role of NO on Hg oxidation.

Besides moisture, the presence of NO in flue gas was reported to exert a strong impact on Hg-oxidation [19, 33]. Due to the absence of N_2 and a re-burn effect of the recycled flue gas in oxy-coal combustion, concentration of NO could be decreased to only 14% of conventional coal combustion [6]. In this set of experiments, the NO concentrations, ranging from 40 to 400 ppm_v, were selected to correspond to that in conventional and oxy-coal combustions. The effects of NO on Hg-oxidation by 100 ppm_v HCl in different carrier gases are reported in Figure 4.4. No data were shown for N_2, since no Hg-oxidation was observed for all concentrations of NO evaluated in this set of experiments. It should be noted that Hg-oxidation by NO in the absence of HCl was negligible. The presence of NO strongly suppressed Hg-oxidation by HCl for all carrier gases. The effect was more pronounced when CO_2 was a carrier gas--the extent of Hg-oxidation was completely inhibited in the presence of NO. For gas mixtures with the same O_2 concentration, no Hg-oxidation was observed at NO concentrations above 200 ppm_v. When air was a carrier gas, the extent of the oxidation was completely suppressed at NO concentration of 400 ppm_v. The inhibitory effects were attributed to the consumption of O, H, and OH by NO. As shown in reaction 12, 13 and 14, Table 4.2, NO competed with HCl for O, H, OH [34], and subsequently impeded the formation of Cl radicals for Hg-oxidation. In pure CO_2, O radicals were much less available than those in gas mixtures. As a result, the complete inhibitory effect was exhibited at lower NO concentrations. When air was a carrier gas, O_2 concentration was highest

(21%) and presumably so was the concentrations of radicals, specifically O. As a result, the complete inhibitory effect exhibited at higher NO concentration.

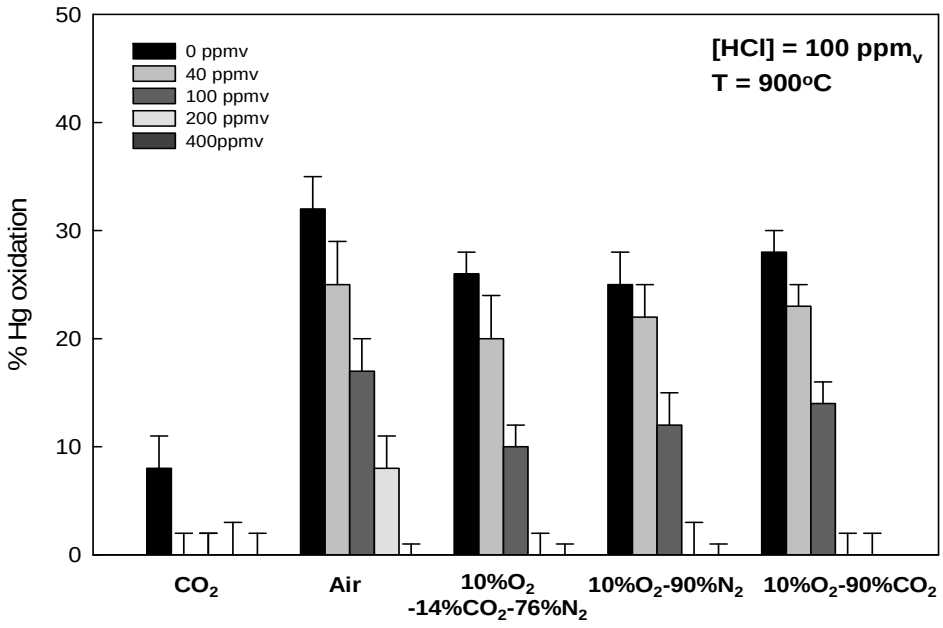

Figure 4.4: Effects of NO on Hg-oxidation by 100 ppm_v HCl in different carrier gas.

4.3.4 Combined effect of H_2O and NO.

Set 4 experiments were designed to evaluate the extent of Hg-oxidation when moisture and NO were present together. The selected moisture content was 7% and 20% by volume and concentrations of NO were 40 and 100 ppm_v. Experimental results are reported in Figure 4.5A and 4.5B. For all gas mixtures, air and CO_2, the presence of H_2O and NO together exhibited stronger inhibitory effects on Hg-oxidation than those found when the individual compounds were present alone. For example, when air was a carrier

gas, the extent of Hg-oxidation decreased from 32% without H_2O present to 25% with 7% H_2O added, it decreased from 32% without H_2O present to 25% when 40 ppm_v NO added, and when 7% H_2O and 40 ppm_v NO were present together, only 12% Hg-oxidation was observed. As previously described, the presence of H_2O and NO individually affects Hg-oxidation via controlling the pool of radicals, including Cl, H, OH, and O. This synergistic effect indicated that the availability of radicals decreased when H_2O and NO were together. Previous researchers had established that HONO formed when nitrogen species and OH radicals present together, shown in reaction 14, Table 4.2 [28,35]. With no activation energy required, HONO could directly scavenge Cl radicals to form HCl and H_2O, shown in reaction 15 in Table 4.2 [36,37]. This resulted in less Cl available for Hg-oxidation. In comparing all gas mixtures and air, the effects of coupling moisture and NO in Hg-oxidation were not found significantly different, 6% for air and ranging between 3% to 4% for gas mixtures at 7% moisture content and 100 ppm_v NO. This indicated that the impact of NO and H_2O on Hg-oxidation exceeded that of the carrier gases demonstrated in Set I experiments.

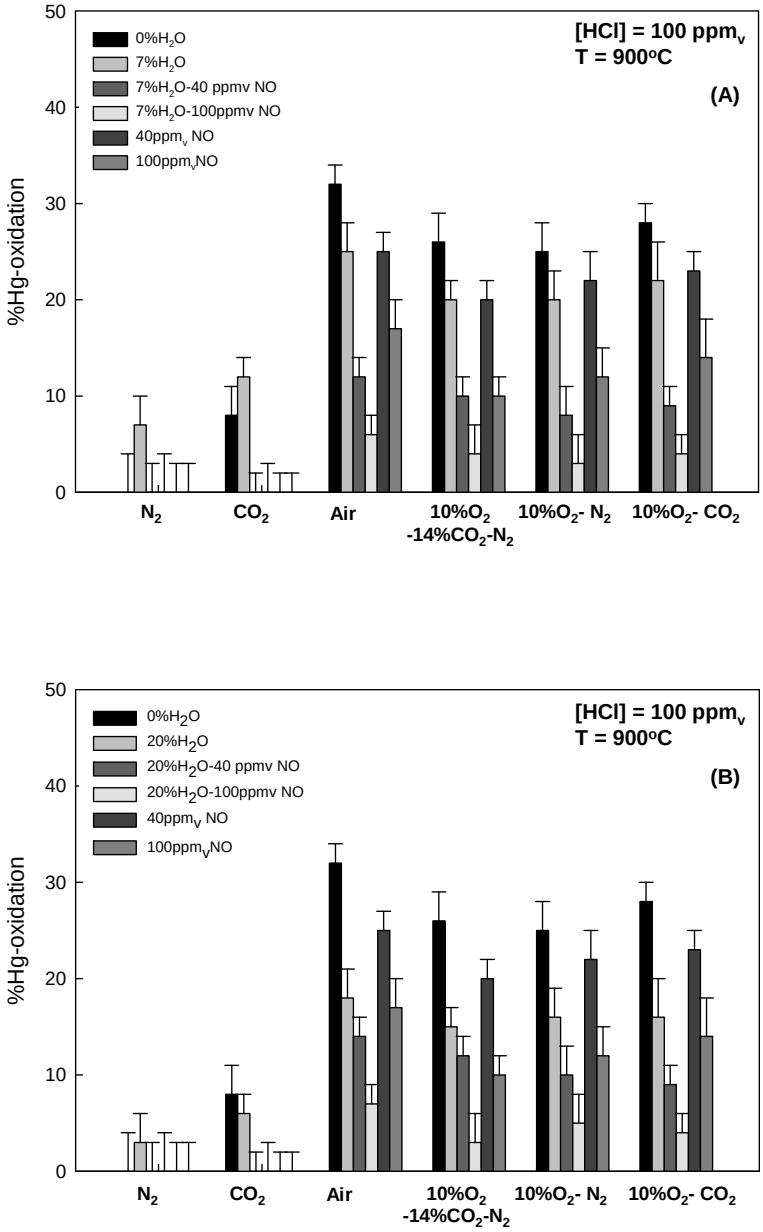

Figure 4.5: The combined effect of NO and H_2O on Hg-oxidation by HCl in different carrier gas. (A) Hg-oxidation at 7%H_2O with 40 and 100 ppm_v NO; (B) Hg-oxidation at 20% H_2O with 40 and 100 ppm_v NO.

In comparing the influence of moisture content on the combined effects of H_2O and NO, the extents of Hg-oxidation slightly decreased when moisture content increased from 7% to 20% for all carrier gases. This indicated that OH radicals that dissociated from H_2O were abundant and that increasing moisture content did not significantly affect the pool of radicals, specifically Cl, and subsequently Hg-oxidation. In oxy-coal combustion, moisture content would be higher than that in conventional coal combustion, while concentration of NO would be lower than that in conventional coal combustion. Our experimental results suggested that Hg-oxidation in oxy-coal combustion would be higher than that found in conventional coal combustion systems.

4.4 CONCLUSION

This study explored the impact of oxy-coal combustion on homogeneous mercury oxidation. The experiments were systematically designed to identify the influence of each constituent and its concentration. Our experimental results demonstrated that CO_2 assisted Hg-oxidation by HCl; however, its influence was outweighed by the presence of O_2. N_2 alone did not participate in the oxidation of Hg. The presence of NO and H_2O inhibited Hg-oxidation for all carrier gases investigated in this study. The inhibitory effects depended strongly on the concentration of NO, but not on moisture content. For all carrier gases, synergistic inhibitory effects were

demonstrated when NO and H_2O were present together. These results were attributed to the impact of flue gas constituents on the pool of Cl that is available to react with Hg^0. Our experimental findings suggested that in oxy-coal combustion, while Hg-oxidation would not be critically affected by highly concentrated CO_2 in the flue gas, it would be impacted by other flue gas constituents, such as NO and H_2O, and their concentrations, which are influenced by oxy-coal combustion.

4.5 REFERENCES

1. Desideri, U. and A. Paolucci, *Performance modeling of a carbon dioxide removal system for power plants.* Energy Conversion and Management, 1999. **40**: p. 1899-1915.

2. Doctor, R.D., J.C. Molburg, and P.R. Thimmapuram, *Oxygen Blown Gasification Combined Cycle: Carbon dioxide recovery, transport and disposal.* Energy Conversion Management, 1997. **38**: p. 575-580.

3. Hektor, B., *Cost effectiveness of measures for the reduction of net accumulation of carbon dioxide in the atmosphere.* Biomass and Bioenergy, 1998. **15**: p. 229-309.

4. White, C.M., et al., *Separation and Capture of CO2 from Large Stationary Sources and Sequestration in Geological Formations -- Coalbeds and Deep Saline Aquifers.* Journal of the Air and Waste Management Association, 2003. **53**: p. 645-715.

5. Liu, H., et al., *Sulfation Behavior of Limestone under High CO2 Concentration in O2/CO2 coal combustion.* Fuel, 2000. **79**: p. 945-953.

6. Liu, H. and K. Okazaki, *Simultaneous Easy CO2 Recovery and Drastic Reduction of SOx and NOx in O2/CO2 Coal Combustion with Heat Recirculation.* Fuel, 2003. **82**: p. 1427-1436.

7. Suriyawong, A., et al., *Submicrometer Partical Formation and Mercury Speciation under O2-CO2 Coal Combustion.* Energy & Fuels, 2006. **20**(6): p. 2357-2363.

8. Suriyawong, A., C.J.J. Hogan, and P. Biswas, *Charged Fraction and Electrostatic Capture of Ultrafine and Submicrometer Particles Formed under O2-CO2 Coal Combustion.* Fuel, 2008. **87**: p. 673-682.

9. Croiset, E. and K.V. Thambimuthu, *NOx and SO2 emissions from O-2/CO2 recycle coal combustion.* Fuel, 2001. **80**(14): p. 2117-2121.

10. EPA, *1999 National Emission Inventory for Hazadous air pollutants*. 1999, Office of Air Quality Planning and Standards and Office of Research and Development, U.S. Environmental Protection Agency.

11. Senior, C., et al., *Gas Phase Transformations of Mercury in Coal-fired Power Plants.* Fuel Processing Technology, 2000. **63**(2-3): p. 197-213.

12. Liu, K., et al., *Study of Mercury Removal in FBC Systems Fired with High-chlorine Coals.* Combustion Science and Technology, 2001. **164**: p. 145-162.

13. Zhuang, Y., et al., *Impact of Calcium Chloride Addition on Mercury Transformations and Control in Coal Flue Gas.* Fuel 2007. **86**: p. 2351-2359.

14. Cao, Y., et al., *Impact of Coal Chlorine on Mercury Speciation and Emission from a 100-MW Utility Boiler with Cold-side Electrostatic Precipitators and Low-NOx Burners.* Energy & Fuels, 2005. **19**(3): p. 842-854.

15. Sliger, R.N., J.C. Kramlich, and N.M. Marinov, *Towards the development of a chemical kinetic model for the homogeneous oxidation of mercury by chlorine species.* Fuel Processing Technology, 2000. **65**: p. 423-438.

16. Zhao, Y., et al., *Effects of Sulfur Dioxide and Nitric Oxide on Mercury Oxidation and Reduction under Homogeneous Conditions.* Journal of the Air & Waste Management Association 2006. **56**(628-635).

17. Zheng, C.G., et al., *Kinetic mechanism studies on reactions of mercury and oxidizing species in coal combustion.* Fuel, 2005. **84**(10): p. 1215-1220.

18. Edwards, J.R., R.K. Srivastava, and J.D. Kilgroe, *Study of Gas-phase Mercury Speciation using Detailed Chemical Kinetics.* Journal of Air and Waste Management Association, 2001. **51**: p. 869-877.

19. Niksa, S., J.J. Helble, and N. Fujiwara, *Kinetic modeling of homogeneous mercury oxidation: The importance of NO and H2O in predicting oxidation in coal-derived systems.* Environmental Science & Technology, 2001. **35**(18): p. 3701-3706.

20. Niksa, S., et al., *A mechanism for mercury oxidation in coal-derived exhausts.* Journal of the Air & Waste Management Association, 2002. **52**(8): p. 894-901.

21. Senior, C.L., J.J. Helble, and A.F. Sarofim, *Emissions of mercury, trace elements, and fine particles from stationary combustion sources.* Fuel Processing Technology, 2000. **65**: p. 263-288.

22. Senior, C.L., et al., *Gas-phase transformations of mercury in coal-fired power plants.* Fuel Processing Technology, 2000. **63**(2-3): p. 197-213.

23. Zhuang, Y., et al., *Kinetic transformation of mercury in coal combustion flue gas in a bench-scale entrained-flow reactor.* Fuel Processing Technology, 2004. **85**(6-7): p. 463-472.

24. Hedrick, E., Lee,T.G.,Biswas, P. Zhuang, Y., *The Development of Iodine Based Impinger Solutions for the Efficient Capture of Hg0 Using Direct Injection Nebulization-Inductively Coupled Plasma Mass Spectrometry Analysis.* Environmental Science and Technology, 2001. **35**(18): p. 3764-3773.

25. Cao, Y., et al., *Investigation of mercury transformation by HBr addition in a slipstream facility with real flue gas atmospheres of bituminous coal and powder river basin.* Energy & Fuels, 2007. **21**(5): p. 2719-2730.

26. Pavlish, J.H., et al., *Status review of mercury control options for coal-fired power plants.* Fuel Processing Technology, 2003. **82**: p. 89-165.

27. Mueller, C., P. Kilpinen, and M. Hupa, *Influence of HCl on the homogeneous reactions of CO and NO in postcombustion conditions - A kinetic modeling study.* Combustion and Flame, 1998. **113**(4): p. 579-588.

28. Roesler, J.F., R.A. Yetter, and F.L. Dryer, *Kinetic Interactions of CO, NOx, and HCl Emissions in Postcombustion Gases.* Combustion and Flame, 1995. **100**(3): p. 495-504.

29. Agarwal, H., et al., *Effects of H2O, SO2, and NO on Homogeneous Hg Oxidation by Cl2.* Energy & Fuels, 2006. **20**: p. 1068-1075.

30. Agarwal, H., et al., *Effects of H2O, SO2, and NO on homogeneous Hg oxidation by Cl-2.* Energy & Fuels, 2006. **20**(3): p. 1068-1075.

31. Suriyawong, A., et al., *Mercury Capture by Nano-structured Titanium Dioxide Sorbent during Coal Combustion: Lab-scale to Pilot-scale Studies.* Aerosol and Air Quality Research, 2009. **(accepted)**.

32. California, S.N.L.i. *Coal Ignition and Devolatilization during Oxy-fuel Coal Combustion with CO2 Recirculation*. [cited 2009 April 8]; Available from: http://www.ca.sandia.gov/.

33. Norton, G.A., et al., *Heterogeneous oxidation of mercury in simulated post combustion conditions.* Fuel, 2003. **82**(2): p. 107-116.

34. Allen, M.T., R.A. Yetter, and F.L. Dryer, *High Pressure Study of Moist/Carbon monoxide/Nitrous Oxide Kinetics.* Combustion and Flame, 1997. **109**.

35. Martinez, A.I. and B.K. Deshpande, *Kinetic modeling of H2O2-enhanced oxidation of flue gas elemental mercury.* Fuel Processing Technology, 2007. **88**(10): p. 982-987.

36. Xu, M.H., et al., *Modeling of homogeneous mercury speciation using detailed chemical kinetics.* Combustion and Flame, 2003. **132**(1-2): p. 208-218.

37. Sable, S.P., W. Jong, and H. Spliethoff, *Combined Homo- and Heterogeneous Model for Mercury Speciation in Pulverized Fuel Combustion Flue Gases.* Energy & Fuels, 2008. **22**: p. 321-330.

Chapter 5

Mercury Capture by Nano-structured Titanium Dioxide during Coal Combustion:

Lab-scale to Pilot-scale Studies*

*This work has been accepted for publication in *Aerosol and Air Quality Research* (in-press).

ABSTRACT

The performance of non-carbon based sorbent, titanium dioxide (TiO_2) used with UV irradiation, was evaluated in a laboratory-scale coal combustor and in a slip-stream drawn from a pilot-scale coal combustor. For the laboratory-scale system, mercury capture efficiency peaked at 94% at a sorbent feed rate of 71 mg/m^3, with sorbent to coal ratio of 0.0074. For the slip-stream system, mercury capture efficiency achieved 92% at a sorbent feed rate of 622 mg/m^3, with sorbent to coal ratio of 0.015. The required sorbent feed rates for both systems were higher than those kinetically estimated from earlier established lab-scale study, indicating the interference of other species in coal combustion flue gas. The sorbent generation technique and injection location significantly affected the physical and chemical properties of the sorbent, and subsequently its performance. Pure anatase crystalline, generated via a pre-synthesized technique, was found to be more effective than a mixture of anatase and rutile crystalline structure generated via in-situ generation and found in commercial TiO_2 (Degussa, P25). This study further revealed that the injection of nano-structured sorbent can be designed to obtain optimal efficiency of the capture.

KEYWORDS: Coal Combustion; Mercury Emission; Nano-structured Sorbent; Pollution Control; Aerosol Modeling

5.1 INTRODUCTION

Mercury emission has been of great concern because of its high toxicity, tendency to bio-accumulate, and difficulty of control. In the United States alone, approximately 120 tons of mercury are released each year from anthropogenic sources [1-2]. Once emitted, mercury can remain airborne and be transported over a long distance before being deposited on the land and water, where it may eventually enter the food chain. Despite a very low concentration of mercury in flue gas (1-30 $\mu g/Nm^3$), coal combustors are the largest anthropogenic source of mercury emission; they contribute about 40 percent of the total emissions [1]. On March 15, 2005, the United States Environmental Protection Agency (US EPA) issued the Clean Air Mercury Rule (CAMR) to regulate Hg emissions from coal-fired power plants using a cap-and-trade approach. Mercury emission from coal-fired power plants would be reduced from 48 tons per year to 15 tons per year, a reduction of nearly 70% [3]. However, the CAMR was challenged by the States and many organizations. On February 8, 2008, the U.S. Court of Appeals for the District of Columbia Circuit vacated the CAMR, and required the US EPA to reconsider the Mercury Rule [4]. It is expected that the mercury regulation will be more stringent and the power plants will be required to install Hg control device. As a result, extensive research and development are in progress for control methodologies.

Several methods have been proposed for control of mercury emissions from coal-fired power plants, including sorbent injection, photo-chemical removal, and catalysts for enhanced mercury oxidation [5-8]. Currently, sorbent injection is the simplest and the most mature approach for gaseous mercury removal. The gaseous mercury contacts the sorbent and adsorbs to its surface; and the sorbent with mercury adsorbed is then collected by existing particle control devices. The sorbent injection technique is simple to control, has minimal impact on plant operation, requires relatively little modification of the utility plants, and has low capital cost. Activated carbon (AC) and activated carbon impregnated with sulfur, chlorine, or iodine, are the most effective sorbents for mercury capture, especially in systems where mercury concentration is high (i.e., municipal waste incinerators). They provide high surface area, approximately 300 m^2/g, for mercury oxidation and adsorption. However, their application to mercury capture in coal-fired power plants is limited mainly because of their low capacity at elevated temperatures and problems with flyash disposal [9].

A number of researchers have therefore proposed the use of inorganic sorbents, such as titanium-, calcium- and iron-based sorbents, for mercury capture [10-11]. Nano-structured titanium dioxide (TiO_2) used with ultraviolet (UV) irradiation is one of the promising technologies for mercury capture [12-14]. In their laboratory-scale studies, Wu et al. (1998) [12] demonstrated mercury capture efficiency of in-situ generated nano-structured TiO_2 with UV light was greater than

98 percent. Nano-structured TiO_2 is the agglomerate of nanometer-sized primary particles, which provides a very high external surface area for adsorption, compared to spherical particles of the same volume. This external surface area is the key parameter governing the efficiency of the sorbent. Mercury capture using the TiO_2 with UV irradiation occurs in a two-step process, as shown in Figure 5.1: photocatalytic activation of TiO_2 agglomerates, followed by mercury oxidation and adsorption. Photocatalytic activation occurs when TiO_2 agglomerates are exposed to UV radiation; the highly reactive hydroxyl radicals (OH^-) are generated on the surface of the particles, referred as the active surface. Then, gaseous mercury molecules adsorb and are oxidized onto the active surface to form a stable sorbent-mercury complex ($HgO\text{-}TiO_{2(complex)}$). The $HgO\text{-}TiO_{2(complex)}$ is retained on the particle surface; therefore, it can be removed from the gas stream by typical particulate control devices. A number of studies have been dedicated to identify the key parameters governing the performance of this control technique. Lee et al. (2004) [13] reported a linear dependence of Hg oxidation on the surface area for a differential bed reactor and an aerosol flow reactor. Lee et al. (2006) [14] evaluated the effect of different light sources and wavelengths on mercury removal efficiency by TiO_2: the efficiency was highest at 365 nm. Rodríguez et al. (2004) [15] and Li and Wu (2006) [16] studied the role of moisture on mercury oxidation and capture. Mercury oxidation was promoted by low water vapor concentrations (700-1800 ppm_v); however, it was inhibited by the competitive adsorption of mercury and moisture at high moisture conditions (greater

than 2,000 ppm_v). In addition to the gas phase mechanistic and kinetic studies, sequential leaching from TiO_2 after mercury capture was also evaluated. Mercury was found to be bound very strongly to the sorbent as a stable sorbent-mercury complex. Thus, the sorbent-fly ash mix could be readily disposed or re-used [17].

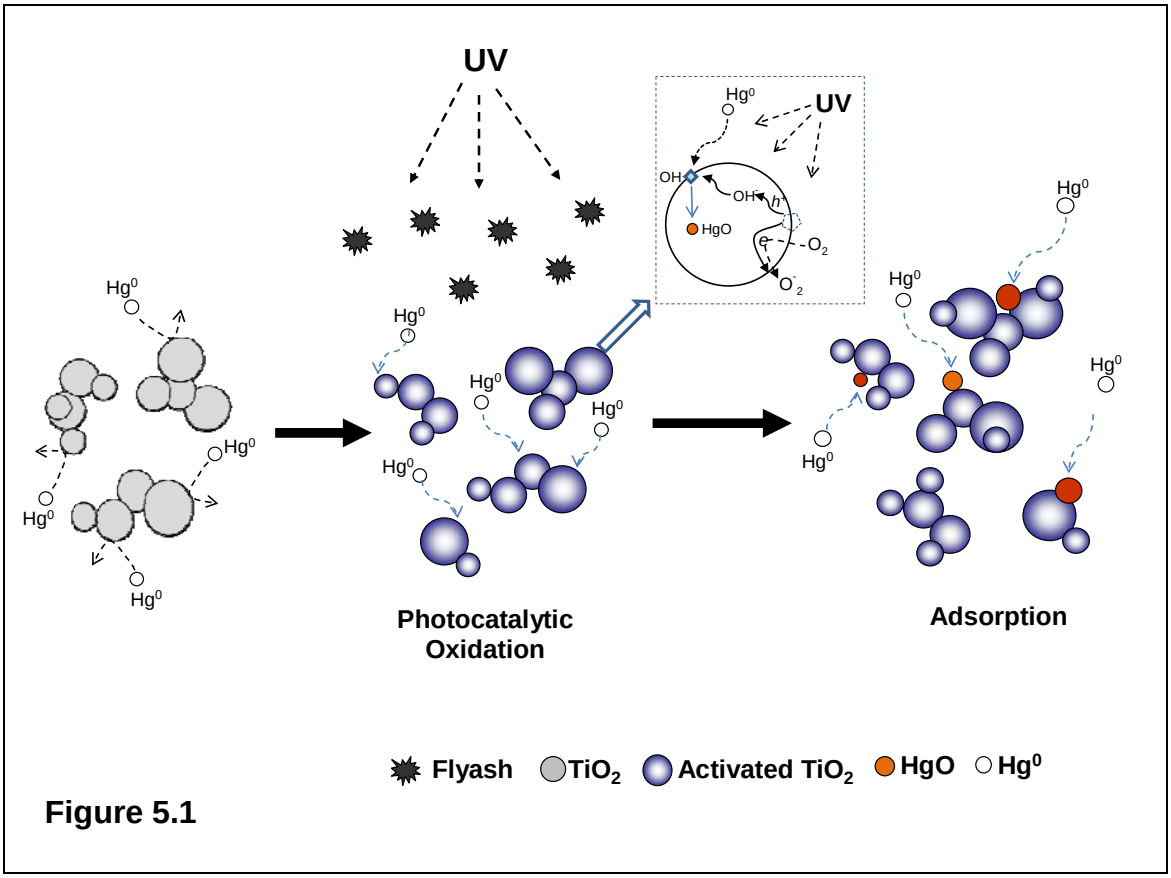

Figure 5.1: Mechanistic pathway of Hg capture by TiO_2 with UV irradiation

While TiO_2 with UV irradiation has been successfully demonstrated in many laboratory-scale experiments using simulated flue gas, before this sorbent can be selected for full-scale application, its effectiveness in coal combustion systems needs to be evaluated. Coal combustion systems pose several challenges to the performance of sorbents, such as the interference of fly ash and other flue gas constituents, and short residence time of flue gas in the system. To date, there has been no study on the nano-structured TiO_2 with UV irradiation for mercury capture in coal combustion systems.

Nano-structured TiO_2 sorbent can be generated by several methods. In-situ oxidation of the sorbent precursor is the simplest technique that provides very high surface area per unit mass. At high temperature, the vapor precursor decomposes and forms molecular-sized particles. These particles undergo aerosol growth dynamics, such as coagulation and sintering, in the combustion system, resulting in agglomerates of molecular- or nanometer-sized particles. The term sintering in this paper refers to coalescence of connected particles through neck formation by solid-state diffusion, which results in a reduction of surface area and agglomerate size. Understanding the evolution of sorbent particles in the system will allow optimal sorbent injection strategy to be developed at the minimal cost.

In this study, the effectiveness of TiO_2 with UV irradiation for mercury capture was investigated in two systems at different scales, (1) a laboratory-scale coal combustor, and (2) a slip-stream system drawn from a pilot scale coal combustor system. The importance of sorbent injection strategy, including sorbent generation and injection locations, on the effectiveness and efficiency of the sorbent was also highlighted. The results of this study allow us to effectively design the sorbent for higher efficiency.

5.2 METHODOLOGY

5.2.1 Test Plan.

The overall objective is to evaluate the effectiveness of TiO_2 with UV irradiation for mercury capture from coal combustion systems. The test plan was designed as outlined in Table 5.1. In Set I of the test, experiments were conducted in a laboratory-scale coal combustion system to determine the role of sorbent injection strategy, including the form of the injected sorbent and the sorbent injection location, on the effectiveness and efficiency of the sorbent for mercury capture. The effects of these variables on the properties of the sorbent were also evaluated. In Set II, the best sorbent injection strategy obtained from Set I was tested with the flue gas from a pilot-scale coal combustion system, using a slip-stream. The slip-stream system allowed us to evaluate the effectiveness of the sorbent in flue gas similar to that of

full-scale coal combustion exhaust, while the key parameters influencing the effectiveness of the sorbent, i.e., residence time and light distribution, were still under proper control. The initial feed rate of TiO_2 was estimated from the kinetic expression developed by Lee et al. (2004) [13] for each system. The designed TiO_2 feed rates are shown in Table 5.1. In Set III, a modeling study was performed on the pilot-scale system to evaluate the effects of sorbent injection strategy, i.e., the forms of sorbent injected and the sorbent injection location, on the properties of the sorbent, including the surface-area-to-mass ratio and the eventual particle size at the exit of the combustion system.

Table 5.1

Set	test	TiO_2 Generation Technique	Injection Location	Selected TiO_2 feed rate (mg/m^3)	TiO_2 feed rate (mg/m^3) Kinetically estimated	[Hg] ($\mu g/m^3$)
I (Lab-scale System	1	in-situ generated	Coal combustor	14.2, 28.4, 71	60.0	1.0 ± 0.1
	2	pre-synthesis	After combustor	14.2, 28.4, 71		
	3	Degussa P25	Coal combustor	10, 50,100		
II (Slip-stream System)	4	pre-synthesis	Before photo-reactor	114, 228, 622	160.0	2.5 ± 0.2
	5	Degussa P25		3,000		
III (Simulation in the Pilot-scale System)	6	in-situ generated	Coal combustor, After combustor, After heat exchanger	1,000		
	7	Degussa P25				

5.2.2 Experimental Setup.

The laboratory-scale coal combustor, the slip-stream system, and the pilot-scale coal combustor system are described in detail below.

5.2.2.1 Laboratory-scale Coal Combustion System.

The laboratory-scale experimental setup is shown in Figure 5.2A and consists of a coal feeding system, a tubular furnace (Lindberg/Blue M, Model HTF55342C, T_{max}=1200ºC, Thermoelectron Corporation, USA) with an alumina reactor tube (5.72 cm inside diameter and 121.92 cm long), sorbent injection systems, and measuring systems. Pulverized Powder River Basin (PRB) sub-bituminous coal, with a mean particle size of 50 μm was introduced into the heated alumina tubular reactor by a fluidized bed coal feeder at a rate of 1.0 g/hr. The furnace temperature was maintained at 1200 $^{\circ}$C with excess air (1.75 lpm air feed rate) to ensure complete combustion. Following the reactor, the exhaust passed through a photochemical reactor irradiated with UV light, and a filter. The photochemical reactor had a diameter of 5.7 cm and a length of 59 cm; at a flow rate of 1.75 lpm this corresponded to a residence time of 52 s in the photochemical reactor cell. The UV lamp, manufactured by Spectronics Corporation (Spectroline Model XX-40 Longwave UV-365 nm), was 122 cm long, with an intensity of 1850 μW/cm^2 at a distance of 8 cm.

Following the filter, 1.0 lpm of the exhaust passed through an impinger sampling train while the remainder of the flow was vented to the fume hood.

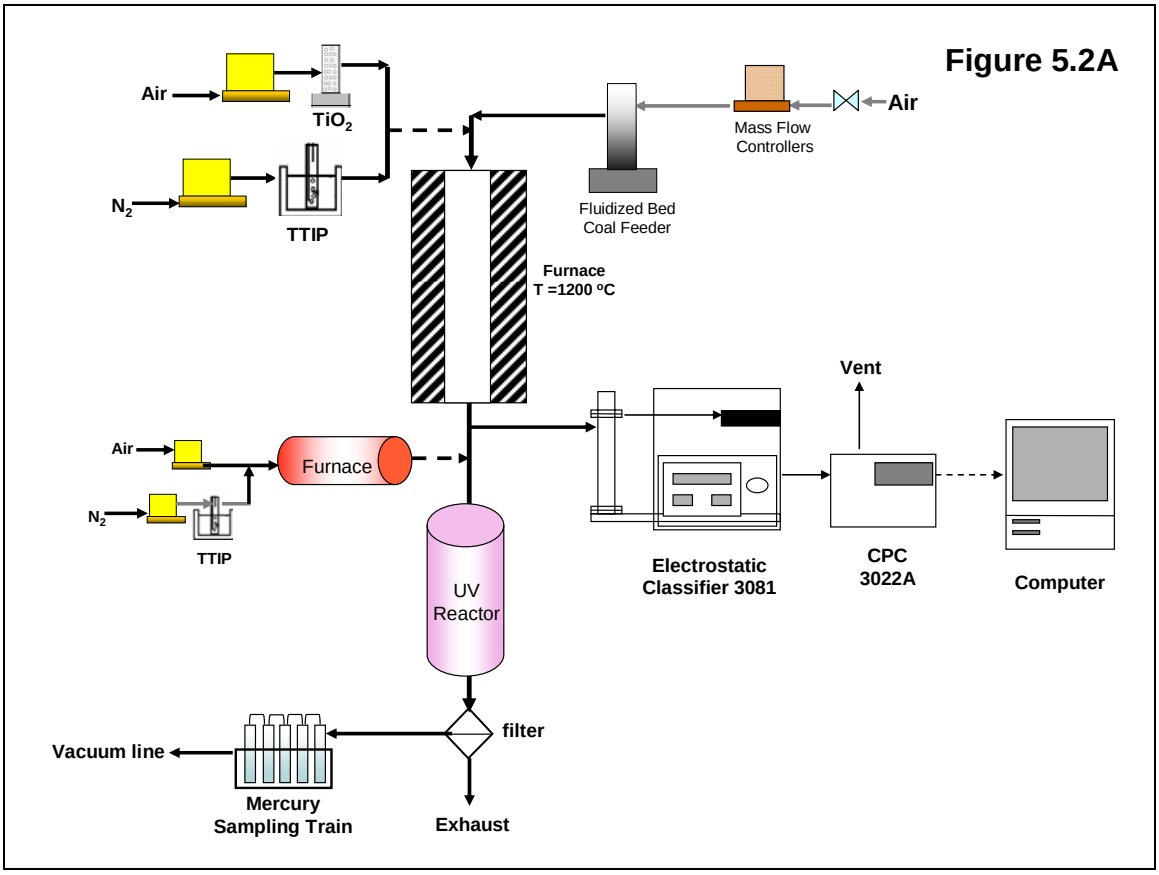

Figure 5.2A: Schematic diagram of a laboratory-scale experimental study

Powder River Basin subituminous coal (PRB) used in this study was supplied by AmerenUE, St. Louis, MO. This coal came from Wyodak-Anderson seam, North Antelope/Rochelle mine, Gillette, WY. This mine supplied approximately 91.5

million tons of compliance coal to 60 power plants throughout the United States in 2007. The proximate and ultimate analyses of the coal are presented in Table 5.2.

Table 5.2

Coal	Lab-scaled System	Pilot-scale System
Proximate Analysis (%wt)		
Volatile Matter[a]	48.3	46.5
Fixed Carbon[a]	42.9	41.2
Ash[a]	8.0	7.4
Moisture[b]	27.7	19.0
Low Heating Value[a] (MJ/kg)	28.04	27.92
Ultimate Analysis (%wt)[a]		
Carbon	67.3	60.6
Nitrogen	0.96	0.66
Hydrogen	4.58	5.57
Oxygen	19.9	26.9
Sulfur	0.57	0.36
Chlorine	0.01	0.008
Mercury (ppm_{wt})	0.08	0.051

Note: [a]: as dry weight basis; [b]: as received weight basis

5.2.2.2 Slip-stream System.

The slip-stream system was fed from the pilot system. The system allowed proper control of the key parameters, including UV light intensity and residence time under UV light. The slip-stream was drawn from the outlet of the electrostatic precipitator (ESP) of the combustion system. The slip-stream experimental setup,

shown in Figure 5.2B, consisted of sorbent injection systems, a photochemical reactor with UV irradiation, and a mercury measurement system. Two types of TiO_2 particles were tested in this system: pre-synthesized TiO_2, and commercial TiO_2. For the pre-synthesized TiO_2, TTIP was injected into a small tubular furnace for decomposition and formation of TiO_2 particles. The furnace temperature was maintained at 900°C to ensure complete decomposition of the sorbent precursor. Following the furnace, combustion flue gas, at the flow rate of 3.0 lpm, was mixed with a 2.0 lpm TiO_2 particle-laden carrier gas before entering a photochemical reactor irradiated with UV light. For the injection of commercial TiO_2, TiO_2 particle-laden air by-passed the furnace and was added into the combustion flue gas prior to entering a photochemical reactor. At a flow rate of 5.0 lpm, this corresponded to a residence time of 18.2 s in the reactor. The temperature in the reactor, as well as the tubing from the sampling location and leading to the furnace and the photochemical reactor were also held at 80°C using heating tape. The reactor was operated at the same condition as that in the laboratory-scale study. After the reactor, 2.0 lpm of flue gas was drawn to a continuous mercury measurement system and the remaining gas was vented to the exhaust.

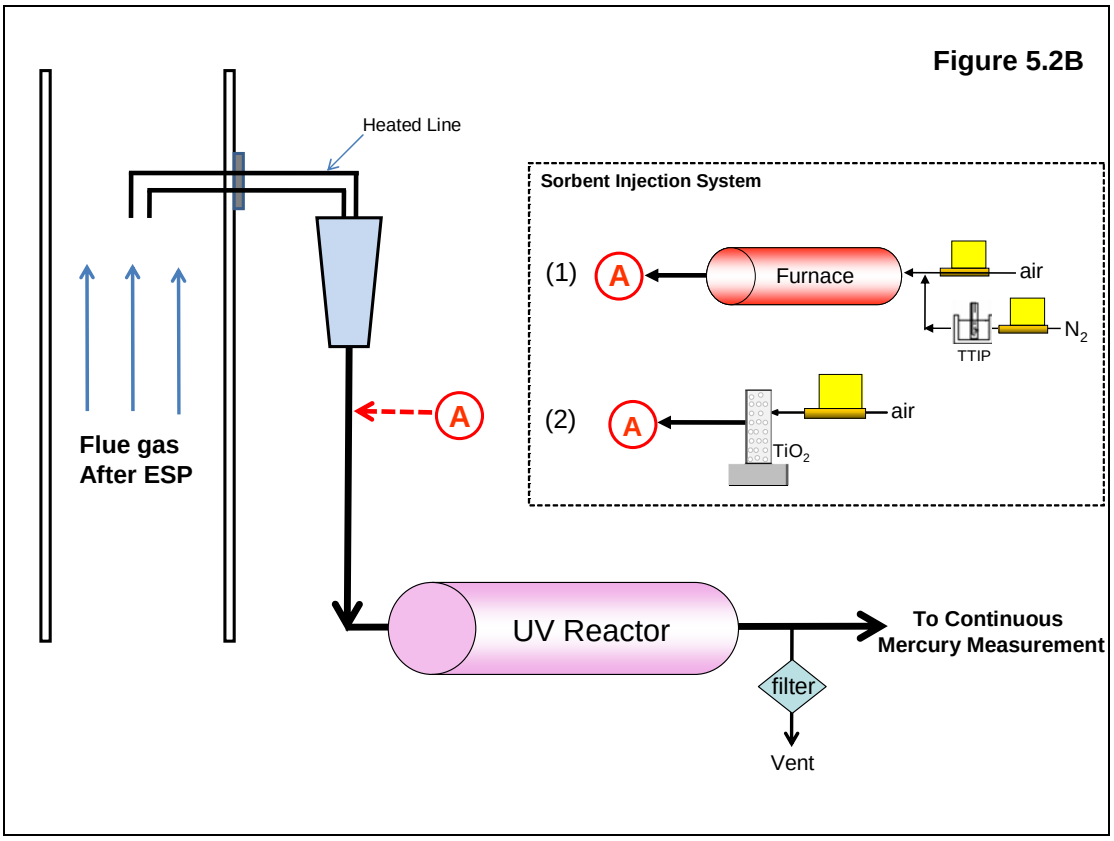

Figure 5.2B: Schematic diagrams of a slip-stream system

5.2.2.3 Pilot-scale Coal Combustion System.

At the Energy and Environmental Research Center (EERC), Grand Forks, ND, a pilot-scale test was conducted, using a 550,000 Btu/hr pulverized coal-fired unit. This system was designed to obtain combustion conditions and characteristics, i.e., a time- temperature profile, similar to that produced in a full-scale utility. A schematic of the system is shown in Figure 5.2C. The system consists of a combustor, cold-water annular heat exchangers, an air heat exchanger, a single-wire tubular electrostatic precipitator (ESP), and a bag house. Pulverized Powder River Basin (PRB) sub-bituminous coal, obtained from the same mine as that used in a laboratory-scale coal combustion study, was introduced with the primary air stream into the combustor at a feed rate of 28 kg/hr via a screw feeder and eductor. Based on the superficial gas velocity, the mean residence time of a particle in the combustor was approximately 3 seconds. The temperature in the coal combustor was approximately 1600^{o}C. After exiting the combustor, combustion flue gas at a flow rate of 340 m^{3}/hr at 1000 ^{o}C passed through a water heat exchanger and an air heat exchanger, which brought the flue gas temperature down to approximately 150^{o}C before it entered the ESP and the fabric filter. The total residence time of the flue gas in the pilot-scale combustion system was approximately 32 s.

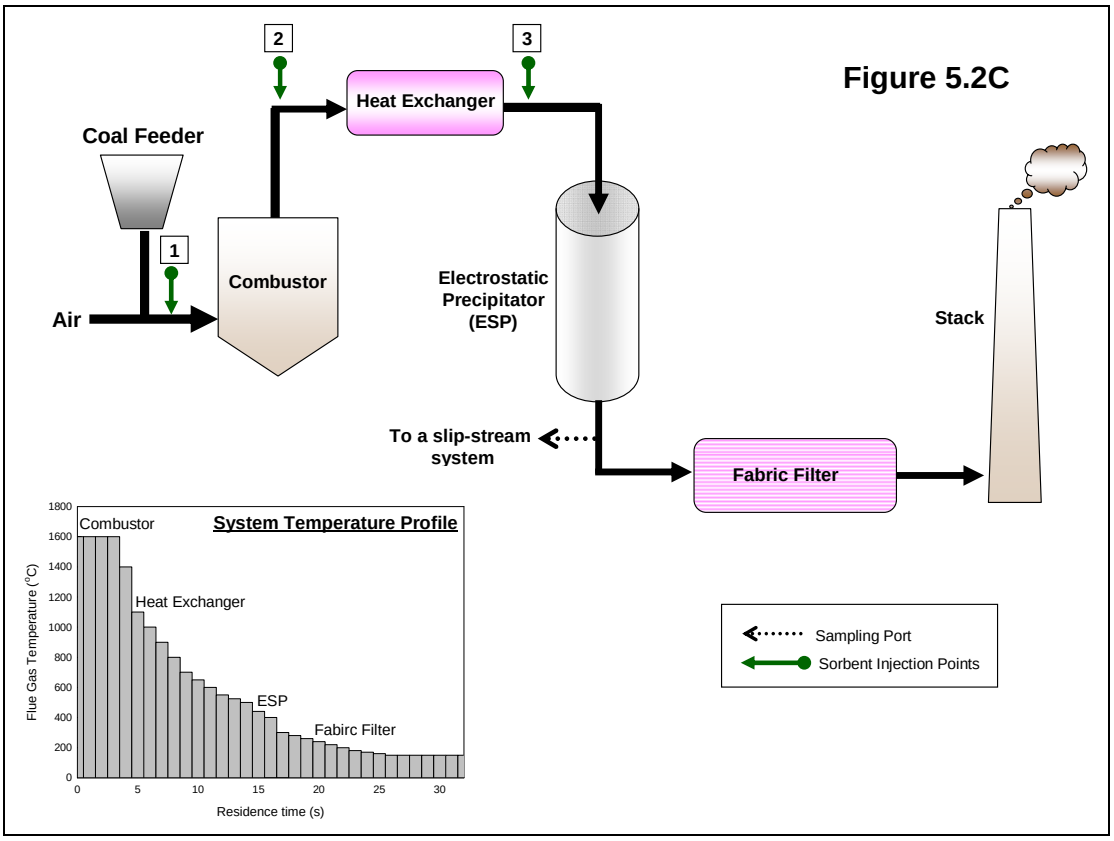

Figure 5.2C: Schematic diagrams of a pilot-scale system

5.2.3 Sorbent Used.

Three types of TiO_2 particles were tested in this study: TiO_2 generated in-situ by oxidation of its precursor, pre-synthesized TiO_2, and commercial TiO_2 (Degussa-Hüls, TiO_2 P25). A vapor phase precursor, titanium tetra-isopropoxide (TTIP, $Ti[OCH(CH_3)_2]_4$; 97% Aldrich), was used for the in-situ synthesized TiO_2 and the production of pre-synthesized TiO_2. For the in-situ generated TiO_2, TTIP was injected into the coal combustor, decomposed, and formed TiO_2 particles. For the pre-synthesized TiO_2, TTIP was injected into a small tubular furnace (Thermolyne, Type 2110) with an alumina reactor (ID = 1.9 cm; L = 50 cm), for decomposition and formation of TiO_2 particles. These particles could be introduced into the combustion system at low temperature locations. The TiO_2 particles formed by these two techniques provided higher external surface area for adsorption than did the bulk sorbent. The sorbent injection techniques applied for each system are summarized in Table 5.1, and the sorbent injection locations for each system are shown in Figure 5.2A, and 5.2C, respectively. TTIP was introduced by into the system in the vapor phase using an impinger (bubbler nozzle with a sintered glass filter) with nitrogen as a carrier gas. The TiO_2 feed rates were varied by changing the N_2 flow rate and bubbler temperature. To minimize nucleation of TTIP, the tubing leading to the inlet manifold was held constant at 80^oC using heating tape. For TiO_2 injection, a fluidized bed solid feeding system was used.

5.2.4 Sorbent Characterization Methods.

The synthesized TiO_2 particles generated in the laboratory-scale and slip-stream systems were well characterized using different analytical techniques. During the synthesis process, the particle mobility size distributions were measured online using a real time scanning mobility particle spectrometry (SMPS) including a differential mobility analyzer (DMA, Model 3081, TSI Inc.) and a condensation particle counter (CPC 3022, TSI Inc.). After particle collection on the filter paper, the X-ray diffraction (XRD) patterns were measured using a Rigaku Geigerflex D-MAX/A Diffractometer with Cu-Ka radiation, $\lambda = 1.5418$ Å. Based on the diffraction patterns, the weight fractions of each phase for mixed anatase and rutile samples were calculated. BET isotherms (Autosorb-1, Quantachrome) were used to measure the specific surface area of the nanoparticles with nitrogen adsorption at 77K.

5.2.5 Mercury Measurement Methods.

Gaseous mercury in our laboratory-scale study was measured using a mercury sampling train and technique based on the method developed by Hedrick et al. (2001) [18]. The sampling train consisted of the following five impinger solutions: two impingers of 1.0 M tris-buffer and EDTA for capture of oxidized mercury, one impinger of 10% hydrogen peroxide and 2% nitric acid for oxidizing and capture of elemental mercury, and two impingers of 0.05 M potassium iodide and 2%

hydrochloric acid for capture of elemental mercury. The impinger solutions were analyzed by inductively coupled plasma mass spectrometry (ICP-MS) to determine the elemental and oxidized fractions of mercury in the exhaust gas. All experiments were repeated at least three times to obtain statistically significant results.

In the slip stream tests, a continuous mercury measurement (Tekran model 2537A, Toronto, Canada) was done with a wet conversion system. The wet conditioning unit consisted of two impingers containing chemical solutions for conditioning the sample gas for elemental mercury and total mercury measurements. The elemental mercury impinger contained a solution of 1.0 M potassium chloride (KCl) and 1.0 M sodium hydroxide (NaOH). The KCl captured oxidized mercury, and the NaOH captured SO_2. The total mercury impinger contained a solution of 2% stannous chloride ($SnCl_2$) and 1 M NaOH. The $SnCl_2$ reduced the oxidized mercury in order to obtain a total mercury measurement. To avoid any residual buildup in the impinger system, fresh solutions were continuously fed to the impingers about 1.5 mL/min by using a peristaltic pump.

5.2.6. Modeling Approach.

A bi-modal model developed by Jeong and Choi (2003) [19] was employed to understand the growth dynamic of sorbent particles in the combustion systems. This model accounted for the morphology of the aggregates in a dynamic manner, which gave a more accurate prediction of the surface area and the collision rates of growth than the traditional models that assumed spherical particles. The detailed description of the model can be found elsewhere [19-20]. In the simulations, TiO_2 is introduced into the system in two forms: as a vapor phase precursor, TTIP, and as commercial TiO_2. For the precursor feed, the initial size of the sorbent is its monomer size (4.02 Å) [21]. In the Set III study, a modeling study was performed for the pilot-scaled system to evaluate the effects of sorbent injection strategy. According to the structure of the pilot-scale facility, three sorbent injection locations were selected: (1) at the combustor, (2) after the combustor, and (3) after heat exchanger, as shown in Figure 2C. The temperatures at these locations are 1600, 1100, and 500^{o}C, respectively. All simulations were performed until the flue gas entered the ESP.

5.3 RESULTS AND DISCUSSION

5.3.1 Mercury Capture in the Laboratory-scale Coal Combustion System.

The mercury capture efficiencies of different injection strategies for an inlet mercury concentration of 1.0 $\pm$ 0.2 $\mu g/m^3$ are shown in Figure 5.3. An average of 0.18 $\mu g/m^3$ (18 %) was oxidized mercury, and 0.95 $\mu g/m^3$ (82%) was elemental mercury. From the proximate analysis of this PRB coal, shown in Table 5.2, this type of coal had low sulfur and chlorine contents, resulting in limiting the extent of mercury oxidation. The elemental composition analysis indicated that all the mercury from the coal was released into the gas phase. The sorbent feed rate selected in this set of experiments ranged between 14.2 to 71.0 mg/m^3. According to the kinetic expression [13], the required feed rates of TiO_2 was approximately 60.0 mg/m^3 at 90% removal efficiency. This designed feed rate resulted in mercury-to-TiO_2 of 0.016 mg Hg per g of TiO_2. Three sorbent injection strategies were evaluated in this lab-scale study. The first injection strategy used in-situ generated nano-structured TiO_2. The sorbent particles were generated from the decomposition of a vapor phase precursor (titanium tetra-isopropoxide, TTIP, $Ti[OCH(CH_3)_2]_4$), inside the coal combustion system. In the second injection strategy, pre-synthesized TiO_2 agglomerates were generated in a small furnace using TTIP, and then introduced to the combustion exhaust gas upstream of the photochemical reactor. In the third

injection strategy, commercial TiO_2 particles were introduced into the combustion system with coal.

Substantial reductions in mercury emissions in the exhaust were observed for all three sorbent injection strategies, as presented in Figure 5.3. The highest reduction, 91%, was obtained from sorbent injection strategy 2 (the pre-synthesized TiO_2), followed by 83% from injection strategy 1 (in-situ generated TiO_2), and 78% from injection strategy 3 (commercial TiO_2). Experimental results demonstrated that for all of the three sorbent injection strategies the amount of sorbent required to achieve 90% mercury removal was higher than that estimated from the kinetic calculation (60.0 mg/m^3). The difference was attributed to the potential interference of flyash, since the effectiveness of TiO_2 sorbent depends on the intensity of the UV light [13]. The presence of flyash could hinder the photocatalytic activation of TiO_2 particles. The flyash loading in this lab-scale coal combustion was approximately 760 mg/m^3. The potential interference of other compositions in flue gas would be negligible since the coal-to-air mass ratio in the laboratory-scale coal combustion system (1:95) was low compared to that in the pilot and full-scale coal combustion systems (ranging between 1:5 and 1:7).

Among the three sorbent injection strategies, the pre-synthesized TiO_2 exhibited the highest mercury removal for all feed rates. This was attributed to the

high surface area for adsorption and to the highly anatase crystalline structure of the TiO_2. The properties of TiO_2 agglomerates generated from different techniques are shown in Table 5.3 and the agglomerate size distributions of the in-situ generated TiO_2 and the pre-synthesized TiO_2 are shown in Figure 5.4. For all sorbent precursor feed rates, the pre-synthesized TiO_2 exhibited a larger geometric mean agglomerated size than that of the in-situ generated TiO_2. The total surface area of the pre-synthesized TiO_2 agglomerates was higher than that of the in-situ generated for all feed rates of sorbent precursor, leading to higher mercury capture. The differences in the surface area were attributed to the sintering effect. The in-situ generated TiO_2 particles were exposed to higher temperature (1200^{o}C) over a much longer residence time than those in the pre-synthesized process (the onset temperature of the pre-synthesized furnace and the residence time were 900^{o}C and 2 s, respectively). Hence, a higher surface area reduction was observed.

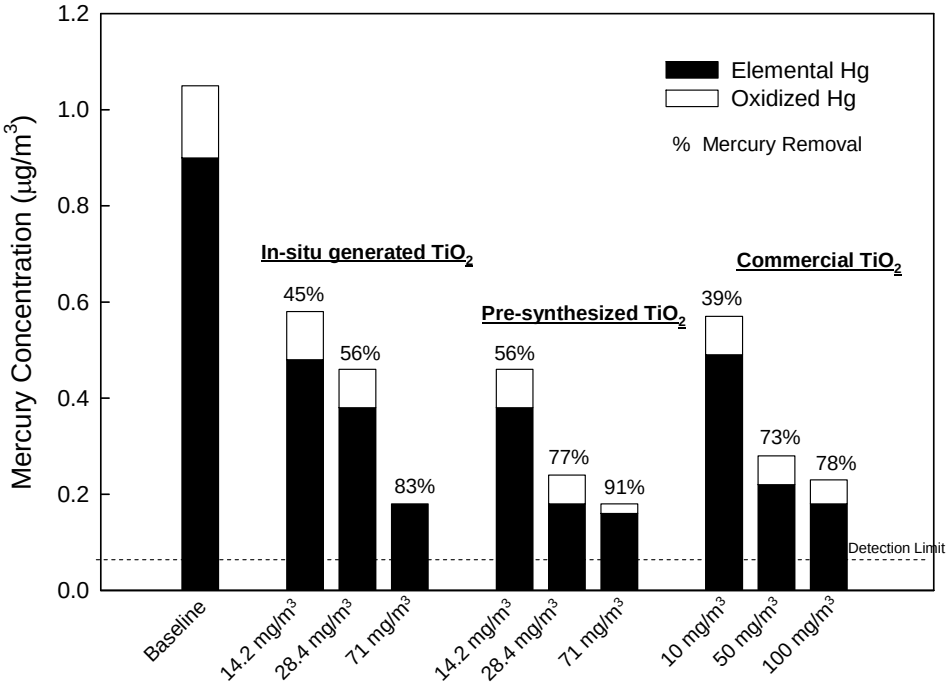

Figure 5.3: Mercury capture in a lab-scale coal combustion study using different sorbent injection strategy

Table 5.3

Combustion system	Sorbent Generation Technique	TiO_2 feed rate (mg/m^3)	Crystal phase	SA[a] (m^2/g)	d[b](nm)
Lab-scale	in-situ generated,	14.2, 28.4, 71	90%A/ 10%R	60.4, 58.6, 57.8	32.2, 37.2, 42.9
	pre-synthesis	14.2, 28.4, 71	100%A	65.5, 63.6, 60.8	44.5, 55.2, 68.5
	Degussa P25*	10, 50,100	80%A/ 20%R*	52	-
	Degussa P25**	10, 50,100	72%A/ 28%R**	48.0, 46.3, 45.0	40.4, 65.8, 80.2
Slip-stream	pre-synthesis	114, 228, 622	100%A	63.5, 62.6, 60.4	80.5, 105.8, 121.3
	Degussa P25*	3,000	80%A/ 20%R	52	-

Note: A: Anatase Phase, R: Rutile Phase
* measured before introduced into coal combustor
** measured after coal combustor
[a] specific surface area of particles measured by N_2 adsorption (BET)
[b] mobility agglomerate size determined by a scanning mobility particle spectrometry

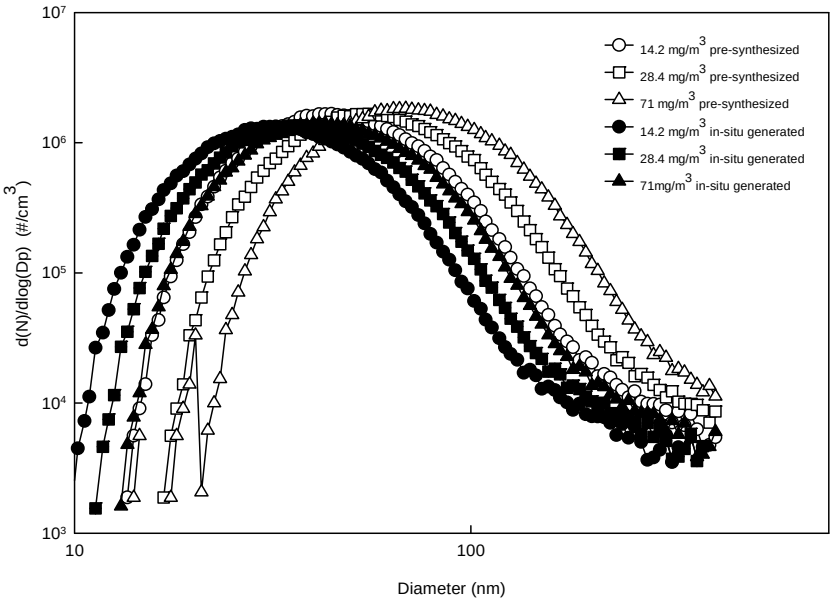

Figure 5.4: Particle size distribution of TiO_2 agglomerates generated by different synthesized technique

The performance of the sorbents also depends on its chemical (crystalline phase) properties. The TiO_2 with anatase crystal structure exhibits more photocatalytic activity than the rutile phase [22], and thus is preferred in mercury capture. All nano-structured TiO_2 prepared in this study have anatase crystal structure. The XRD spectra of TiO_2 agglomerates synthesized by different techniques and commercial Degussa TiO_2 are shown in Figure 5.5, along with the standard peak distributions of anatase and rutile. The crystalline structure of the in-situ generated TiO_2 was 90% anatase and 10% rutile, while 100% anatase was found in the pre-synthesized TiO_2. For Degussa TiO_2, the crystalline structure was altered from 80% to 72% anatase and 20% to 28% rutile after it passed through the combustor. Anatase, a meta-stable crystal form, tends to transform into the thermodynamically stable polymorph, rutile, when the particles are exposed to high temperature for a long period [23]. Both in-situ generated TiO_2 particles and Degussa TiO_2 particles encountered higher temperature in the coal combustor (1200^{o}C), with a longer residence time (~1 min) than those that had undergone the pre-synthesized process, resulting in small fraction of rutile crystalline formed.

The results obtained from this set of experiments indicate that the sorbent synthesis technique and the sorbent injection location significantly affect both the physical and chemical properties of the sorbent, and subsequently its performance. These findings can guide effective and efficient designs for mercury removal.

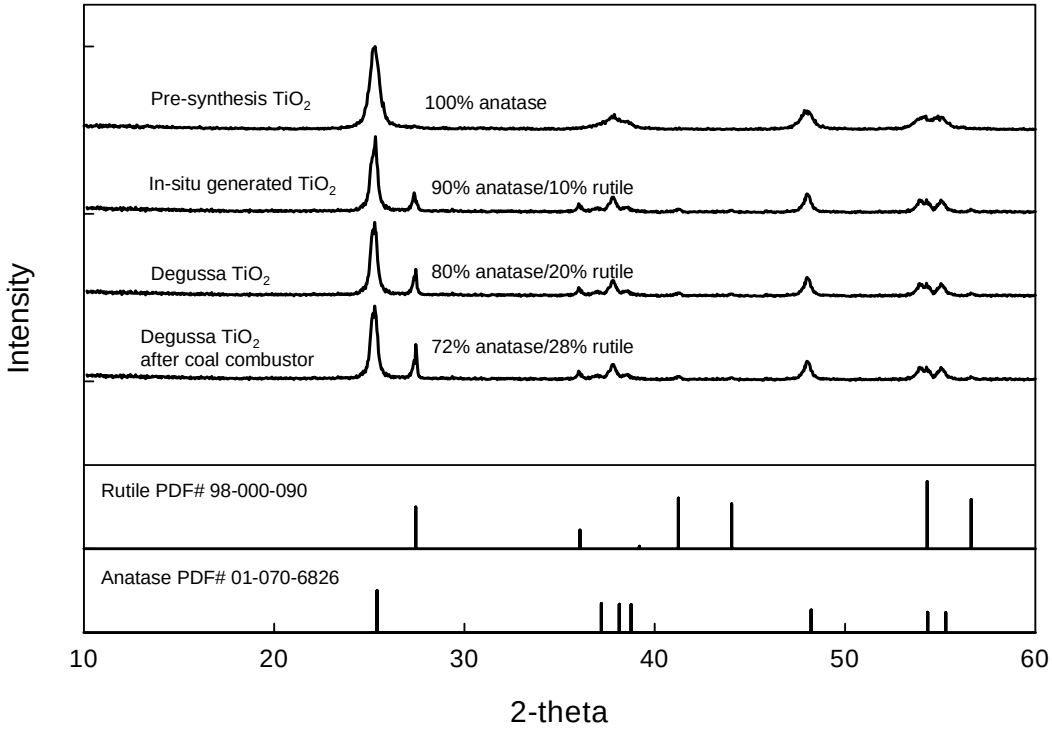

Figure 5.5: The XRD pattern of TiO_2 particles synthesized by different synthesized techniques

5.3.2 Mercury Capture in the Slip-stream Coal Combustion System.

The measured mercury concentrations from the slip-stream drawn from the pilot-scale coal combustion system are shown in Figure 5.6. The mercury concentration was slightly lower than that in actual flue gas because the flue gas was diluted with TiO_2 laden carrier gas. Most of the mercury was in elemental form,

which was consistent with the findings of our laboratory-scale study. Because of the high ash loading in flue gas upstream of the ESP, approximately 2.5 g/m^3, UV light distribution in the photocatalytic reactor was essentially prevented, and the slip-stream was drawn from the outlet of the ESP. The pre-synthesized TiO_2 and commercial Degussa TiO_2 were evaluated in this study. Both types of TiO_2 sorbent showed a substantial reduction of gaseous mercury. According to the kinetic expression from Lee et al. (2004) [13], the designed feed rates of TiO_2 were approximately 160 mg/m^3 at 90% removal. The selected injection rates of pre-synthesized TiO_2 were 114, 228, and 622 mg/m^3, resulting in mercury reductions of 13%, 46%, and 90%, respectively. The differences were attributed to the interference of flue gas constituents. Since flue gas was drawn from the outlet of the ESP, the potential interference of flyash was negligible. One of the potential interferences is moisture. Moisture is known to be the important parameter effecting both photocatalytic oxidation and adsorption. Moisture is necessary for generating hydroxyl radicals, the active reagents for photocatalytic oxidation. However, high moisture reduces adsorption capacity by occupying active sites on the TiO_2 particle, and thus its efficiency [16, 24]. Moisture concentration in the coal combustion flue gas, approximately 8% by volume, was much higher than the optimal concentration (700-1800 ppm_v) where both adsorption and photocatalytic oxidation can occur [15]. As a result, mercury oxidation rate was decreased. Furthermore, in coal combustion flue gas, other metallic species are also present, which may result in the competitive

occupancy of the available adsorption sites. For commercial Degussa TiO_2, the required feed rate to achieve 93% mercury reduction was approximately 3,000 mg/m^3. The pre-synthesized TiO_2 demonstrated higher efficiency than commercial TiO_2 because it exhibited pure anatase crystal structure and higher available surface area for adsorption, which were consistent with the study in the laboratory-scale coal combustion system.

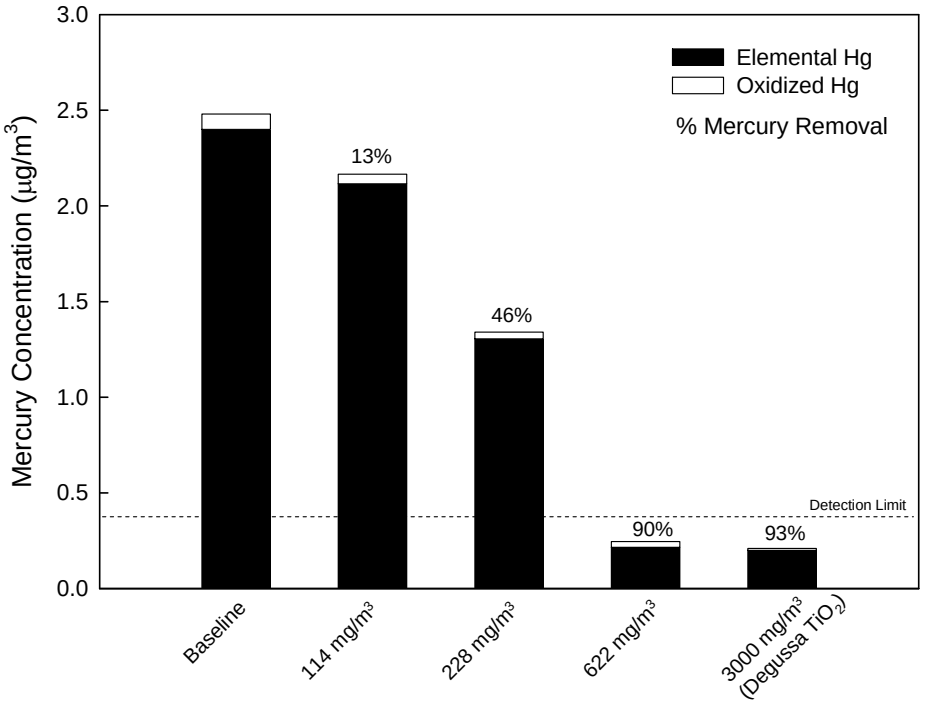

Figure 5.6: Mercury capture in a slip-stream study using pre-synthesized TiO_2 agglomerates and commercial TiO_2

5.3.3 Sorbent Injection Strategy the Pilot-scale Coal Combustion System.

The previous sections have shown that that the surface area exposed to UV light significantly affects the efficiency of the sorbent. To effectively prevent mercury emission into the atmosphere, the spent sorbents have to be captured by a particulate control device. The large agglomerate size would result in the most effective capture in an existing particle control device, such as ESP [25]. In addition, as cost is important, minimal sorbent loading while achieving good removal efficiency is always preferred. Hence, it is important to develop the sorbent injection strategy to effectively and efficiently implement nano-structured TiO_2 with UV irradiation for Hg capture. A model simulation was employed to understand the growth dynamic of the sorbent and to determine the optimal sorbent injection strategy. In the simulations, TiO_2 is introduced into the system in two forms: as a vapor phase precursor, TTIP, a commercial TiO_2. Three sorbent injection locations are selected: (1) at the combustor, (2) after combustor, and (3) after heat exchanger. The temperatures at these locations are 1600, 1100, and 500^oC, respectively. All simulations were performed until the flue gas entering an ESP.

The key parameters used to determine the best injection strategies are surface area per unit mass and agglomerate size. The results from the simulations are shown in Figure 5.7A and 5.7B. The in-situ generated TiO_2 sorbent exhibits higher surface

area per unit mass than that of commercial TiO_2 particles for all injection locations, except at location 1 (at the combustor), where the surface area per unit mass of both types of TiO_2 were the same. The high surface area per unit mass of in-situ generated TiO_2 resulted from the molecular-sized TiO_2 particles in the agglomerates, while the commercial TiO_2 agglomerates consisted on nanometer-sized particles. The simulation results further show the important of sorbent injection location. The in-situ generated TiO_2, injected at location 2, exhibited higher surface area per unit mass than at other injection locations, followed by injection locations 3 and 1. The differences are attributed to decomposition of the vapor precursor and the sintering effect. At locations 1, the temperatures of the flue gas are high, resulting in rapid decomposition of the Ti-vapor precursor, formation of TiO_2 particles, and growth by Brownian coagulation forming aggregates of molecular-sized TiO_2 particles. However, due to the high temperature environment, the connected particles sintered into closer to spherical shapes, resulting in a reduction of surface area. The temperature inside the combustor is much higher than that after the combustor; thus, there is higher surface area reduction. The differences in the surface area per unit mass for locations 2, and 3 can be attributed to effect of temperature on the decomposition and oxidation rates of Ti-vapor-precursor. At location 2, the flue gas temperature is much higher than injection location 3. Hence, there are faster decomposition, particle formation, and sintering rates. As shown in Figure 5.7A, the surface area per unit mass of in-situ generated TiO_2 injected at location 2

instantaneously increased after the injection, then decreased due to sintering, and became constant afterwards. At location 3, this parameter gradually increased with the residence time, indicating continuous particle generation in the flue gas.

For the commercial TiO_2 sorbent, the surface area per unit mass was highest at injection location 3. The effect of sintering on the reduction of surface area was also observed only at locations 1 and 2. However, the effect was not as significant as that observed in the in-situ generated process because the required sintering time (τ_s) is proportional to the fourth power of the primary particle size [26-27]. The initial size of the primary particle of commercial TiO_2 was larger than that of the in-situ generated process; thus, less impact was observed. The simulations also showed that at location 1, the in-situ generated sorbent and the commercial TiO_2 resulted in the same the surface area per unit mass, indicating that the high temperature and long residence time in the combustor outweighed the effect of primary particle size. The efficiency of the sorbent would be minimized if injected into the combustor.

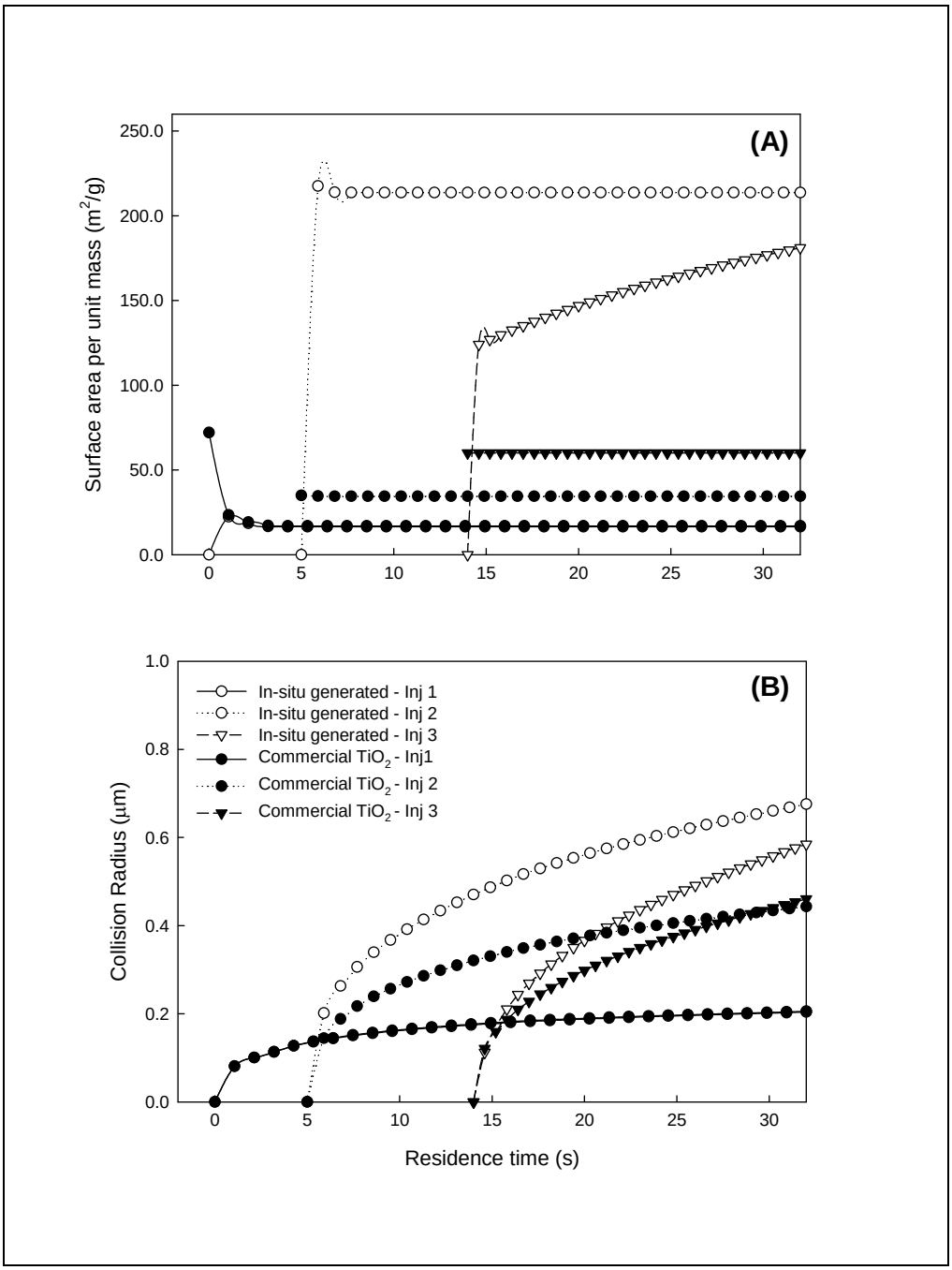

Figure 5.7: (A) Evolution of surface area of TiO_2 sorbent generated in-situ and commercial TiO_2 (Degussa, P25) injected at different locations. **(B)** Evolution of agglomerate size of TiO_2 sorbent generated in-situ and commercial TiO_2 (Degussa, P25) injected at different locations

Another important property of the sorbent for Hg capture is its eventual size at the particulate control device. This parameter indicates the capture effectiveness of the sorbent by particulate control device. Results of the simulations are illustrated in Figure 5.7B. The in-situ generated TiO_2 sorbent exhibited larger agglomerate size than that of commercial TiO_2 particles for all injection locations, except at location 1 (at the combustor), where the eventual agglomerate size of both types of TiO_2 were the same. Among the in-situ generated TiO_2, the Ti-precursor injected at location 2 exhibited largest agglomerate size, approximately 0.6 μm at the exit of the combustion system, followed by that at location 3 and 1. The differences are attributed to decomposition of the vapor precursor and the sintering effect, as previously discussed. For commercial TiO_2, the eventual agglomerate size was relatively the same for injection locations 2 and 3, and it was smallest when the sorbent was injected at location 1.

The results of Set III study demonstrated the importance to sorbent injection strategy in the properties of the sorbent. As cost is important, minimal sorbent loading while achieving good removal efficiency is always desired. The sorbent injection needs to be designed, so that the sorbent is effectively and efficiently utilized.

5.4 CONCLUSIONS

Titanium dioxide (TiO_2) particle with UV irradiation had been shown to be effective in the capture of gaseous mercury in laboratory-scale experiments using simulated flue gas. This study evaluated the effectiveness and efficiency of the sorbent in two coal combustion systems at different scales, a laboratory-scale coal combustor and a slip-stream system drawn from a pilot scale coal combustor system. In the laboratory-scale coal combustion system, 94% mercury capture was achieved at a TiO_2 feed rate of 71 mg/m^3. In the slip-stream system, 92% mercury capture was achieved at a feed rate of 622 mg/m^3. The required sorbent feed rates were higher than those estimated using previously established kinetics expression due to interference by other species present in coal combustion flue gas, e.g., flyash and moisture. The sorbent injection strategy played an important role in the efficiency of the sorbent. Pre-synthesized nano-structured TiO_2 demonstrated the highest efficiency, followed by in-situ generated and commercial TiO_2. The differences in the efficiency were attributed to the properties of the sorbent, including available surface area per unit mass and crystalline structure. This study further demonstrated the importance of sorbent injection strategy, including sorbent generation and injection locations, on the physical properties of the sorbent in a pilot-scale coal combustion system. Sorbent injection should be carefully designed, so that high-surface-area agglomerates result and the sorbent is efficiently utilized. Results of this study also emphasize the

importance of the system variables, such as time-temperature profile, coal type, and mercury concentration on the sorbent performance.

Since UV light is also a critical factor governing mercury removal efficiency of the sorbent and the time-scale for the experiments in this study are relatively longer than those in full scale systems (varying from 60 s to120 s), future studies should focus on designing the distribution of UV light and conducting experiments over relevant time-scales. After effective design of UV light distribution and full-scale studies, nano-structured titanium dioxide with UV irradiation, it could become a promising technology for mercury capture from coal-burning utilities. This inorganic sorbent oxide process does not increase the carbon-content in flyash. The sorbent-flyash mix could be readily disposed or re-used as is done currently since mercury was found to be bound very tightly to the sorbent as established by sequential leachability studies. The TiO_2 sorbent can be efficiently utilized since the sorbent can be injected in high temperature flue gas, which increases contact time of sorbent and mercury. Furthermore, TiO_2 particles can potentially oxidize other hydrocarbon species, i.e. VOCs and PAHs, and suppress nucleation of other metallic species generated in combustion systems.

5.5 REFERENCES:

1. U. S. Environmental Protection Agency (1999). "1999 National Emission Inventory for Hazadous air pollutants." Retrieved November 23, 2004 <http:epa.gov/ttn/chief/net/1999inventory.html.>

2. Keeler, G. J., Landis, M. S., Norris, G. A., Christianson, E. M., Dvonch, J. T. (2006), "Sources of mercury wet deposition in Eastern Ohio, USA." *Environ. Sci. and Technol.* **40**(19), 5874-5881.

3. U. S. Environmental Protection Agency (2005). "Clean Air Mercury." Retrieved January 23, 2009 < http://www.epa.gov/air/mercuryrule/>

4. Edison Electric Institute (2008). "EPA Mercury Regulation." Retrieved January 23,2009<http://www.eei.org/ourissues/TheEnvironment/Air/Pages/EPAMercuryRegulation.aspx>

5. Biswas, P. and Wu, C. Y. (1998). "Control of toxic metal emissions from combustors using sorbents: A review." *J. Air & Waste Manage.* **48**(2), 113-127.

6. Biswas, P., Senior, C., Chang, R., Vidic, R., Laudal, D., Brown, T. (1999). "Mercury measurement and its control: What we know, have learned, and need to further investigate." *J. Air & Waste Manage.* **49**(12), 1469-1473.

7. Brown, T. D., Smith, D. N., O'Dowd, W. J., Hargis, R. A. (2000). "Control of mercury emissions from coal-fired power plants: a preliminary cost assessment and the next steps for accurately assessing control costs." *Fuel Process Technol.* **65**, 311-341.

8. Granite, E.J. and H.W. Pennline (2002). "Photochemical removal of mercury from flue gas." *Ind. Eng. Chem. Res.* **41**(22), 5470-5476.

9. Scotto, M. V., Uberoi, M., Peterson, T. W., Shadman, F. and Wendt, J. O. L. (1994). "Metal Capture by Sorbents in Combustion Processes." *Fuel Process Technol.* **39**(1-3), 357-372.

10. Pavlish, J. H., Sondreal, E. A., Mann, M. D., Olson, E. S., Galbreath, K. C., Laudal, D. and Benson, S. A. (2003). "Status review of mercury control options for coal-fired power plants." *Fuel Process Technol.* **82**, 89-165.

11. Zhuang, Y., Thompson, J. S., Zygarlicke, C. J. and Pavlish, J. H. (2007). "Impact of calcium chloride addition on mercury transformations and control in coal flue gas" *Fuel* **86**(15), 2351-2359.

12. Wu, C. Y., Lee, T. G., Tyree, G., Arar, E., Biswas, P., (1998). "Capture of mercury in combustion systems by in situ-generated titania particles with UV irradiation." *Environ. Eng. Sci.* **15**(2), 137-148.

13. Lee, T. G., Biswas, P. and Hedrick, E. (2004). "Overall kinetics of heterogeneous elemental mercury reactions on TiO2 sorbent particles with UV irradiation." *Ind. Eng. Chem. Res.* **43**(6), 1411-1417.

14. Lee, Y. G., Park, J. W., Kim, J. H., Min, B. R., Jurng, J., Kim, J. and Lee, T. G. (2006) "Comparison of Mercury Removal Efficiency from a Simulated Exhaust Gas by Several Types of TiO2 under Various Light Sources", *Chemistry Letters* **33**(1).

15. Rodriguez, S., Almquist, C., Lee, T. G., Furuuchi, M., Hedrick, E. and Biswas, P.
(2004) "A Mechanistic Model for Mercury Capture with In-situ Generated Titania
Particles: Role of Water Vapor", *J. Air & Waste Manage.* **54**(2), 149-156.

16. Li, Y. and Wu, C. Y. (2006) "Role of Moisture in Adsorption, Photocatalytic Oxidation, and Reemission of Elemental Mercury on a SiO2-TiO2 Nanocomposite", *Environ. Sci. and Technol.* **40**, 6444-6448.

17. Noel, J. D., Biswas, P., Giammar, D.E. (2007). "Evaluation of a sequential extraction process used for determining mercury binding mechanisms to coal combustion byproducts." *J. Air & Waste Manage.* **57**(7), 856-867.

18. Hedrick, E., Lee,T.G., Biswas, P., Zhuang, Y. (2001). "The Development of Iodine Based Impinger Solutions for the Effecient Capture of Hg0 Using Direct Injection Nebulization-Inductively Coupled Plasma Mass Spectrometry Analysis." *Environ. Sci. and Technol.* **35**(18), 3764-3773.

19. Jeong, I. J. and M. Choi (2003). "A Simple Bimodal Model for the Evolution of Non-Spherical Particles Undergoing Nucleation, Coagulation and Coalescence." *J. Aerosol Sci.* **34**, 965-976.

20. Kim, S.B., Kim, S. S., Biswas, P. (2009), "Simple trimodal model for evolution of multicomponent aerosol dynamics." *J. Aerosol Sci.* (submitted).

21. Jeong, S. K., Kim, S. B., Kim, S. S., Chen, X. and Biswas, P. (2007), "Simultaneous Removal of Cd and Pb from Flue Gases using In-situ Generated Nano-sized sorbents" *Ind. Eng. Chem. Res.* **13**, 1154-1161.

22. Kim, S. J., Lee, E. G., Park, S. D., Jeon, C. J., Cho, Y. H., Rhee, C. K., Kim, W. W. (2001). "Photocatalytic effects of rutile phase TiO2 ultrafine powder with high specific surface area obtained by a homogeneous precipitation process at low temperatures." *J. Sol-Gel Sci. and Technol.* **22**(1-2): 63-74.

23. Yan, M. C., Chen, F., Zhang, J. L., Anpo, M. (2005). "Preparation of controllable crystalline titania and study on the photocatalytic properties." *J. Physical Chemistry B* **109**(18): 8673-8678.

24. Pitoniak, E., Wu, C. Y., Mazyck, D. W., Bonzonco, J. J., Powers, K. and Sigmud, W. (2004). "Nano-structured silica gel doped with tio2 for vapor mercury capture" *J. Nanoparticle Res.* **5**, 281-292.

25. Suriyawong, A., Hogan, C. J., Jiang, J., Biswas, P. (2008). "Charged fraction and electrostatic collection of ultrafine and submicrometer particles formed during O2-CO2 coal combustion." *Fuel* **87**(6), 673-682.

26. Kruis, F. E., Kusters, K. A., Pratsinis, S. E. (1993). "A Simple model for the evolution of the characteristics of aggregate particles undergoing coagulation and sintering." *Aerosol Sci. and Technol.* **19**, 514-526.

27. Friedlander, S. K. (2000). *Smoke, dust, and haze: fundamentals of aerosol dynamics*. New York, Oxford University Press.

Chapter 6

Nano-structured Sorbent Injection Strategies for Heavy Metal Capture in Combustion Exhausts*

* This work has been submitted for publication in *Aerosol Science and Technology*.

ABSTRACT

Nano-structured sorbent injection is a promising technique for heavy metal capture in combustion systems. This importance of sorbent injection strategies, including the form of the sorbent and its injection location, on the performance in metal capture and removal is investigated in this study. A multi-component tri-modal aerosol dynamic model was employed to understand the evolution of heavy metals and sorbents, as well as their interactions in the incineration system. Experiments were conducted to assess the performance of in-situ generated SiO_2, compared with bulk Ti-PICL sorbent, in capturing lead and cadmium from a demilitarization incineration system. Nano-structured SiO_2 generated in-situ was found to be more efficient than the bulk Ti-PICL sorbent, because it offers a higher external surface area for condensation. The sorbent injection location is important as it affects the physical properties of the sorbent and the pathway for heavy metal capture. Extensive sintering and reduction in the surface area were observed when sorbent was injected into high temperature flue gas, i.e., directly into the combustor. However, when injected into much lower temperature flue gas, the pathway for heavy metal capture was altered from condensation to inter-coagulation due to the nucleation of heavy metal species. This study further revealed that new emission standards can be readily met with an optimal sorbent injection strategy.

Keywords*:* Metal Emissions; Sorbents; Adsorption; Condensation; Pollution Control; Ammunitions; Incinerators; Toxic Elements; Aerosol Modeling.

6.1 INTRODUCTION

Heavy metal emissions are of great concern because of their toxicity to human health and the environment. In the past decades, heavy metal loading in the atmosphere has substantially increased from anthropogenic emission sources, such as coal-fired power plants and waste incinerators. To limit the emissions, in 1999 the U.S. Environmental Protection Agency (USEPA) issued the National Emission Standard for Hazardous Air Pollutants (NESHAP) from combustion sources. Due to the increased awareness of the potential hazards of the pollutants, in October 2005, the standards were tightened to further reduce the emissions. For example, the emission standards for semi-volatile metals (lead and cadmium) from incinerators were reduced from 240 $\mu g/m^3$ to 230 $\mu g/m^3$ for existing sources and from 24 $\mu g/m^3$ to 10 $\mu g/m^3$ for new sources. Similarly, the emission standard for mercury was reduced from 45 $\mu g/m^3$ to 8.1 $\mu g/m^3$ for new sources [1]. The tightened emission standards call not only for a thorough evaluation of the performance of current control technologies, but also the development of new control techniques.

To effectively design a control methodology, it is important to understand the transformation of metallic species in the combustion environment. These metallic species are encountered both as a natural, trace constituent in fuels and as an industrially processed commodity. When introduced into a combustor, volatile heavy

metals vaporize at high temperatures, undergo several reactions, and then nucleate in the cooler downstream regions to form aerosols which ultimately grow to submicrometer size ranges [2-4]. Combustion sources are a major source of heavy metals in the atmosphere. Such sources are abundant, and conventional particle control devices typically have minimal collection efficiency in submicrometer size ranges, where toxic metals are predominant [5, 6].

Several control methodologies have been proposed for control of toxic metal emissions from combustion systems. In sorbent injection, which is both promising and widely used, sorbents are injected into the combustion system to chemically adsorb heavy metal vapors or scavenge fine-heavy metal particles [7, 8]. The former pathway for heavy metal capture is more effective, and thus is preferred. Several factors, such as the physical properties of the sorbent and the evolution of heavy metal size distribution in the system, play an important role in determining this pathway, and subsequently on the effectiveness and the efficiency of the sorbent. Bulk sorbent particles, typically in the micrometer or millimeter size range have been shown to be effective for capturing heavy metal species in combustion systems; however, they are hampered by several physico-chemical limitations [9-11]. Once the metallic species has chemisorbed to the outer surface, the inner volume is rendered ineffective [2, 12, 13]. Thus, a large volume of bulk sorbent is required to capture trace metals.

In an alternative approach, nano-structured sorbent agglomerate has demonstrated effectiveness in heavy metal capture with lower sorbent-to-heavy-metal ratios, than with bulk sorbents [14, 15]. Owen and Biswas (1996 a;b) [16, 17] reported the effective suppression of lead species nucleation using small quantities of sorbent materials, ratios as low as 5:1 for silica-lead reactions. Wu et al. (1998) [18] applied the in-situ generated nano-structured sorbent technique using titanium-based precursors in conjunction with ultraviolet irradiation for mercury capture. They reported a low required mercury to titania ratio of 1:150, much less than mercury to bulk activated carbon ratio of 1:50,000 [19]. Nano-structured sorbent consists of an agglomerate of nanometer-sized primary particles; thus, the agglomerate has a very high external surface area for adsorption, compared to spherical particles of the same volume. This external surface area is the key parameter governing the efficiency of the sorbent.

Nano-structured sorbent can be generated in-situ by injecting vapor-phase of the sorbent-precursors, such as tetramethyldisiloxane (TMDS) for silica (SiO_2) or titanium tetra-isopropoxide (TTIP) for titania (TiO_2) particles. At high temperatures, the precursor vapors decompose and form nanometer-sized particles. These particles grow by coagulation and sintering in the combustion system, resulting in agglomerates of nanometer-sized primary particles. Lee et al. (2005) [13] reported 99% capture efficiency of cadmium species using in-situ generated nano-structured

silica sorbent, with firm binding (less than 3% leaching of cadmium from cadmium-sorbent products). Jeong et al. (2007) [20] demonstrated simultaneous removal of cadmium and lead species using in-situ generated nano-structured silica sorbent. These advantages make nano-structured sorbent a promising technique to meet the new emission standards with less additional cost and modifications to the facility.

While the effectiveness of nano-structured sorbent for heavy metal capture has been successfully demonstrated in many laboratory-scale experiments, its application in pilot- and full-scale facilities needs to be carefully designed. To minimize the cost, it is important to minimize mass loading while achieving desirable capture efficiencies. Understanding the evolution of heavy metal compounds, the growth dynamic of sorbent particles, and their interactions will allow optimal injection strategies to be developed. Using both experimental and numerical approaches, this study establishes a mechanistic understanding of the evolution of heavy metals (lead and cadmium) and sorbent particles, as well as the interactions among them at different sorbent injection strategies in a demilitarization incineration system. The importance of the form of the sorbent and its injection location on the effectiveness and efficiency of the sorbent for heavy metal capture is highlighted, and the optimal sorbent injection strategy for such a system is proposed.

6.2 METHODOLOGY

6.2.1 Test Plan The test plan was designed as outlined in Table 6.1. In Set I, experimental measurements and numerical simulations were conducted to understand the transformation of the metallic species in a demilitarization incineration system. The particle size distributions and elemental analysis of particulate samples were measured from a slip-stream drawn from three different locations, shown in Figure 6.1A. The results of Set I provided a baseline for the sorbent injection strategy study in Set III. In Set II, experiments were conducted in a slip-stream system to compare the performance of a nano-structured sorbent and a bulk Ti-PICL sorbent, using flue gas from a full-scale incinerator. In Set III a modeling study was carried out to determine the effects of sorbent injection strategy on the properties of the sorbent, including external surface area and eventual agglomerate size, and on the interaction of the sorbent and heavy metals in the incineration system. The optimal sorbent injection strategy was established based on the results from Set III.

Table 6.1

Set	Objective	Test	Sampling Location	Sorbent Type	Sorbent Feed rate (g/m^3)	[PbO] (mg/m^3)	[CdO] (mg/m^3)
I (full-scale system)	Understanding the evolution of heavy metal compounds in the incineration system	1	Before the afterburner	-	-	4.14 ± 0.8	1.88 ± 0.2
		2	Before the baghouse				
		3	At the stack				
II (slip-stream system)	Evaluating the performance a nano-structured SiO_2 and a bulk Ti-PICL sorbent using the flue gas from the full-scale incinerator	4	After the afterburner	In-situ generated SiO_2, Bulk Ti-PICL	6 – 20	2.2 ± 0.3	1.1 ± 0.2
		5					
III (simulation in a full-scale system)	Determining the roles of sorbent injection strategy on the effectiveness and efficiency of the sorbent for heavy metal capture	8*	At the afterburner	In-situ generated SiO_2, Bulk Ti-PICL		4.14 ± 0.8	1.88 ± 0.1
		9*	After the afterburner				
		10*	Before the baghouse				

Note: * sorbent injection location

6.2.2 Experimental Method. Experiments were conducted on a 250 kg/day munitions demilitarization incinerator, APE1236, at Tooele Army Depot, Tooele, UT. The system, shown in Figure 6.1A, consisted of a rotary kiln combustor, a cyclone, an afterburner, and a ceramic baghouse. Munitions, including bullets, shell cases, primers, and powder, were introduced into a rotary kiln combustor where they were burnt or detonated. The large metal particle residues entrained in flue gas passed through a cyclone, where they were collected and recovered. The flue gas then traveled through the afterburner, combusting the organics and residues, and the ceramic baghouse, where particulate ash and heavy metals were removed from the

exhaust stream before it was emitted into the atmosphere. In this particular system, the flue gas flow rate was approximately 113.3 m^3/min, with a gas velocity of 4.2 m/s in the duct. A 2.5 lpm slip-stream was drawn from three locations: before the afterburner, at the baghouse inlet, and at the stack, as shown in Figure 6.1A. The aerosols entrained in the flue gas were measured by an electrical low pressure impactor (ELPI, Dekati Ltd.) and a real time Scanning Mobility Particle Sizer (SMPS, TSI Inc., Shoreview, MN, USA) to determine the particle size distribution ranging from 10 nm to 10 μm. The coarse and fine aerosols were separated using a cascade impactor (Mark III, Pollution Control System Corp., Seattle, WA) with a final stage 50% cut-off particle size of 1.0 μm. Both coarse and fine particles were also collected on a glass fiber filter (Whatman, EPM 2000) for lead and cadmium species analysis. The analysis was carried out using the ASTM D6357- ICP-MS standard method. The procedure includes a complete digestion of the matrix in a microwave system with strong acids (HF, HNO_3, and HCl), and analyses of the digested samples by inductively-coupled plasma mass spectroscopy (ICP-MS).

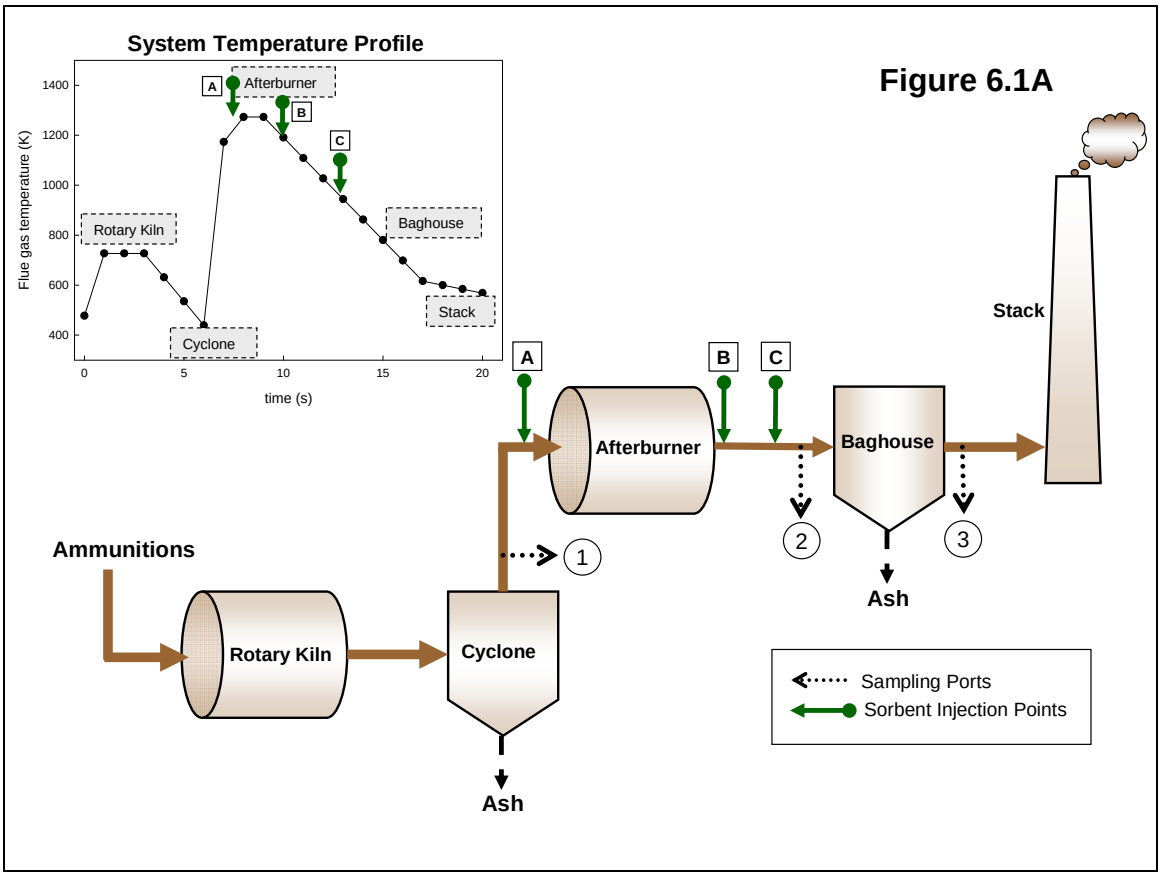

Figure 6.1A: A schematic diagram of a 250 kg/day munitions demilitarization incinerator, Tooele, Army Depot, Tooele, UT.

The experimental system for conducting sorbent capture experiments is shown in Figure 6.1B. The system consisted of a sorbent injection system, a tubular furnace (Lindberg/Blue M, Model HTF55342C, T_{max}=1200^{o}C) with a stainless steel reactor tube (2.54 cm I.D. and 90.0 cm long), and a measuring system. A 2.5 lpm slip-stream drawn from the incinerator was introduced into the furnace with a sorbent, resulting in a residence time of 2 s inside the furnace. Two types of sorbents, a vapor phase silica precursor (1,1,3,3-Tetramethyldisiloxane ($(CH_3)_2SiH)_2O$, Aldrich)-TMDS) and a solid phase titania-pillared clay (Ti-PICL) sorbent, were used. TMDS was introduced into the furnace using a bubbler with 0.1 lpm nitrogen as a carrier gas. The solid Ti-PICL powders were introduced into the furnace using a fluidized bed feeder. The furnace temperature was maintained at 1000 ^{o}C. At the exit of the furnace, particle-free air at a flow rate of 12.5 lpm was added to reduce the flue gas temperature and quench the aerosol dynamics and chemical reactions. The resultant aerosol was measured by an ELPI and a SMPS to determine the particle size distribution. The coarse and fine aerosols were separated using a six-stage cascade impactor and collected on a glass fiber filter (Whatman, EPM 2000) for leachability testing. The leachability test based on the Toxicity Characteristic Leaching Procedure (TCLP, USEPA Method 1311), was conducted to determine how strongly lead and cadmium were bonded to the sorbent. The dissolution test was performed using 0.04 milli-Q water and 0.1 M acetic acid solution as the extraction fluids. The filters were placed in 50 ml Falcon™ tubes with the respective solutions. Each sample was fixed

by an extraction vessel holder and agitated for 24 hrs at the rotating speed of 8 rpm (Agitator: Barnstead International, Model 4152110). After agitation, the samples were left for 24 hours to allow the insoluble solids to settle. Then 10.0 ml of solution was sampled, filtered with a 0.45 μm membrane filter, and analyzed by an ICP-MS for the concentrations of lead and cadmium species.

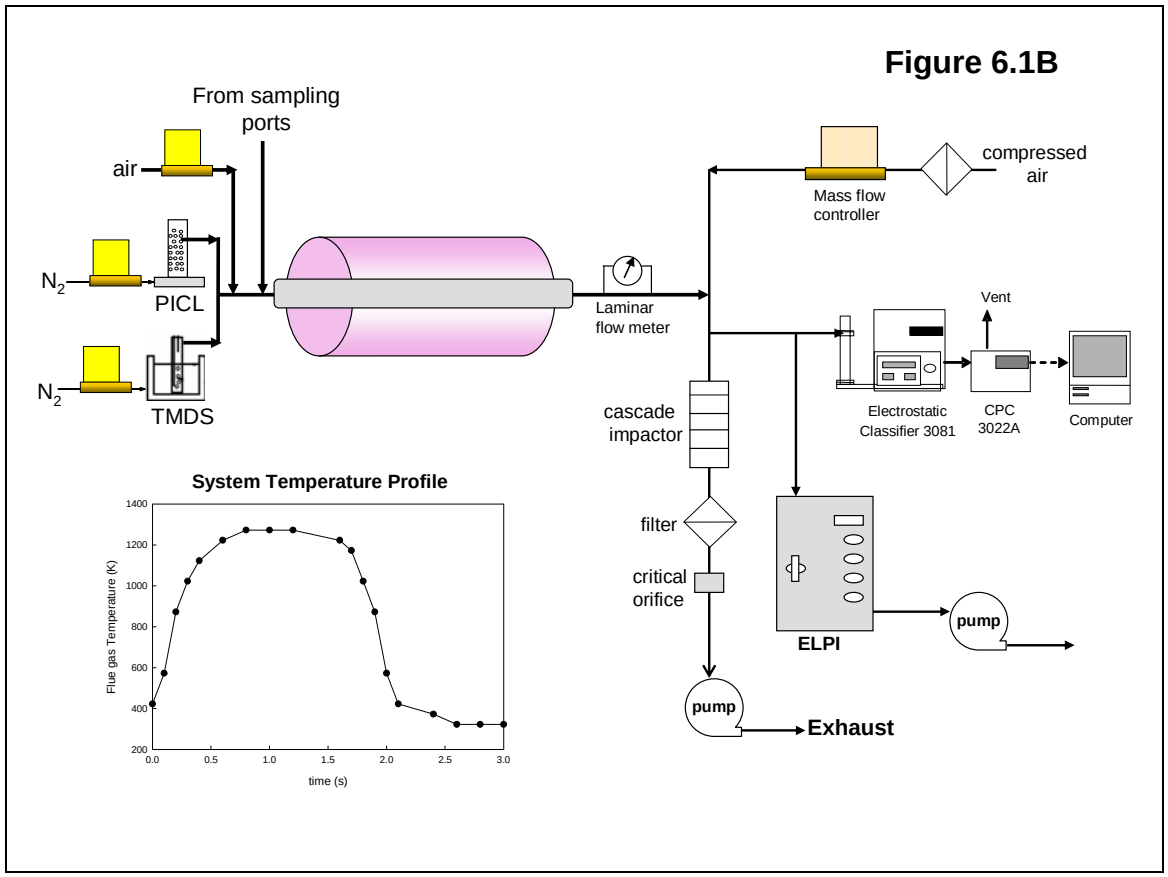

Figure 6.1B: A schematic diagram of a slip-stream study.

6.2.3 Modeling Approach.

To understand the growth dynamics of sorbent particles and its effect on the interaction between metals and sorbent particles in the system, a generalized n-modal and m-species model for evolution of multi-component aerosol dynamics, developed by Kim et al. (2009) [21], was employed. This model describes particle formation and evolution of multi-component aerosols, and also accounts for the collisional growth of aggregate-liked particle morphology and the change in surface area due to both collisions and sintering.

6.2.3.1 Model Description. Figure 6.2 shows a schematic representation of metals and sorbent interaction via a generalized n-modal and m-species model for evolution of multi-component aerosol dynamics. While the model is generalized for any number of components [21], only the three-component model, representing the interaction of sorbent, lead and cadmium species, was used in this paper. In the three-component model, there are three monomer modes, representing the vapor phases of the two individual heavy metal species and the sorbent precursor, three nucleation modes (mode 1), representing lead, cadmium and sorbent particles formed via nucleation, and one accumulation mode (mode 2), representing the products of the collisions among particles and the condensation of vapor molecules on the particles. Each mode of the model is considered to have a monodisperse size distribution from the viewpoint of particle volume, similar to a monodisperse model developed by

Kruis et al.(1993) [22], and a bi-modal model developed by Jeong and Choi (2003) [23].

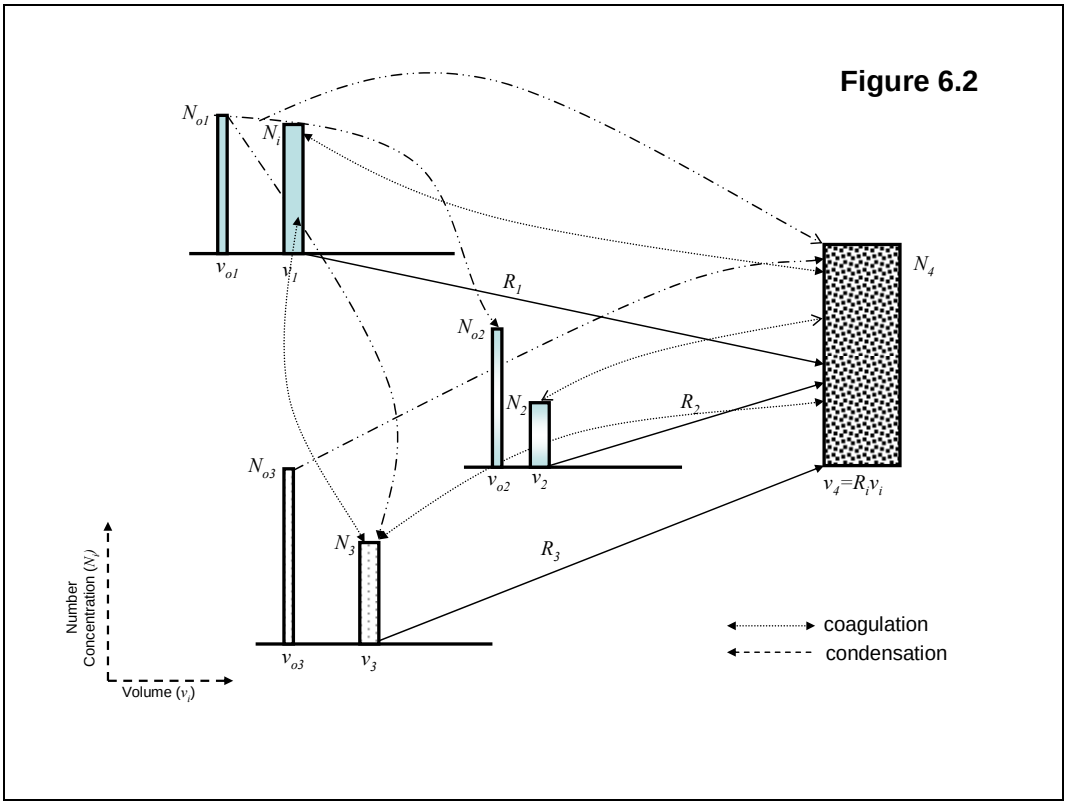

Figure 6.2: A schematic diagram of a three-component tri-modal model.

The volume of the monomer balance of heavy metal species can be obtained by

$$\frac{dN_{oi}}{dt} = I_{oi} - J_i^* \frac{\upsilon_i^*}{\upsilon_{oi}} - \sum_{j=1}^{m} K_j^{oi} N_{oi} N_j \qquad (1),$$

where I_{oi} is the vapor generation rate, J^*_i is the nucleation rate of the component, υ_i^* is the volume of the critical cluster of component I, υ_{oi} is the monomer volume of component i, N_j is the number concentration of each component in mode 1 and mode 2, and K^{oi}_i is the modified Fuchs-Sutugin condensation coefficient between the monomer and particles in mode 1 or 2 [24]. The subscript "o" denotes the monomer, "i" denotes the component, and "m" represents the number of components: two heavy metal species, sorbent, and metal-sorbent aggregate. The heavy metal species are typically vaporized completely and rapidly in the combustor; thus, the subsequent generation rate of heavy metal vapor, I_{oi}, is set to zero. The nucleation rate, J^*_i, of heavy metal species is calculated using the Becker-Doering classical nucleation theory [24]. The nano-structured sorbent is generated by the decomposition and oxidation of the vapor precursor; hence, the decomposition rate of the sorbent precursor, $k_s N_{os}$, is substituted for the nucleation rate, J^*_i, of the sorbent particles.

Considering the nucleation mode, the number concentration equation is described as

$$\frac{dN_i}{dt} = J_i^* \frac{\upsilon_i^*}{\upsilon_i} + \sum_{j=1}^{m} \frac{\upsilon_{oj}}{\upsilon_i} K_i^{oj} N_{oj} N_i - \sum_{i=1}^{m} \frac{1}{2} \beta_{i,i} N_i^2 \frac{R_i}{R_i - 1} - \sum_{j=1}^{m} \frac{1}{2} \beta_{i,j} N_i N_j \frac{\upsilon_j}{\upsilon_i (R_i - 1)}$$

$$- \beta_{i,m+1} N_i N_{m+1} \qquad (2),$$

where $R_i = \upsilon_2 / \upsilon_i$, and υ_2 is the volume of the aggregate in mode 2. On the right hand side, the first term represents the nucleation, and the second term represents the condensation of vapor on the particle component *i*. The remaining terms describe the coagulation process. The coefficients $R_i/(R_i - 1)$ and $v_j/v_i(R_i - 1)$ are introduced to apportion the volume of particles that are produced by intra-coagulation and inter-coagulation among the particles in mode 1. The apportionment depends on the volume ratio of each representative size, i.e., $v_2 = R_1 v_1$. This apportionment conserves the volume of all species in the system:

$$\frac{dV_t}{dt} = \frac{d}{dt}\left(\sum_{i=1}^{m} V_{oi} + \sum_{i=1}^{m} V_i \right) = \sum_{i=1}^{m} I_{oi} \upsilon_{oi} \ , \qquad (3).$$

For the accumulation mode (mode 2), the conservation equations for number, volume, and area concentrations are given by

$$\frac{dN_m}{dt} = \sum_{i}^{m-1} \frac{1}{2} \beta_{i,i} N_i^2 \frac{1}{R_i - 1} + \sum_{i=1}^{m-1} \sum_{j \neq i}^{m-1} \frac{1}{2} \beta_{i,j} N_i N_j \frac{\upsilon_j}{\upsilon_i (R_i - 1)} - \frac{1}{2} \beta_{m,m} N_m^2 \qquad (4),$$

$$\frac{dV_m}{dt} = \sum_{i=1}^{m-1} \frac{1}{2} \beta_{ii} N_i^2 \frac{R_i}{R_i - 1} v_{ii} + \sum_{i=1}^{m-1} \beta_{i,m} N_i N_m \upsilon_i + \sum_{i=1}^{m-1} \sum_{j \neq i}^{m-1} \frac{1}{2} \beta_{i,j} N_i N_j \frac{\upsilon_j}{R_i - 1}$$

$$+ \sum_{i}^{m-1} K_m^{oi} N_{oi} N_m \upsilon_{oi} \,, \qquad (5),$$

$$\frac{dA_m}{dt} = \sum_{i=1}^{m-1} \frac{1}{2} \beta_{ii} N_i^2 \frac{R_i}{R_i - 1} a_i + \sum_{i=1}^{m-1} \beta_{i,m} N_i N_m a_i + \sum_{i=1}^{m-1} \sum_{j \neq i}^{m-1} \frac{1}{2} \beta_{i,j} N_i N_j \frac{\upsilon_j}{(R_i - 1)\upsilon_i} a_i$$

$$+ \sum_{i}^{m-1} K_m^{oi} N_{oi} N_m a_{oi} - \frac{1}{\tau_{eff}} (A_m - N_m a_{(m)s}) \,, \qquad (6),$$

where τ_{eff} is the effective characteristic sintering time, and a_s is the surface area of completely fused (spherical) aggregate.

The collision diameter, d_c, of the aggregates in the accumulation mode (mode 2) was adopted to consider the non-sphericity of aggregate particles as defined by Kruis et al. (1993) [22]:

$$d_c = d_p (n_p)^{1/D_f} \,, \qquad (7),$$

where d_p and n_p represent the diameter and the number of primary particles in the accumulation mode, respectively. A fractal dimension, D_f , of 1.8 was used in this study. The geometric mean collision diameter, d_{gc}, is the parameter selected to compare with the experimental results. This parameter is defined as:

$$d_{gc} = \prod_{i=1}^{m} d_i^{N_i / \Sigma N} \,. \qquad (8).$$

6.2.3.2 Simulation Parameters. This study tested in-situ generated nano-structured silica (SiO_2) sorbent and titania pillared clay (Ti-PILC) bulk sorbent. The in-situ generated SiO_2 was produced by the decomposition of sorbent vapor precursor (TMDS) in high temperature flue gas, resulting in molecular-sized SiO_2 particles. Both nano-structured SiO_2 and Ti-PILC bulk sorbent with a particle size of 100 μm were modeled in this study, and their effectiveness on heavy metal removal was determined. It should be noted that the model assumes that both sorbent particles are initially spherical. This study focused primarily on the capture of lead and cadmium species because they were the primary components of the incinerated munitions [25]. The concentrations of lead and cadmium, 4.16, and 2.0 mg/m^3, respectively, used in the simulation were estimated based on the total amount of lead and cadmium in the particulate matter (reported in Table 6.3), the flue gas flow rate, and the percent enrichment of the metals in the particulate matter, which were found in the Emission Measurements Report from the facility [25]. This report indicated that more than 99.9% of the lead and greater than 95% of the cadmium were found in the particulate matter, and the major components of these metals existed in oxide forms, i.e., lead oxide (PbO) and cadmium oxide (CdO). The values of the important parameters used in the model are shown in Table 6.2. The properties of SiO_2, CdO, and PbO, tabulated in Table 6.2, are obtained from the CRC Chemistry Handbook (1999-2000) [26], unless otherwise indicated below the Table.

The temperature profile of the flue gas plays an important role in the evolution of the heavy metal species as well as the changing properties of the sorbents. The temperature profile of the munitions demilitarization incinerator, shown in Figure 6.1A, was used in the simulation. According to the layout of the system, three sorbent injection locations were selected: (1) in the afterburner, (2) after the afterburner, and (3) before the baghouse filter. Sorbent injection prior to the cyclone was impractical since the sorbent would be removed in the cyclone, resulting in the ineffective heavy metal removal. All simulations were performed until the flue gas entered the baghouse.

Table 6.2

Sorbent:

- **In-situ generated silica (SiO_2)**

$$Si_2O(CH_3)_6 \xrightarrow{instantly} 2Si_{(g)} + O_2 \xrightarrow{k_s} SiO_{2(g)}$$

  - $k_s = 4.86 \times 10^{17} \exp(-48288.67/T)$ ($cm^3\ mole^{-1}\ s^{-1}$)
  - initial diameter = 0.33 nm

- **Bulk Titania pillared clay (Ti-PICL)**
  - initial diameter = 100 μm

Heavy Metals:

	Lead oxide (PbO)	**Cadmium oxide (CdO)**
Surface tension (dyne/cm)	250.0**	470.0*
Density (kg/m^3)	10.1×10^3	8.15×10^3
Molecular volume (m^3)	3.67×10^{-29}	2.67×10^{-29}
Molecular mass (kg)	3.70×10^{-25}	2.10×10^{-25}
Saturation vapor expression (Pascal)	A = 9.502	A = 11.632
$\log_{10}P_s$= A-B/T	B = 11552	B = 12114

Note: * estimated from pure cadmium value
** Gmelin, H. (1969). *Der Anorganischen Chemie*, Verlag Chemies, GmBH, Weinheim/Bergstr., Teil C-Lieferung, 1, p.72.

Table 6.3

	Size range	Total particle mass conc. (mg/m^3)	Metal Concentration in Particulate Matter		Leaching Test (leached amount per sampling gas volume, mg/m^3)			
			Lead (% by wt)	Cadmium (% by wt)	Lead		Cadmium	
					Milli-Q Water	0.1 N acetic acid	Milli-Q water	0.1 N acetic acid
Ammunition only	< 1μm	121.5	3.09	1.44	0.015	3.60	0.010	1.74
	> 1μm	17.5	2.21	0.70	0.006	0.72	0.005	0.35
Ammunition + SiO_2 (1 g/hr)	< 1μm	1860.0	0.24	0.10	0.006	0.14	0.004	0.013
	> 1μm	100.0	0.54	0.02	0.010	0.05	0.006	0.012
Ammunition + Ti-PICL (1 g/hr)	< 1μm	2,360	0.11	0.08	0.010	2.89	0.012	1.26
	> 1μm	990.0	0.09	0.001	0.008	0.65	0.008	0.45

Note: Flue gas sampling from baghouse inlet

6.3 Results and Discussion

6.3.1. Evolution of heavy metals in the incineration system (Set I).

It has been well-established that particle formation pathways dictate the eventual particle size [3, 4, 12]. The particle size distributions were determined by sampling during detonation of munitions without any sorbent addition from three different locations: port 1, after the cyclone, port 2, at the baghouse inlet, and port 3, at the stack. The results are shown in Figure 6.3. A bimodal particle size distribution, centered at approximately 0.02-0.08 μm and 0.2-0.5 μm in diameter, was observed for flue gas from port 1, after the cyclone. This indicates that at least two particle formation mechanisms, nucleation and fragmentation, occurred in the system prior to the sampling location. In a rotary kiln, where ammunition was detonated, metallic compounds may vaporize or fragment. While large residues resulting from the fragmentation were collected and removed in the cyclone, the diminutive residues remained entrained in the flue gas along with the vaporized metallic species. As the flue gas cooled, the vaporized species nucleated or condensed onto the surface of existing particles. Because of different particle formation pathways, these diminutive residues and nucleated particles resulted in a bi-modal particle size distribution. The ultrafine particle mode (less than 100 nm in diameter) was formed via the vaporization-nucleation pathway, and the submicrometer particle mode (less than 1μm and greater than 100 nm in diameter) was formed by fragmentation.

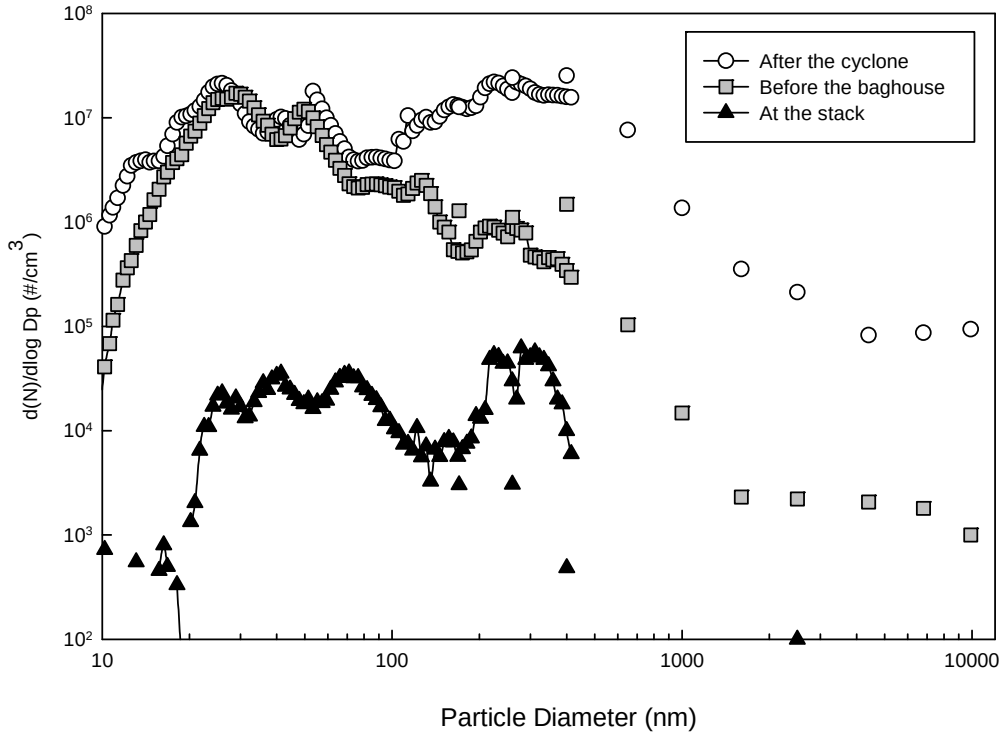

Figure 6.3: Particle size distributions generated during munitions incineration at different locations

On comparison of the size distributions sampled from port 1 and port 2, no significant differences were apparent for the ultrafine particles. However, the particles in the submicrometer mode were significantly decreased at port 2 (at the baghouse inlet). At the afterburner, the remaining residues generated by fine-fragmentation in the rotary kiln were vaporized at a temperature of approximately 1273 K. The metallic species that nucleated previously might also re-vaporize and re-nucleate, resulting in an ultrafine particle size distribution similar to that found in sampling

location 1. On comparison of the resultant size distributions from port 2 (at the baghouse inlet) and port 3 (at the stack), a significant reduction of particle numbers were observed, greater than 99% based on the total particle number concentration. Despite this high efficiency of the baghouse, considerable amounts of ultrafine- and submicrometer-sized particles still penetrated through, and were subsequently emitted into the atmosphere.

A multi component tri-modal model was adopted to understand the evolution of PbO and CdO in the system. The simulations were conducted from the afterburner, where both PbO and CdO existed in vapor forms, to the baghouse inlet. The results of the simulations, shown in Figure 6.4, are reported as a function of the total residence time in the incineration system. The predicted concentrations of lead and cadmium vapor are shown in Figure 6.4A, and the particle number concentration and the geometric mean particle size are given in Figure 6.4B. At the total system residence time of 10 s, flue gas exited the afterburner and subsequently cooled, increasing the vapor concentrations of PbO and CdO, and the saturation ratios of the metals. At a residence time of approximately 11 s, the vapor concentration of PbO sharply decreased and the particle concentration of PbO drastically increased, due to nucleation. At a residence time of approximately 12 s, the vapor concentration of CdO started decreasing; however, no CdO particles were formed at this point, and there was no spike in the total particle concentration. This result implied that the

nucleated PbO particles served as the seed for condensation of both PbO and CdO vapors. This prediction was consistent with the experimental observation by Jeong et al. (2007) [20]. The predicted geometric particle diameter of 38 nm was also in the range which had been experimentally measured.

The evolution of PbO and CdO in the system suggested a possible scheme to effectively remove the metals from the system flue gas. Because saturation ratio (S), the ratio of the metal vapor concentration to its saturation concentration, increase with decreasing temperature, nucleation and condensation are competitive mechanisms for the conversion to an aerosol phase. Nucleation occurs when the saturation ratio of the metal vapor exceeds its critical saturation ratio (S^*) for nucleation, while condensation initiates when S greater than 1. In the interim period, where the saturation ratio is in between 1 and S^*, the metal vapor is available for condensation on the existing particles. The presence of sorbent particles would allow the metallic vapor to condense out, which is an effective way of minimizing the formation of the submicrometer mode. Comparisons of characteristic times for nucleation and condensation also provide confirmation of the dominant mechanism [2, 13, 27].

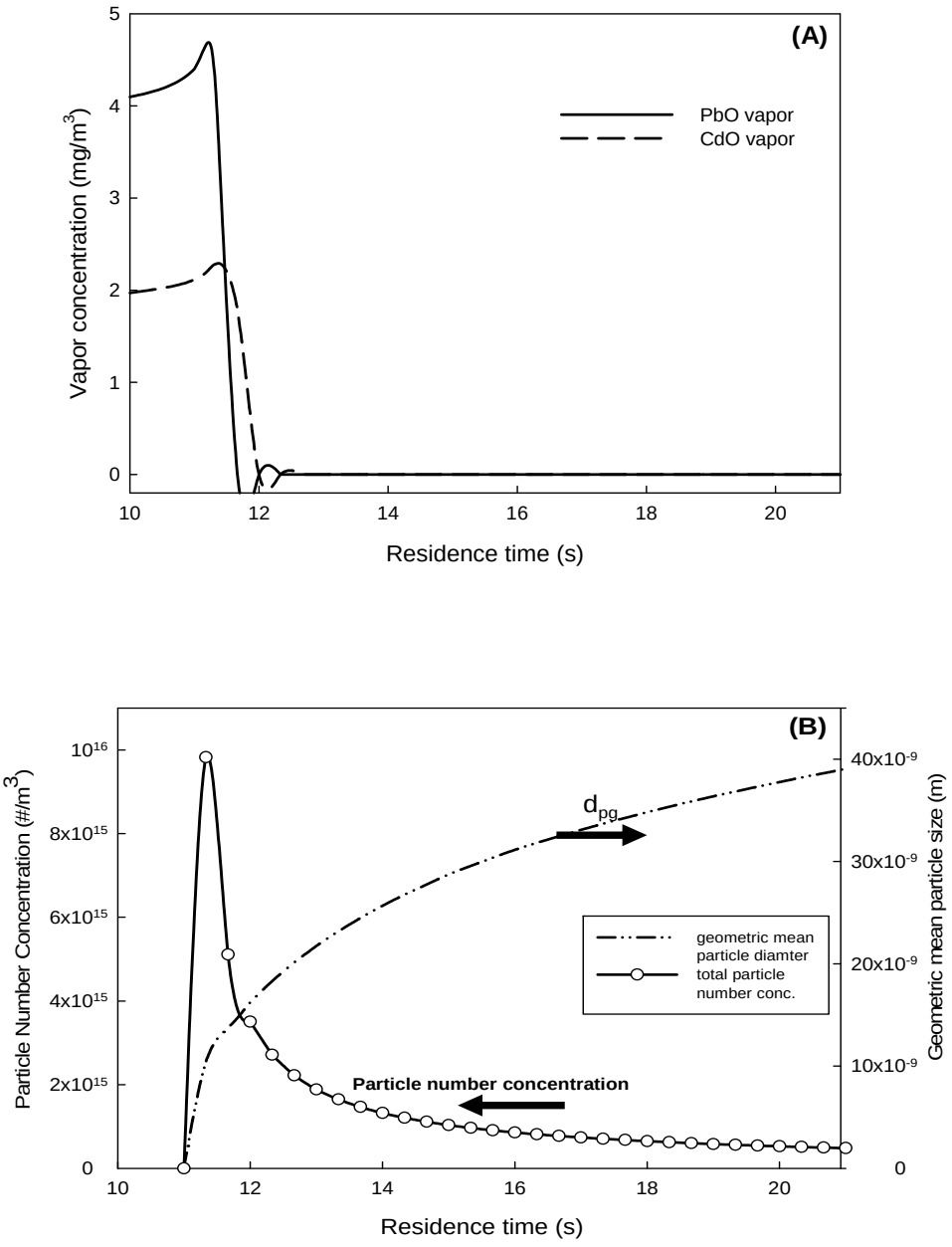

Figure 6.4: (A) The changing of lead and cadmium vapor concentrations. (B) The evolutions of the particle number concentration and the geometric mean particle diameter. Left axis is for the particle number concentration. Right axis is for the geometric mean particle size.

6.3.2. Heavy metals and sorbent interactions – a slip stream test (Set II).

The performance of two different sorbents, in-situ generated SiO_2 and bulk Ti-PICL, on capturing lead and cadmium species entrained in the incineration flue gas was evaluated using a slip-stream system. Flue gas, drawn from port 2 (baghouse inlet), was re-heated in the furnace to 1000^{o}C to mimic the condition at the afterburner and to re-vaporize the nucleated heavy metal species. Sorbents were also introduced into the furnace, where they reacted with heavy metal species. Figures 6.5A and 6.5B show the results of the in-situ generated SiO_2 and bulk Ti-PICL for heavy metal capture. When the in-situ generated SiO_2 was injected, the ultrafine particles disappeared, as shown in Figure 6.5A. At a sorbent feed rate of 1.0 g/hr, particles smaller than 20 nm vanished, and at a sorbent feed rate of 3.0 g/hr, particles smaller than 70 nm completely disappeared. Comparing the resultant size distributions of the sorbent with and without heavy metal species, little change in the particle size distributions toward the larger size was observed when heavy metals were present with the sorbent. The disappearance of ultrafine particles and the slight shift of the sorbent particle size distributions when the sorbent and heavy metals were present together indicate the condensation of the heavy metal species on the surface of the sorbent particles, and consequently the suppression of nucleation.

The effectiveness of bulk Ti-PICL on heavy metal capture was also evaluated. The particle size distribution results are shown in Figure 6.5B. The mean size of Ti-PICL particles was approximately 100 μm at room temperature; however, when the particles were exposed to high temperature, the particle mean size dropped to around 1 μm. When the sorbent was injected at feed rates of 1.0 and 2.0 g/hr, some reduction in the number of ultrafine particles was observed. The particle size distributions of the sorbent and slip-stream co-feed tests lay between the sorbent only and the slip-stream tests for both sorbent feed rates. The reduction of fine particles indicated condensation of the vaporized metal species on the sorbent; however, the existence of fine particles implied the nucleation of the remnant metal vapor. These results further suggested that the metal species were not effectively captured by bulk Ti-PICL sorbent at these feed rates.

The effectiveness of both in-situ generated SiO_2 and bulk Ti-PICL for lead and cadmium capture was also evaluated with leachability test (Table 6.3). The dissolution of Cd and Pb from the fine (<1 μm) and coarse (>1μm) fractions of the entrained particles in the incinerator flue gas without sorbent injection were determined as a baseline. The dissolution of both metals in Milli-Q water was low, which is consistent with the low solubility of CdO and PbO. The dissolution of lead and cadmium species in 0.1 N acetic acid solution is much higher than in the milli-Q water since PbO and CdO are soluble in low pH solution (CRC, 1999-2000). Similar

dissolution tests were carried out for the particles collected from the sorbent injection experiments. At the same extraction condition, the dissolution of lead and cadmium from particles collected from sorbent injection experiments was less than the baseline. The in-situ generated SiO_2 sorbent demonstrated effective immobilization of both lead and cadmium species, especially in comparison to the bulk Ti-PICL sorbent. The low leachability of metal species from in-situ generated SiO_2 can be attributed to the formation of metal-sorbent complex, such as lead silicate and cadmium silicate, which has much lower leachability than that of PbO and CdO in the acetic acid solution [21].

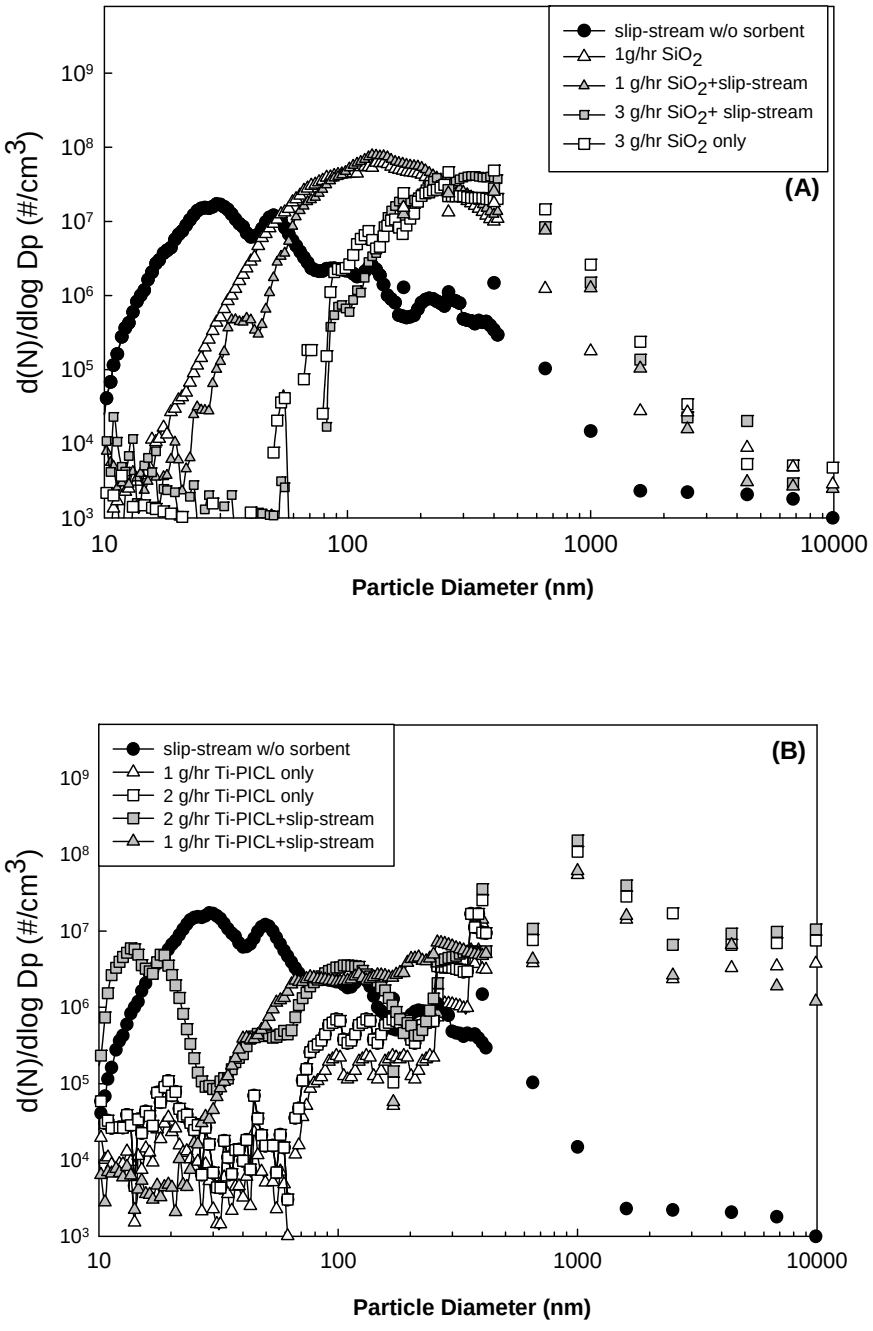

Figure 6.5: Particle size distributions from slip-stream experiments: (A) using in-situ generated SiO_2; (B) using bulk Ti-PICL

To understand the interactions among lead, cadmium, and sorbent particles, a tri-modal model was employed. The predicted concentrations of lead and cadmium vapor and the particle number concentration are reported in Figure 6.6A for in-situ generated SiO_2 and 6B for Ti-PICL. When SiO_2 vapor precursor was injected into the reactor, it decomposed instantaneously and formed SiO_2 particles. The SiO_2 particles then coagulated and formed aggregates of molecular-sized SiO_2 particles, reducing the total particle number concentration along the reactor. At a residence time of 1.6 s, the vapor concentrations of lead and cadmium in the flue gas increased as the flue gas cooled upon exiting the reactor. Because of a large surface area of the aggregates, 45 m^2/g at 1.0 g/hr sorbent feed rate, condensation of cadmium and lead vapors was promoted. The nucleation of these metals was also suppressed as the total particle number concentration flue gas did not increase. These predictions were consistent with the experimental results.

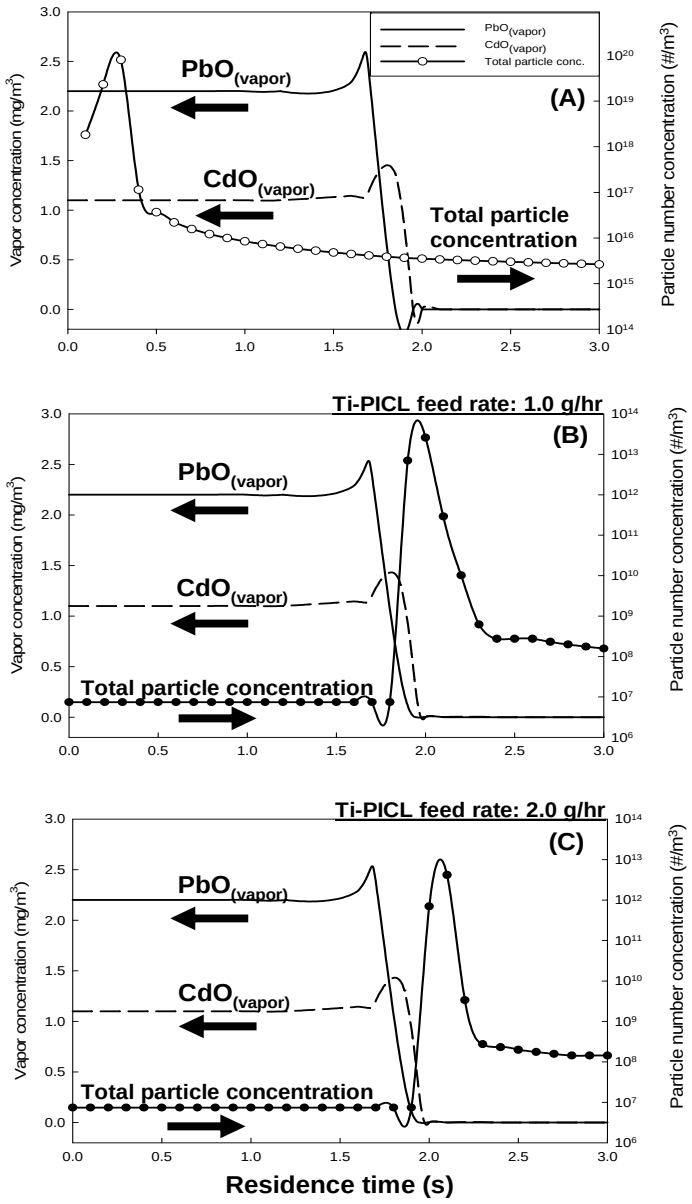

Figure 6.6: The changing of lead and cadmium vapor concentrations and total particle number concentration in a slip-stream system: (A) with 1.0 g/hr in-situ generated SiO_2; (B) with 1.0 g/hr bulk Ti-PICL; (C) with 2.0 g/hr bulk Ti-PICL. Left axis is for the vapor concentration. Right axis is for the total particle number concentration.

For the bulk Ti-PICL sorbent, results shown in Figure 6.6B and 6.6C, at both sorbent feed rates of 1.0 and 2.0 g/hr, a drastic decrease in the vapor concentrations of both CdO and PbO were demonstrated, along with a sharp increase in the total particle number concentrations in the flue gas exiting the reactor. Because of the exponential dependence of the saturation metal vapor concentrations with on flue gas temperature, the saturation ratios of the metals rapidly increased as the flue gas temperature decreased, resulting in competitive mechanisms between particle formation via nucleation and particle growth by condensation. At the sorbent feed rate of 1.0 g/hr, and a residence time of 1.7 s, the model prediction showed a spike in the total particle number concentration and a drastic decrease in the vapor concentration of PbO, indicating nucleation of PbO particles. Slightly after the nucleation of PbO, the vapor concentration of CdO also decreased; however, the total particle number did not increase. This result indicated the condensation of CdO vapor on the surfaces of the sorbent and the nucleated PbO particles. When the sorbent feed rate increased to 2.0 g/hr, the simulation results showed that the vapor concentration of PbO decreased at a residence time of 1.7 s, followed by a decline in CdO vapor concentration and a sharp increase in the total particle number concentration at a residence time of approximately 1.9 s. These results implied that the increased sorbent feed rate promoted condensation of PbO vapor; however, the total surface area for condensation was still not enough to suppress the nucleation of PbO and CdO particles. The critical saturation ratios of the metals were quickly reached as the flue

gas temperature sharply dropped after exiting the reactor. These simulation results were also consistent with the experimental results. At the sorbent feed rate of 1.0 g/hr, the ultrafine particles, centered at approximately 30-100 nm, co-existed with the bulk particles. When the sorbent feed rate was increased to 2.0 g/hr, an additional ultrafine mode particle, centered on 15 nm, was present, indicating the later nucleation of the remnant metal vapors. The results of Set II suggested the metallic compounds, PbO and CdO, were effectively captured by the in-situ generated SiO_2 for both tested sorbent feed rates. The bulk Ti-PICL sorbent did not capture the metallic compounds effectively because the sorbent did not provide enough surface area to remove vapor by condensation and subsequently suppress nucleation of the metals when the saturation ratios were sharply increased as the temperature of the flue gas dropped. These results further underline the importance of the properties of the sorbent (e.g., surface area) the characteristics of heavy metals (e.g., saturation vapor pressure), and the system parameters (e.g., temperature gradient) on the interplay between particle formation and growth mechanisms. These factors greatly affect the performance of the sorbent in heavy metal capture.

6.3.3. Heavy metal capture - effects of sorbent injection strategy (Set III).

In pilot- and full-scale facilities, several factors, such as the growth dynamics of heavy metals and sorbents and the interactions among them in

the system, play an important role in the effectiveness and the efficiency of the sorbent. To understand their effects, a tri-modal model was employed. Two sets of simulations were conducted to examine the effects of sorbent injection strategies, including the sorbent injection location and type of sorbent, on the performance of the sorbent. The first set was performed without heavy metal present. This set evaluated the effects of the sorbent injection strategy on the physical properties of the sorbent, including external surface area and eventual size. The second set was conducted to determine the required sorbent-to-metals-ratios in order to meet the new emission standard of 230 $\mu g/m^3$ for lead and cadmium. It should be noted that the emitted concentrations of lead and cadmium were determined by the combined amount of vapor-phase and nucleated metal particles of the metal. The metals associated with sorbent particles were assumed to be removed from the flue gas at the particulate control device. According to the layout of the system, three sorbent injection locations were selected: (1) in the afterburner, (2) after the afterburner, and (3) before the baghouse, as shown in Figure 6.1. Sorbent injection prior to the cyclone was impractical since the sorbent could be removed in the cyclone, resulting in ineffective heavy metal removal.

The influences of injection location on the key properties of the sorbent, including surface area per unit mass and eventual particle size are shown in Figure 6.7A. The simulations were conducted in the absence of heavy metals. For all

injection locations, the in-situ generated SiO_2 sorbent exhibited much higher external surface area per unit mass than that of bulk Ti-PICL particles. This is attributed to the primary size of the sorbent particles. In the in-situ generated process, the molecular-sized SiO_2 particles sorbent were generated via the decomposition of the sorbent vapor precursor. Thus, they offered higher external surface area per unit mass than that of micrometered-sized particles. For the in-situ generated SiO_2 particles, the surface-area-to-mass ratios instantaneously increased after the injection, then decreased due to sintering, and became constant afterwards, indicating complete decomposition of the vapor precursor for all injection locations. The Si-vapor precursor injected at location 3, exhibited the highest surface area to mass ratio, followed by injection locations 2 and 1. These differences are attributed to sintering. After rapid decomposition of the vapor precursor, the SiO_2 particles coagulated and formed aggregates of molecular-sized SiO_2 particles. Due to high temperature, the connected particles coalesced by solid-state diffusion, sintering, into more nearly spherical shapes, reducing the surface area and aggregate size. The temperature inside the injection location 1 (the afterburner) was much higher than those of injection location 2 (after the afterburner) and 3 (before the baghouse). Thus, it resulted in faster sintering rates. For bulk sorbent particles, the effects of sintering were also observed, as shown in Figure 6.7A. However, the effects were not as significant as that seen in the in-situ generated process because the required sintering time is proportional to the fourth power of the primary particle size [22]. The initial size of

the bulk Ti-PICL particles was much larger than that of the in-situ generated process, so less impact was observed.

Another important property of the sorbent is its eventual size at the particulate control device. This parameter indicates the effectiveness with which metal-sorbent particle can be captured in a particulate control device. Results of the simulations are illustrated in Figure 6.7B. The in-situ generated sorbent injected at location 3 exhibited the largest agglomerate size, approximately 3.5 μm, followed by injection locations 2 and 1. The differences are attributed to sintering, as discussed earlier. The eventual sizes of bulk sorbent particles are relatively the same as their initial size for all injection locations. From all simulation conditions, the eventual agglomerated sizes of SiO_2 sorbent ranged between 0.9 to 100 μm; hence they would be effectively captured by particulate control devices, such as baghouses and ESPs.

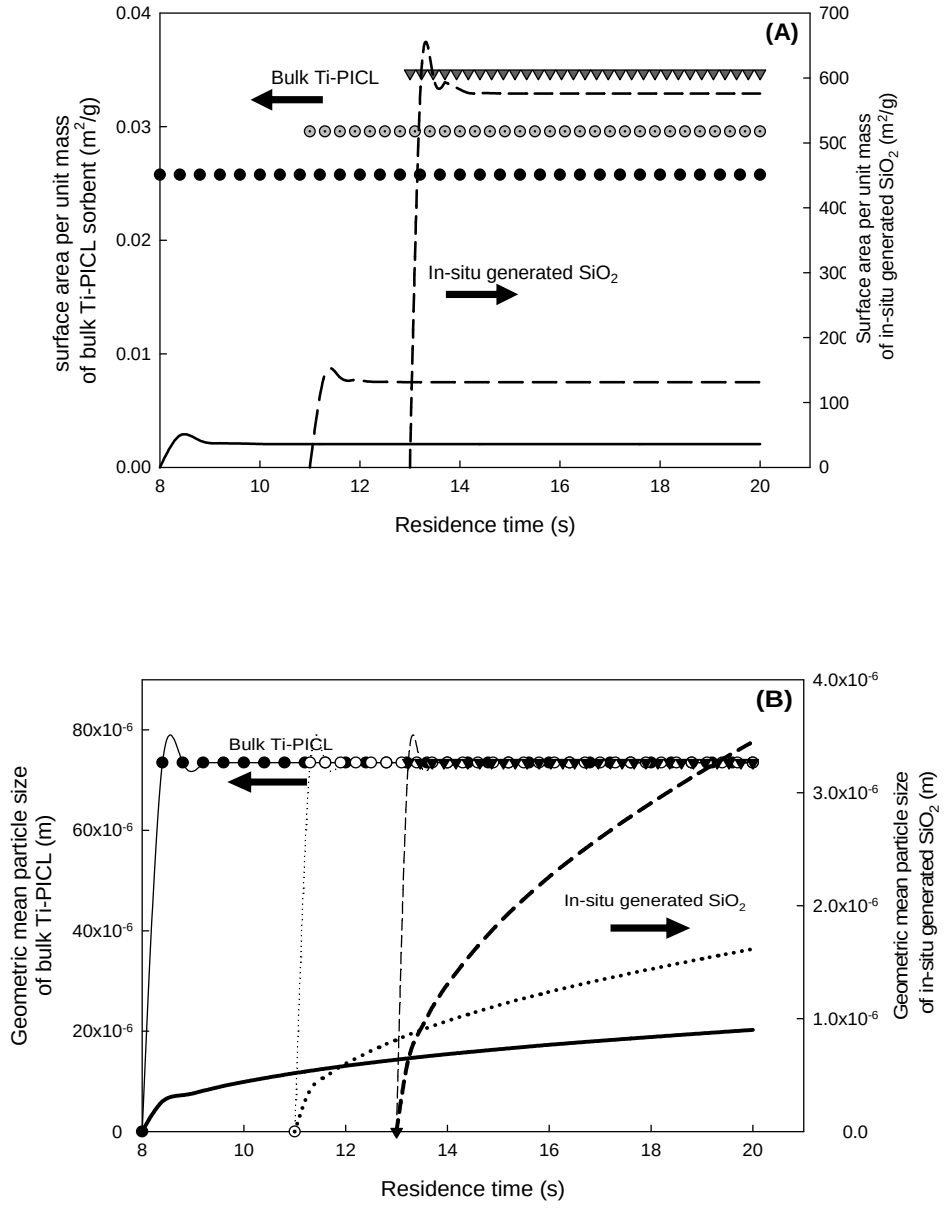

Figure 6.7: (A) The evolution of the total surface area at different sorbent injection locations. (B) The evolution of the geometric mean diameter at different sorbent injection locations. Left axis is for Ti-PICL sorbent with symbol legends. Right axis is for in-situ generated SiO_2 with line legends.

To determine the effects of sorbent injection strategy on the efficiency of the sorbent, Set II simulations were performed. The results, shown in Figure 6.8, are presented as the required mass ratio of sorbent to heavy metal to meet the emission standard of 230 $\mu g/m^3$. The in-situ generated SiO_2 was far more effective than the bulk Ti-PICL sorbent for all injection locations. These results are attributed to the key properties of the sorbent and the generation process. The in-situ generation offered higher surface area per unit mass and higher particle number concentration than the bulk sorbent. High surface area promotes condensation of metal vapors, which subsequently suppress nucleation of metal particles. High particle number concentration increases coagulation rates of sorbent-metal products in the system. For the in-situ generated sorbent, the required sorbent-to-metal ratio decreased from injection location 1 to 2 and increased at injection location 3. The decrease was attributed to a higher surface area per unit mass when the sorbent precursor injected at location 2 than that of location 1, as previously discussed. The increase in the sorbent required at injection location 3 was attributed to the mechanism for capturing heavy metal species. According to the evolutions of PbO and CdO in the system discussed in Section 3.1, PbO vapor nucleated prior to injection location 3; hence, inter-coagulation was the mechanism for removing PbO particles. Since the coagulation rate depends on particle number concentration, more sorbent was required [28, 29]. For bulk sorbent, there was no significant difference in the required amounts of sorbent between injection location 1 and 2; however, the required amount was

substantially increased at injection location 3. The former results indicated that sintering was not significant for the bulk sorbent, which is consistent with the previous findings. The substantial increase of the required sorbent at injection location 3 resulted from the inter-coagulation mechanism. At the same mass concentration, the bulk sorbent offers much lower particle number concentration, resulting in much more sorbent required.

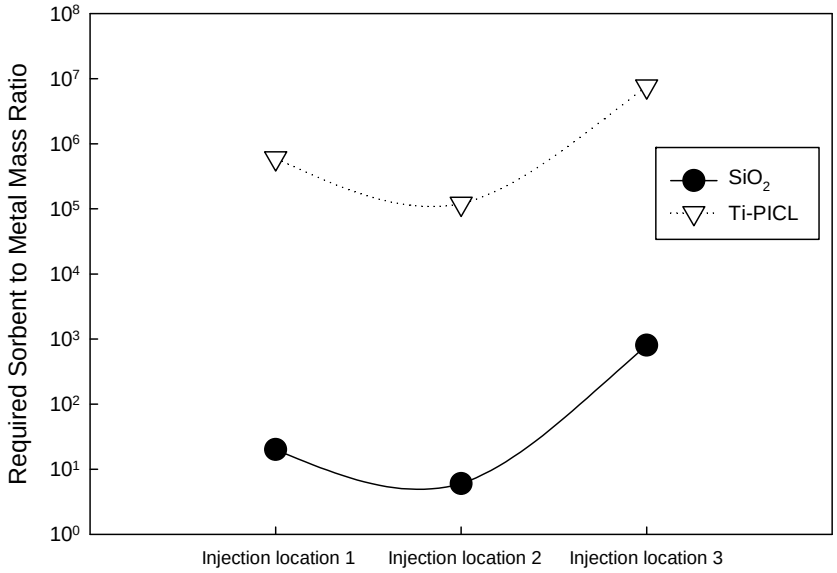

Figure 6.8: Required sorbent to metal mass ratio at different injection locations to meet the emission standard of 230 $\mu g/m^3$.

As cost is always important, an optimal sorbent injection strategy is needed. For this incineration system, the in-situ generated sorbent is more efficient, and the

sorbent precursor should be injected after the afterburner. In this location, the precursor was completely decomposed, the metallic compounds existed in the vapor-phase, and surface area reduction was not significant, allowing for dominant capture by condensation.

6.4 CONCLUSIONS

Sorbent injection is one of the promising techniques to control heavy metal emissions from combustion sources. In this study, the evolution of lead and cadmium compounds in a demilitarized incineration system was established. The performance of nano-structured SiO_2 and bulk Ti-PICL sorbent was evaluated under the incinerator flue gas using a slip-stream system. The injection strategy, including the form of sorbent injected and the injection location, on the effectiveness and efficiency of the sorbent were also demonstrated. The results from this study emphasized that understanding the evolution of heavy metal species, the growth dynamic of sorbent particles, and their interactions in the system is essential in optimizing the sorbent used. Sorbent injection should be carefully designed, so that high-surface-area agglomerates result and nucleation of heavy metals suppressed. The new emission standards can be achieved using the sorbent injection technology in conjunction with a well-designed sorbent injection strategy.

6.5 REFERENCES:

1. Federal Register (2005), Vol. 70.

2. Handbook of Chemistry and Physics, 80th ed., Cleveland, OH, 1999-2000.

3. Biswas, P., Suriyawong, A., Smallwood, M., Noel, J., Lee, M. and Giammar, D. E. (2005). "Nanostructured sorbents for heavy metals emissions control - a review" *Abstr Pap Am Chem S* **229**, U869.

4. Biswas, P. and Wu, C. Y. (1998). "Control of toxic metal emissions from combustors using sorbents: A review", *J. Air Waste Manage. Assoc.* **48**(2), 113-127.

5. Biswas, P. and Zachariah, M. R. (1997). "In-situ immobilization of lead species in combustion environments by injection of gas phase silica sorbent precursors", *Environ Sci Technol* **31**(9), 2455-2463.

6. Boddu, V. M. and Hay, K. J. (2003). "Characterization of lead and cadmium species in emissions from deactivation furnace at tooele army depot", U.S. Army Engineer Research and Development Center.

7. Chen, X., Lee, M. H., Jeong, S. K., Kim, S. B., Suriyawong, A., Higginson, K., Shah, A. and Biswas, P. (2007). "Heavy metal formation in munition waste incinerators and nano-structured sorbents for their control", *American Chemical Society*, Chicago, IL.

8. Friedlander, S. K. (2000). *Smoke, dust, and haze: Fundamentals of aerosol dynamics*, Oxford University Press, New York.

9. Friedlander, S. K., Koch, W. and Main, H. H. (1989). "Scavenging of a coagulation fine aerosol by a coarse particle mode", *Aerosol Sci. Technol.* **20**(8), 887-890.

10. Gale, T. K. and Wendt, J. O. L. (2002), "High temperature interactions between multiple-metals and kaolinite", *Combust Flame* **131**(3), 299-307.

11. Gale, T. K. and Wendt, J. O. L. (2005). "In-furnace capture of cadmium and other semi-volatile metals by sorbents", *Proceedings of the Combustion Institute* **30**, 2999-3007.

12. Granite, E. J. and Pennline, H. W. (2002). "Photochemical removal of mercury from flue gas", *Ind Eng Chem Res* **41**(22), 5470-5476.

13. Jeong, I. J. and Choi, M. (2003). "A simple bimodal model for the evolution of non-spherical particles undergoing nucleation, coagulation and coalescence", *J. Aerosol Sci.* **34**, 965-976.

14. Jeong, S. K., Kim, S. B., Kim, S. S., Chen, X. and Biswas, P. (2007). "Simultaneous removal of cd and pb from flue gases using in-situ generated nano-sized sorbents", *Ind Eng Chem Res* **13**(7), 1154-1161.

15. Kim, S. B., Jeong, S. K., Kim, S. S. and Biswas, P. (2009) "Generalized n-modal and m-species model for evolution of multi-component aerosol dynamics", *J. Aerosol Sci.*, (submitted).

16. Kruis, F. E., Kusters, K. A. and Pratsinis, S. E. (1993). "A simple model for the evolution of the characteritics of aggregate particles undergoing coagulation and sintering", *Aerosol Sci. Technol.* **19**(4), 514-526.

17. Lee, M. H., Cho, K., Shah, A. P. and Biswas, P. (2005). "Nanostructured sorbents for capture of cadmium species in combustion environments", *Environ Sci Technol.* **39**(21), 8481-8489.

18. Lee, S. R. and Wu, C. Y. (2005). "Size distribution evolution of fine aerosols due to intercoagulation with coarse aerosols", *Aerosol Sci. Technol.* **39**, 358-370.

19. Linak, W. P. and Wendt, J. O. L. (1993). "Toxic metal emissions from incineration - mechanisms and control", *Prog Energ Combust* **19**(2), 145-185.

20. Linak, W. P. and Wendt, J. O. L. (1994). "Trace-metal transformation mechanisms during coal combustion", *Fuel Process. Technol.* **39**(1-3), 173-198.

21. Owens, T. M. and Biswas, P. (1996). "Reactions between vapor phase lead compounds and in situ generated silica particles at various lead-silicon feed ratios: Applications to toxic metal capture in combustors", *J. Air Waste Manage. Assoc.* **46**(6), 530-538.

22. Owens, T. M. and Biswas, P. (1996). "Vapor phase sorbent precursors for toxic metal emissions control from combustors", *Ind Eng Chem Res.* **35**(3), 792-798.

23. Suriyawong, A., Gamble, M., Lee, M.-H., Axelbaum, R. L. and Biswas, P. (2006) "Submicrometer particle formation and mercury speciation under O2-CO2 coal combustion with carbon dioxide recycle", *Energ Fuel.* **20**(6), 2357-2363.

24. Suriyawong, A., Hogan, C. J., Jiang, J. K. and Biswas, P. (2008). "Charged fraction and electrostatic collection of ultrafine and submicrometer particles formed during O2-CO2 coal combustion", *Fuel* **87**(6), 673-682.

25. Uberoi, M., Punjak, W. A. and Shadman, F. (1990). "The kinetics and mechanism of alkali removal from flue-gases by solid sorbents", *Prog Energ Combust* **16**(4), 205-211.

26. Uberoi, M. and Shadman, F. (1990). "Sorbents for removal of lead compounds from hot flue-gases", *American Institute of Chemical Engineers Journal* **36**(2), 307-309.

27. Wu, C. Y., Lee, T. G., Tyree, G., Arar, E. and Biswas, P. (1998) "Capture of mercury in combustion systems by in situ-generated titania particles with uv irradiation", *Environ. Eng. Sci.* **15**(2), 137-148.

28. Yao, H., Mkilaha, I. S. N. and Naruse, I. (2004). "Screening of sorbents and capture of lead and cadmium compouds during sewage sludge combustion", *Fuel* **83**(7-8), 1001-1007.

29. Zhuang, Y. and Biswas, P. (2001) "Submicrometer particle formation and control in a bench-scale pulverized coal combustor", *Energ Fuel*. **15**(3), 510-516.

Chapter 7

Conclusions and Suggestions for Future Work

This chapter presents a summary of major findings from the study and outlines some suggestions for future work. The significant contributions of this dissertation have also been summarized.

7.1 CONCLUSIONS AND SUGGESTIONS FOR FUTURE WORK

Coal is the dominant energy source now and in the near future. The use of coal has posed world wide environmental challenges, including the emissions of submicrometer particles, mercury, trace elements and CO_2. These challenges have called for not only extensive research in expanding a fundamental understanding of the formation and characteristics of the pollutants, but also in developing control technologies to minimize emissions. Oxy-coal combustion with CO_2 recycled is one of the promising technologies to enable capture of CO_2. Before this system can be employed, the effects of this combustion system on the emissions of pollutants into the environment need to be investigated. This dissertation explored two aspects of coal combustion process: (1) pollutant formation, specifically submicrometer particles and mercury, and (2) pollutant control. The findings presented here are broadly divided into three parts. The first part reported the influence of oxy-coal combustion on submicrometer particle formation and capture using an ESP. The second part addressed the impacts of oxy-coal combustion on mercury speciation. In

the third part, the performance of nano-structured sorbent for controlling heavy metal emissions from combustion process was demonstrated.

The major conclusions are summarized as follows:

- In Chapter 2, the effects of oxy-coal combustion on the formation characteristics of submicrometer particles were investigated. The results showed that submicrometer particles formed under oxy-coal combustion are not only smaller in average particle size, but also lower in particle number concentration, compared to conventional (air) coal combustion systems. The differences are attributed to the property and the presence in higher concentration of CO_2. CO_2 has a higher heat capacity than N_2, especially at the elevated temperature (C_P at 1200 ºC: N_2 = 20.78 kJ/kmol-ºC, and CO_2 = 58.84 kJ/kmol-ºC). The higher specific heat capacity of CO_2 leads to lowering the surface temperature of the burning coal particles by approximately 400-500 ºC and increasing the ignition time of coal and char particles. In addition, the mass diffusivity of O_2 in CO_2 is lower than that of O_2 in N_2 ($D_{O2/CO2}$ = 1.3 x 10^{-4} m^2/s and $D_{O2/N2}$ = 1.7 x 10^{-4} m^2/s). The coal burning process is a diffusion limited process; oxygen diffuses from the bulk gas to the surface of the burning particles. A lower diffusivity of O_2 in CO_2 (compared to O_2 in N_2) slows down the particle burning and heat generation rates. The shape of primary particles formed under both conventional and oxy-coal combustions confirmed that vaporization and nucleation mechanisms are the formation pathway of submicrometer particles. These

results further indicate that the change in combustion condition from air to oxy-coal does not alter particle formation mechanisms, but only the rates.

This study took a holistic approach to develop an understanding of the effects of oxy-coal combustion on the formation and characteristics of submicrometer particles. The results shown in this study represent the condition at which CO_2 was recycled from the exhaust stream, where flue gas was already treated by pollution control devices. In practice, CO_2 can be recycled from any location, at which some pollutants may not be removed. For example, if the CO_2 recycled stream contains suspended particles; they may act as seeds that provide surface area for condensation of volatile species, and subsequently, alter particle formation pathways and characteristics of the submicrometer-sized particles. Future studies should investigate the influence of recycling location, i.e., before and after particulate control device, on the formation pathways and characteristics of submicrometer particles. Understanding this effect will allow appropriate operational and design strategies to be selected to minimize emissions.

- In Chapter 3, the effects of oxy-coal combustion on the particle penetration through the ESP were investigated. Experimental results revealed that particles generated from coal combustion carried charge; however, the fraction of the charged particles was insufficient for high particle collection efficiency in the ESP. Thus,

additional particle charging via corona generation is needed. In positive coronas, particle penetration through the ESP in O_2–CO_2 environments was 1–2 orders of magnitude higher than in O_2–N_2 environments at the same current level. Numerical simulations showed that the positive ion concentration generated in O_2-CO_2 systems is much lower than in O_2-N_2 systems, resulting in decreasing the amount of charged particles and greatly increasing particle penetration through ESPs. In addition, with a positive applied potential, the corona inception voltage and the voltage required to reach a given current level in the ESP for gas mixtures composed of O_2 and CO_2 were higher than those composed of O_2 and N_2, while similar voltages were needed for negative corona generation. Thus, little difference in particle penetration between O_2–N_2 and O_2–CO_2 was observed in negative coronas.

The results of the study demonstrated clear implications on the effects oxy-coal combustion will have on the operation of ESPs. Power plants operating ESPs with positive applied voltages will need to increase the applied voltage in order to obtain the same current level as the ESPs operated under conventional coal combustion system, and therefore increasing power consumption. The increase in power consumption can be estimated from the ratio of voltage applied in the oxy-coal combustion system to the voltage applied in air in order to obtain the same current level. For example, a 15% increase in power would be needed to operate a positive corona at 10μA in 80% CO_2- 20%O_2 as compared to air. Furthermore, in order to

achieve the same collection efficiency as the ESP operated in a conventional coal combustion system, oxy-coal power plants need to enhance particle charging inside ESPs. This can be obtained by a number of ways, including increasing ion concentration generated inside ESPs via increasing the electrode-to-electrode current, or enhancing ionization of the gas molecules. For power plants operating ESPs with negative applied voltage, the effects of oxy-coal combustion on the performance of electrostatic precipitators are minimized.

Future studies should be expanded on developing techniques to enhance the performance of electrostatic precipitators when it is operated in oxy-coal combustion system. The studies can be aimed at improving ionization of gas molecules with minimal energy input, and increasing particle charging efficiency, especially in the submicrometer- and nanometer-sized range.

- Chapter 4 explored the impact of oxy-coal combustion on homogeneous mercury oxidation. The gas mixtures examined were chosen to mimic gas mixtures that one might find in oxy-coal and conventional (coal-air) combustions. Pure CO_2, pure N_2 and air were also studied for comparison. The experiments were systematically designed to identify the influence of each constituent and its concentration. Our experimental results demonstrated that CO_2 assisted Hg-oxidation by HCl; however, its influence was outweighed by the presence of O_2. N_2 alone did

not participate in the oxidation of Hg. The presence of NO and H_2O inhibited Hg-oxidation for all carrier gases investigated in this study. The inhibitory effects depended strongly on the concentration of NO, but not on moisture content. For all carrier gases, synergistic inhibitory effects were demonstrated when NO and H_2O were present together. These results were attributed to the impact of flue gas constituents on the pool of Cl that is available to react with Hg^0. Our experimental findings suggested that in oxy-coal combustion, while Hg-oxidation would not be critically affected by highly concentrated CO_2 in the flue gas, it would be impacted by other flue gas constituents, such as NO and H_2O, and their concentrations, which are influenced by oxy-coal combustion.

The results of this study hold direct implications to the current development of mercury control methodology. Understanding on the impacts of oxy-coal combustion on mercury speciation will help facilitate the application of the technology. Since this is the first time the effects of oxy-coal combustion on mercury speciation are investigated, it is imperative to evaluate the primary impacts of high concentration of CO_2 as carrier gas. Future studies should be conducted using CO_2 recycled stream, as several other oxidizing species may further influence mercury oxidation.

- In Chapter 5, the performance of a non-carbonaceous, titanium dioxide (TiO_2) sorbent with UV irradiation, was evaluated in a lab-scale coal combustor, and

a slip-stream drawn from a pilot-scale coal combustor. TiO_2 with UV irradiation demonstrated greater than 90% capture of Hg in both lab-scale and slip-stream systems. Under UV irradiation, radicals were generated on the surface of titania particles. When mercury adsorbed on the surface, it was oxidized and formed mercury-oxide-titania-complexes. The sorbent generation and injection location played an important role on the physical and chemical properties of the sorbent, and subsequently its performance. Pure crystalline anatase phase TiO_2, generated via pre-synthesized technique, was found to be more effective than a mixture of anatase and rutile crystalline structure. The in-situ generated process was found to be more efficient than the traditional bulk sorbents as the agglomerated nanosized primary particles formed in such a process provided better exposure to UV radiation and offered higher surface area for contact with mercury. The results of high, greater than 90%, mercury removal, from a slip-stream drawn from a pilot-scale coal combustion system indicated that titania particles with UV radiation is one of the promising sorbent for mercury capture. Designing and scaling-up this process, specifically sorbent injection and distribution of UV light, for pilot- and full-scale systems are the areas that need be further explored.

- In Chapter 6, the importance of sorbent injection strategies, including the form of the sorbent and its injection location for metal capture and removal is investigated. A multi-component tri-modal aerosol dynamic model was employed to

understand the evolution of heavy metals and sorbents, as well as their interactions in the incineration system. Experiments were conducted to assess the performance of in-situ generated SiO_2, compared with bulk Ti-PICL sorbent, in capturing lead and cadmium from a demilitarization incineration system. The influence of sorbent injection strategy, including the forms, injection location and rate on the effectiveness of the sorbent were found significant. Nano-structured sorbents were found to be better than the traditional bulk particles, as the agglomerated nanosized primary particles offered a higher surface area for adsorption of heavy metal. Significant decrease in surface area of nano-structured sorbent due to sintering effect was observed when the sorbent was injected into the high temperature environment, i.e., directly into the combustor. However, if the sorbent is injected into flue gas at lower temperature, the vapor precursor of the sorbent may not completely decompose to form larger agglomerates. In addition, heavy metal vapor may have already nucleated; thus, the pathway for capture is altered from condensation of the vapor onto the surface of the sorbent to intercoagulation of heavy metal particles and sorbent particles, which is not as effective as the former.

The study underlines the important role of sorbent injection strategy on the physical properties and the efficiency of the sorbent. However, the effectiveness of the sorbent for heavy metal capture depends on the chemical binding between sorbent and heavy metals. The system parameters, such as time-temperature history of flue

gas may play an important role on the reactivity of the sorbent. Future work can be aimed at incorporating the chemical reactions between sorbent and heavy metal into the model and develop a strategic approach for optimal used of the sorbent. Furthermore, many combustion systems, such as coal combustion, contain multiple heavy metal species, resulting in much more complicated interactions between heavy metal species and sorbent. Future study can also be expanded to understand and assess the interaction among sorbent and multiple heavy metal species.

7.2 SIGNIFICANT CONTRIBUTIONS OF THIS DISSERTATION

The significant contributions of this dissertation can be summarized as follows:

1. The effects of oxy-coal combustion on the formation and characteristics of submicrometer particles, including particle size distribution and charged fraction, are reported (Chapter 2 and 3).

2. The impacts of carrier gas, especially the gas mixtures primarily composed of CO_2 and O_2, on the performance of electrostatic precipitators with regards to ion generation and particle collection have been demonstrated for the first time (Chapter 3).

3. The influences of oxy-coal combustion on the extent of mercury oxidation by HCl have been reported for the first time (Chapter 4).

4. A computational approach to establish sorbent injection strategy for maximizing heavy metal capture has been demonstrated (Chapter 6).

5. A holistic approach for recovering energy from industrial by-products, i.e., recovered paint solids from automobile operation, by co-combustion of coal and a solution of a waste disposal problem has been proposed for the first time. Their potential impacts to the environment were also evaluated (Appendix I).

Appendix I

Energy Recycling by Co-combustion of Coal and Recovered Paint Solids from Automobile Paint Operations

* This work was published in the *Journal of Air and Waste Management Association*, 59(5), 560-567, 2009.

ABSTRACT

During the past decade, there has been substantial interest in recovering energy from many unwanted by-products from industries and municipalities. Co-combustion of these products with coal seems to be the most cost-effective approach. The combustion process typically results in emissions of pollutants, especially fine particles and trace elements. This paper presents the results of an experimental study of particulate emission and the fate of thirteen trace elements (As, Ba, Cd, Cr, Cu, Co, Mn, Mo, Ni, Pb, Hg, V, and Zn) during combustion tests of recovered paint solids (RPS) and coal. The emissions from combustions of coal or RPS alone were compared with those of co-combustion of RPS with subbituminous coal. The distribution/partitioning of these toxic elements between a coarse mode ash (particle diameter larger than 0.5 μm), a submicrometer mode ash (particle diameter smaller than 0.5 μm), and flue gases was also evaluated. Submicrometer particles generated by combustion of RPS alone were lower in concentration and smaller in size than that from combustion of coal. However, co-combustion of RPS and coal increased the formation of submicrometer-sized particles, due to the higher reducing environment in the vicinity of burning particles and the higher volatile chlorine species. Mercury was completely volatilized in all cases; however the fraction in the oxidized state increased on co-combustion. Most trace elements, except zinc, were retained in ash during combustion of RPS alone. Molybdenum was mostly retained in all samples.

The behavior of elements, except manganese and molybdenum, varied depending on the fuel samples. Arsenic, barium, chromium, cobalt, copper, and lead were vaporized to a greater extent from co-combustion of RPS and coal than from combustion of either fuel. Evidence of the enrichment of certain toxic elements in submicrometer particles has also been observed for As, Cd, Cr, Cu, and Ni during co-combustion.

IMPLICATIONS

Combustion or co-combustion with fossil fuels of municipal or industrial by-products is one of the promising techniques for recovering energy from unwanted by-products, and a solution for a waste disposal problem. This technique should take a holistic approach for energy recovery; however, other potential impacts need to be evaluated. Understanding the pathway of formation and fate of pollutants will enable appropriate operational and design strategies to be selected to minimize adverse impacts, and promote adaptation of such co-combustion and energy recovery techniques. The results presented in this paper have implications for policymakers and researchers evaluating techniques for recovering energy via combustion and controlling emissions of fine particles and trace elements.

INTRODUCTION

Energy is an issue of great importance in the current times. This concern has not only called for extensive research and development in renewable energy and energy efficient technologies, but also increased interest in recovering energy from many unwanted by-products from municipal and industrial sources to reduce consumption of fossil fuels[1-5]. Recovered Paint Solids (RPS) from automobile paint operations are one such industrial by-product that has high energy content (~24.9 MJ/kg) and is currently disposed into a landfill. Paint solids are generated from overspray liquid paint and clear coating during the spraying process of an automobile paint operation. The overspray paint and overspray clear coating are collected in a water solution, which contains a de-foamer and a de-tackifier for charge neutralization of the overspray. The content is then solidified via flocculation, skimming, and dewatering processes. For a standard size vehicle, approximately 2.5 kg of paint solids are recovered. RPS are composed mainly of solid residues from resins, polymers, and water. This type of residue has considerable heating value, rendering attractive their use as a fuel. In North America, approximately 22 million vehicles are assembled each year, resulting in the disposal of nearly 35,000 tons of RPS into landfills. For landfill disposal, RPS is generally dried; thus, a heated sludge drier is typically used. This drying process and landfill disposal are the major costs associated with recovered paint solids in automobile paint operations.

Coal, the cheapest and most abundant fossil fuel, is currently one of the most widely used energy sources globally. Coal accounts for approximately 60% of electrical energy generation in the US, and will continue to be dominant for many decades. The use of coal can be promoted by co-combustion with biomass and/or wastes[6-11]. Co-combustion provides several benefits, including the generation of electricity from a potentially renewable source, the reduction of greenhouse gas emissions, a decrease in the cost of waste treatment, and a solution to waste disposal problems. Hence, the utilization of biomass and/or waste with coal in power plants seems to be the most cost-effective approach for recovering energy from unwanted by-products, such as RPS. In addition, RPS may also contain ingredients that act as effective sorbents for toxic species capture. For example, titanium dioxide content could be engineered for mercury capture in coal combustion systems[12, 13].

Utilization of coal in combustion process has been reported to result in releases of fine particles and toxic elements in several ways[14-16]. Suriyawong et al[17] reviewed particle formation mechanisms during coal combustion and showed possible routes along which trace metals are partitioned into vapor, submircon, and supermicron particles. The more volatile elements, such as Hg, Pb, and Cd, may be emitted in the gas phase or enriched in the fine (submicrometer) particulate fraction and, hence, escape capture by electrostatic precipitators (ESPs), fabric filters (FFs), or other air-pollution control devices (APCDs). Alternatively, trace elements may reside

in the fly ash collected by gas-cleaning devices or in the bottom ashes or slags. Their ultimate fate in the latter case will depend upon the utilization and/or disposal options chosen for the ash or slag. Several factors play an important role in the fate of heavy metals during combustion. The composition and quantity of halogen species, mainly the chlorine content, dictates the degree of volatilization, due to the formation of volatile chlorinated species. This factor influences the partitioning of heavy metals and the degree of heavy metal enrichment in submicrometer particles. The temperature of combustion is also one of the key parameters, because volatilization is greatly enhanced at temperatures above 750/850 ^{o}C for certain metals, depending on the presence of sulfur and the stability of sulphate metals species that might be formed [9-11, 16, 18-23]. Combustion mechanisms are also influenced by the carbon characteristics of fuels, i.e., its presence as fixed carbon or as volatile matter, and by the content and nature of the inorganic matter that contributes to the formation of ashes. In this context, the fate of heavy metals may be influenced by the nature of the fuels, and thus by the co-combustion process.

This study was performed to evaluate fine particle formation and to examine the behavior of thirteen trace elements, including arsenic, barium, cadmium, chromium, cobalt, copper, lead, mercury, manganese, molybdenum, nickel, vanadium and zinc during the co-combustion of coal and RPS. The results were compared to those of each fuel combusted alone. These elements were chosen based

on their perceived toxicity, volatility, and abundance in the fuel samples. The results presented here can be used to assess the feasibility of co-combustion of biomass and/or waste and coal for energy recovery and for a solution to waste disposal problems.

EXPERIMENTAL

The experimental setup is shown in Figure 1 and consists of two solid feeding systems, a tubular furnace (Lindberg/Blue M, Model HTF55342C, T_{max}=1200ºC, Thermoelectron Corporation, USA) with an alumina reactor tube (5.72 cm inside diameter and 121.92 cm long), a cascade impactor, and measuring systems. Both RPS and coal were ground to approximately 50-80 μm in diameter before combustion. This size distribution is comparable to the pulverized coal-fired utility industry standard of 70-80% -200 mesh. Particle-free air at flow rates of 2.0 and 4.0 lpm was introduced into fluidized bed solid feeders to carry coal and RPS particles into the electrically heated alumina tubular reactor. The furnace temperature was set at 1200 ºC. These air-feed rates yielded coal and RPS solid feed rates of 1.2 and 0.4 g/hr, respectively. The total air flow rate of 6.0 lpm was maintained for all experiments conducted. For single feed combustion experiments, the same flow rate of air was by-passed from a solid feeder and fed into the combustor to maintain the same residence time of 36.5 s for all experiments. At the exit of the combustor, particle-

free air, at a flow rate of 8.0 lpm at 25^{o}C, was added to quench the aerosol dynamics and chemical reactions. All measurements refer to the conditions at the exit of the combustor. A six-stage cascade impactor (Mark III, Pollution Control System Corp., Seattle, WA) with a final stage 50% cut-off particle size of 0.5 μm, was used to separate the coarse ash (dp > 0.5 μm) and fine ash (dp < 0.5 μm). Temperature at the wall of the impactor was relatively constant at 40^{o}C during the run, indicating that heat transfer had reached steady state. A slip stream of 0.3 lpm was drawn downstream of the impactor and introduced into a real time Scanning Mobility Particle Sizer (SMPS, TSI Inc., Shoreview, MN, USA) to determine the particle size distribution ranging from 12 to 500 nm. Both coarse ash and fine ash were measured and also collected on Teflon filters over a 24 hour duration for chemical analysis. The analysis was carried out using the standard method of ASTM D6357- ICP-MS. The procedure includes a complete digestion of the matrix in a microwave system with strong acids (HF, HNO_3, and HCl), and analysis of the digested samples by inductively-coupled plasma mass spectroscopy (ICP-MS). These analyses were conducted by Standard Laboratories, INC., Freeburg, IL.

Gaseous mercury emission was also measured downstream of the impactor. A 1.0 lpm flow of combustion gas was passed through a mercury sampling train. A total of 90 liters of gas was sampled over a 90 minute duration. The sampling train and technique used for gaseous mercury measurement were based on the method

developed by Hedrick et al.[24]. The sampling train consists of 15 ml of each of the following five impinger solutions: two impingers of 1.0 M tris-buffer and EDTA for capture of oxidized mercury, one impinger of 10% hydrogen peroxide and 2% nitric acid by volume for oxidizing and capturing elemental mercury, and two impingers of 0.05 M potassium iodide and 2% hydrochloric acid by volume for capture of elemental mercury. The impinger solutions were analyzed by an ICP-MS.

Three types of combustion tests were performed. The combustion of coal alone was a baseline for comparison of results obtained during the co-combustion and combustion of RPS alone. All experiments were repeated at least three times to obtain statistical results.

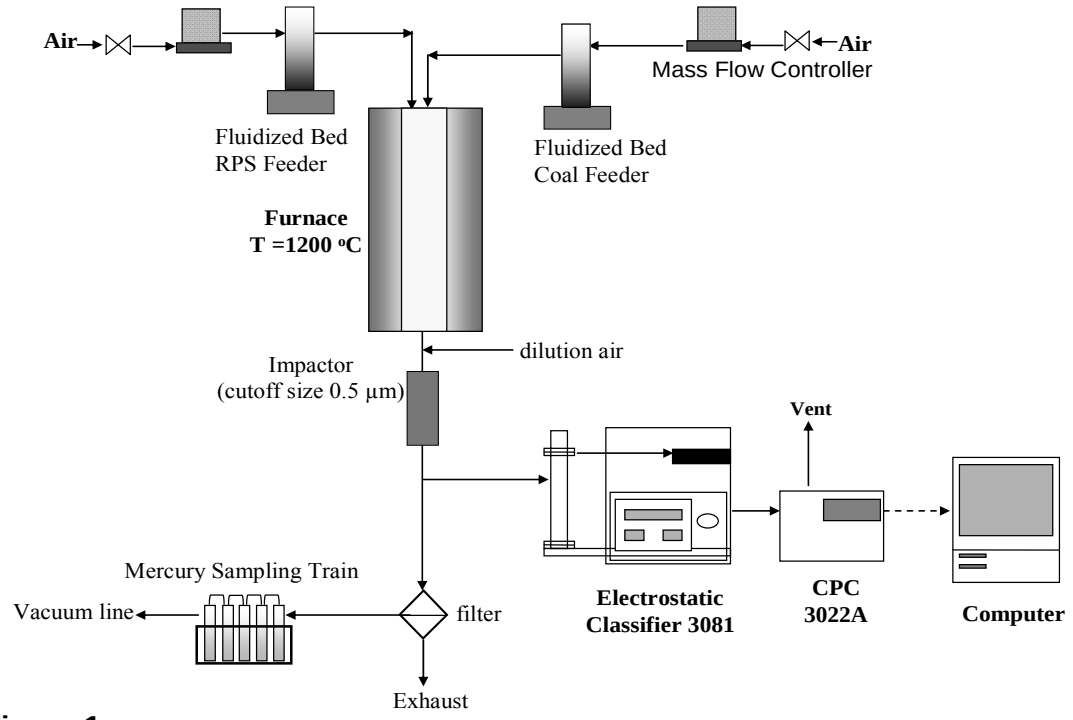

Figure 1

Figure 1. A schematic diagram of the experimental setup

RESULTS AND DISCUSSION

Fuel Characteristics

The RPS used in this study was taken from the Chrysler St. Louis North Assembly Plant, Fenton, MO. RPS is primarily an assemblage of water based paint overspray, clear coating overspray, and water based purge solvent. Paint solids are separated from paint booth water via a standard procedure of flocculating, skimming, and de-watering. The RPS used in this study was de-watered via a dewatering container, which results in approximately 50% moisture content. After being left in an ambient environment for three days, the RPS became dry granular material, dark-brown, and approximately 2-5 mm in diameter. The main characteristics of RPS are its high volatile matter (76.5% as dry basis), moisture (46.3%), and ash (20.1%) contents. The proximate and ultimate analyses of RPS compared with the coal used in this study are shown in Table 1. It is also important to note that there is a considerable amount of chlorine in RPS, which can affect partitioning of toxic elements during combustion.

Powder River Basin subituminous coal (PRB) used in this study was supplied by AmerenUE, St. Louis, MO. This coal came from Wyodak-Anderson seam, North Antelope/Rochelle mine, Gillette, WY. This mine supplied approximately 91.5

million tons of compliance coal to 60 power plants throughout the United States in 2007. The proximate and ultimate analyses of PRB coal are also presented in Table 1. This type of coal has low sulfur and chlorine contents. The sulfur in this coal is more than three times that of RPS, while the chlorine in this coal is substantially less than that in RPS. Table 2 shows compositions of the major elements present in coal and RPS ashes. Coal ash comprised mainly of silica (SiO_2), lime (CaO), and alumina (Al_2O_3), with 38%, 19.7%, and 16.1% by weight, respectively. For RPS ash, almost 50% by weight was titania (TiO_2) and approximately 24% by weight was alumina. TiO_2 is widely used in paints and coatings because of its brightness and very high reflective index (n=2.7). TiO_2 also exhibits other properties, such as photocatalyst, which, if engineered, may extend further benefits of RPS, besides as fuel. However, the advantages of RPS in this aspect were not included in this study. Trace element analyses of RPS and coal are shown in Table 3. As can be seen, the amount of heavy metals present in the coal is quite low, while RPS contains somewhat higher for some of these elements.

Table 1. Characteristics of coal and RPS

Fuel Type	Coal	RPS
Proximate Analysis (%wt)		
Volatile Matter[a]	48.3	76.5
Fixed Carbon[a]	42.9	3.4
Ash[a]	8.0	20.1
Moisture[b]	27.7	46.3
Low Heating Value[a] (MJ/kg)	28.04	24.92
Ultimate Analysis (%wt)[a]		
Carbon	67.3	50.6
Nitrogen	0.96	4.66
Hydrogen	4.58	6.57
Oxygen	19.92	17.91
Sulfur	0.29	0.19
Chlorine[c]	10.0	3,419
Fluorine[c]	67	76

Note: [a]: as dry weight basis;
[b]: as received weight basis;
[c]: ppm unit

Table 2. Concentrations of major elements in coal and RPS

Fuel Type	Coal	RPS
Major elements (% by wt)		
SiO_2	37.9	19.3
TiO_2	1.2	47.4
Al_2O_3	16.1	23.8
CaO	19.7	0.9
Fe_2O_3	5.93	5.2
MgO	4.93	3.1
K_2O	0.6	0.5
Na_2O	1.4	0.1
P_2O_5	1.7	0.05

Table 3. Concentrations of trace elements in coal and RPS

Fuel Type	Coal	RPS
Trace elements (ppmw[a])		
As	0.6	3.2
Ba	482	863
Cd	0.05	0.23
Cr	4	59
Co	2.1	3.9
Cu	11	738
Pb	2.5	2.5
Mn	9	143
Mo	0.4	3.1
Hg	0.05	0.02
Ni	4.0	14
Se	0.4	<0.1
V	12	7
Zn	11	99

Note: [a]: as dry weight basis

Production of Ash

The resultant ash was classified into a coarse mode (dp > 0.5 μm) and a submicrometer mode (dp < 0.5 μm). The total mass of ash (~96 mg/g of coal) formed during combustion of coal alone was much less than that generated during combustion of RPS alone (~206 mg/g of RPS). The amounts of total ash from combustion of either coal or RPS alone were comparable to their initial ash content from proximate analysis, 8% and 20% by weight for coal and RPS, respectively. This confirms that the carbonaceous species is completely oxidized in our combustor. The submicrometer/coarse ash mass fraction during coal combustion alone is six times

higher than that of RPS alone (Table 4) because of the differences in physical and chemical properties of the fuels. Coal contains approximately equal amounts of fixed carbon (~43% by weight) and volatile matter (~48.3% by weight); thus, combustion of coal proceeds on the surface of the burning particle. In contrast, for combustion of RPS, due to its low fixed carbon content (~3%) but high volatile matter (~71%), combustion mostly occurs in the gas phase. As a result, the temperature inside and on the surface of RPS particles could be lower than that of coal, leading to lower vaporization and subsequent particle formation by nucleation. In the case of co-combustion, the fine to coarse mass fraction increased, implying that volatilization of the compounds in RPS particles was promoted. Subsequently, composition of the combustion gas was altered, resulting in formation of different volatile species than those found during combustion of RPS alone.

Table 4. Summary of size distribution statistics for combustion experiments

Test	Material	Mass Fraction (fine/coarse)	Geometric Mean Size (nm)	Total Number Conc. (# cm^{-3})	Total mass (mg m^{-3})	Geometric Standard Deviation
1	Coal	0.32	36.4 ± 1.48	1.11×10^{7}	6.53×10^{10}	1.48
2	RPS	0.05	16.0 ± 0.49	7.96×10^{6}	3.20×10^{10}	1.62
3	Coal +RPS	0.18	24.5 ± 1.60	5.99×10^{7}	1.30×10^{12}	1.50

The submicrometer particle size distributions formed during combustion of coal or RPS alone, and on co-combustion were measured. The results, shown in Figure 2, are presented in terms of normalized-number particle size distributions. This parameter is defined as the number concentration of particles of specific sizes divided by the maximum particle number concentration measured during combustion of coal or RPS alone and during co-combustion, 4.16×10^6 #/cm^3 in this study. The size distribution statistics are summarized in Table 4. For combustion of coal and RPS alone, and co-combustion of coal and RPS, the geometric mean particle sizes were 36.4, 16.0, and 24.5 nm, respectively. The total number concentration in the exhaust for combustion of coal and RPS alone, and for co-combustion of coal and RPS, were 1.11×10^7, 7.96×10^6, and 5.99×10^7 #/cm^3, respectively. Since the total residence time in all tests was the same, retardation of vaporization and particle formation resulted in less time available for the growth processes, such as condensation and coagulation. The smaller size and higher number concentration of particles generated during co-combustion than those generated during combustion of coal alone indicate that combustion of coal occurred first, and that the local coal combustion environment promotes vaporization of RPS particles, which supports our earlier explanation.

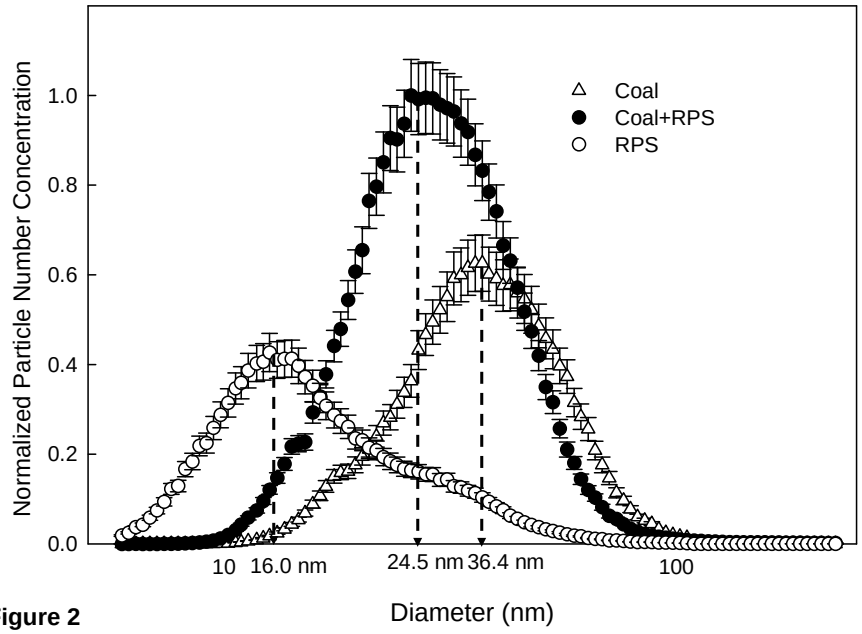

Figure 2

Figure 2. Submicrometer particle size distributions from combustion of coal and RPS alone, and co-combustion of coal and RPS. Particle number concentrations were normalized by the maximum particle number concentration (4.16×10^6 #/cm^3) measured for all tests.

Partitioning and Fate of Trace Elements

During combustion, trace elements bound in fuels are distributed into bottom ash, fly ash, and flue gas. The behavior of trace elements during combustion can be expressed in many ways, such as the degree of retention and the relative enrichment. Degree of retention is defined as the ratio between the mass of an element retained in the ash residue and that introduced into the combustor in the fuel. This parameter reveals the maximum amount of the element in the gas phase in the combustor.

Relative enrichment is the ratio of the concentration of a particular element in fly ash to that in bottom ash. In this study, relative enrichment is defined as the ratio of the concentration in the submicrometer mode to that in the coarse mode. This parameter provides information about the propensity of volatile trace elements that condense on small ash particles, due to their greater surface area-to-mass ratios. Relative enrichment less than unity implies a lack of mobility during combustion of the element.

The trace element statistics relative to combustion material over several runs are shown in Table 5. The degree of retention and relative enrichment of trace elements in this study are presented in Figures 3 and 4, respectively. The results indicate a strong retention of all elements in the ash, except for Hg. However, the comparison of the results of combustion of coal or RPS alone, and co-combustion of coal with RPS clearly demonstrates the differences in the trace element partitioning trends. In combustion of coal or RPS alone, the retention of most elements in the coarse mode ash was above 70%. In the case of co-combustion of RPS and coal, lower quantities of trace elements were retained in the coarse mode ash (ranging between 30% to 80%). The amounts of the elements released in gaseous forms and associated with fine particles were more significant. This effect was found to be more pronounced for As, Cr and Pb, suggesting that it could be related to the higher volatilization tendency of these metals and the formation of volatile chlorine species,

such as $PbCl_{4(g)}$, $CrO_2Cl_{2(g)}$and $AsCl_{3(g)}$[25]. Higher chlorine content in RPS may explain the formation of different compounds with greater volatilities. In addition, the local combustion environment, in terms of oxygen (O_2) and carbon monooxide (CO), may influence the rate of volatilization and partitioning of trace elements[17, 22]. When coal was present, because of its high fixed carbon content (~43% by weight) compared to that of RPS (~3% by weight), the local combustion environment could be more reducing; thus, volatilization in RPS was promoted.

Table 5. Summary of trace element concentrations relative to combustion material

Table 5

Fuel Type	**Coal**		**RPS**		**Coal+RPS**	
(µg/g fuel) *(ng/g fuel)	coarse mode (dp >0.5µm)	fine mode (dp <0.5µm)	coarse mode (dp >0.5µm)	fine mode (dp <0.5µm)	coarse mode (dp >0.5µm)	fine mode (dp <0.5µm)
As*	420 ± 60	30 ± 8	2900 ± 250	100 ± 15	80 ± 12	60 ± 18
Ba	362 ± 60	14.5 ± 1.8	734 ± 95	26 ± 3.5	300 ± 17	35 ± 6.2
Cd*	40 ± 6.0	3.0 ± 0.5	210 ± 45	7 ± 0.8	70 ± 12	8 ± 1.2
Cr	3.3 ± 0.4	0.2 ± 0.05	52 ± 8.5	2.4 ± 0.40	11.5 ± 1.8	1.3 ± 0.2
Co	1.6 ± 0.2	0.042 ± 0.007	3.0 ± 1.2	0.3 ± 0.06	1.5 ± 0.2	0.13 ± 0.02
Cu	8.1 ± 1.2	0.6 ± 0.075	627 ± 112	30.0 ± 3.2	112 ± 25	14 ± 1.3
Pb*	2,200 ± 400	30 ± 3.0	2,100 ± 112	80.0 ± 15	900 ± 240	130 ± 20
Mn	7.5 ± 1.2	0.18 ± 0.01	114 ± 22	2.9 ± 0.32	33.2 ± 4.3	3.0 ± 0.4
Mo*	340 ± 60	12 ± 1.8	3,000 ± 340	60 ± 14	900 ± 140	53 ± 10
Ni*	3,300 ± 520	40 ± 8	12,800 ± 2,200	300 ± 26	4,100 ± 600	520 ± 130
V	9.0 ± 1.2	0.4 ± 0.03	6.3 ± 1.3	0.14 ± 0.016	8.6 ± 1.2	0.54 ± 0.08
Zn	5.3 ± 0.52	0.8 ± 0.15	64 ± 12	3.0 ± 0.16	17.8 ± 3.3	2.0 ± 0.3

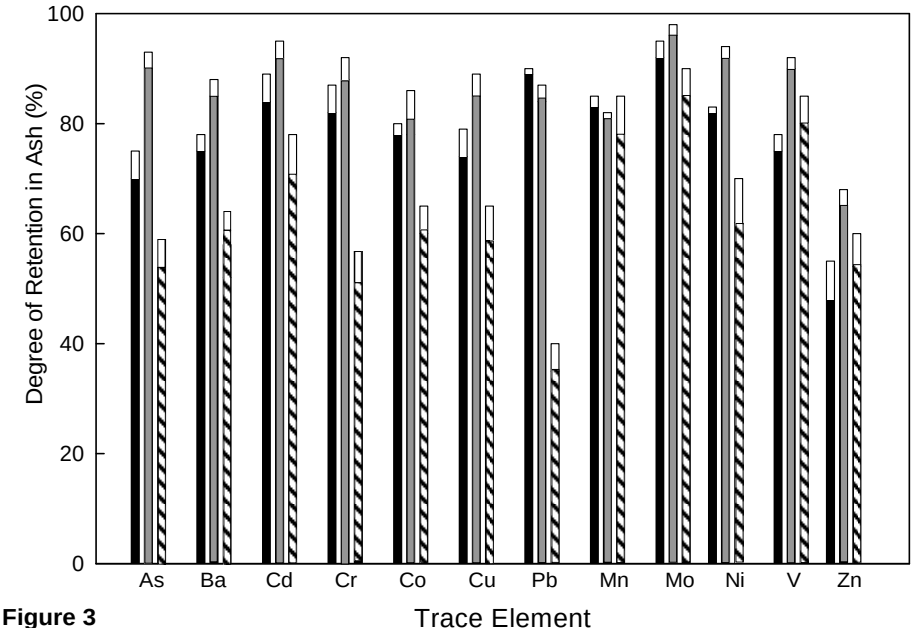

Figure 3. Degree of retention of trace elements in ash during combustion of coal or RPS alone, and co-combustion of coal and RPS: ■ coarse mode coal combustion; ▒ coarse mode RPS combustion; ▨ coarse mode co-combustion; □ submicrometer mode

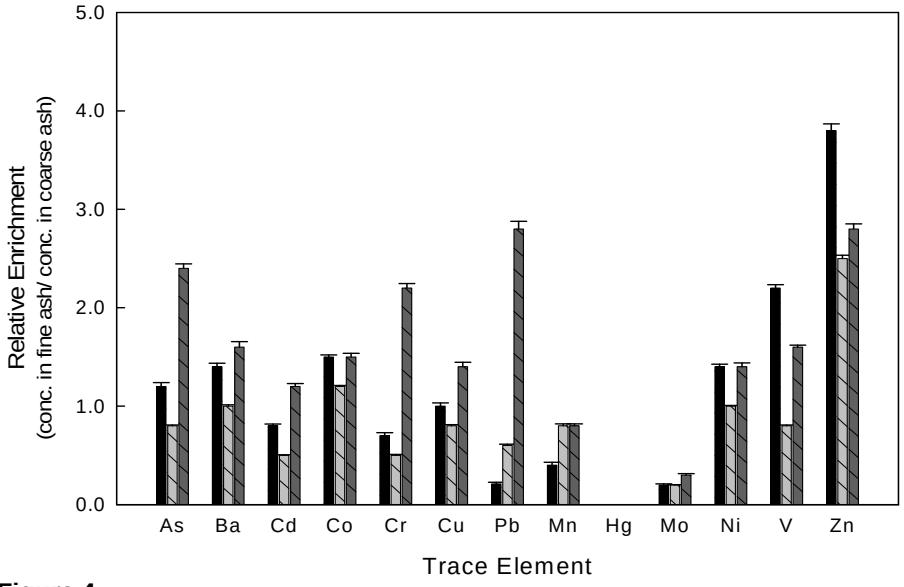

Figure 4

Figure 4. Relative enrichment trace elements in ash during combustion of coal or RPS alone, and co-combustion of coal and RPS: ■ coal combustion; ▨ RPS combustion; ▨ co-combustion of coal and RPS

Trace elements can be emitted into the atmosphere as vapor species, as an aerosol, or on the surface of ultrafine particulate matter. Despite the high efficiency of electrostatic precipitators in removing particles, small particles (dp<0.5 μm) are not effectively captured due to inefficient diffusion charging[26]. Hence, a 'fine particle and vapor factor in the combustor' is defined as the ratio of mass of the element associated with fine particles (dp<0.5μm) and that emitted in vapor form to the mass in the fuel introduced into the combustor. This is shown in Figure 5 for a range of elements. Results from trace element analyses in total ash, coarse mode ash, submicrometer mode ash were consistent, and within acceptable ranges (100±20%).

The fine particle and vapor factor in the combustor from combustion of coal or RPS alone were quite low, representing less than 20% for most of the trace metals in relation to the input fuel, except for Hg (~100%) and Zn (~ 50%). In the co-combustion tests, the factor for As, Cr and Pb increased significantly. However, the value of the factor for Cu, Co, Cd, Mn, V, Ni, Mo, and Zn were not substantially increased (less than two times). This clearly indicates that the species of trace elements were different for co-combustion compared with those for combustion of coal or RPS alone, resulting in different physical and chemical properties of the element. A number of parameters, such as the combustion process and chlorine content, may influence these observations.

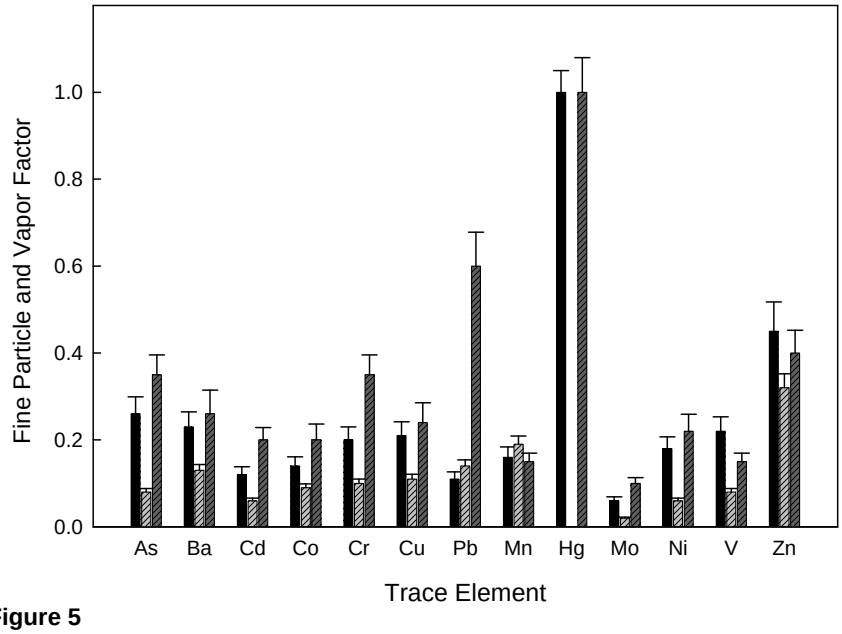

Figure 5

Figure 5. Fine particle and vapor factor during combustion of coal or RPS alone, and co-combustion of coal and RPS: ■ coal combustion; ▨ RPS combustion; ▨ co-combustion of coal and RPS

The effect of the combustion process on the release of trace elements was explained in an earlier section. The effects of high chlorine content on speciation of metals were clearly observed in the gaseous mercury speciation results, shown in Figure 6. Mercury is very volatile and hence was not retained in ash for all tests. The PRB coal used in this study had a low chlorine content; thus gaseous mercury was found mainly in the elemental form ($Hg^0_{(g)}$). RPS contains negligible amounts of mercury; therefore, no gaseous mercury was detected during combustion of RPS alone. In the case of co-combustion, however, a significant amount of oxidized

mercury ($HgX_{(g)}$) was detected. The ratio of oxidized mercury to elemental mercury increased by 62% (from 0.53 to 0.85). This oxidized mercury was presumed to be $HgCl_2$, which is the major species present at equilibrium at a low temperature condition. $HgCl_2$ is water soluble; thus, it can be removed in other pollutant control devices, such as wet scrubbers. The presence of high chlorine in the combustion environment typically promotes the formation of metal chlorides, such as $PbCl_4$, CrO_2Cl_2, and $CdCl_2$ [14, 25]. The dominant metal chloride species depends on the relative of affinity for chlorine of the metals present in the environment. Wu et al. (1993) reported that Pb, Cr, Hg, As, and Cd all have high affinity for chlorine, ranging from highest to lowest[25]. This explanation is consistent with the results in this study. Pb, Cr, and As were found to be more associated with fine particles during co-combustion, possibly resulting from the formation of $PbCl_4$, CrO_2Cl_2 and $AsCl_3$, which are more volatile species.

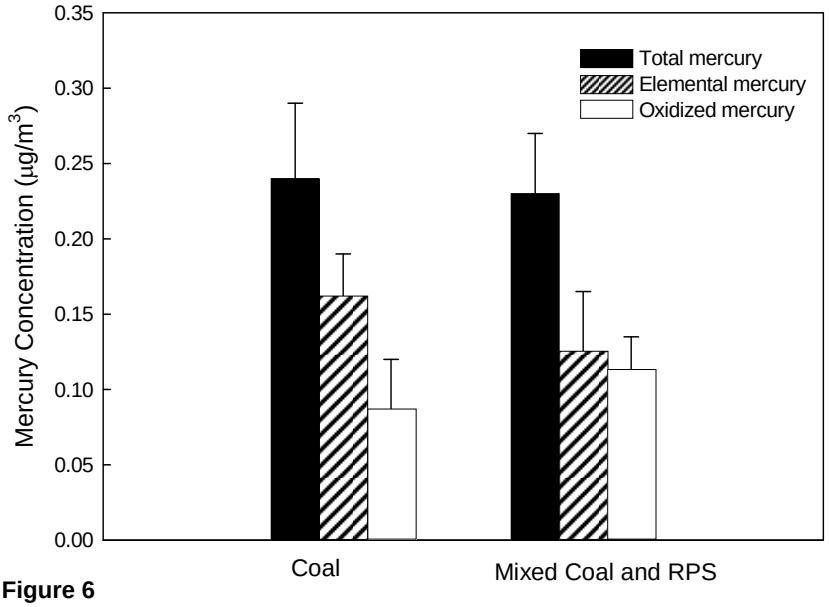

Figure 6

Figure 6. Mercury species concentration measured at the combustor exit for different conditions.

CONCLUSIONS

The fate of particulate matter and the behavior of trace elements from combustion of coal or RPS alone, and from co-combustion of coal and RPS were studied. Submicrometer particle formation was found to be higher in the case of co-combustion than that of combustion of a single fuel, due to the difference in the combustion environment, i.e., the reducing conditions and chemical compositions in the environment. The trace metals introduced with coal and RPS were generally retained in ash; however during the co-combustion process, the presence of RPS

modified the partitioning of the elements, decreasing their fixation in ash and leading to higher fractions in the gas phase as aerosol or vapor. This suggests that more intense volatilization occurred in the co-combustion test, which could be attributed to slightly higher local temperatures, a more reducing environment in the region near the RPS particles, and the high volatile chlorine species. This effect was more pronounced in the case of the more volatile metals such as Pb and As. In the case of Hg, an increase in gaseous oxidation was observed. This species is presumably $HgCl_2$, which is water soluble; hence, it can be removed by other pollution control devices, such as a wet scrubber. Co-combustion of RPS and coal may potentially enhance gaseous mercury capture in conventional pollution control devices. The presence of certain forms of titanium dioxide in RPS can be engineered to enhance mercury capture, but also needs to be investigated in future studies.

ACKNOWLEDGMENTS

Partial support from USDOE grant number DE-FGZ6-05NT42531 and the Chrysler Summer Professor Research Program is gratefully acknowledged.

REFERENCES

1. Kobayashi, N., et al., *A new pulverized biomass utilization technology.* Powder Technology, 2008. **180**(3): p. 272-283.

2. Kar, Y. and Y. Tekeli, *The potential of biomass residues in Turkey and their importance as energy resources.* Energy Sources Part a-Recovery Utilization and Environmental Effects, 2008. **30**(6): p. 483-493.

3. Goyal, H.B., D. Seal, and R.C. Saxena, *Bio-fuels from thermochemical conversion of renewable resources: A review.* Renewable & Sustainable Energy Reviews, 2008. **12**(2): p. 504-517.

4. Demirbas, A., *Co-firing coal and municipal solid waste.* Energy Sources Part a-Recovery Utilization and Environmental Effects, 2008. **30**(4): p. 361-369.

5. Xu, G.W., et al., *Energy production with light-industry biomass process residues rich in cellulose.* Progress in Chemistry, 2007. **19**(7-8): p. 1164-1176.

6. Diaz-Somoano, M., S. Unterberger, and K.R.G. Hein, *Prediction of trace element volatility during co-combustion processes.* Fuel, 2006. **85**(7-8): p. 1087-1093.

7. Elled, A.L., et al., *The fate of trace elements in fluidised bed combustion of sewage sludge and wood.* Fuel, 2007. **86**(5-6): p. 843-852.

8. Folgueras, A.B., et al., *Volatilisation of trace elements for coal-sewage sludge blends during their combustion.* Fuel, 2003. **82**(15-17): p. 1939-1948.

9. Gregg, J.J., G.K. Zander, and T.L. Theis, *Fate of trace elements in energy recovery from recycled paper sludge.* Tappi Journal, 1997. **80**(9): p. 157-162.

10. Miller, B.B., R. Kandiyoti, and D.R. Dugwell, *Trace element emissions from co-combustion of secondary fuels with coal: A comparison of bench-scale experimental data with predictions of a thermodynamic equilibrium model.* Energy & Fuels, 2002. **16**(4): p. 956-963.

11. Miller, B.B., R. Kandiyoti, and D.R. Dugwell, *Trace element behavior during co-combustion of sewage sludge with polish coal.* Energy & Fuels, 2004. **18**(4): p. 1093-1103.

12. Lee, T.G., P. Biswas, and E. Hedrick, *Overall kinetics of heterogeneous elemental mercury reactions on TiO2 sorbent particles with UV irradiation.* Industrial & Engineering Chemistry Research, 2004. **43**(6): p. 1411-1417.

13. Wu, C.Y., et al., *Capture of mercury in combustion systems by in situ-generated titania particles with UV irradiation.* Environmental Engineering Science, 1998. **15**(2): p. 137-148.

14. Frandsen, F., K. Damjohansen, and P. Rasmussen, *Trace-Elements from Combustion and Gasification of Coal - an Equilibrium Approach.* Progress in Energy and Combustion Science, 1994. **20**(2): p. 115-138.

15. Senior, C.L., J.J. Helble, and A.F. Sarofim, *Emissions of mercury, trace elements, and fine particles from stationary combustion sources.* Fuel Processing Technology, 2000. **65**: p. 263-288.

16. Bool III, L.E. and J.J. Helble, *A Laboratory Study of the Partitioning of trace Elements during Pulverized-Coal Combustion.* Energy&Fuels, 1995. **9**: p.880-887.

17. Suriyawong, A., et al., *Submicrometer Partical Formation and Mercury Speciation under O2-CO2 Coal Combustion.* Energy & Fuels, 2006. **20**(6): p. 2357-2363.

18. Brown, C.W. and R.E. Imhoff, *The Fate of Mercury in the Ducts and Plume of a Coal-Fired Power-Plant.* Abstracts of Papers of the American Chemical Society, 1995. **210**: p. 104.

19. Charon, O., A.F. Sarofim, and J.M. Beer, *Distribution of Mineral Matter in Pulverized Coal.* Progress in Energy and Combustion Science, 1990. **16**(4): p. 319-326.

20. Fujiwara, N., et al., *Mercury transformations in the exhausts from lab-scale coal flames.* Fuel, 2002. **81**(16): p. 2045-2052.

21. Galbreath, K.C. and C.J. Zygarlicke, *Mercury transformations in coal combustion flue gas.* Fuel Processing Technology, 2000. **65**: p. 289-310.

22. Helble, J.J. and A.F. Sarofim. *Trace-Element Behavior During Combustion*. in *Abstracts of Papers of the American Chemical Society*. 1993.

23. Linak, W.P. and J.O.L. Wendt, *Trace-metal transformation mechanisms during coal combustion.* Fuel Processing Technology, 1994. **39**: p. 173-198.

24. Hedrick, E., Lee,T.G.,Biswas, P. Zhuang, Y., *The Development of Iodine Based Impinger Solutions for the Efficient Capture of Hg0 Using Direct Injection Nebulization-Inductively Coupled Plasma Mass Spectrometry Analysis.* Environmental Science and Technology, 2001. **35**(18): p. 3764-3773.

25. Wu, C.Y. and P. Biswas, *An Equilibrium-Analysis to Determine the Speciation of Metals in an Incinerator.* Combustion and Flame, 1993. **93**(1-2): p. 31-40.

26. Jiang, J., M.H. Lee, and P. Biswas, *Model for Nanoparticle Charging by Diffusion, Direct Photoionization, and Thermionization Mechanisms.* Journal of Electrostatics, 2007. **65**: p. 209-220.

Appendix II

Measurement and Capture of Fine and Ultrafine Particles from a Pilot-Scale Pulverized Coal Combustor with an Electrostatic Precipitator

* This work was published in the *Journal of Air and Waste Management Association*, 59(5), 553-559, 2009.

ABSTRACT

Experiments were carried out in a pilot-scale pulverized coal combustor at the Energy and Environmental Research Center (EERC) burning a Powder River Basin (PRB) subbituminous coal. A Scanning Mobility Particle Sizer (SMPS) and an Electrical Low Pressure Impactor (ELPI) were used to measure the particle size distributions (PSDs) in the range of 17 nm to 10 μm at the inlet and outlet of the Electrostatic Precipitator (ESP). At the ESP inlet, a high number concentration of ultrafine particles was found with the peak at around 75 nm. A trimodal PSD for mass concentration was observed with the modes at around 80–100 nm, 1–2 μm, and 10 μm. The penetration of ultrafine particles through the ESP increased dramatically as particle size decreased below 70 nm, due to insufficient or partial charging of the ultrafine particles. Injection of nanostructured fine particle sorbents for capture of toxic metals in the flue gas caused high penetration of the ultrafine particles through the ESP. The conventional ESP was modified to enhance charging using soft X-ray irradiation. A slipstream of flue gas was introduced from the pilot-scale facility and passed through this modified ESP. Enhancement of particle capture was observed with the soft X-ray irradiation when moderate voltages were used in the ESP, indicating more efficient charging of fine particles.

IMPLICATIONS

Emissions of fine and ultrafine particles from pulverized coal combustors are potentially of great concern. The pilot-scale results reported in this paper contribute to a better understanding of the particle size distributions that result on the combustion of sub-bituminous coals. It is confirmed that penetration of ultrafine particles (particularly those less than 50 nm) through conventional ESPs can be significant. This paper also provides useful strategies of how to enhance the capture of ultrafine particles.

INTRODUCTION

Significant research is currently underway related to particulate matter (PM) exposure and its adverse effects on human health. Fine ($d < 2.5$ μm) and ultrafine ($d <$ 0.1 μm) particles are of special interest because they can penetrate into the alveolar regions of the lungs upon inhalation. It has been demonstrated that fine particles are associated with increased symptoms and deaths from cardiovascular and respiratory causes[1-4]. In 1997, the United States Environmental Protection Agency established a regulation of $PM_{2.5}$ (particles less than 2.5 μm in aerodynamic diameter) in addition to the existing PM_{10} (particles less than 10 μm in aerodynamic diameter) standards[5]. One of the major anthropogenic sources of $PM_{2.5}$ in the atmosphere is direct emissions from stationary combustion systems (utility and industrial boilers, incinerators, cooking, residential combustors, and others)[1]. One of the largest source categories is electric utility coal combustion accounting for 570,000 tons/yr of $PM_{2.5}$ emissions in the United States in 2001[6]. To help reduce the emissions of fine particles and to protect public health, it is important to characterize particle size distributions (PSDs) from coal-fired utility boilers, especially in the fine and ultrafine size fractions.

Laboratory, pilot-, and full-scale studies have been conducted previously to measure the PSDs from pulverized coal combustors, which showed significant

fraction of fine/ultrafine particles before PM control devices, e.g. electrostatic precipitator (ESPs) and/or baghouses. Zhuang and Biswas[7] studied submicrometer particle formation in a bench-scale pulverized coal combustor and found that the geometric mean particle size (based on number concentration) ranges from 63 to 84 nm, which is consistent with a vaporization-nucleation-condensation formation and growth mechanism. Chang et al.[8] measured ultrafine particle size distributions from a pilot-scale coal-fired combustor and observed that the peak of particle number concentrations for medium sulfur bituminous coal was at 40-50 nm. Linak and Miller[9] observed trimodal PSDs (peaks at 0.07-0.08 μm, 0.8-2.0 μm, and 7-10 μm based on mass concentration) when burning one subbituminous and two bituminous coal seams in a 50 kW pulverized coal combustor. Yoo et al.[10] observed bimodal PSDs (peaks at 0.1-1.0 μm and 5-10 μm) when burning one anthracite and two bituminous coal seams in a commercial coal-fired boiler, where the PSD of the anthracite facility showed a distinct mode near 0.1 μm. While the majority of the above literature reported PSDs burning bituminous coals, few data are available on burning subbituminous coals. Subbituminous coals account for the second largest U.S. coal reserves, with Powder River Basin (PRB) coal being the major source. Quann et al.[11] reported chemical composition of combustion generated submicron particles for eleven coals including two subbituminous coals; however, no details on PSDs were reported. Senior et al.[12] studied pilot-scale combustion of a PRB coal and reported that particles in the submicrometer range centered at 80 nm. However, data

for particles smaller than 40 nm were not reported. Hence, a more comprehensive study is needed on the resultant PSDs obtained on burning subbituminous coal seams, particularly PRB coal.

ESPs are widely used as particulate control devices in industry and their overall mass collection efficiency typically exceed 99%[13]. However, there is a theoretical minimum collection efficiency in the size range of 0.1-1 μm, due to the combination effect of diffusion charging (increase with decreased particle size) and field charging (increase with increased particle size)[14, 15]. Correspondingly, a "penetration window" is observed in the submicrometer range where the ESP collection efficiency can reach as low as 70~80%[16-18]. Contrary to the theoretical calculations[14], many experimental observations have shown that ESP collection efficiency decreases with decreasing particle diameter in the ultrafine size range. Zhuang et al.[19] tested a lab-scale cylindrical ESP using Al_2O_3 and NaCl particles and found a decrease in collection efficiency as the particle size decreases below 100 nm. Huang and Chen[13] studied the ESP performance using monodisperse sucrose particles (in the range of 10~60 nm) and reported that aerosol penetration through their single- and two-stage ESPs increased significantly for particles below 20 and 50 nm, respectively. Yoo et al.[18] reported that the collection efficiency of a two-stage ESP decreases significantly for NaCl particles below 30 nm. Suriyawong et al.[20] studied charging and electrostatic collection of coal-combustion particles in laboratory

experiments and reported that natural particle charging within the combustor itself is very low and that penetration of combustion particles increases as particle size decreases below 40 nm, regardless of the combustion gases used (air or O_2-CO_2 mixtures). It should be noted that most of the above findings were based on bench-scale studies. Very few studies[17, 21] have been reported on the penetration characteristics of pilot- and full-scale ESPs in the ultrafine size range. Hence, more studies on larger scale ESPs are needed, and are now feasible due to the availability of several real time fine particle size distribution measurement instruments. In addition, the technology of sorbent particle injection in full-scale power plants is being proposed for the capture of certain toxic metals in the combustor[22]. For example, *in situ* generated TiO_2 agglomerates by injecting titanium isopropoxide (TTIP) as the precursor exhibited high efficiency in capturing gas-phase mercury in combustion flue gas[23-25]. The sizes of primary TiO_2 particles and TiO_2 agglomerates are around 5 nm and 200 nm, respectively[25]. Prior to large scale use of such sorbents, the effectiveness of the ESP system to trap these materials is to be established. The results will provide for feasible size ranges of sorbents that can be readily used in such systems.

As the bench-scale studies concluded that the significant decrease in collection efficiency of ultrafine particles was caused by partial or insufficient charging[7, 13, 18], methods of charging ultrafine particles more efficiently are needed.

Soft X-ray irradiation has been applied recently to effectively improve nanoparticle charging in several lab-scale studies[26-28]. X-ray radiation can charge the particles by two mechanisms: direct photoelectric charging and diffusion charging [26, 28, 29]. In direct photoelectric charging, the atoms or molecules on the surface of the aerosol particle are photoionized, whereas in diffusion charging the gas molecules get ionized by the radiation and then attach to the particles resulting in their electrical charging. To the best of our knowledge, no study has examined the effectiveness of soft X-ray in enhancing ultrafine particle capture in pilot-scale coal combustors.

This paper reports experimental results from studies conducted on a pilot-scale pulverized coal combustor. Four aspects were studied: (1) resultant particle size distributions on burning a PRB subbituminous coal, measured before and after the pilot-scale ESP, (2) ESP collection efficiency as a function of particle size, particularly penetration of fine and ultrafine particles across the ESP, (3) ESP performance in the scenario of sorbent injection, and (4) the effect of soft X-ray irradiation on ultrafine particle capture conducted on a slip stream taken from the combustor.

EXPERIMENTAL METHODS

Description of the Pilot-Scale Coal Combustor

The experiments were conducted burning PRB subbituminous coal in a pilot-scale unit at the Energy and Environmental Research Center (EERC) at the University of North Dakota. It is a 160 kW pulverized coal-fired unit designed to generate fly ash representative of that produced in a full-scale utility boiler. The combustor is oriented vertically to minimize wall deposits. A refractory lining helps to ensure adequate flame temperature for complete combustion and prevents rapid quenching of the coalescing or condensing fly ash. The coal nozzle fires axially upward from the bottom of the combustor. The flue gas flow rate was 130 scfm or 210 N m^3/hr and the mean residence time of a coal particle in the combustor was approximately 3 sec. A single-wire, tubular ESP (denoted as EERC-ESP) with a wire-to-tube spacing of 28 cm is used to collect fly ash particles. The EERC-ESP was operated at 40-60 kV with a corona current of approximately 4 mA. The actual plate current was continuously monitored to ensure consistent operation of the EERC-ESP from test to test. Downstream of the EERC-ESP is a heat-traced and insulated baghouse. It contains three bags (L = 400 cm; D = 13 cm), and each bag is cleaned separately with its own diaphragm pulse valve.

Apparatus and Methods

The schematic diagram of the PM sampling system is shown in Figure 1. PM samples were isokinetically collected from the flue gas at both EERC-ESP inlet and outlet, where the flue gas temperature was approximately 150 °C. The sampling line was heated to prevent thermophoretic deposition of particles. The sample was then diluted in a dilution chamber, where the dilution gas was circulated as shown in Figure 1. The dilution gas was drawn by a pump from the bottom of the dilution chamber and then treated in a desiccator to remove moisture. Then the gas passed through a high efficiency particulate air (HEPA) filter to remove all particles. The particulate free gas was finally introduced to the top of the dilution chamber and the dilution cycle was complete. The flow rate of the dilution gas was measured by a flow meter and maintained around 40 lpm. Characterization of dilution systems for particle loss and transmission has been outlined elsewhere in our earlier work[30]. After dilution, the PM samples were independently measured by two aerosol instruments, an electrical low pressure impactor (ELPI, Dekati Ltd., Tampere, Finland) and a scanning mobility particle sizer (SMPS, TSI Inc., St. Paul, MN, USA). The ELPI is a real-time size spectrometer which measures particle size distribution in the range of 0.03−10 μm with 12 channels. The SMPS consists of a differential mobility analyzer (DMA, Model 3081), an electrostatic classifier (Model 3080), and a condensation particle counter (CPC, Model 3022A). It measures particles in the size ranges of 10 – 422 nm.

To investigate the effect of soft X-ray irradiation on ultrafine particle capture, a cylindrical-wire ESP developed by Washington University (denoted as WU-ESP) was used with a mounted soft X-ray emitter (Model L6941, Hamamatsu Photonics Ltd., Japan), as shown in Figure 1. The WU-ESP had a stainless steel outer collecting electrode 15 cm in length and 5 cm in diameter. Varying voltages were applied to the central wire electrode of the WU-ESP using a Bertan high voltage power supply (Model 206-20, Spellman High Voltage Co., Valhalla, NY, USA). The ion current generated after corona inception was measured using a microammeter connected to the WU-ESP ground electrode. A 2 cm circular hole was drilled through the middle of the collecting electrode to allow for soft X-ray irradiation penetration inside the WU-ESP. X-ray irradiation (3.5–9.5 keV, λ = 0.12–0.41 nm) was spread inside the ESP at an angle of approximately 120°. To prevent particles from depositing on the X-ray emitter and to keep the system airtight, a thin polyamide film (KaptonTM 30HN, DuPont Corp., 30 μm thick) was placed in front of the X-ray emitter.

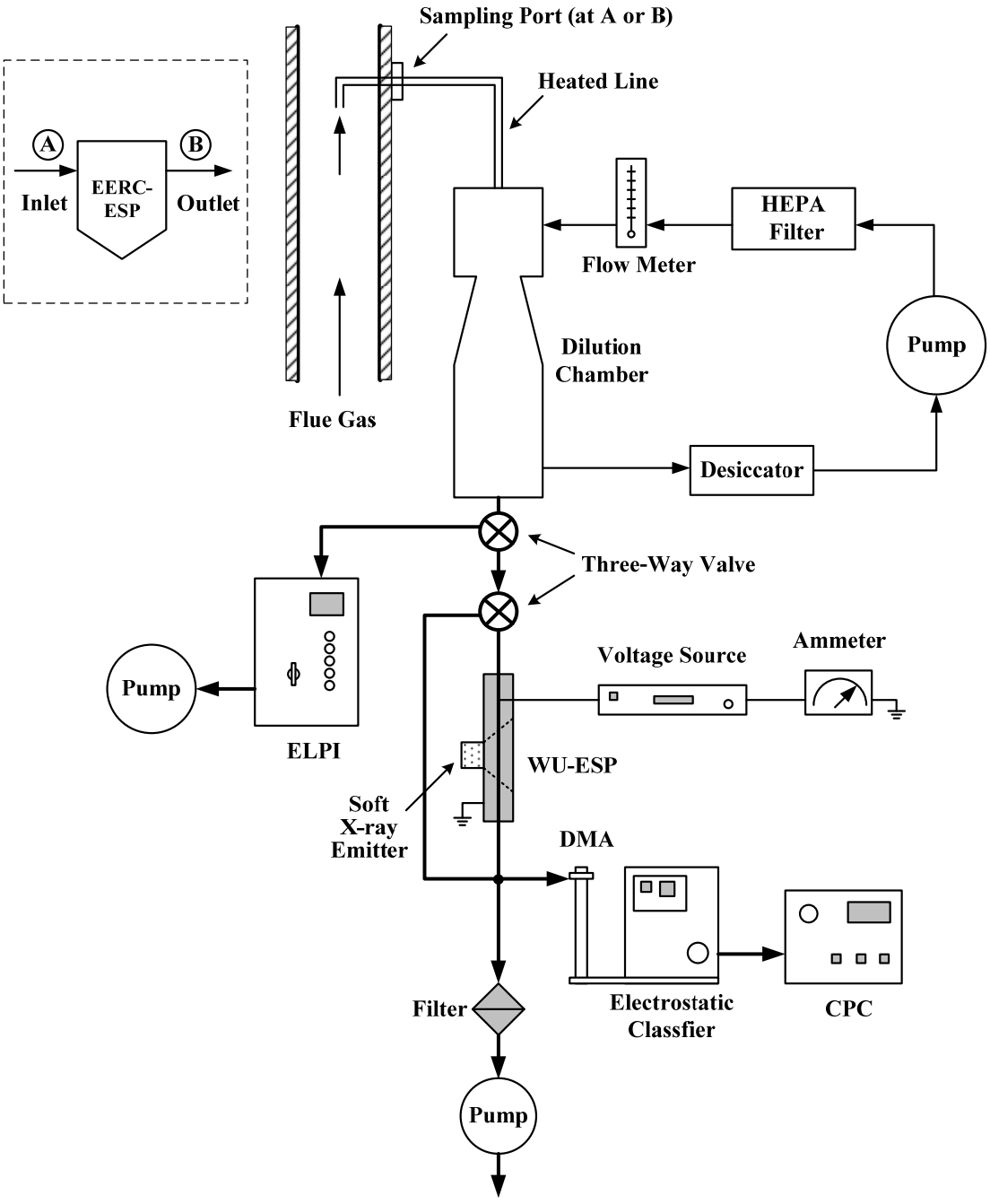

Figure 1. Schematic diagram of PM sampling system

The test plan is summarized in Table 1 which includes four sets of experiments. In Sets I and II, ELPI and SMPS were used respectively to measure baseline PSDs at both EERC-ESP inlet and outlet. The particle collection efficiency of the EERC-ESP can be calculated from the inlet and outlet data. Set III was designed to test the performance of EERC-ESP in the scenario of sorbent injection as a strategy of capturing toxic metals. TTIP, the precursor of TiO_2 particles, was injected at 800 g/hr upstream of the EERC-ESP where the flue gas temperature was around 900 °C. In Set IV, a slipstream of flue gas was drawn at 5 lpm through WU-ESP at two levels of negative voltages (-8.5 and -10 kV). The soft X-ray was turned on and off and the enhancement of soft X-ray irradiation on particle capture was examined.

Table 1. Summary of experimental conditions

Set	PM Sampling Port	Aerosol Instrument	Operating Conditions	
I	EERC-ESP Inlet and Outlet	ELPI	Baseline	
II	EERC-ESP Inlet and Outlet	SMPS	Baseline	
III	EERC-ESP outlet	SMPS	Sorbent (TTIP) Injection	
IV	EERC-ESP Inlet and Outlet*	SMPS	WU-ESP@ -8.5 kV	Soft X-ray off
				Soft X-ray on
			WU-ESP@ -10 kV	Soft X-ray off
				Soft X-ray on

* PSDs are measured after WU-ESP

RESULTS AND DISCUSSION

Baseline PSDs and Particle Collection Efficiency

In the baseline tests (Sets I and II), particle number and mass distribution data were collected at both EERC-ESP inlet and outlet, and are shown in Figure 2. When converting to mass, a particle density of 1200 kg/m^3 was used. Information on particle shape was not available, and thus particles were assumed to be spherical. Note that errors may be associated with this assumption because fine particles from coal combustion are typically agglomerates with complex structures. The ELPI and SMPS data agreed with each other in part of the overlapping measurement range (150–300 nm). For particles in the nanosize (< 100 nm) range, SMPS gave one order of magnitude higher concentration than ELPI at the EERC-ESP inlet, but the difference between SMPS and ELPI was much less significant at EERC-ESP outlet. This difference can be contributed by the systematical error of the two aerosol instruments since they are based on different operating principles. In addition, because different sampling flow rates were used for the two instruments (SMPS = 0.3 lpm; ELPI = 10 lpm) and the dilution gas flow rate remained constant (40 lpm), the dilution ratio of the PM samples for SMPS was much higher than that for ELPI. Meanwhile, the residence time in the dilution chamber was the same (1.2–1.5 s) for both measurements. At the relatively low sampling temperature (150 °C) all the ash-forming compounds have already been condensed, and thus, it was not likely that

nucleation or condensation would happen inside the dilution chamber. However, coagulation can be strongly affected by dilution rate at a certain residence time. A lower dilution ratio for ELPI leads to a higher initial particle concentration in the dilution chamber. As a result, particles may shift to larger sizes and lower number concentrations due to coagulation, when measured by ELPI compared to SMPS. This observation is consistent with the results reported in literature. Lipsky et al.[31] reported that residence time and dilution rates do not influence particle mass emission rates from coal combustion but affect the size distributions and number concentrations due to coagulation (e.g. ultrafine particle concentration is higher at a larger dilution ratio). In another study by Lipsky et al.[32], they indicated that when sampling after the baghouse the PSD and total particle number emission rate do not depend on dilution ratio because of the much lower particle number concentrations in diluted sample and the absence of nucleation. It agrees with the results in this study that the PSDs measured by SMPS and ELPI did not vary much at the outlet of EERC-ESP even though the dilution ratios are very different.

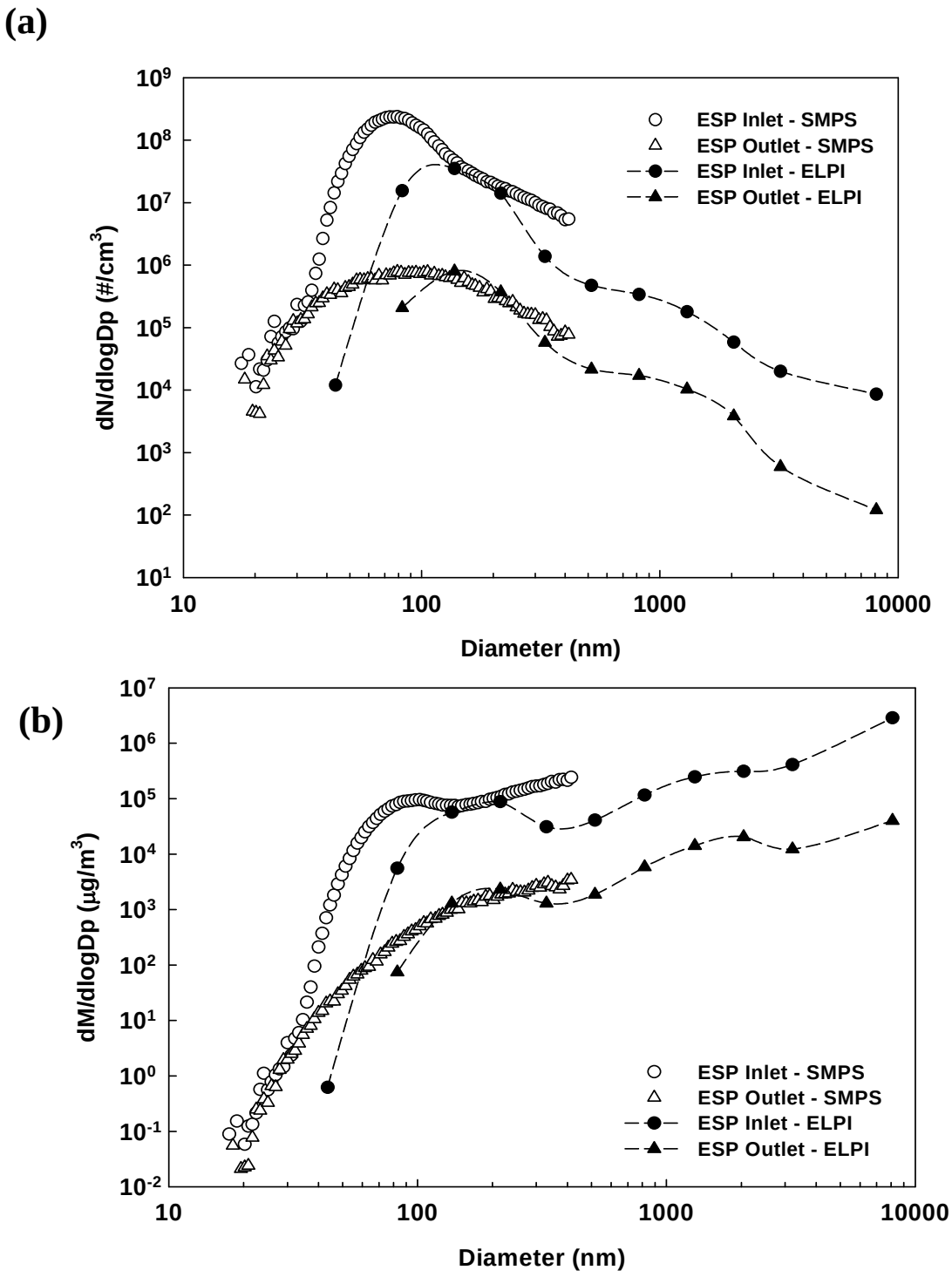

Figure 2. Particle size distributions based on (a) number and (b) mass measured at EERC-ESP inlet and outlet.

At the EERC-ESP inlet, a large number of ultrafine particles were observed and the mode particle size based on number concentration was around 75 nm (Figure 2a). The mass concentrations at the EERC-ESP inlet followed a trimodal distribution (Figure 2b), although the modes did not stand out prominently when plotted in logarithmic scale. The three modes are at around 80–100 nm, 1–2 μm, and 10 μm, representing ultrafine particle mode, accumulation mode, and coarse particle mode, respectively. The PSD result was in agreement with typical coal combustion PSDs reported in the literature[7-10]. At the EERC-ESP outlet, the PSDs followed similar trend as those measured at the EERC-ESP inlet but with a lower number and mass concentration for particles larger than 40 nm. For particles smaller than 40 nm, the difference between inlet and outlet concentration was not significant, indicating significant peneration. Quantitatively, the particle penetration through the ESP at a certain particle size (d_p) can be calculated as:

$$P(d_p) = \frac{N_{out}}{N_{in}} \quad (1),$$

where N_{in} and N_{out} are particle number concentrations (# cm^{-3}) of particles of size d_p at the ESP inlet and outlet, respectively. The data for particles less than 32 nm exhibited significant scatter (Figure 2), possibly due to very low particle concentration, and thus, they were not included in the penetration calculation. Figure 3 shows the penetration as a function of particle size. The lowest penetration (P = 0.002) occurred around 70 nm. For particles larger than 70 nm, the penetration

increased as particle size increased, and reached a plateau (P = ~0.015) in the range of 150–400 nm measured by the SMPS. The maximum penetration observed in this size range is consistent with that reported in the literature[16-18]. For the ELPI data, however, the highest penetration occurred at around 2 μm. Again, the discrepancy between the SMPS and ELPI results is likely because of the smaller dilution rate used by ELPI, where the curve of N_{in} (at ESP inlet) for ELPI has shifted toward the right (larger particle size) due to coagulation. For particles smaller than 70 nm, the penetration increased as the size decreased. The penetration increased to around 0.01 at 50 nm and reached high values (P = 0.55) at 32 nm. The results are consistent with those from laboratory scale studies that significant particle penetration was observed when particles are smaller than 50 nm[13, 18, 19].

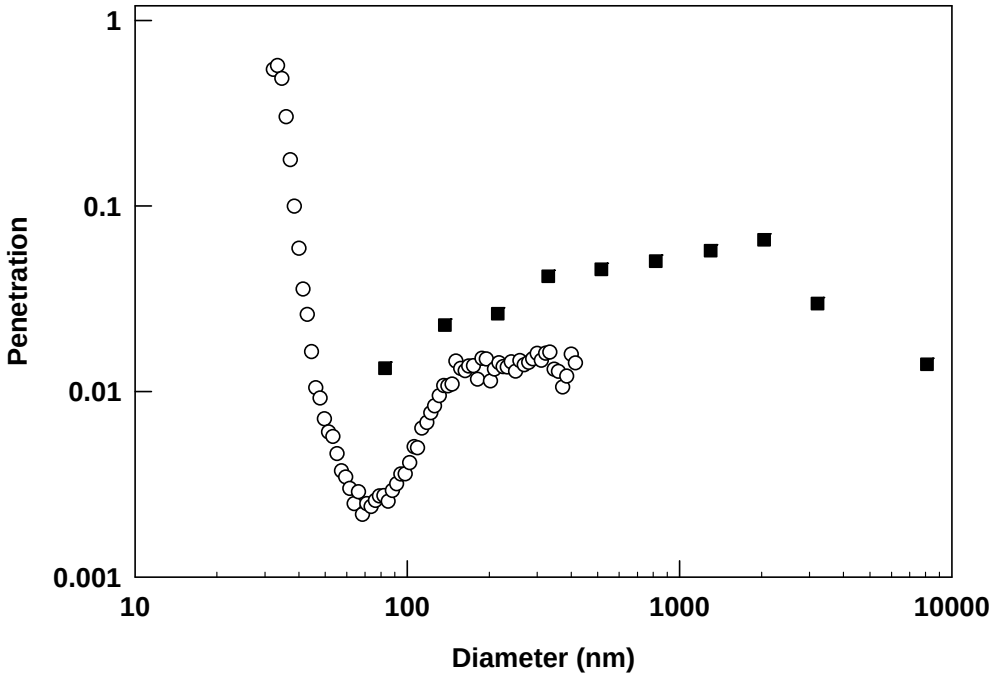

Figure 3. Particle penetration of EERC-ESP as a function of particle size. (○: Data from SMPS; ■: Data from ELPI)

Effect of Sorbent Injection on PSDs

In Set III experiments, TTIP was sprayed through a pre-calibrated nozzle into the flue gas upstream of the EERC-ESP where the gas temperature was around 900 °C. The TTIP droplets decomposed at this high temperature forming TiO_2 particles. TTIP was injected at 800 g/hr which resulted in a total TiO_2 particle concentration of 1.07 g/Nm^3. During the 2-hr period of sorbent injection, the operation of EERC-ESP was not apparently affected since the sorbent-to-ash mass ratio was not significant (less than 0.1). Figure 4 compares the PSDs at both the EERC-ESP inlet and outlet under baseline (without sorbent injection) and sorbent injection conditions, respectively. With sorbent injection, the particle number concentration at the EERC-ESP inlet was an order of magnitude higher than that in the baseline for almost the entire size range. At the EERC-ESP outlet, the TTIP injection caused significant penetration of particles that are smaller than 100 nm. With TTIP injection, the mode concentration (at 55 nm) was 4 times higher than the baseline, and the total number concentration was 2.5 times higher than the baseline. The charging characteristics of the sorbent particles may also be different (TiO_2 is a highly resistive material) – resulting in lower capture. The results indicate that proper design considerations must be taken into account to ensure that nanostructured sorbents used for pollutant removal do not escape collection in the ESP system. Appropriate injection rates of sorbents can ensure that the sizes are appropriate for effective capture in ESPs.

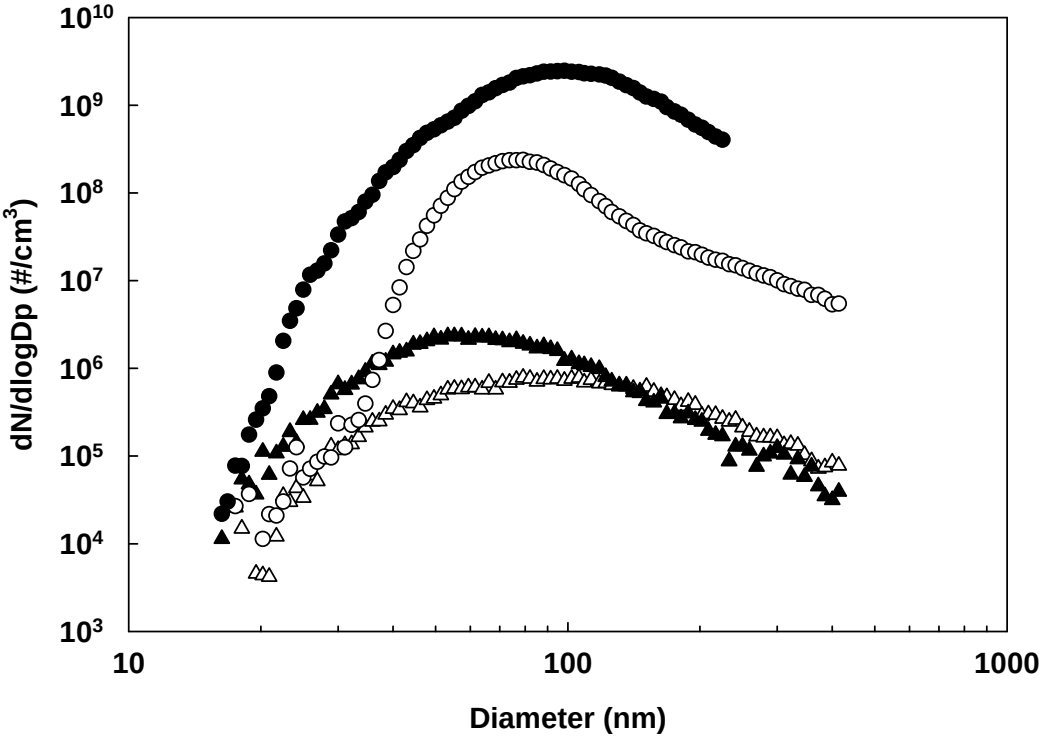

Figure 4. Comparison of particle size distributions with and without sorbent injection.
Legend: ○ EERC-ESP inlet baseline; ● EERC-ESP inlet with TTIP injection; △ EERC-ESP outlet baseline; ▲ EERC-ESP outlet with TTIP injection

Effect of Soft X-Ray Irradiation on Particle Capture

In Set IV experiments, a slipstream of flue gas was introduced to the WU-ESP with the soft X-ray emitter. The SMPS was used to measure the PSD after the WU-ESP and the effect of the soft X-ray irradiation was examined. Generally, at a given voltage of the WU-ESP, the measured current with the presence of soft X-ray irradiation is significantly higher than without. Estimated ion concentrations with and without soft X-ray were in the order of 10^{14} and 10^{12} cm^{-3}, respectively, when the WU-ESP was operated at -8.5 kV. Operational details of the WU-ESP coupled with soft X-ray, as well as the current-voltage characteristics have been reported in our previous studies[20, 26].

Figure 5 shows the effects of ESP voltage and soft X-ray radiation on particle penetration calculated by equation (1). The slipstream was first introduced from the EERC-ESP inlet and the results are shown in Figure 5a. When the soft X-ray was off and the WU-ESP was operated at -8.5 kV, its inception voltage (the voltage at which the current starts increasing at a much faster rate due to formation of the corona), the performance of the WU-ESP was similar to the EERC-ESP. The particle penetration reached a minimum ($P \approx 0.001$) in the range of 50–80 nm, increased slightly when the particle size was greater than 80 nm, and increased dramatically when the particle size decreased below 50 nm ($P = 0.07$ at 30 nm). This result again verified that ultrafine particles, especially particles less than 50 nm, are difficult to be captured by

ESPs. When the soft X-ray was turned on with the WU-ESP operated at -8.5 kV, the particle penetration decreased significantly throughout the measured size range, due to the enhanced charging of particles under X-ray radiation. The mechanism of charging the particles is due to the enhanced ion concentration and direct photo-ionization. However, on increasing the applied voltage to -10 kV, a very low penetration was observed for all sizes, similar to the -8.5 kV with soft X-ray irradiation. Hence, an increased ion concentration region in a small scale ESP can also enhance the capture of the particles smaller than 50 nm. However, this is not feasible in larger scale ESPs, as has been demonstrated in our earlier measurements and the few other pilot scale studies. Increase of applied voltage also increases power requirements, and enhances instability of operation due to sparking. Thus, the use of photo-ionization systems such as the soft X-ray would be very beneficial at enhancing ultrafine particle capture with low power consumption, and increased stability of the corona. Experiments with soft X-ray and the higher voltage (-10 kV) resulted in an interesting observation – the creation of a large number of particles. This could be due to two reasons: the soft X-ray neutralizing the ions resulting in a decrease in charging efficiency. Or, a large number of ions were escaping the ESP and entering the particle measurement device (CPC) and resulting in new particle formation due to ion-induced nucleation. Controlled studies in the laboratory could not duplicate this observation of enhanced particle formation with soft x-ray irradiation at high voltages (-10 kV). More studies are necessary to firmly understand the performance of the

soft X-ray under high voltage conditions where ion concentrations are very high. Clearly, the use of a soft X-ray system would not require the use of higher voltages; hence, this may not be a very important aspect.

Figure 5b shows the results when the slipstream was introduced to the WU-ESP from the EERC-ESP outlet, where the particle concentration was much lower than that from the EERC-ESP inlet. Applying a voltage of -8.5 kV to the WU-SEP resulted in an average particle penetration of $P \approx 0.04$ for particles smaller than 200 nm. Either turning on the X-ray or increasing the voltage to -10 kV caused remarkable decrease in particle penetration ($P < 0.01$) for particles smaller than 200 nm. The unusual large number of particles were detected again when turning the soft X-ray on at -10 kV ESP voltage.

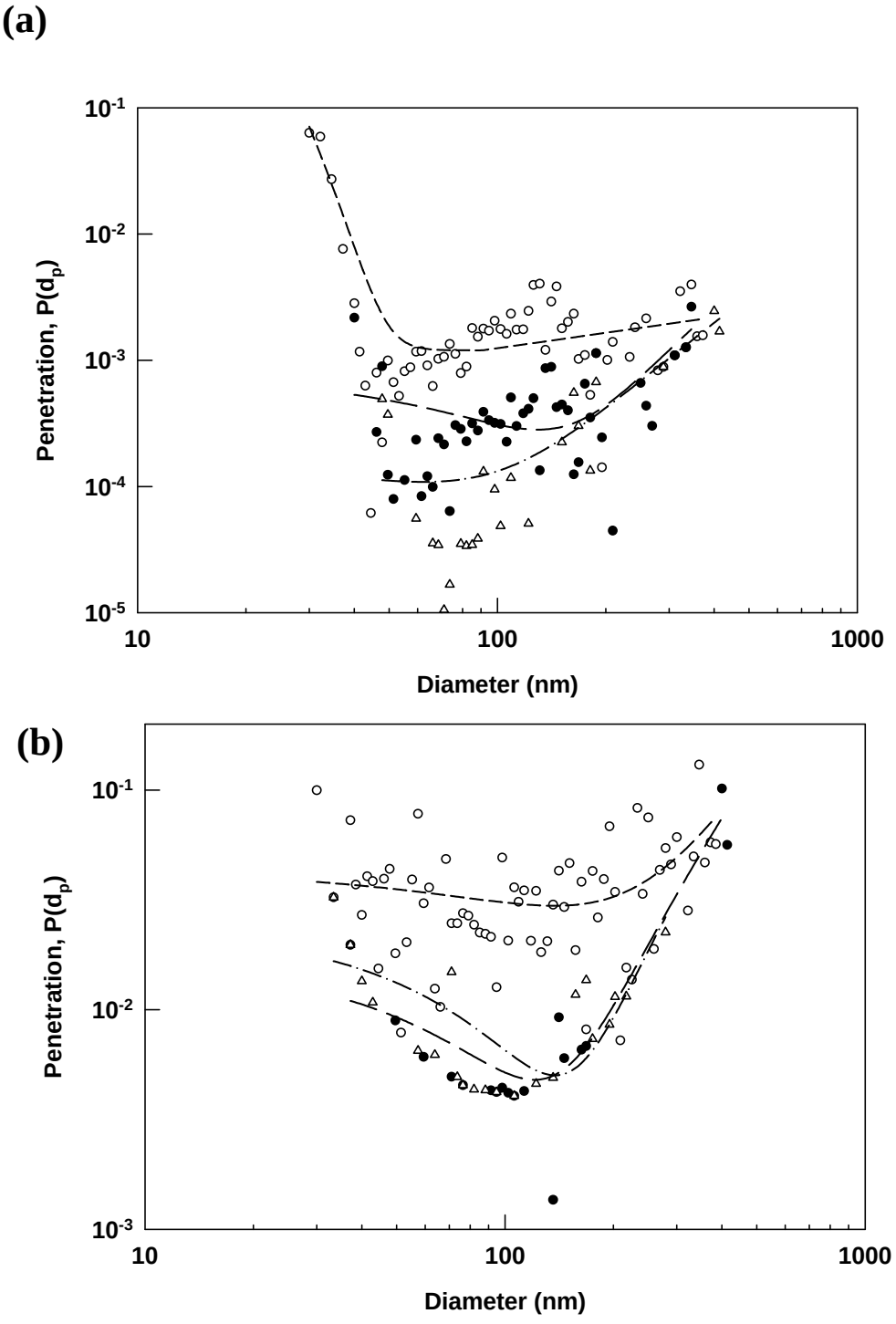

Figure 5. Effects of ESP voltage and soft X-ray irradiation on particle penetration through WU-ESP with slipstream drawn from (a) EERC-ESP inlet and (b) EERC-ESP outlet. Legend: Short dashed line & ○: -8.5 kV with X-ray off; Long dashed line & ●: -8.5 kV with X-ray on; Dash-dot line & △: -10 kV with X-ray off)

CONCLUSIONS

The particle size distributions in the range of 17 nm to 10 μm were measured in a pilot-scale (EERC) pulverized coal combustor burning a PRB subbituminous coal. At the EERC-ESP inlet, high number concentrations of ultrafine particles were observed with the mode around 75 nm. The mass concentrations at the EERC-ESP inlet followed a trimodal distribution with the modes at around 80–100 nm, 1–2 μm, and 10 μm. The penetration of ultrafine particles increased as particle size decreased below 70 nm; and significant penetration was observed for particles smaller than 50 nm. Injection of fine particle sorbents as a strategy of capture toxic metals in the flue gas needs to be designed carefully to ensure that the sorbent particles are captured in the ESP. Insufficient or partial charging of the ultrafine particles caused a decrease in their collection efficiency. The WU-ESP which is mounted with a soft X-ray emitter was used for slipstream studies and the effect of X-ray irradiation on particle capture was examined. At relatively low electrode voltages (-8.5 kV), the soft X-ray significantly enhanced particle charging and collection efficiency.

ACKNOWLEDGEMENTS

This work was supported by grants from the USDOE grant number DE-FGZ6-05NT42531 and Ameren UE, St. Louis, through contract number W-0001-06 Missouri Department of Natural Resource.

REFERENCES

1. Biswas, P.; Wu, C. Y., 2005 Critical Review: Nanoparticles and the environment. *J. Air Waste Manage. Assoc.* **2005,** 55, 708-746.

2. Liao, D. P.; Creason, J.; Shy, C.; Williams, R.; Watts, R.; Zweidinger, R., Daily variation of particulate air pollution and poor cardiac autonomic control in the elderly. *Environ. Health Perspect.* **1999,** 107, 521-525.

3. Samet, J. M.; Dominici, F.; Curriero, F. C.; Coursac, I.; Zeger, S. L., Fine particulate air pollution and mortality in 20 US Cities, 1987-1994. *N. Engl. J. Med.* **2000,** 343, 1742-1749.

4. Seaton, A.; Macnee, W.; Donaldson, K.; Godden, D., Particulate Air-Pollution and Acute Health-Effects. *Lancet* **1995,** 345, 176-178.

5. USEPA., Fed. Regist. 62 FR 38652. **1997**.

6. Davidson, C. I.; Phalen, R. F.; Solomon, P. A., Airborne particulate matter and human health: A review. *Aerosol Sci. Technol.* **2005,** 39, 737-749.

7. Zhuang, Y.; Biswas, P., Submicrometer particle formation and control in a bench-scale pulverized coal combustor. *Energy Fuels* **2001,** 15, 510-516.

8. Chang, M. C. O.; Chow, J. C.; Watson, J. G.; Hopke, P. K.; Yi, S. M.; England, G. C., Measurement of ultrafine particle size distributions from coal-, oil-, and gas-fired stationary combustion sources. *J. Air Waste Manage. Assoc.* **2004,** 54, 1494-1505.

9. Linak, W. P.; Miller, C. A., Comparison of particle size distributions and elemental partitioning from the combustion of pulverized coal and residual fuel oil. *J. Air Waste Manage. Assoc.* **2000,** 50, 1532-1544.

10. Yoo, J. I.; Seo, Y. C.; Shinagawa, T., Particle-size distributions and heavy metal partitioning in emission gas from different coal-fired power plants. *Environ. Eng. Sci.* **2005,** 22, 272-279.

11. Quann, R. J.; Neville, M.; Sarofim, A. F., A Laboratory Study of the Effect of Coal Selection on the Amount and Composition of Combustion Generated Submicron Particles. *Combust. Sci. Tech.* **1990,** 74, 245-265.

12. Senior, C. L.; Bool, L. E.; Srinivasachar, S.; Pease, B. R.; Porle, K., Pilot scale study of trace element vaporization and condensation during combustion of a pulverized sub-bituminous coal. *Fuel Process. Technol.* **2000,** 63, 149-165.

13. Huang, S. H.; Chen, C. C., Ultrafine aerosol penetration through electrostatic precipitators. *Environ. Sci. Technol.* **2002,** 36, 4625-4632.

14. Hinds, W. C., *Aerosol technology: properties, behavior, and measurement of airborne particles*. Wiley-Interscience: New York, 1982.

15. Friedlander, S. K., *Smoke, Dust, and Haze: Fundamentals of Aerosol Dynamics*. Oxford University Press: 2000.

16. Senior, C. L.; Helble, J. J.; Sarofim, A. F., Emissions of mercury, trace elements, and fine particles from stationary combustion sources. *Fuel Process. Technol.* **2000,** 65, 263-288.

17. Ylatalo, S. I.; Hautanen, J., Electrostatic precipitator penetration function for pulverized coal combustion. *Aerosol Sci. Technol.* **1998,** 29, 17-30.

18. Yoo, K. H.; Lee, J. S.; Oh, M. D., Charging and collection of submicron particles in two-stage parallel-plate electrostatic precipitators. *Aerosol Sci. Technol.* **1997,** 27, 308-323.

19. Zhuang, Y.; Kim, Y. J.; Lee, T. G.; Biswas, P., Experimental and theoretical studies of ultra-fine particle behavior in electrostatic precipitators. *J. Electrostatics* **2000,** 48, 245-260.

20. Suriyawong, A.; Hogan, C. J.; Jiang, J. K.; Biswas, P., Charged fraction and electrostatic collection of ultrafine and submicrometer particles formed during O_2-CO_2 coal combustion. *Fuel* **2008,** 87, 673-682.

21. McCain, J. D.; Gooch, J. P.; Smith, W. B., Results of field measurements of industrial particulate sources and electrostatic precipitator performance. *J. Air Pollution Control Assoc.* **1976,** 25, 117-121.

22. Biswas, P.; Wu, C. Y., Control of toxic metal emissions from combustors using sorbents: A review. *J. Air Waste Manage. Assoc.* **1998,** 48, 113-127.

23. Lee, T. G.; Biswas, P.; Hedrick, E., Comparison of Hg^0 capture efficiencies of three in situ generated sorbents. *AICHE J.* **2001,** 47, 954-961.

24. Wu, C. Y.; Lee, T. G.; Tyree, G.; Arar, E.; Biswas, P., Capture of mercury in combustion systems by in situ-generated titania particles with UV irradiation. *Environ. Eng. Sci.* **1998,** 15, 137-148.

25. Lee, T. G.; Hyun, J. E., Structural effect of the in situ generated titania on its ability to oxidize and capture the gas-phase elemental mercury. *Chemosphere* **2006,** 62, 26-33.

26. Kulkarni, P.; Namiki, N.; Otani, Y.; Biswas, P., Charging of particles in unipolar coronas irradiated by in-situ soft X-rays: enhancement of capture efficiency of ultrafine particles. *J. Aerosol Sci.* **2002,** 33, 1279-1296.

27. Hogan, C. J.; Lee, M. H.; Biswas, P., Capture of viral particles in soft X-ray-enhanced corona systems: Charge distribution and transport characteristics. *Aerosol Sci. Technol.* **2004,** 38, 475-486.

28. Jiang, J.; Lee, M. H.; Biswas, P., Model for nanoparticle charging by diffusion, direct photoionization, and thermionization mechanisms. *J. Electrostatics* **2007,** 65, 209-220.

29. Lee, H. M.; Kim, C. S.; Shimada, M.; Okuyama, K., Bipolar diffusion charging for aerosol nanoparticle measurement using a soft X-ray charger. *J. Aerosol Sci.* **2005,** 36, 813-829.

30. Biswas, P., Measurement of High Concentration and High Temperature Aerosols. In *Aerosol Measurement: Principles, Techniques and Applications*, Baron, P.; Willeke, K., Eds. John Wiley and Sons: New York, 2001; pp 903-928.

31. Lipsky, E.; Stanier, C. O.; Pandis, S. N.; Robinson, A. L., Effects of sampling conditions on the size distribution of fine particulate matter emitted from a pilot-scale pulverized-coal combustor. *Energy Fuels* **2002,** 16, 302-310.

32. Lipsky, E. M.; Pekney, N. J.; Walbert, G. F.; O'Dowd, W. J.; Freeman, M. C.; Robinson, A., Effects of dilution sampling on fine particle emissions from pulverized coal combustion. *Aerosol Sci. Technol.* **2004,** 38, 574-587.

Achariya Suriyawong

Education:

- **Doctor of Philosophy in Energy, Environmental and Chemical Engineering**
  Washington University in St. Louis, St. Louis, MO.
- **Master of Engineering in Environmental Engineering**
  Old Dominion University**,** Norfolk, VA
- **Bachelor of Engineering with Honors in Environmental Engineering**
  Chiang-mai University**,** Chiang-mai, Thailand.

Awards:

- Cecil & Bertha Winingham Lue-Hing Scholarship, Washington University in St.Louis (2004-2005)
- Otis, Dorothy and Bryce Sproul Scholarship, Washington University in St.Louis (2003-2004)
- Graduate Fellowship, University of Cincinnati (2002-2003)
- The Association of Pacific Rim University Fellowship to visit University of Oregon, USA, and Seoul National University, Korea (2002)

Professional Activities:

- **Vice President –** The Air & Waste Management Association (AWMA), Student Chapter, Washington University in St. Louis (2004–2008), led the student chapter won "The Best Student Chapter Award" in 2004 and 2005.
- **Board Member –** Committee on Environmental Quality (CEQ), Washington University in St. Louis (2004-2009)
- **Board Member and Event Chair** – Association of Graduate Engineering Students (AGES), Washington University in St.Louis (2005-2006)
- **Vice President –** The Environmental Engineering Student Association (ENVESA), Washington University in St. Louis (2004 – 2006)

Reviewer:

1. Fuel Processing Technology
2. Journal of the Air & Waste Management Association

Peer-reviewed Publications:

1. **Suriyawong, A.**, Gamble, M., Lee, M.H., Axelbaum, R.L., and Biswas P., Submicrometer Particle Formation and Mercury Speciation under O_2-CO_2 Coal Combustion, *Energy and Fuels,* 20(6), 2357-2363, 2006.
2. **Suriyawong, A.**, Hogan C., Jiang, J., and Biswas P., Charged Fraction and Electrostatic Capture of Ultrafine and Submicrometer Particles Formed under O_2-CO_2 Coal Combustion, *Fuel*, 87, 673-682, 2008.
3. Worathanakul, P., Kongkachuichay, P., Noel, J.D., **Suriyawong, A.**, Giammar, D. E., and Biswas P., Evaluation of Various Nanostructured Sorbents for Elemental Mercury Capture in Different Bed Reactors, *Environmental Engineering Science*, 25 (7), 1061-1070, 2008.
4. Li, Y., Daukoru, M., **Suriyawong, A.**, Biswas, P., Mercury Capture Using Potassium Iodine: Bench-Scale and Pilot-Scales Studies, *Energy and Fuels*, 23 (1), 236–243, 2009.
5. Li, Y., **Suriyawong, A.,** Daukoru, M., Zhuang, Y., and Biswas, P., Measurement and Capture of Fine and Ultrafine Particles from a Pilot-Scale Pulverized Coal Combustor, *Journal of Air and Waste Management Association*,59(5), 553-559, 2009.
6. **Suriyawong, A.**, Magee, R., Peebles K.O., and Biswas P. Energy Recycling by Co-combustion of Recovery Paint Solids from Automobile Paint Operations and Coal. *Journal of Air and Waste Management Association*, 59(5), 560-567, 2009.
7. **Suriyawong, A.**, Smallwood, M., Li, Y., and Biswas, P., Mercury Capture by Nano-structured Titanium Dioxide Sorbent during Coal Combustion: Lab-scale to Pilot-scale Studies, *Aerosol and Air Quality Research,* in-press.
8. **Suriyawong, A.**, Chen, X., and Biswas P., Nano-structured Sorbent Injection Strategies for Heavy Metal Capture in Combustion Exhausts, *Aerosol Science and Technology,* submitted.
9. **Suriyawong, A.**, and Biswas P., Homogeneous Mercury Oxidation under Simulated Exhaust Gas of Oxy-coal Combustion. *Chemosphere,* in preparation.

Selected Conference Presentations:

1. Li, Y., Daukoru, M., **Suriyawong, A.,** Biswas, P. Bench- and Pilot-Scale Studies on Mercury Removal by Potassium Iodide In Coal-Fired Flue Gas. *2008 AIChE Annual Meeting*, Philadelphia, PA, November 16-21, 2008
2. Li, Y. **Suriyawong, A.**, Daukoru, M., Zhuang, Y., Biswas, P. Pilot-Scale Study of Particle Size Distributions and Particulate Emission Control Strategies for a Pulverized Coal Combustor. *The 27th American Association for Aerosol Research Annual Conference*, Orlando, FL, October 20-24, 2008.
3. **Suriyawong, A.**, Skeen, S., Roseman, A., Axelbaum, R., and Biswas P., Characterization of Aerosols and Mercury under Enriched Oxygen Coal Combustion, *2007 AIChE Annual Meeting*, Salt Lake City, UT, 2007.

4. Biswas, P., **Suriyawong, A.,** Giammar, D.E., Noel, J.D., Applications of Nanoparticles and Nanostructured Films Synthesized by Aerosol Routes for Environmental and Renewable Energy Technologies, *The 233rd American Chemical Society National Meeting, Chicago*, IL, 2007.
5. Xu C., Biswas, P., Jeong S.K., Lee, M.H., Kim, S.B., **Suriyawong, A.**, Higginson, K., and Shah, A. Heavy Metal Formation in Munition Waste Incinerators and Nanostructured Sorbents for Their Control, *The 233rd American Chemical Society National Meeting, Chicago*, IL, 2007.
6. **Suriyawong, A.**, Skeen, S., Axelbaum, R., and Biswas P., Submicrometer Particle Formation during Oxy-coal Combustion in Multi-scale Coal Combustion Systems, *The 23rd International Pittsburgh Coal Conference, Pittsburgh, PA, 2006.*
7. **Suriyawong, A.**, and Biswas P., Homogeneous Mercury Speciation in Oxy-Coal Combustion Simulated Flue Gas, *The 23rd International Pittsburgh Coal Conference*, Pittsburgh, PA, 2006.
8. **Suriyawong, A.**, Hogan,C., and Biswas P., Submicrometer and Ultrafine Particle Charging and Collection in Different Carrier Gases, *The 7th International Aerosol Conference*, St. Paul, MN, 2006.
9. Noel, J.D., **Suriyawong, A.**, Biswas, P., and Giammar, D.E., Partitioning and Speciation of Mercury during Coal Combustion with Addition of a Titanium Dioxide Sorbent, *The 232nd American Chemical Society National Meeting*, San Francisco, CA, 2006.
10. **Suriyawong, A.**, Gamble, M., Lee, M.H., and Biswas P., Submicrometer Particle Formation under Enriched Oxygen Coal Combustion, *The 22nd International Pittsburgh Coal Conference*, Pittsburgh, PA, 2005.
11. **Suriyawong, A.**, Smallwood, M., Noel, J.D., Lee, M.H., Giammar, D.E., and Biswas, P., A Strategic Approach for Optimizing the Use of Sorbents for Mercury Removal from Coal-burning Utilities, *The Air and Waste Management Association's 98th Annual Conference and Exhibition*, Minneapolis, MN, 2005.
12. Noel, J.D., Smallwood, M., Mohatt, J.L., **Suriyawong, A.**, Giammar, D.E., and Biswas, P., Evaluation of Mercury Binding Mechanisms to Coal Combustion By-products through a Sequential Extraction Process. *The 229th American Chemical Society National Meeting*, San Diego, CA, 2005.
13. **Suriyawong, A.,** Smallwood, M., Noel, J.D., Lee, M.H., Giammar, D.E., and Biswas, P., Nanostructured-sorbents for Heavy Metals Emissions Control – A Review. *The 229th American Chemical Society National Meeting*, San Diego, CA, 2005.
14. Saiyasitpanich, P., **Suriyawong, A.,** and Keener, T.C., The Effects of Different Applied Loads on Sulfur Content in Diesel Fuel on Particulate Matters Emission from Diesel Engine, *The Air and Waste Management Association's 96th Annual Conference and Exhibition*, San Diego, CA, 2003.
15. Noel, J.D., **Suriyawong, A.**, and Worathanakul, P. Mercury Speciation from Coal Burning Utilities and Capture Using Inorganic Sorbents. *St. Louis Air and Waste Management Association Meeting*, St. Louis, MO, 2007.